Active Bandsaw Control

Ra Cleave

A thesis presented for the degree of
Doctor of Philosophy
in
Mechanical Engineering
at the
University of Canterbury,
Christchurch, New Zealand.

12 October 2001

ENGINEERING
LIBRARY
TS
850
.C623
2001

ABSTRACT

This thesis investigates the modelling and active control of narrow and wide bandsaw blades, with application to the sawmilling industry. Strings, beams and plates are considered in the modelling work, with advances made in the modelling of exogenous influences and multispan saw blades. Beams and plates are considered in the control work, with classical and optimal controllers considered. Importance is placed on closed-loop robustness with respect to parametric variation, closed-loop performance in vibration suppression and in providing a physically realisable solution to the control problem.

In the string and beam work exogenous influences are modelled by pointwise and distributed forces, including; lateral stiffness, lateral damping and a "follower" force that comprises an in-line and a lateral component. Pointwise actuation and arbitrary disturbance forces as well as pointwise sensing are also included. Successful comparison with results of other contributors, as well as comprehensive experimental work, validates the modelling. The experimental validation also concentrates on system damping and the integration of sensing and actuation.

The plate work considers the single-span cutting blade presented by other contributors, and extends it to include saw guides and partial-span cutting forces. These cutting forces include damping, stiffness and follower loads, and act over a partial length of the cutting edge. While this three span model is not experimentally verified, it is shown to produce credible results.

The control work is in two parts. A comprehensive study of the robustness of various controllers with respect to translation speed and band tension is performed for the beam; theoretically and experimentally. The theory-practice gap was small regarding trends in robustness, but unmodelled effects such as the band weld degraded the agreement of absolute values at higher band speeds. Classical controllers were abandoned due to high frequency noise amplification, and a near optimal $\mathcal{H}_\infty$ loop shaping controller was found to be superior to others of its type and various $\mathcal{H}_2$ formulations. The plate work is entirely theoretical, but uses the same actuator and sensor dynamics that were successful in the beam work to maintain the physical feasability of the controllers. Both single span and multispan systems are considered, with the central cutting span of the blade being controlled via actuation

16 APR 2002

and sensing of the upstream and downstream noncutting spans. Robustness studies were conducted, with satisfactory robustness achieved with respect to a large number of parameters. Furthermore, substantial increases in maximum allowable cutting loads were achieved, as well as reduced vibration energy.

The control actuation used in this work is electromagnetic force, with eddy current sensors used to sense the blade position. A noncontacting collocated actuator-sensor was developed that, with appropriate control of the winding current, performed excellently in both the validation and control work. Further development of this could lead to a versatile tool in experimental vibration analysis and distributed systems control research and applications.

ACKNOWLEDGEMENTS

First and foremost I extend my thanks and appreciation to Dr Christopher Damaren, my mentor and supervisor. His enthusiasm for engineering science, dedication as a supervisor and knowledge of the subject have been invaluable and inspirational to me.

I also thank Emeritus Professor Harry McCallion for his humour, approachability and ability to ask the trickiest of questions.

This work would not have even started without the ongoing work of Dr Lan Le-Ngoc from Industrial Research Limited. Dr Le-Ngoc's technical support and advice throughout the entirety of my research, and continual supply of equipment has been greatly appreciated.

Dr Ian Huntsman I thank for taking over my supervision when Dr Damaren left the University. His encouragement as well as his checks on my progress were both welcome and effective.

Throughout this work my closest technical colleague has been Andrew Cree. The many discussions about controls implementation and problems thereof were irreplaceable. Andrew is also responsible, in his role as a departmental technician, for designing and building much of the specialised electronic equipment and software I required in this work.

To my office mates and true compatriots Sue Wilkinson and Charles Breurkes I extend huge thanks. I shall always keep with me the shared memories of coffee breaks, frustrating times, successful times and times when the brain simply felt too full. Also, thanks to Jonathan Harrington for years of late night discussions and cups of tea.

For their financial support I would like to thank the Department of Mechanical Engineering at the University of Canterbury, Industrial Research Limited in Christchurch, New Zealand and the Todd Foundation of Todd Energy, New Zealand. Without such support this work could never have been done; I now look forward to the time when I can be part of an institution that supports such efforts.

On a different level I thank all those people who have given me personal support and encouragement. Firstly to Leonie, Paul and Peter, my parents, who have

shown unending support throughout. Also to Miriam, Fiona, Kate and the Wednesday crowd, for their sacrifices, support and comments like " . . . are you finished yet?" The list of course goes on; my apologies to those I have omitted.

CONTENTS

LIST OF FIGURES

LIST OF TABLES

Chapter 1

INTRODUCTION

1.1 BANDSAWS

Bandsaws, or more properly, bandmills, are the most common machine used to produce boards from logs in the sawmilling industry. The first saws were built in the mid 1800s but produced unsatisfactory lumber in comparison to sash saws and circular saws. The 1880s saw some earnest yet ad-hoc developments and soon after this time bandsaws superseded circular saws as the most common means of cutting logs. A bandmill comprises the structure and machinery required to strain, drive and track a bandsaw, which is the continuous loop of steel that actually cuts the timber. A modern example is pictured in Figure 1.1. Logs are fed through the saw using feed machinery. For a thin band of steel to remain on the band wheels it must be under some strain. The mechanism that provides such strain is the most important part of a bandmill, as this maintains blade position in the face of varying cutting loads, feed loads and operating speeds.

Bandmill strain. Throughout much of the 1900s blade tension was maintained by pivoting the top wheel shaft on a rocker arm, with the weight of the wheel assembly reacted by a linkage attached to an arm and mass arrangement. This simple counterweight mechanism worked well but lacked mechanical damping (aside from friction), and was replaced in the 1970's by air-strain mechanisms that reacted the wheel assembly mass using compressed air. The compressed air improved damping characteristics and removed the inertia of the hanging weights, thus improving response times. Since then actively controlled hydraulic systems have evolved, further improving dynamic response and damping.

Wheels. The wheels of a bandmill are usually spoked and made from cast iron. The faces of the wheels are usually crowned, so that the middle width is a larger diameter than the edges. This aids tracking as the band tends to run at the highest point. The top wheel can often be tilted about the horizontal axis that is perpendicular to the

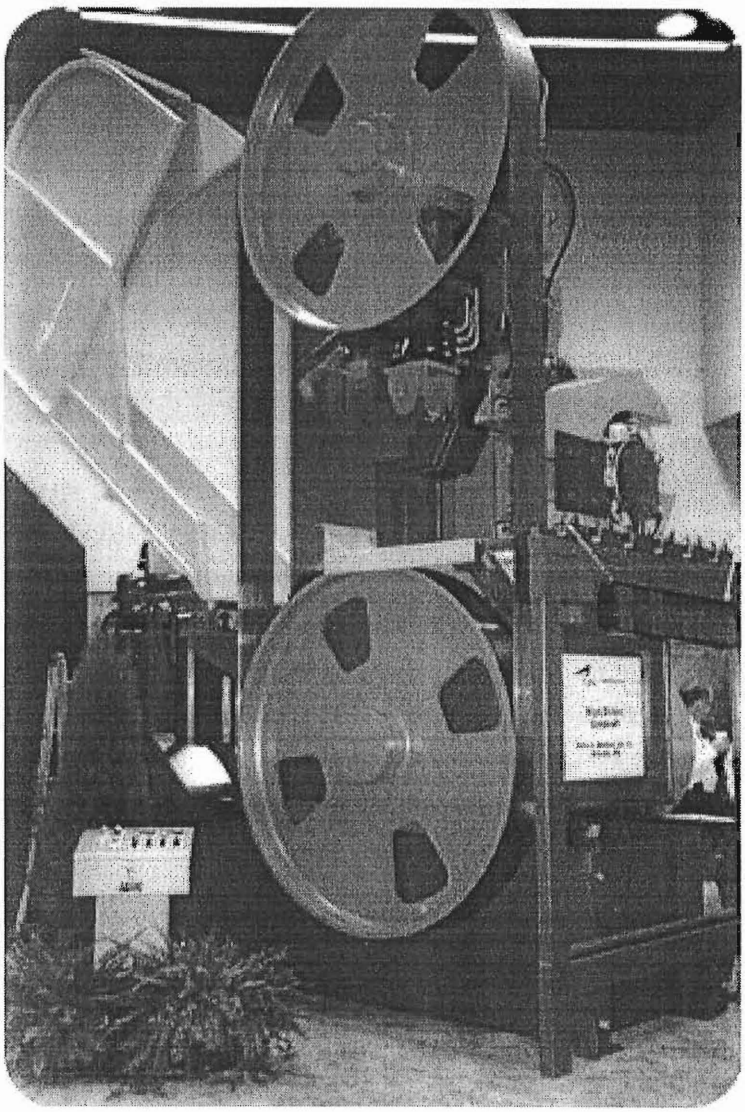

Figure 1.1: *Modern bandmill.*

axis of rotation. Such wheel tilting does improve saw tracking, but is most commonly used when the saw tensioning (defined below) has become unsatisfactory.

Bandsaw. The bandsaw itself has also received technological attention over the years. The major factors affecting bandsaw performance are the "set" of the teeth and the tensioning of the blade. Initially bandsaws were made with offset teeth (called "spring set"), however this was soon replaced with swage set teeth, which are symmetrical about the centre plane of the blade but flared so that the tooth width, or kerf width, is larger than the blade thickness. In the early 1980s tipped teeth were being used and now most large bandsaws use stellite tipped teeth, which offer better wear resistance but must be welded onto the blade. The cutting edge is heated more than the trailing edge during operation, and the lengthening caused by this heating is offset by lengthening the trailing edge prior to use. This is in addition to a lengthening of the middle width to fit the crowning of the band wheels. Such relative lengthening is termed "tensioning" in the art of saw-doctoring.

Figure 1.2 defines some of the parameters involved in the cutting teeth. The gullet size is also important to blade stability. Gullets that are too small fill with saw dust quickly, and "clumps" of excess dust get forced between the side of the blade and the sawn timber, creating unwanted lateral loads.

Guides. Bandsaws usually have two guides, one on either side of the workpiece. For increased saw stability they are placed as close as possible to the workpiece, and the top guide is often adjustable — sometimes automatically so. Thin bandsaws often use roller guides, while wide bandsaws use low friction, wear resistant materials. The guides enact a constant lateral pressure to the blade so the cutting span is offset from the line joining the band wheels. Some guides are lubricated, with the translation of the blade over the oil film creating a fluid bearing. Some saw millers quote superior performance without guides; however this is not the norm.

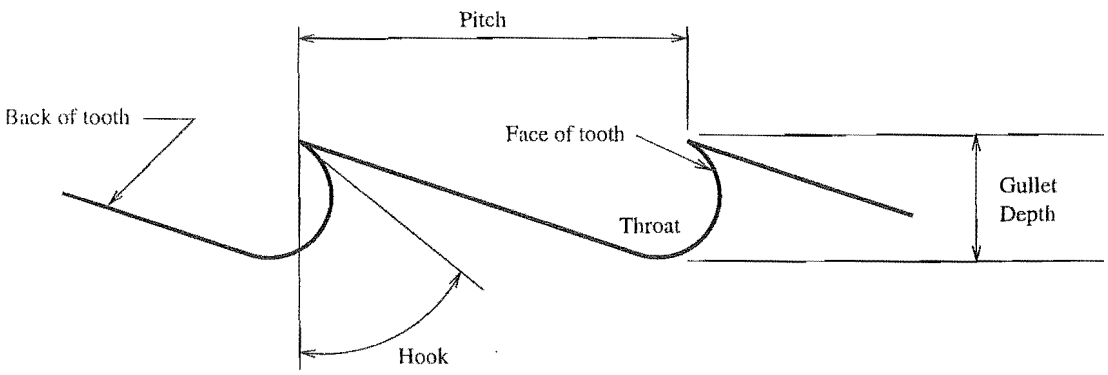

Figure 1.2: *Bandsaw tooth parameters.*

Wijesinge (1998) is an excellent reference containing introductory, historical and operational information on the bandmill and bandsaw.

1.2 ANALYTICAL TREATMENT OF AXIALLY MOVING CONTINUA

Not until the pioneering work of Mote in 1965 did analytical science enter the previous century of ad-hoc optimisation that bandsaws had undergone. Mote's work was seminal in the wide bandsaw arena but relied upon the work of Skutch (1897) which was the first theoretical investigation of axially moving continua. Mote has been a principal author up to the present day, with other notable contributors being Naguleswaren, Ulsoy, Wickert, Wang, Okai, Kimura, Yokai, Lengoc, McCallion, Lehmann and Hutton. Full literature reviews are presented in Chapters 2 and 3.

Work on the active control of axially moving continua has been considered since the late 1980s, with a large number of authors contributing over this time. A full literature review of this work is given in Chapter 5.

1.3 MOTIVATION FOR FURTHER IMPROVEMENT

From the foreword in Wijesinge (1998), typical yields of the British Columbian sawmilling industry in 1968 were approximately 40% (from log to finished product). By 1972 this figure was 53.3%, and today yields of 70% are required to remain competitive. In contrast, yields in tropical countries throughout Africa, Asia and Latin America are currently around 40-55% (Loehnertz et al., 1994). As well as high yield, high throughput is of major concern to saw millers. A limiting factor to high throughput is the speed with which logs and boards can be fed through the machines (known as the feed rate or speed) before saw stability is compromised. Also, machine down times reduce throughput, so long blade and guide lives are important.

To improve yield and throughput, the following may be reduced:

- **Kerf width.** Thinner kerfs obviously mean less waste, and is limited by the allowable stress of the blade and teeth. In aeronautical and other high cost markets kerf becomes especially important.

- **Washboarding.** This phenomenon causes a pattern on the sawn lumber that resembles a washboard, and is caused by high frequency blade vibration. Removal of this pattern requires increased machining and hence more waste.

- **Snake.** This is a low frequency "snaking" of the blade along the length of the log or board, again producing excess waste.

- **Snipe.** A sudden change in blade position at the start or end of the cut, requiring the removal of the ends of boards.

- **Wedging.** This is a change in blade position throughout the depth of the cut, causing wedge shaped boards and again increased waste.

These phenomena are all related to blade stability, so increasing blade stability increases yield. This is the major motivation for this research into the active control of sawblade vibration.

1.4 CHAPTER PRÉCIS

1.4.1 Strings and Beams

Hamilton's principle is applied to the kinetic, potential and non-conservative energies of the travelling string. The string is subjected to distributed and pointwise cutting and actuator forces, and the deflection is discretised using the method of Ritz. Pointwise sensing is also discussed. Material stiffness is then added and results for both the string and beam given. This work is not new but formulates and solves the string problem in detail, and combines and compares the work of other contributors.

1.4.2 Plates

This chapter presents the major contribution of this work to the analysis of bandsaws. Firstly the literature is surveyed and background theory developed. The non-conservative "follower force" used by other contributors to model cutting loads is then formulated to act only along a partial length of the leading edge of the blade. The interaction between the body of the blade and the sawn lumber surface is neglected throughout. This is done as a matter of project scope and to restrict the modelling to the linear domain. Also, guides are modelled so that the three spans of the saw between the wheels are considered. This is done to provide a model that allows investigation of quelling vibrations in the centre (cutting) span by sensing and actuation of the upstream and downstream spans. In addition to the follower force, additional stiffening and damping of the cutting edge is modelled. Where appropriate, results are compared with those of other contributors, however results for the full three span system are delayed until the control work.

1.4.3 Experimental apparatus

This chapter develops a noncontacting collocated actuator-sensor, and uses it to validate the string, beam and plate models. The actuation is electromagnetic, and provides the first step toward an industrial solution. The validation work is comprehensive, covering speed effects, bandmill tension, damping and actuator-sensor dynamics. The damping and actuator-sensor work is particularly important to the ensuing control work.

1.4.4 Control

Investigation of the active and passive control of axially moving continua first received attention in the late 1980s, and the work to date is summarised. This work focuses on the active control of bandsaws, using modern, model-based controllers. The bandsaw problem is cast as a control problem, and the required control theories discussed with continual application to the bandmilling arena. This work focuses on using lateral control to further stabilise the blade; this is a matter of project scope and potential application to other fields. Further improvements to current strain mechanisms, including activation is of course feasible, but not considered here.

An experimental study of the moving beam is presented using the experimental rig of the previous chapter. The robustness of controllers with respect to bandmill tension and blade speed is investigated, as well as the accuracy of control simulations. A theoretical robustness study of the moving plate is also considered. The single and three span cutting plate models are then placed in feedback loops, and performance and robustness considered with respect to band speed, bandmill tension, and in the case of the multispan system, the position of the upper guide.

Chapter 2

STRINGS AND BEAMS

The vibration of axially moving continua has been studied for over a hundred years, beginning with strings and progressing to beams and plates. Applications are tape ribbons, belts, pipes containing flowing fluids, power transmission chains and belts, aerial cable ways and bandsaws. This chapter formulates linear finite-dimensional models for translating strings and beams that are subject to exogenous influences, and examines the resulting behaviours. The exogenous influences describe effects such as forces from read/write heads on magnetic tapes, cutting forces on bandsaw blades and control actions.

Skutch (1897) was the first to solve the moving string problem, and since then many have contributed to the area. The effect of translation upon vibration frequencies and modal forms was first considered using linear theory and then using nonlinear methods. Thorough reviews of the literature may be found in Mote (1972), Wickert and Mote (1988), and references here will only be made that are pertinent to the discussion at hand. Miranker (1960) showed that there exists a periodic transfer of energy into and out of the span of a travelling string, and Mote and Wickert (1989) quantified this energy transfer for various boundary conditions. Because this transfer is of second order in the lateral component of the translation of the string it is ignored throughout this treatment. Exogenous influences first received attention in 1967 by Alspaugh, who considered the torsional vibration of a moving strip under the influence of a pointwise edge load. Also, the effect of read-write heads on magnetic tapes was considered by Ono (1979), and later Chonan (1986) considered a moving strip subjected to a stationary lateral load system. Wickert and Mote (1990) provided a general solution to axially moving strings subjected to arbitrary but mathematically tractable lateral loads.

Following is the formulation and solution of models for strings and beams that are subject to pointwise and distributed loads describing viscous damping, inertial loads, spring forces and follower forces (which were first applied to axially moving continua by Lengoc and McCallion (1995c)). It provides a unification and extension to the contributions of the aforementioned references. For completeness the formu-

lation and solution of motion equations is detailed in this chapter but omitted in the next.

2.1 THE TRANSLATING STRING

Figure 2.1 shows a tensioned string translating at speed c between two frictionless guides and vibrating in the wx-plane. The string has mass density ρ, cross-sectional area A, is laterally loaded by a distributed force $f_w(x,t)$, and is under tension $R(x,c,t)$ which varies due to in-line loads $f_x(x,t)$ and the transport speed c.

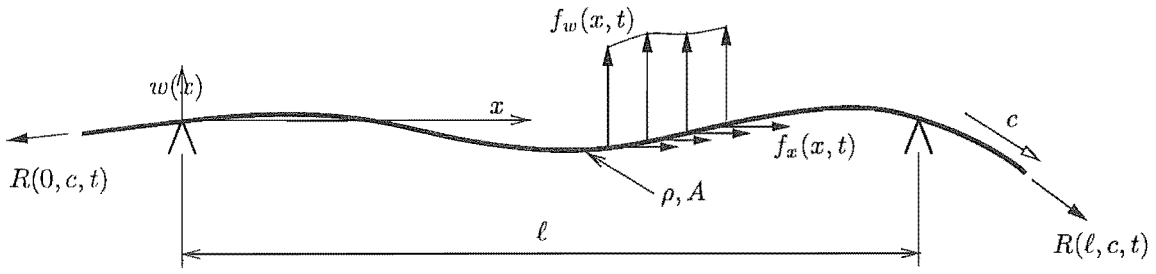

Figure 2.1: *The translating tensioned string.*

Hamilton's principle may be used to generate motion equations for the various systems considered. Hamilton's principle states that the true motion of a conservative system throughout the interval of time $[t_1, t_2]$ is such that the integral

$$I = \int_{t_1}^{t_2} \mathcal{L} dt \tag{2.1}$$

is rendered stationary. Here $\mathcal{L} = \mathcal{T} - \mathcal{V}$ is called the *Lagrangian*, and is the difference between the system's kinetic energy, $\mathcal{T}$, and its potential energy, $\mathcal{V}$. The kinetic energy is assumed to depend on the positions and velocities of the components of the system, whereas the potential energy depends only upon the positions. If the position of the system can be uniquely specified by as many geometrical quantities as there are degrees of freedom for the system, then the Lagrangian may be written in terms of these quantities, which are called *generalised coordinates* of the system.

From the definition of the Lagrangian it is apparent that the extremisation of (2.1) seeks the motion of the system that best equalises the kinetic and potential energies throughout $[t_1, t_2]$. Extremisation of such integrals with respect to functions rather than simple coordinates requires the calculus of variations (Weinstock, 1952, Hildebrand, 1965) rather than the differential calculus. If the quantity I is stationary for the actual motion of the system then its *variation* (written δI) with respect to neigh-

bouring motions must be zero. Then, Hamilton's principle may be expressed as

$$\delta I = \delta \int_{t_1}^{t_2} \mathcal{L} dt = \int_{t_1}^{t_2} \{\delta \mathcal{T} - \delta \mathcal{V}\} dt, \tag{2.2}$$

where $\delta \mathcal{T}$ and $\delta \mathcal{V}$ are variations (with respect to neighbouring motions) in the kinetic and potential energies of the system. In nonconservative systems Hamilton's *extended* principle, which includes the virtual work done by nonconservative forces, is used. This may be written as

$$\int_{t_1}^{t_2} \{\delta \mathcal{T} - \delta \mathcal{V} + \delta \mathcal{W}_{nc}\} dt = 0, \tag{2.3}$$

where $\delta \mathcal{W}_{nc}$ is the virtual work done on the system by nonconservative forces. In the development below the conservative work caused by exogenous lateral forces is combined into the virtual work term, rather than into the potential energy. This is to clarify the development, and so henceforth this term shall be labelled $\delta \mathcal{W}_{ex}$. Once expressions for the system energies and virtual work are found, (2.3) may be solved to find the governing equations of motion.

2.1.1 Kinetic and potential energies

The velocity of an element of the moving string comprises components from the x- and w-directions. The lateral (w-direction) component arises from the instantaneous vibration velocity, $\partial w/\partial t$, and the w-component of the transport velocity of the string, $c(\partial w/\partial x)$. The x-component comes from the translation speed c, and thus the kinetic energy $\mathcal{T}$, may be written as

$$\mathcal{T} = \tfrac{1}{2} \int_0^{\ell} \rho A \left[c^2 + \left(\frac{\partial w}{\partial t} + c \frac{\partial w}{\partial x} \right)^2 \right] dx. \tag{2.4}$$

The absence of material stiffness in a string means the strain due to vibration is simply caused by the length of the string changing. The resulting strain energy is given by

$$\mathcal{V} = \tfrac{1}{2} \int_0^{\ell} R(x, c) \left(\frac{\partial w}{\partial x} \right)^2 dx, \tag{2.5}$$

where $R(x, c)$ is the tension along the length of string.

2.1.2 Exogenous forces

The work done by exogenous forces $f_{ex} = f_w(x,t)$ in displacing the string by a virtual amount δw is given by

$$\delta \mathcal{W}_{ex} = \int_0^\ell f_{ex} \delta w dx, \tag{2.6}$$

where expressions for these forces depends on the system being analysed. Figure 2.2

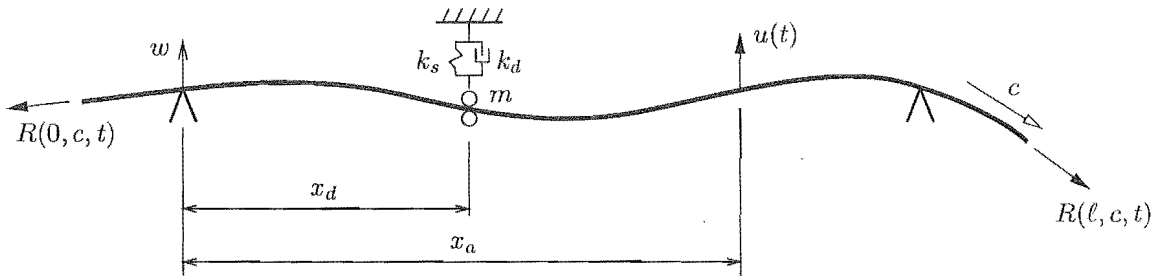

Figure 2.2: *Stationary mass-spring-damper system attached mid-span.*

shows a string in contact with a mass-spring-damper located part way along the span. The spring provides a force in proportion to but acting against the deflection at the point of contact, while the damper produces one acting in proportion to but against the lateral velocity of the string. Also, friction caused by the contact forces produces a force in line with and against the direction of travel of the string, which again acts at the point of contact. Follower forces act so that the direction of force follows the slope of the deflected shape. The initial application of this idea was missile stability, where follower forces acting at one end of a free-free beam were used to model thrust force. This follower force has a component in the x-direction, detailed below, and a component in the w-direction which depends upon the slope of the string. Also shown in Figure 2.2 is a time varying force, $u(t)$, acting at $x = x_a$, which when combined with the other lateral loads gives the exogenous force

$$f_{ex} = -\left[k_s w + k_d \frac{\partial w}{\partial t} + k_f \frac{\partial w}{\partial x}\right] \bar{\delta}(x - x_d) + u(t)\bar{\delta}(x - x_a), \tag{2.7}$$

where k_s, k_d[1] and k_f are the spring, damping and friction force coefficients respectively, and $\bar{\delta}(x - x_d)$ is Dirac's delta function located at x_d. Equation 2.7 is a fair model for a contacting passive actuator, or the heads of high speed tape drives. However, more applicable to the sawmilling industry is the situation where the forces act in a

[1] Some authors considered the damping force to be proportional to $-(\partial w/\partial t)$ (as shown in (2.7)) as well as in proportion to $-(\partial w/\partial t + c\partial w/\partial x)$.

distributed fashion along the entire length ℓ. Then (2.7) becomes

$$f_{ex} = -k_s w - k_d \frac{\partial w}{\partial t} - k_f \frac{\partial w}{\partial x} + u(t)\bar{\delta}(x - x_a), \tag{2.8}$$

with the obvious changes in units of k_s, k_d and k_f.

2.1.3 Other effects

Variation of tension with speed

Maintaining the tension of wheel and band systems is achieved by a variety of straining mechanisms depending on the application. In bandmills the blade is dynamically tensioned through dampened counterbalances attached to the nondriving wheel. This mechanism removes large fluctuations in the tension due to speed changes and cutting influences. Mote (1965) first considered the relationship of tension to speed, finding that

$$R(c) = R_o + \eta \rho A c^2, \tag{2.9}$$

which can be explained by the acceleration of the blade moving around the wheels.

For a bandmill with wheels fixed in space the centripetal acceleration of the blade around the wheels requires a force which reduces the interference pressure between the wheels and the blade. As the overall band length is not changing the tension remains at the initial value R_o. If the interference pressure remains constant (by the use of a counterweight mechanism applied to one wheel), then the centripetal acceleration is reacted by an increase in band tension, this increase being equal to $\rho A c^2$. Thus a value of $\eta = 0$ in (2.9) describes the situation for fixed wheels, while a value of $\eta = 1$ describes the counterweight mechanism. If a finite stiffness is applied to one wheel assembly then the centripetal acceleration is reacted partially by an increase in tension and partially by a decrease in the force on the wheel assembly, and so a value of $0 < \eta < 1$ is appropriate. Mote (1965) details calculation of η given a certain stiffness of the wheel assembly.

Variation of tension along the length

The x-component of the follower force discussed in the previous section gives rise to a change in tension along the length, ℓ. This change may be approximated in the distributed loading as a linear increase in tension along the length, and in the pointwise loading as a step change at $x = x_d$. For a simple counterweight mechanism the tension at the upstream ($x = 0$) boundary must remain constant, and so the cutting

load must be reacted by an increase in the tension at the downstream ($x = \ell$) boundary, which is supplied by the drive motor. So, the tension at $x = 0$ (the nondriving end) increases from the nominal value $R_o + \rho Ac^2$ to $R_o + \rho Ac^2 + k_f$ at $x = \ell$. If the strain mechanism is an air strain or clamped system, then the blade tension at the undriven pulley boundary may vary, and thus the cutting force may reduce the tension at this boundary. The drive motor must still react the cutting load, however the overall bandmill tension (and therefore blade tension) is reduced.

For point loading the increase in tension will be a step change at $x = x_d$. This step may be modelled using the Heaviside function $H(x - x_d)$, so that (2.5) becomes

$$\mathcal{V} = \tfrac{1}{2}\int_0^\ell \left[R_o - \iota k_f + \eta\rho Ac^2 + k_f H(x - x_d)\right]\left(\frac{\partial w}{\partial x}\right)^2 dx. \tag{2.10}$$

where the dependence on transport speed has been added, and the ιk_f term allows for a hanging weight system when $\iota = 0$ and fixed wheels when $\iota = 1$.

In the case of distributed loading the tension is assumed to vary linearly along the length, giving

$$\mathcal{V} = \tfrac{1}{2}\int_0^\ell \left[R_o - \iota k_f + \eta\rho Ac^2 + k_f \frac{x}{\ell}\right]\left(\frac{\partial w}{\partial x}\right)^2 dx \tag{2.11}$$

for the potential energy.

Added mass

The mass of the mass-spring-damper arrangement simply adds to the system's kinetic energy, again using a delta function to provide the pointwise effect. With mass m_{msd} the kinetic energy contributed by the mass-spring-damper is

$$\mathcal{T}_{msd} = \tfrac{1}{2}\int_o^\ell m_{msd}\left(\frac{\partial w}{\partial t}\right)^2 \bar{\delta}(x - x_d)dx, \tag{2.12}$$

where m_{msd} is a lumped mass under point loading and a mass per unit length for distributed loading. Naturally the $\bar{\delta}$ function is omitted in the distributed case. Equation (2.12) may be added to (2.4) giving the total system kinetic energy.

2.1.4 Application of Hamilton's principle

With the system energies and exogenous influences accounted for, Hamilton's extended principle may be applied. Two approaches are shown below. The first performs the calculus of variations by substituting the energy expressions into Hamilton's extended principle and taking the variation in the displacement w, yielding a partial differential equation describing the system. The second method substitutes

a *Ritz* discretisation for the deflection w into the energy expressions and then performs the variation with respect to the coefficients of the discretisation. The equations of the first method are useful in considering the form of the forces on the string. However, the set of ordinary differential equations produced by the second method are more applicable to higher order systems, more complicated forces and controller formulation.

Method 1

Considering distributed loading, equations (2.4), (2.12), (2.11) and (2.8) may be substituted into Hamilton's extended principle (2.3), to give

$$\begin{aligned}\int_{t_1}^{t_2}\int_0^{\ell}\Bigg\{&\delta\Bigg[\tfrac{1}{2}\rho Ac^2+\tfrac{1}{2}m_{msd}\left(\frac{\partial w}{\partial t}\right)^2+\tfrac{1}{2}\rho A\left(\frac{\partial w}{\partial t}\right)^2+\rho Ac\frac{\partial w}{\partial t}\frac{\partial w}{\partial x}\\&+\tfrac{1}{2}\rho Ac^2\left(\frac{\partial w}{\partial x}\right)^2\Bigg]-\delta\Bigg[\tfrac{1}{2}\left(R_o-\iota k_f+\eta\rho Ac^2\right)\left(\frac{\partial w}{\partial x}\right)^2+\tfrac{1}{2}k_f\frac{x}{\ell}\left(\frac{\partial w}{\partial x}\right)^2\Bigg]\\&-\left[k_s w+k_d\frac{\partial w}{\partial t}+k_f\frac{\partial w}{\partial x}-u(t)\bar{\delta}(x-x_a)\right]\delta w\Bigg\}\,dxdt=0,\end{aligned}\tag{2.13}$$

which after performing the variation on each term (methods are analogous to those of the differential operator $\frac{d}{dw}$) becomes

$$\begin{aligned}\int_{t_1}^{t_2}\int_0^{\ell}\Bigg\{&\rho A\frac{\partial w}{\partial t}\frac{\partial}{\partial t}(\delta w)+\rho Ac\left(\frac{\partial w}{\partial t}\frac{\partial}{\partial x}(\delta w)+\frac{\partial w}{\partial x}\frac{\partial}{\partial t}(\delta w)\right)+\rho Ac^2\frac{\partial w}{\partial x}\frac{\partial}{\partial x}(\delta w)\\&+m_{msd}\frac{\partial w}{\partial t}\frac{\partial}{\partial t}(\delta w)-(R_o-\iota k_f+\eta\rho Ac^2)\frac{\partial w}{\partial x}\frac{\partial}{\partial x}(\delta w)-k_f\frac{x}{\ell}\frac{\partial w}{\partial x}\frac{\partial}{\partial x}(\delta w)\Bigg]\\&-\left[k_s w+k_d\frac{\partial w}{\partial t}+k_f\frac{\partial w}{\partial x}-u(t)\bar{\delta}(x-x_a)\right]\delta w\Bigg\}\,dxdt=0.\end{aligned}\tag{2.14}$$

Each term in (2.14) involving partial derivatives of δw may be integrated by parts to form

$$\begin{aligned}-\int_{t_1}^{t_2}\int_0^{\ell}\Bigg\{&(\rho A+m_{msd})\frac{\partial^2 w}{\partial t^2}+2\rho Ac\frac{\partial^2 w}{\partial t\partial x}\\&+((1-\eta)\rho Ac^2-R_o+\iota k_f)\frac{\partial^2 w}{\partial x^2}-k_f\left(\frac{1}{\ell}\frac{\partial w}{\partial x}+\frac{x}{\ell}\frac{\partial^2 w}{\partial x^2}\right)\\&+k_s w+k_d\frac{\partial w}{\partial t}+k_f\frac{\partial w}{\partial x}-u(t)\bar{\delta}(x-x_a)\Bigg\}\,\delta w dxdt=0,\end{aligned}\tag{2.15}$$

where the integrated terms arising from integration by parts all vanish because $\delta w = 0$ at $t = t_1, t_2$ since w is prescribed, and also at $x = 0, \ell$ due to the simply supported nature of the problem. Since δw is arbitrary between t_1 and t_2 the terms inside the braces of (2.15) must sum to zero, and this provides the equation of motion for the free vibration of the taut string under distributed loading.

If the energy and virtual work expressions for point loading ((2.4), (2.12), (2.10) and (2.7)) are substituted into Hamilton's principle and the first variation taken, we have

$$\int_{t_1}^{t_2}\int_0^{\ell}\Big\{\rho A\frac{\partial w}{\partial t}\frac{\partial}{\partial t}(\delta w)+\rho Ac\Big(\frac{\partial w}{\partial t}\frac{\partial}{\partial x}(\delta w)+\frac{\partial w}{\partial x}\frac{\partial}{\partial t}(\delta w)\Big)$$
$$+\rho Ac^2\frac{\partial w}{\partial x}\frac{\partial}{\partial x}(\delta w)+m_{msd}\frac{\partial w}{\partial t}\frac{\partial}{\partial t}(\delta w)\bar{\delta}(x-x_d)$$
$$-(R_o-\iota k_f+\eta\rho Ac^2)\frac{\partial w}{\partial x}\frac{\partial}{\partial x}(\delta w)-k_fH(x-x_d)\frac{\partial w}{\partial x}\frac{\partial}{\partial x}(\delta w)$$
$$-\Big[k_sw+k_d\frac{\partial w}{\partial t}+k_f\frac{\partial w}{\partial x}\Big]\bar{\delta}(x-x_d)\delta w+u(t)\bar{\delta}(x-x_a)\delta w\Big\}\,dxdt=0,$$

which after integration by parts becomes

$$\int_{t_1}^{t_2}\int_0^{\ell}\Big\{\rho A\frac{\partial^2 w}{\partial t^2}+m_{msd}\bar{\delta}(x-x_d)\frac{\partial^2 w}{\partial t^2}+2\rho Ac\frac{\partial^2 w}{\partial t\partial x}$$
$$+((1-\eta)\rho Ac^2-R_o+\iota k_f)\frac{\partial^2 w}{\partial x^2}-\Big[k_fH(x-x_d)\frac{\partial^2 w}{\partial x^2}+k_f\frac{\partial w}{\partial x}\bar{\delta}(x-x_d)\Big] \qquad (2.16)$$
$$+\Big[k_sw+k_d\frac{\partial w}{\partial t}+k_f\frac{\partial w}{\partial x}\Big]\bar{\delta}(x-x_d)-u(t)\bar{\delta}(x-x_a)\Big\}\,\delta w dxdt=0$$

where the term in braces of (2.16) gives the equation of motion for the string under point loading described.

In the conservative case and some simple nonconservative formulations a general, closed form solution of the moving string is possible. However, for complicated loads and with the aim of control implementation an approximate, finite dimensional solution is more appropriate, for which the following method is more appropriate.

Method 2

Instead of applying Hamilton's principle to the energy and exogenous work functions directly, a discretisation of the deflection w may be made, and Hamilton's principle applied using the approximate energies. The Ritz discretisation is a linear combination of m functions, such that

$$w(x,t)=\sum_{\alpha}^{m}\phi_\alpha(x)q_\alpha(t), \qquad (2.17)$$

where the functions $\phi_\alpha(x)$ are prescribed functions that form a basis for the approximate modes of vibration, and each satisfy the geometric boundary conditions of the problem. The actual form of these functions is discussed in Section 2.1.5. This method describes the energy terms in terms of *generalised coordinates*, these be-

ing the coefficients of the $q_\alpha(t)$ functions in the Ritz expansion. So, proceeding as outlined, the integrand in (2.4) may be expanded with the actuator mass taken into account, and the deflection expansion substituted to give

$$\begin{aligned}\mathcal{T} &= \tfrac{1}{2}\int_0^\ell \left[\rho A\left(\frac{\partial w}{\partial t}\right)^2 + 2\rho Ac\frac{\partial w}{\partial t}\frac{\partial w}{\partial x} + \rho Ac^2\left(\frac{\partial w}{\partial x}\right)^2 + m_{msd}\left(\frac{\partial w}{\partial t}\right)^2\right]dx \\ &= \tfrac{1}{2}\sum_\alpha^m\sum_\beta^m\left[(\rho A + m_{msd})\dot{q}_\alpha\int_0^\ell \phi_\alpha\phi_\beta dx\dot{q}_\beta + 2\rho Ac\dot{q}_\alpha\int_0^\ell \phi_\alpha\phi'_\beta dx q_\beta\right. \\ &\quad \left. + \rho Ac^2 q_\alpha\int_0^\ell \phi'_\alpha\phi'_\beta dx q_\beta\right] \\ &= \tfrac{1}{2}\left[\rho A\dot{\mathbf{q}}^T\mathbf{M}\dot{\mathbf{q}} + m_{msd}\dot{\mathbf{q}}^T\mathbf{M}_{msd}\dot{\mathbf{q}} + 2\rho Ac\dot{\mathbf{q}}^T\mathbf{G}\mathbf{q} + \rho Ac^2\mathbf{q}^T\mathbf{K}_o\mathbf{q}\right], \end{aligned} \tag{2.18}$$

where the pointwise form of the actuator mass may be used instead of the distributed form shown here. The actual entries in each matrix in (2.18) may be inferred from the previous equality, eg. $M_{\alpha\beta} = \int_0^\ell \phi_\alpha\phi_\beta dx$, where $M_{\alpha\beta}$ is the entry of $\mathbf{M}$ in the α'th row and β'th column. Upon expansion and substitution of the Ritz expansion the potential energy expression of (2.5) becomes

$$\mathcal{V} = \tfrac{1}{2}\sum_\alpha^m\sum_\beta^m q_\alpha\int_0^\ell \left[R_o - \iota k_f + \eta\rho Ac^2 + k_f\left(\frac{x}{\ell}\right)\right]\phi'_\alpha\phi'_\beta dx q_\beta, \tag{2.19}$$

in the distributed case, or for point loading

$$\mathcal{V} = \tfrac{1}{2}\sum_\alpha^m\sum_\beta^m q_\alpha\int_0^\ell \left[R_o - \iota k_f + \eta\rho Ac^2 + k_f\big(H(x-x_d)\big)\right]\phi'_\alpha\phi'_\beta dx q_\beta, \tag{2.20}$$

each of which may be expressed as

$$\mathcal{V} = \tfrac{1}{2}(R_o - \iota k_f + \eta\rho Ac^2)\mathbf{q}^T\mathbf{K}_o\mathbf{q} + k_f\mathbf{q}^T\mathbf{K}_{ft}\mathbf{q}. \tag{2.21}$$

Using a similar approach the pointwise and distributed virtual work equations ((2.7) and (2.8)) can be expressed as

$$\delta\mathcal{W}_{ex} = -k_s\delta\mathbf{q}^T\mathbf{K}_s\mathbf{q} - k_d\delta\mathbf{q}^T\mathbf{D}_d\dot{\mathbf{q}} - k_f\delta\mathbf{q}^T\mathbf{K}_f\mathbf{q} + \delta\mathbf{q}^T\mathbf{B}_u u, \tag{2.22}$$

where the terms comprising each matrix can be easily inferrred from the original work expressions. Substituting equations (2.18), (2.21) and (2.22) into Hamilton's

extended principle (2.3) and performing the variation yields

$$\begin{aligned}
\delta I &= \tfrac{1}{2}\int_{t_1}^{t_2}\Big\{\delta\Big(\rho A\ell c^2 + \rho A\dot{\mathbf{q}}^T\mathbf{M}\dot{\mathbf{q}} + m_{msd}\dot{\mathbf{q}}^T\mathbf{M}\dot{\mathbf{q}} + 2\rho Ac\dot{\mathbf{q}}^T\mathbf{G}\mathbf{q} \\
&\quad +\rho Ac^2\mathbf{q}^T\mathbf{K}_o\mathbf{q}\Big) - \delta\Big((R_o - \iota k_f + \eta\rho Ac^2)\mathbf{q}^T\mathbf{K}_o\mathbf{q} + k_f\mathbf{q}^T\mathbf{K}_{ft}\mathbf{q}\Big) \\
&\quad -2\Big[k_s\delta\mathbf{q}^T\mathbf{K}_s\mathbf{q} + k_d\delta\mathbf{q}^T\mathbf{D}_d\dot{\mathbf{q}} + k_f\delta\mathbf{q}^T\mathbf{K}_f\mathbf{q} - \mathbf{B}_u u\Big]\Big\}dt \\
&= \tfrac{1}{2}\int_{t_1}^{t_2}\Big\{\rho A\delta\dot{\mathbf{q}}^T(2\mathbf{M}\dot{\mathbf{q}}) + m_{msd}\delta\dot{\mathbf{q}}^T(2\mathbf{M}_{msd}\dot{\mathbf{q}}) + 2\rho Ac\delta\dot{\mathbf{q}}^T(\mathbf{G}\mathbf{q}) \\
&\quad + 2\rho Ac\delta\mathbf{q}^T(\mathbf{G}^T\dot{\mathbf{q}}) + \rho Ac^2\delta\mathbf{q}^T(2\mathbf{K}_o\mathbf{q})\big] - (R_o - \iota k_f + \eta\rho Ac^2)\delta\mathbf{q}^T(2\mathbf{K}_o\mathbf{q}) \\
&\quad -k_f\delta\mathbf{q}^T(2\mathbf{K}_{ft}\mathbf{q}) - 2\delta\mathbf{q}^T\big[k_s\mathbf{K}_s\mathbf{q} + k_d\delta\mathbf{q}^T\mathbf{D}_d\dot{\mathbf{q}} + k_f\mathbf{K}_f\mathbf{q} - \mathbf{B}_u u\big]\Big\}dt \\
&= \int_{t_1}^{t_2}\Big\{\rho A\frac{\partial}{\partial t}(\delta\mathbf{q}^T)(\mathbf{M} + \mathbf{M}_{msd})\frac{\partial\mathbf{q}}{\partial t} + \rho Ac\frac{\partial}{\partial t}(\delta\mathbf{q}^T)\mathbf{G}\mathbf{q} \\
&\quad - \rho Ac\delta\mathbf{q}^T\mathbf{G}\frac{\partial\mathbf{q}}{\partial t} - (R_o - \iota k_f - (1-\eta)\rho Ac^2)\delta\mathbf{q}^T\mathbf{K}_o\mathbf{q} - k_f\delta\mathbf{q}^T\mathbf{K}_{ft}\mathbf{q} \\
&\quad -\delta\mathbf{q}^T\big[k_s\mathbf{K}_s\mathbf{q} + k_d\delta\mathbf{q}^T\mathbf{D}_d\dot{\mathbf{q}} + k_f\mathbf{K}_f\mathbf{q} - \mathbf{B}_u u\big]\Big\}dt \qquad (2.23) \\
&= 0
\end{aligned}$$

Integrating the first two terms of (2.23) by parts gives

$$\begin{aligned}
&\Big[\rho A\delta\mathbf{q}^T(\mathbf{M} + \mathbf{M}_{msd})\frac{\partial\mathbf{q}}{\partial t}\Big]_{t_1}^{t_2} - \int_{t_1}^{t_2}\rho A\delta\mathbf{q}^T(\mathbf{M} + \mathbf{M}_{msd})\frac{\partial^2\mathbf{q}}{\partial t^2}dt \\
&\quad + \Big[\rho Ac\delta\mathbf{q}^T\mathbf{G}\mathbf{q}\Big]_{t_1}^{t_2} - \int_{t_1}^{t_2}\rho Ac\delta\mathbf{q}^T\mathbf{G}\frac{\partial\mathbf{q}}{\partial t}dt \\
&\quad - \int_{t_1}^{t_2}\Big\{\rho A\delta\mathbf{q}^T\mathbf{G}\frac{\partial\mathbf{q}}{\partial t} + (R_o - \iota k_f - (1-\eta)\rho Ac^2)\delta\mathbf{q}^T\mathbf{K}_o\mathbf{q} + k_f\delta\mathbf{q}^T\mathbf{K}_{ft}\mathbf{q} \qquad (2.24) \\
&\quad -\delta\mathbf{q}^T\big[k_s\mathbf{K}_s\mathbf{q} + k_d\delta\mathbf{q}^T\mathbf{D}_d\dot{\mathbf{q}} + k_f\mathbf{K}_f\mathbf{q} - \mathbf{B}_u u\big]\Big\}dt = 0,
\end{aligned}$$

for which the terms evaluated at $t = t_1, t_2$ equal zero as the variations $\delta\mathbf{q}$ all equal zero at these limits. So (2.24) becomes

$$\begin{aligned}
&-\int_{t_1}^{t_2}\delta\mathbf{q}^T\big\{\rho A(\mathbf{M} + \mathbf{M}_{msd})\ddot{\mathbf{q}} + \big[2\rho Ac\mathbf{G} + k_d\mathbf{D}_d\big]\dot{\mathbf{q}} + \big[(R_o - \iota k_f - (1-\eta)\rho Ac^2)\mathbf{K}_o \\
&+k_f\mathbf{K}_{ft} + k_s\mathbf{K}_s + k_f\mathbf{K}_f\big]\mathbf{q} - u\mathbf{B}_u\big\}dt = 0, \qquad (2.25)
\end{aligned}$$

and as the variations $\delta\mathbf{q}^T$ are all arbitrary throughout the interval $t = t_1, t_2$ the term in braces must equal zero. This then gives the m approximate equations of motion

for the free vibration of the taut string

$$\rho A(\mathbf{M}+\mathbf{M}_{msd})\ddot{\mathbf{q}}+\left[2\rho Ac\mathbf{G}+k_d\mathbf{D}_d\right]\dot{\mathbf{q}}+\left[(R_o-\iota k_f-(1-\eta)\rho Ac^2)\mathbf{K}_o\right.$$
$$\left.+k_f\mathbf{K}_{ft}+k_s\mathbf{K}_s+k_f\mathbf{K}_f\right]\mathbf{q}=u\mathbf{B}_u. \tag{2.26}$$

The distributed formulation of (2.26) is equivalent to the distributed equation of motion found using the first method, as is the pointwise formulation with the pointwise equation of the first method. The mass matrix $\mathbf{M}+\mathbf{M}_{msd}$ is symmetric and positive definite, the gyric matrix $2\rho Ac\mathbf{G}$ is skew-symmetric, and $\mathbf{D}_d$ symmetric and positive definite. The stiffness matrices $\mathbf{K}_o$, $\mathbf{K}_{ft}$ and $\mathbf{K}_s$ are symmetric and positive definite while $\mathbf{K}_f$ is skew-symmetric and positive semi-definite.

2.1.5 Discretisation of the deflection

Both polynomials and sinusoids have been used as basis functions in this work, so that comparisons between the two types may be made and suitability as regards their use in axially moving continua assessed. The sinusoids are of the form

$$\phi_\alpha=\sin\left(\frac{\alpha\pi x}{\ell}\right), \tag{2.27}$$

and are the eigenfunctions of the stationary problem. The polynomials used are those discussed by Bhat (1985), and are generated as follows. A polynomial that satisfies the geometric boundary conditions of the problem at hand (in this case the conditions describing simple supports at $x=0,\ell$) is found, and used to generate others using a Gram-Schmidt process. In this case the starting polynomial is

$$\phi_1=\frac{x}{\ell}-2\frac{x^3}{\ell^3}+\frac{x^4}{\ell^4}, \tag{2.28}$$

which is used to generate as many higher order functions as required. The effects of this are considered in the following section. Once generated, the functions may be normalised to produce an orthonormal set.

2.1.6 Solution of approximate equations of motion

The approximate equation of motion (2.26) may be made more tractable (and more amenable to feedback control synthesis) by transforming the equations of motion so that the coefficient matrix of the second derivative of the generalised coordinates becomes the identity matrix. To fix ideas, consider (2.26), which may be written as

$$\rho A(\mathbf{M}+\mathbf{M}_{msd})\ddot{\mathbf{q}}+\left[2\rho Ac\mathbf{G}+k_d\mathbf{D}_d\right]\dot{\mathbf{q}}+\mathbf{K}\mathbf{q}=u\mathbf{B}_u, \tag{2.29}$$

where $\mathbf{K} = (R_o - \iota k_f - (1-\eta)\rho A c^2)\mathbf{K}_o + k_f\mathbf{K}_{ft} + k_s\mathbf{K}_s + k_f\mathbf{K}_f$. Considering the stationary, unforced case, we have

$$\rho A(\mathbf{M} + \mathbf{M}_{msd})\ddot{\mathbf{q}} = -R_o\mathbf{K}_o\mathbf{q}, \tag{2.30}$$

which may be cast as an eigenproblem by seeking solutions of the form of $\mathbf{q}(t) = \Re\{\hat{\mathbf{q}}e^{\lambda t}\}$. The associated eigenvectors may be normalised relative to the mass term so that $\rho A\mathbf{E}^T(\mathbf{M}+\mathbf{M}_{msd})\mathbf{E} = \mathbf{I}$, where $\mathbf{E}$ is a matrix with the (normalised) eigenvectors as columns. If (2.29) is premultiplied by $\mathbf{E}^T$ and the change of variables $\mathbf{q} = \mathbf{E}\eta$ made then

$$\ddot{\eta} + \left[2\rho Ac\mathbf{E}^T\mathbf{G}\mathbf{E} + k_d\mathbf{E}^T\mathbf{D}_d\mathbf{E}\right]\dot{\eta} + \mathbf{E}^T\mathbf{K}\mathbf{E}\eta = \mathbf{E}^T\mathbf{B}_u u, \tag{2.31}$$

which may be presented in the first order state-space form of

$$\begin{aligned}\dot{\mathbf{x}} &= \underbrace{\begin{bmatrix}\mathbf{O} & \mathbf{I}\\ -\mathbf{E}^T\mathbf{K}\mathbf{E} & -(2\rho Ac\mathbf{E}^T\mathbf{G}\mathbf{E} + k_d\mathbf{E}^T\mathbf{D}_d\mathbf{E})\end{bmatrix}}_{\mathbf{A}}\mathbf{x} + \underbrace{\begin{bmatrix}\mathbf{O}\\ \mathbf{E}^T\mathbf{B}_u\end{bmatrix}}_{\mathbf{B}}u\\ &= \mathbf{A}\mathbf{x} + \mathbf{B}u,\end{aligned} \tag{2.32}$$

where $\mathbf{x} = \begin{bmatrix}\eta^T & \dot{\eta}^T\end{bmatrix}^T$. The modal transformation matrix $\mathbf{E}$ has been proposed by Damaren and Le-Ngoc (2000) as a method of model reduction. Firstly, $\mathbf{E}$ is partitioned such that $\mathbf{E} = \begin{bmatrix}\mathbf{E}_c & \mathbf{E}_r\end{bmatrix}$, where $\mathbf{E}_c$ comprises the eigenvectors of the first N_d stationary modes. Then, the premultiplication by $\begin{bmatrix}\mathbf{E}_c^T & \mathbf{E}_r^T\end{bmatrix}^T$ and substitution of $\mathbf{q} = \begin{bmatrix}\mathbf{E}_c & \mathbf{E}_r\end{bmatrix}\begin{bmatrix}\eta_c\\ \eta_r\end{bmatrix}$ in (2.29) gives the partitioned version of (2.31)

$$\begin{bmatrix}\ddot{\eta}_c\\ \ddot{\eta}_r\end{bmatrix} + \left(2\rho Ac\begin{bmatrix}\mathbf{G}_{11} & \mathbf{G}_{12}\\ \mathbf{G}_{21} & \mathbf{G}_{22}\end{bmatrix} + k_d\begin{bmatrix}\mathbf{G}_{d,11} & \mathbf{D}_{d,12}\\ \mathbf{D}_{d,21} & \mathbf{D}_{d,22}\end{bmatrix}\right)\begin{bmatrix}\dot{\eta}_c\\ \dot{\eta}_r\end{bmatrix} + \begin{bmatrix}\mathbf{K}_{11} & \mathbf{K}_{12}\\ \mathbf{K}_{21} & \mathbf{K}_{22}\end{bmatrix}\begin{bmatrix}\eta_c\\ \eta_r\end{bmatrix} = \begin{bmatrix}\mathbf{B}_{u,1}\\ \mathbf{B}_{u,2}\end{bmatrix}u, \tag{2.33}$$

where, for instance, $\mathbf{G}_{11} = \mathbf{E}_c^T\mathbf{G}\mathbf{E}_c$. The blocks corresponding exclusively to η_c may be taken to give the first order, dimension $2N_d$ system

$$\dot{\mathbf{x}} = \underbrace{\begin{bmatrix}\mathbf{O} & \mathbf{I}\\ -\mathbf{K}_{11} & -(2\rho Ac\mathbf{G}_{11} + k_d\mathbf{D}_{d,11})\end{bmatrix}}_{\mathbf{A}}\mathbf{x} + \underbrace{\begin{bmatrix}\mathbf{O}\\ \mathbf{B}_{u,1}\end{bmatrix}}_{\mathbf{B}}u,$$

where $\mathbf{x}$ is now defined as $\mathbf{x} = \begin{bmatrix}\eta_c^T & \dot{\eta}_c^T\end{bmatrix}^T$. So the reduction ignores the modes higher in frequency than the N_d'th one, and also terms coupling the higher modes with the lower ones, such as $\mathbf{G}_{12} = \mathbf{E}_c^T\mathbf{G}\mathbf{E}_r$. Ignoring this coupling is of course valid

in the stationary case, where the modal coordinates are by definition orthogonal, however will deteriorate with inherent coupling of the system. This reduction is revisited in the control work; until then all state-space matrices should be considered to describe the full order dynamics of (2.32). For $u(t) = 0$, (2.32) may be solved using standard eigenanalysis and results for the free vibration of the travelling string considered.

2.1.7 Sensing

One matter left to resolve is sensing the blade dynamics. This is covered in detail in subsequent chapters but introduced here. For now it is assumed that a finite number of pointwise measurements of either the deflection or the time rate of change of this deflection are available, anywhere along the string. Defining the output of the k'th sensor as $y_k(t)$, position sensing may be incorporated into the model via

$$y_k(t) = w\bar{\delta}(x - x_s) = \sum_{\alpha=1}^{m} \phi_\alpha(x_s) q_\alpha. \tag{2.34}$$

This may be expressed in matrix form by

$$\mathbf{y} = \hat{\mathbf{C}}\mathbf{q}, \tag{2.35}$$

where the number of rows of $\hat{\mathbf{C}}$ equals the number of sensors. In terms of the state space description we may write

$$\mathbf{y} = \mathbf{C}\mathbf{x}, \tag{2.36}$$

where $\mathbf{C} = \begin{bmatrix} \hat{\mathbf{C}} & \mathbf{O} \end{bmatrix}$. For velocity measurements $\mathbf{C} = \begin{bmatrix} \mathbf{O} & \hat{\mathbf{C}} \end{bmatrix}$. As an aside, there may be more than one input $u(t)$, so that $\mathbf{u} = col\{u_k\}$, with the number of columns of B equaling the number of inputs.

2.2 THE TRANSLATING BEAM: ADDING MATERIAL STIFFNESS

If the material has sufficient bending stiffness then the formulation of the potential energy (2.5) must be altered, becoming

$$\mathcal{V} = \tfrac{1}{2} \int_0^\ell R(x, c) \left(\frac{\partial w}{\partial x} \right)^2 dx + \tfrac{1}{2} \int_0^\ell EI \left(\frac{\partial^2 w}{\partial x^2} \right)^2 dx. \tag{2.37}$$

Obviously, when the tension term is much larger than the bending term the effect of bending strain becomes negligible and string-like behaviour dominates.

2.3 RESULTS

The results in this chapter serve three main purposes; to present the major results of axially moving continua to validate the model with respect to the literature and to present and ratify the results stemming from the new formulations. In Chapter 4 these results are compared with experimental data.

For consistency with following chapters the results are all for a band of steel with the properties shown in Table 2.1. Where the parameters are changed from those shown here special mention is made.

2.3.1 Preliminary results

To fix ideas, consider the equation of motion for the translating string under no loading (Equation (2.15) with $\eta = k_s = k_d = k_f = 0$),

$$\rho A\left(\frac{\partial^2 w}{\partial t^2} + 2c\frac{\partial^2 w}{\partial t \partial x} + c^2\frac{\partial^2 w}{\partial x^2}\right) - R_o\frac{\partial^2 w}{\partial x^2} = 0. \tag{2.38}$$

The bracketed term includes the radial, Coriolis and centripetal accelerations respectively while the last term gives the restoring force due to the deflection $w(x)$. Every term is in phase or in anti-phase with the deflection w, except the Coriolis acceleration which lags the deflection by 90°. This produces complex modal forms such that the real and imaginary parts are 90° out of phase, each part being made up of combinations of either even (symmetric) or odd (asymmetric) eigenfunctions of the stationary problem. This (a)symmetry is a compelling reason to use these eigenfunctions as the basis for the translating case. Once substituted into (2.17) the actual vibrations of the system are of nonconstant phase, and hence the waves propagate from one end of the string to the other, moving in the direction opposite to the transport speed (see Figure 2.3). Detailed discussion of this phenomena can be found in Wickert and Mote (1990) and Lengoc and McCallion (1996b,a).

The i'th exact free vibration frequencies for a moving string is given by (Lengoc and McCallion, 1996b)

$$\omega_i = \frac{i\pi}{a\ell}(a+c)(a-c), \tag{2.39}$$

where $a = \sqrt{\frac{R_o - \iota k_f}{\rho A}}$ is the material wave velocity and represents the critical speed at which all modes of vibration undergo divergent instability. Figure 2.4 plots the first

Table 2.1: *Nominal parameters for results of Chapter 2.*

ℓ	b	h	E	R_o	m	η	ι	x_d
600mm	22mm	0.6mm	205GPa	150N	10	0	1	0.3ℓ

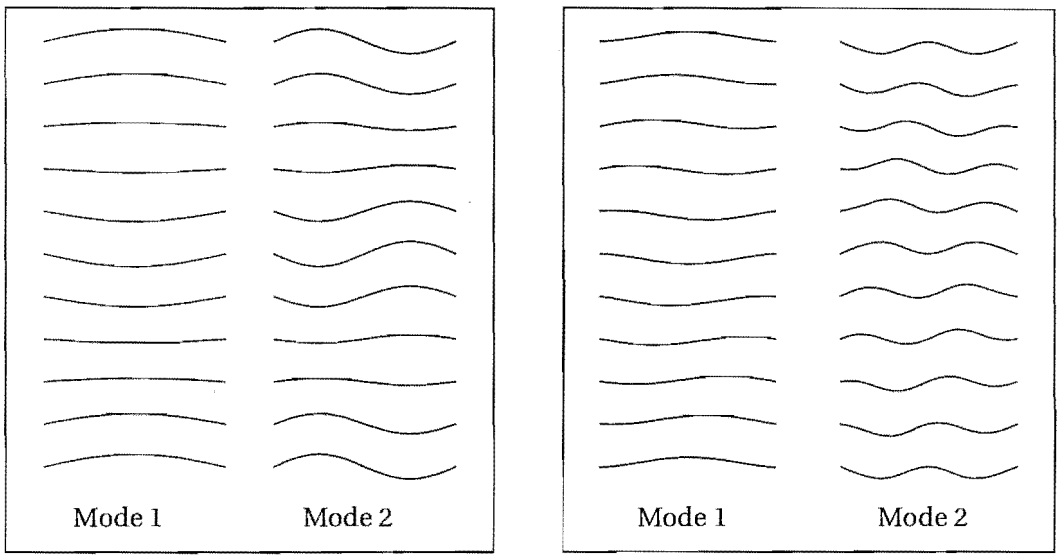

(a) Stationary form.

(b) Moving form (axial motion is from left to right).

Figure 2.3: *Phase propagation in the first and second modes of vibration. Each set shows one full cycle of vibration.*

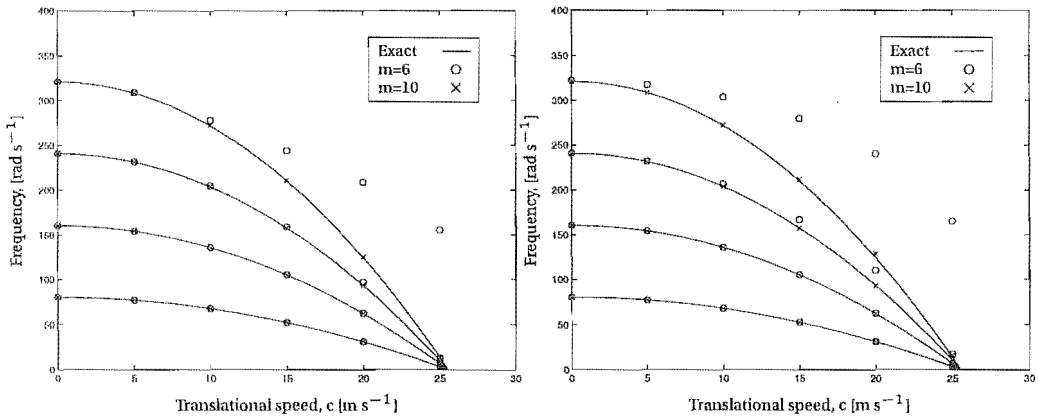

(a) Sinusoidal basis functions

(b) Polynomial basis functions

Figure 2.4: *Approximate and exact frequencies versus speed for a translating string.*

four curves given by (2.39) and compares them against the approximate results produced by the modelling of Section 2.1. Of note is the way that the sinusoids produce better approximations than the polynomials for a given number of basis functions, and that with higher numbers of basis functions the approximation accuracy is also improved.

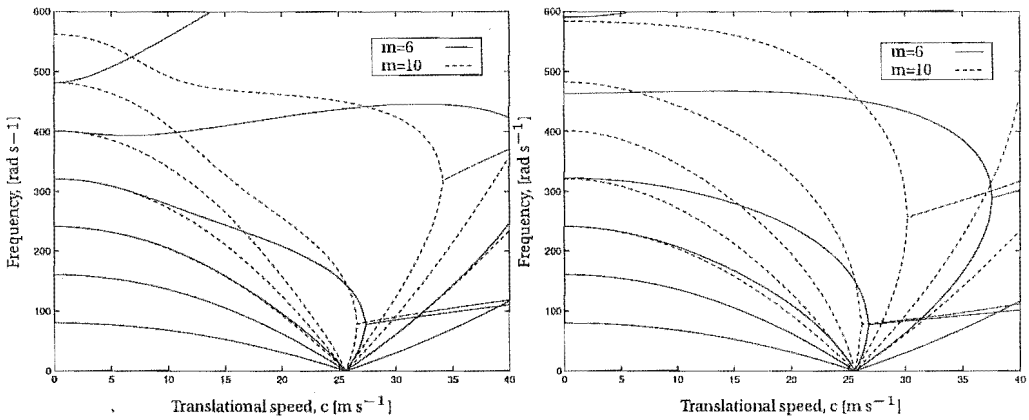

(a) Sinusoidal basis functions (b) Polynomial basis functions

Figure 2.5: *Approximate frequency versus speed for a translating string.*

The behaviour beyond the critical speed is plotted in Figure 2.5, where the apparent mode of instability is that of flutter, which is incorrect for an unloaded string. Increasing the number of basis functions serves to reduce the speed at which an apparent flutter instability occurs until the critical speed is reached, whereupon the mode of instability is again divergent. This points out the need to compare results for different numbers of functions to ensure that pointwise convergence of the eigenvalues has been achieved with respect to the number of basis functions used. Also, considering the practical application of this treatment and the limitation of the linear theory at transport speeds near or above the critical speed (Mote, 1966), it is unwise to use this modelling for high transport speeds.

2.3.2 Forced vibration

The following results are organised so that distributed loads are considered first and point loads second. The spring, damping and follower forces are considered individually and then in unison. Where results from the literature are available they are used for comparison.

2.3.2.1 Distributed loads

The effect of increasing the spring force on a translating string, when no damping or follower loads are present ($k_d = k_f = 0$), is to increase monotonically all frequencies of vibration, as long as the transport speed is subcritical. The critical speed is not altered by the spring action in the case of the string; however, for the beam the critical speed is increased with increasing k_s. The eigenvalues remain purely imaginary as no damping has been introduced.

For $k_s = k_f = 0$ and $k_d \neq 0$ the eigenvalues contain nonzero real parts, the size of which depends on the amount of damping present. Figure 2.6 shows the change in frequency with increasing k_d, for stationary and moving strings. The different basis functions create different errors in the modal damping for the moving string at higher k_d, with neither type producing superior performance. These errors may be reduced using more basis functions, but at the expense of computation and model size.

The follower force may be analysed by considering the x- and w-components separately, before considering their combined effect. Figure 2.7 shows a constant distributed follower load acting along the length of the string, and the corresponding lateral or w-component of that force.

Figure 2.8 shows the effect of increasing lateral load upon the eigenvalues of the beam model. Here the tension has been reduced to zero to aid evaluation. The dotted line represents better accuracy in the Ritz approximation and shows the convergence in eigenvalues below follower loads of $k_f = 700\text{N/m}$ in all of the four modes shown, (in fact values on the dotted line below $k_f = 1000\text{Nm}^{-1}$ are convergent). The most interesting phenomenon in Figure 2.8 is the stiffening action of the lateral load upon the first mode of vibration, and the subsequent flutter instability around $k_f = 100\text{N/m}$. To verify this flutter instability Figure 2.9 plots typical modal forms for the first two modes at different values of k_f. The two modes are obviously coalescing into one.

Figure 2.10 plots the variation in natural frequencies for a tensioned beam ($R_o = 150\text{N}$) with increasing follower load. In this analysis $\iota = 1$ (Table 2.1), and so the tension at $x = \ell$ remains at R_o. This creates the destiffening seen in Figure 2.10(b), which dominates the behaviour shown in Figure 2.10(c). The added stiffness given by tensioning the beam has also lowered the second and third flutter instabilities (c.f. Figures 2.8 and 2.10(a)), however these higher modes have not converged and in fact the modes creating flutter instabilities change depending upon whether m is odd or even. This does not change the form of Figure 2.10(c). For a translating beam the instability becomes divergent again, and the critical speed is reduced with increasing follower force. The symmetry and asymmetry mentioned in Section 2.3.1 is reduced with increasing follower force, and so the sinusoids are no longer superior

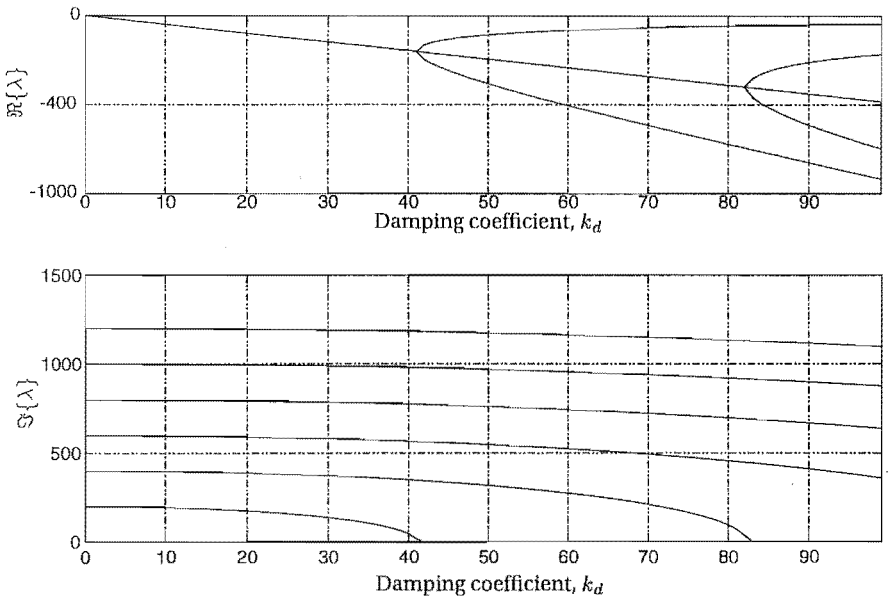

(a) Stationary string, (m =10).

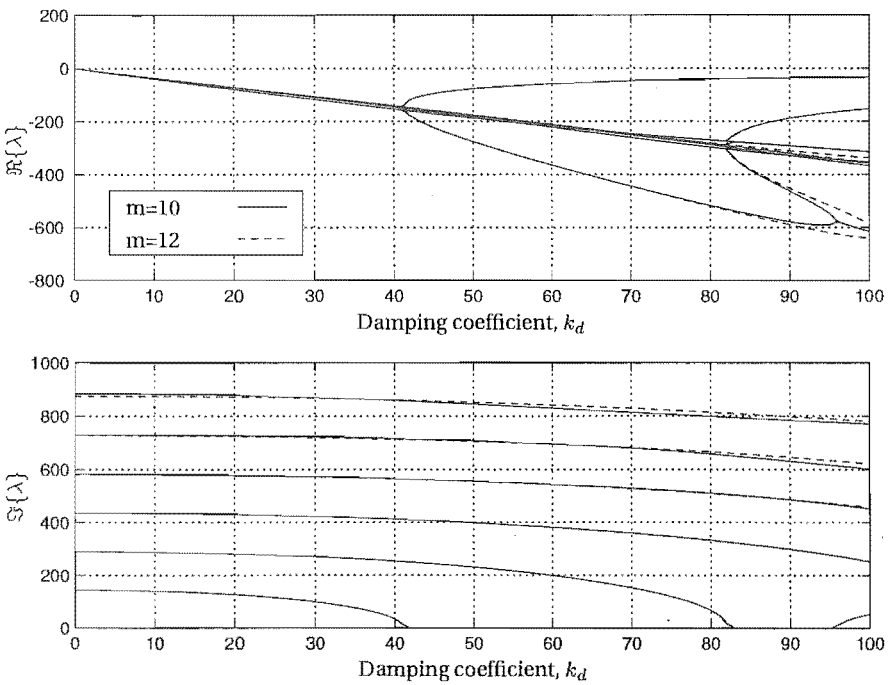

(b) Translating string, (c = 20m/s).

Figure 2.6: *Effect of distributed damping on vibration frequencies for the moving string.*

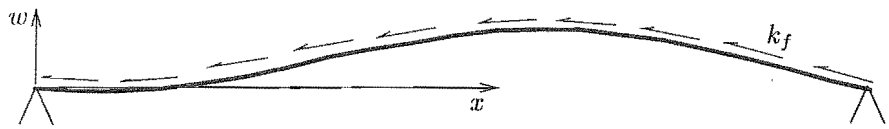

(a) Constant follower force.

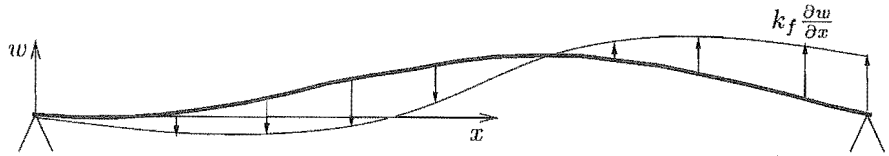

(b) Lateral component of follower force in (a), $(k_f \frac{\partial w}{\partial x})$.

Figure 2.7: *Distributed follower load and corresponding lateral component.*

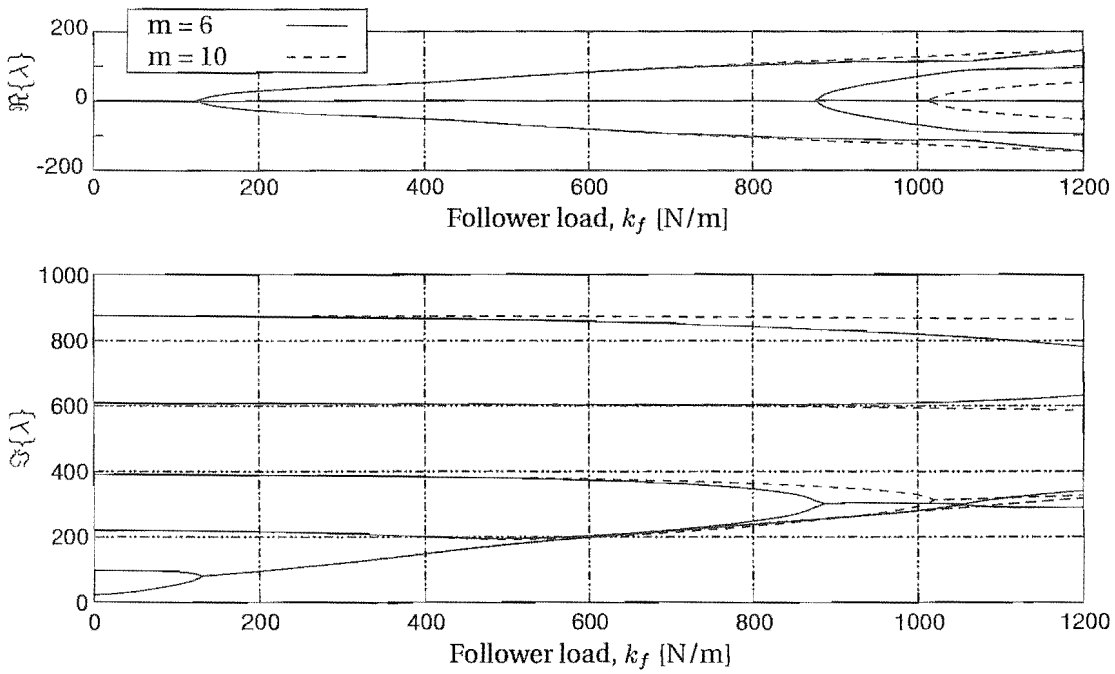

Figure 2.8: *Effect of lateral component of the distributed follower force on vibration frequencies for the stationary, untensioned beam.*

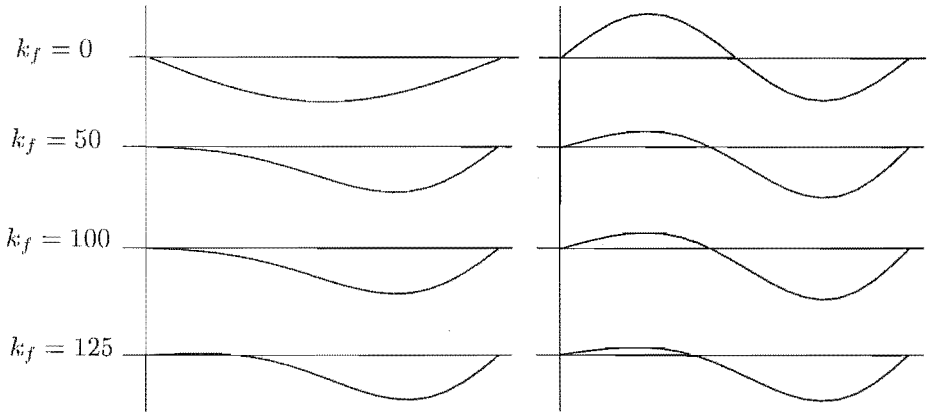

Figure 2.9: *Modal forms of the first two modes of the stationary untensioned beam as lateral follower load increases.*

over polynomials as basis functions.

2.3.2.2 Point loads

Chen (1997) developed approximate solutions to the moving string under the point loadings described in this treatment, and Lengoc and McCallion (1999) provided analytical results. Figure 2.11 compares the analytical results with this formulation. As expected the analytical results are lower than predicted using the approximate results. Large numbers of basis functions are required to attain the analytical results as the very high spring stiffness (for which the results differ most) forces a discontinuous slope in the modal forms at $x = x_d$. It is obvious that the basis functions used in this work cannot cope with such a restriction. However, such a high stiffness splits the string into two uncoupled spans (Lengoc, 1990), rendering the practical use of such a high stiffness useless.

Finally the effect of the follower point load acting on the moving string is shown in Figure 2.12. It is apparent that every mode except the third is markedly affected, with the critical speed being reduced to half that observed with no follower force. This is because the load is positioned half way along the length, at which point the slope of the deflection in odd-numbered modes is small, thereby creating a small lateral component.

2.3.3 Conclusion

This treatment has extended the work currently available in the literature on translating strings and beams to include distributed spring, damping and follower loads, as well as pointwise actuation/disturbance forces and sensed outputs. Comparison with other contributors has been used to validate the modelling.

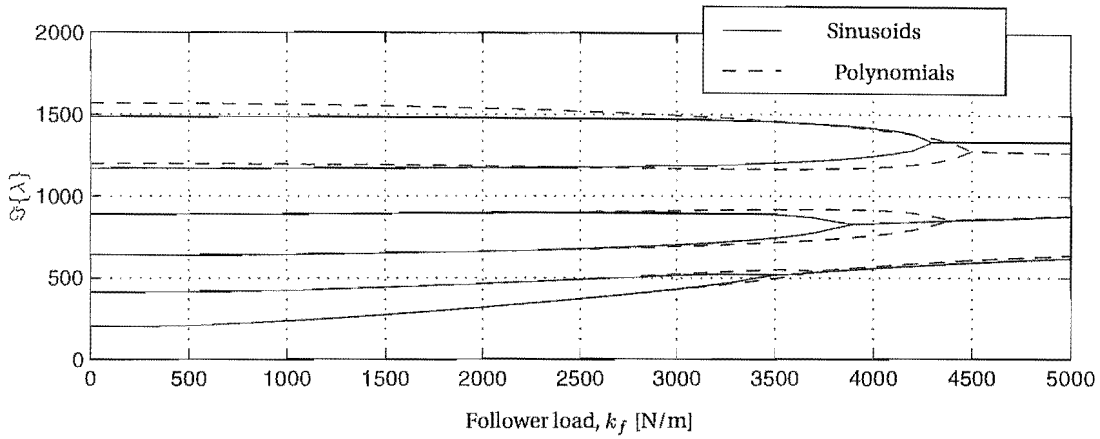

(a) Lateral component of distributed follower force.

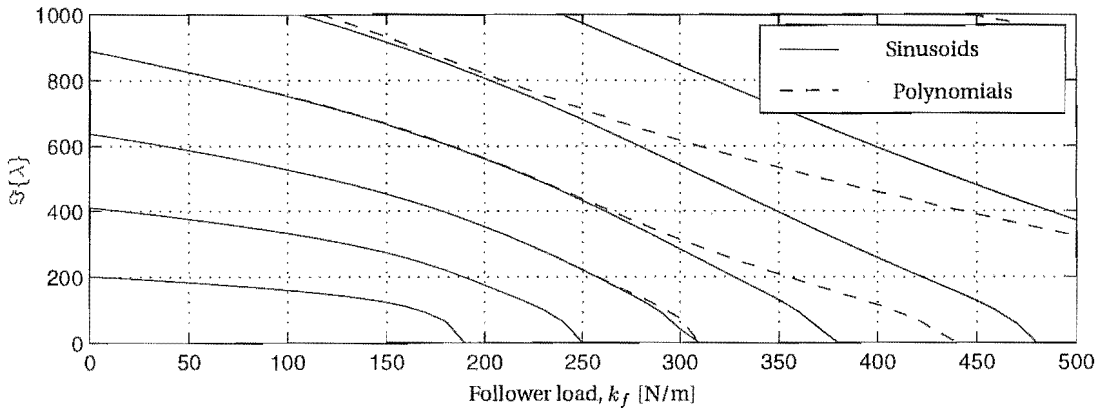

(b) In-line component of distributed follower force.

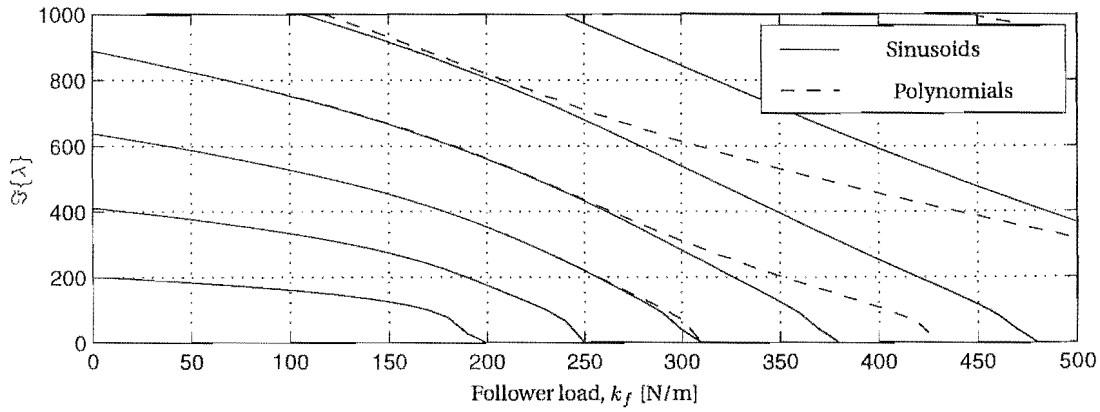

(c) Full distributed follower load

Figure 2.10: *Effect of distributed follower load on vibration frequencies of the stationary beam. 2.10(c) shows that the in-line component dominates the behaviour. Note that the axis of 2.10(a) differs from the other plots.*

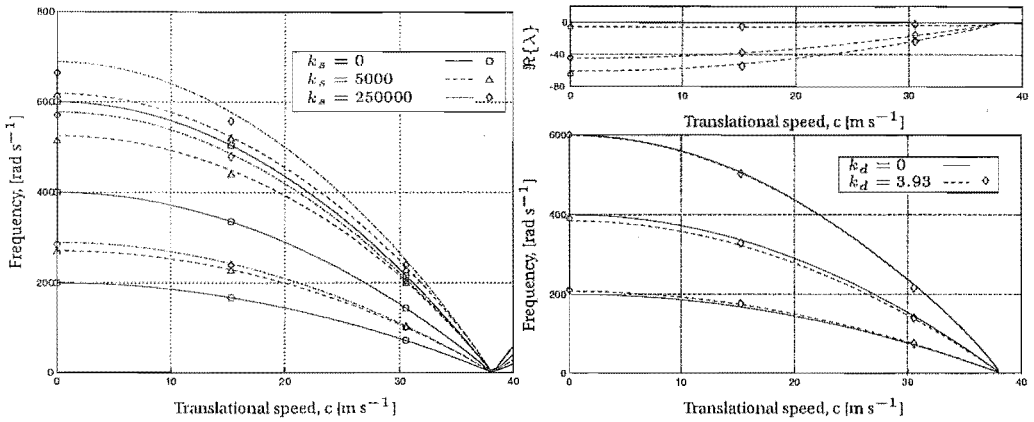

(a) Comparing spring action with points taken from Lengoc and McCallion (1999).

(b) Comparing damping action with points taken from Lengoc and McCallion (1999).

Figure 2.11: *Effect of pointwise spring force and damping on vibration frequencies for the moving string. Isolated points indicate data from Lengoc and McCallion (1999).*

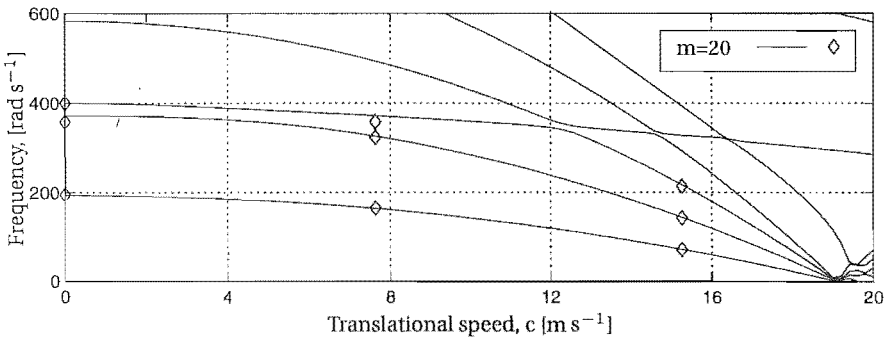

Figure 2.12: *Effect of pointwise follower load on vibration frequencies for the moving string. Isolated points indicate data from Lengoc and McCallion (1999).* $x_d = 0.5\ell$, $k_f = \frac{3}{4}R_o = 112.5N$

It has been shown that the gains of using the eigenfunctions of the stationary problem as basis functions are reduced when external loadings are applied, making the comparatively simple polynomials more attractive. However, use of the Gram-Schmidt process resulted in numerically unsound higher order polynomials, meaning that very large numbers of basis functions could not be accurately generated. Using a modified Gram-Schmidt procedure improved the situation to a degree.

The models put forward are easily used in standard control frameworks and are general enough to be used in applications in the textile, sawmilling, power transmission belt, and magnetic tape industries. The following chapter extends this work to moving plates and provides an even more general formulation of external influences; although the focus narrows to the sawmilling industry.

Chapter 3

PLATES

This chapter considers current methods of describing axially moving plates that are influenced by in-plane tensions and edge loads, and proposes a new method which allows for more complex edge loading. The main application is high-strain wide bandsaws. The development of motion equations covered in the previous chapter is assumed, and therefore results follow directly from new formulations of relevant energy expressions. The new method of describing edge loadings considers the cutting loads to act along a partial span of the blade, and also models the feed force during the cutting process. Also, the guides used on large bandsaws are modelled using two methods. Results for partial cutting system with guides is deferred until Chapter 5.

3.1 LITERATURE REVIEW AND BACKGROUND THEORY

Work on axially moving plates was started by Ulsoy and Mote (1982), by combining the kinetic energy due to translation with the bending and strain energies of plates. Defining the deflection surface to be $w = w(x, y, t)$, and the plate to be ℓ metres long, b metres wide and h metres thick, the kinetic energy is

$$\mathcal{T} = \tfrac{1}{2}\int_0^b \int_0^\ell \rho h\left[c^2 + \left(\frac{\partial w}{\partial t} + c\frac{\partial w}{\partial x}\right)^2\right] dx dy, \tag{3.1}$$

where c is the velocity of translation of the plate and is positive in the positive x-direction, and ρ is the blade density. The strain energy due to bending is given by

$$\mathcal{V}_b = \frac{D}{2}\int_0^b \int_0^\ell \left\{\left(\frac{\partial^2 w}{\partial x^2} + \frac{\partial^2 w}{\partial y^2}\right)^2 + 2(1-\nu)\left[\left(\frac{\partial^2 w}{\partial x \partial y}\right)^2 - \frac{\partial^2 w}{\partial x^2}\frac{\partial^2 w}{\partial y^2}\right]\right\} dx dy, \tag{3.2}$$

where $D = Eh^3/12(1-\nu^2)$ is the plate rigidity. Ulsoy and Mote also considered the effects of bandmill strain, blade tension, wheel crown and wheel tilt. These factors

create stresses throughout the blade, for which the resulting strain energy is

$$\mathcal{V}_s = \frac{1}{2}\int_0^b \int_0^\ell \left\{ N_x \left(\frac{\partial w}{\partial x}\right)^2 + 2N_{xy}\frac{\partial w}{\partial x}\frac{\partial w}{\partial y} + N_y \left(\frac{\partial w}{\partial y}\right)^2 \right\} dxdy, \tag{3.3}$$

where $N_x(x,y)$, $N_y(x,y)$ and $N_{xy}(x,y)$ are forces per unit length defining the planar stress field throughout the plate. The conventions are that tensile stress is positive and that positive shear elongates the diagonal joining the origin to the corner $(x,y) = (\ell, b)$. Both strain energy expressions are standard results for isotropic plates (see Timoshenko and Woinowsky-Krieger (1959) and Leissa (1969)). Ulsoy and Mote (1982) also compared experimental data from production scale bandmills with the theoretical results, but only for the transverse modes of vibration.

A series of three papers (Lengoc and McCallion, 1995a,b,c), considered tangential edge loading as a model of the cutting force, and assessed the blade stability in relation to parametric excitation of these loads. Furthermore, Lengoc and McCallion applied the idea of a follower force to the cutting edge, producing a nonconservative out of plane load as well as the tangential loading. The combined effects of bandmill strain, pretension and wheel tilting, translation speed and cutting loads were also considered in detail.

Lehmann and Hutton (1996) modelled the cutting loads on a more microscopic level, considering the cutting forces to act on each tooth. Also, the lumber density was assumed to vary analytically with proximity to a knot, and the gradient of the hardness function used to determine lateral loading on the blade. A full dynamic model of the band was presented, but not used because experimental cutting data was presented that showed the blade motion comprising primarily of frequencies below 5Hz. This led to the assumption of a "quasi-static" process, where the static blade stiffness rather than the blade dynamics influenced the sawn lumber surface. Therefore, the blade was assumed to be in static equilibrium, with the restitutive forces from the blade stiffness balancing the lateral cutting loads as well as forces from the interaction of the face of the blade with the sawn surfaces. Such a model will not account for the washboarding phenomenon, but is perhaps valid for low frequency effects such as snake and snipe. Lehmann and Hutton (1997) first uses the model of the previous work to establish the affect on tooth tip stiffness of parameters such as blade thickness, width, band strain etc. Then, the contact algorithm used in determining the side loads caused by the blade interaction with the sawn surfaces was shown to markedly affect the path of the blade near the idealised knot.

Washboarding was experimentally investigated in Zhan and Hutton (1989), and two distinct types of the phenomenon were shown to exist. It was postulated that the first type was a function of the impacting teeth causing tooth and hence blade vibration, and the second type was related to side loads acting on the teeth. No the-

oretical mechanisms were presented in this work. Okai et al. (1996) considered the washboarding phenomenon in isolation of the bandsaw blade dynamics. The depth of cut was assumed small in relation to the blade length, so that each tooth embedded in the cut vibrated with the same amplitude. Then, assuming a constant sinusoidal lateral motion of the blade with time, and constant tooth passing frequency and feed speed, an analytical form of the washboarding pattern was produced. Also, knowledge from circular saw vibration was used to propose that only tooth passing frequencies slightly higher than a natural frequency of the blade would cause self-excited vibration and hence washboarding. This was experimentally verified, and washboarding was shown to be caused by both transverse and torsional modes. Lengoc and McCallion (1999) extended the theoretical work of Okai et al. (1996), and combined this extension with their modelling of bandsaw dynamics (Lengoc and McCallion, 1995a). The experimental results of Okai et al. were compared with the theoretical modelling subjected to periodic point loading, with large amplitude vibrations noted near torsional frequencies only.

3.2 PRELIMINARY RESULTS

If the three energy expressions (3.1, 3.2, 3.3) are worked through Hamilton's principle as shown in Section 2.1.4 the standard MGK system results. The basis functions used are the polynomials of Chapter 2 in both the x- and y-directions. Sinusoids are feasible in the x-direction but offer no real gain for loaded translating continua (Section 2.3.2), and also the formulation described later in this chapter is afforded by the use of polynomials.

The frequencies of vibration resulting from the eigenvalue problem for an unloaded, stationary plate are compared in Table 3.1 with results[1] from Leissa (1973). The modal form is given by two digits, the first giving the number of half waves in the x-direction and the second those in the y-direction. The results compare well with Leissa's work with accuracy increasing with the number of basis functions used.

The gyric precession noted in Chapter 2 is shown for plates in Figure 3.1 for the first four modes of vibration over full cycles of vibration. The plate aspect ratio is 4:1 and the translational speed is $c = \frac{1}{2}c_{cr}$. For the first natural mode the translational speed couples the first two stationary transverse modes, and in the second mode the first two torsional modes are coupled. This theme continues for higher modes. Again, the waves travel in the opposite direction to the blade. Figure 3.2 expresses the same information but by showing the deflections arising from the real and imag-

[1]Such dimensionless parameters are very useful, as they are easily modified to produce the natural frequencies of vibration for any plate material, thickness and aspect ratio. However, several authors use these dimensionless parameters for their dimensionless nature alone, even when the results are not applicable to different geometries. Therefore, this work usually presents results in MKS units.

Table 3.1: *Natural frequencies for a plate that is simply supported on two opposite boundaries and free on the other two.*

		Frequency parameter, $\lambda = \omega a^2 \sqrt{\rho/D}$		
Aspect ratio (ℓ/b)	**Leissa shape**	**6x4 basis functions**	**8x10 basis functions**	**Leissa**
0.4	1,1	9.8157	9.7602	9.7600
	1,2	11.1321	11.0369	11.0368
	1,3	15.7972	15.0638	15.0626
	1,4	26.1510	21.7083	21.7064
1.0	1,1	9.6815	9.6314	9.6314
	1,2	16.2231	16.1348	16.1348
	1,3	39.1623	36.7257	36.7256
	2,1	40.6266	38.9452	38.9450
2.5	1,1	9.4873	9.4841	9.4841
	1,2	33.6702	33.6228	33.6228
	2,1	38.4438	38.3629	38.3629
	2,2	75.5199	75.2037	75.2037

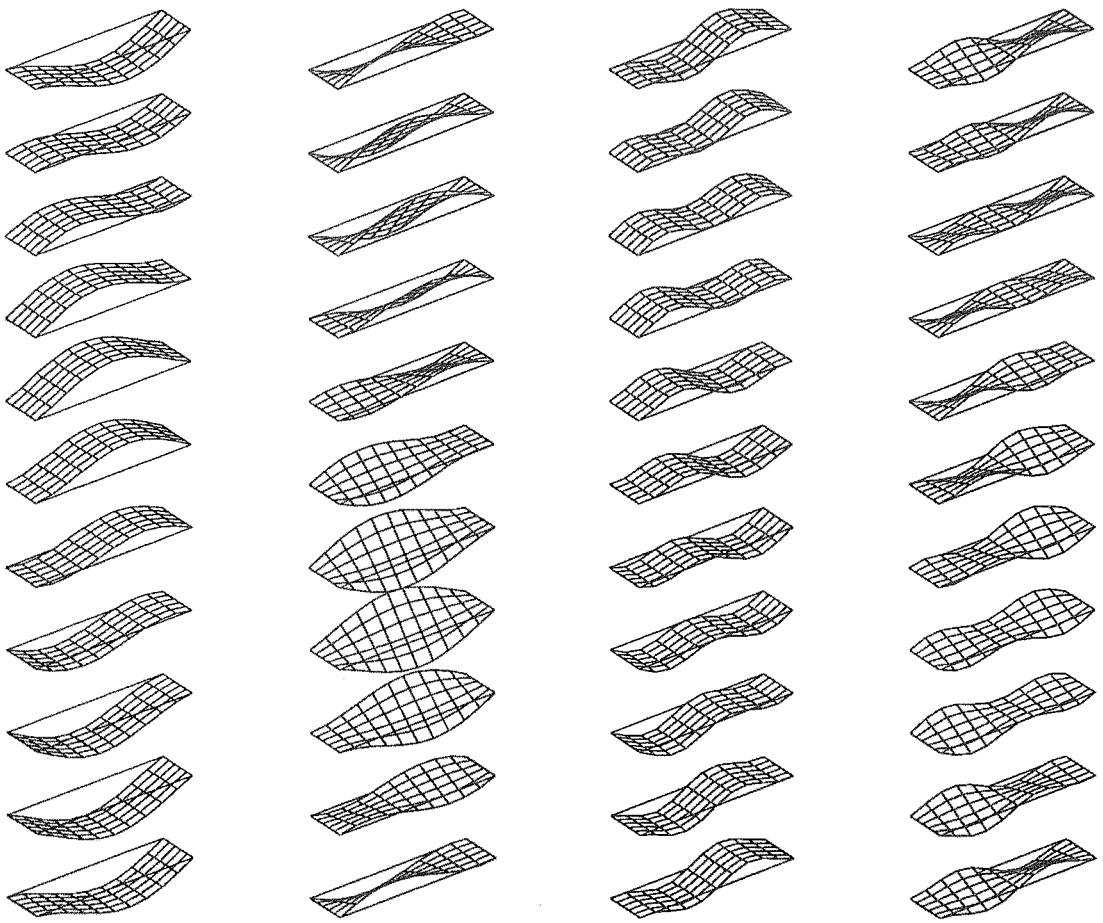

Figure 3.1: *Modal precession for first four natural modes of vibration,* $c = \frac{1}{2}c_{cr}$

inary parts of the eigenvectors. The actual vibratory forms shown in Figure 3.1 result from the superposition of these real and imaginary parts, with the real part leading the imaginary by 90°.

The blade tensioning, wheel crowning and wheel tilting mentioned in Chapter 1 combine to produce an in-plane stress distribution at the ends of the plate of the form shown in Figure 3.3, which in this work is approximated by a linear variation across the width, b. Finding the corresponding planar stress field throughout the plate (given by N_x, N_y, and N_{xy}) requires the *Airy stress function*, $\Phi(x, y)$, which for two-dimensional problems satisfies (Goodier and Timoshenko, 1951) the biharmonic equation

$$\frac{\partial^4 \Phi}{\partial x^4} + 2\frac{\partial^4 \Phi}{\partial x^2 \partial y^2} + \frac{\partial^4 \Phi}{\partial y^4} = 0, \tag{3.4}$$

and is related to the in-plane stress components by

$$N_x = \frac{\partial^2 \Phi}{\partial y^2}, \; N_{xy} = -\frac{\partial^2 \Phi}{\partial x \partial y}, \; N_y = \frac{\partial^2 \Phi}{\partial x^2}. \tag{3.5}$$

The simple case of a linear variation of tension across the width can be achieved by applying pure bending stresses along the edges $x = 0$ and $x = \ell$ and superimposing this with the nominal bandmill strain. An acceptable stress function to provide pure

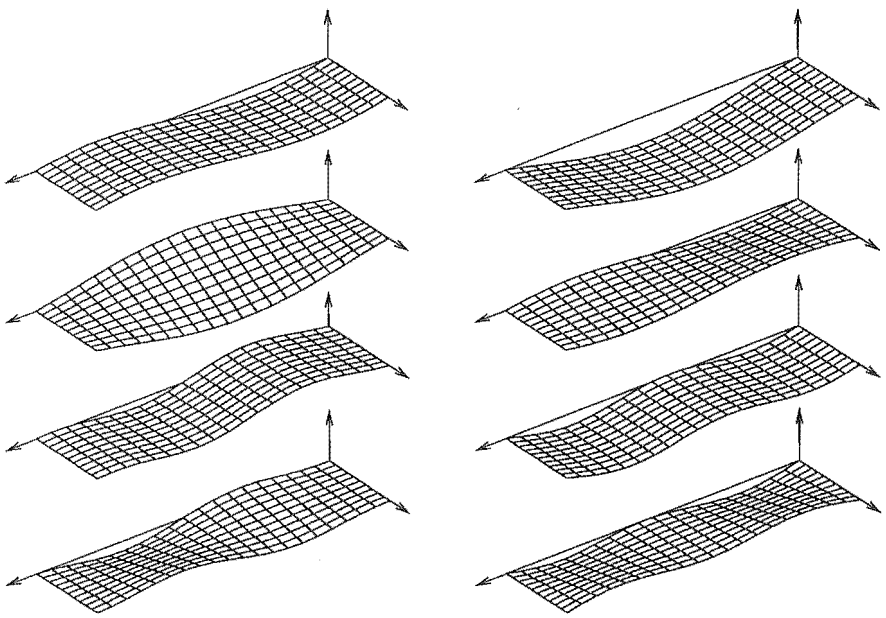

(a) Real parts. (a) Imaginary parts.

Figure 3.2: *Deflections arising from the real and imaginary parts of the eigenvectors of the first four modes of vibration,* $c = \frac{1}{2}c_{cr}$

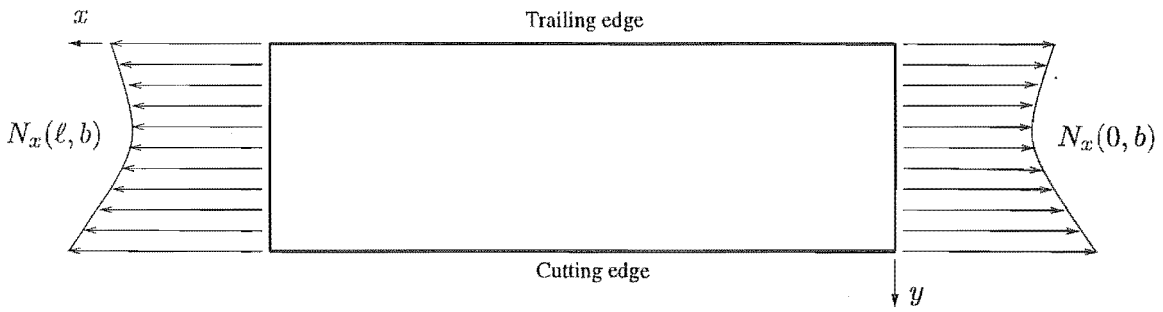

Figure 3.3: *Plate end loads created by blade tensioning, wheel crown and wheel tilt.*

bending in the plate is

$$\Phi = R_b\Big(\frac{y}{3b} - \frac{1}{2}\Big)y^2 \tag{3.6}$$

which gives $N_x = -R_b$ along the trailing edge, $N_x = R_b$ along the leading edge and no stress along the middle-width, with no shear stress or normal stress in the y-direction. Superimposing this with the nominal tension and the strain mechanism term (Section 2.1.3), we have

$$N_x(x, y) = R_o - R_b + 2R_b\frac{y}{b} + \eta\rho hc^2. \tag{3.7}$$

Figure 3.4 shows the effect of R_b upon the natural frequencies of vibration, with results being compared with Lengoc (1990, see pp. 169). The major result is that the stress distribution increases the torsional frequencies and reduces the transverse ones. Also shown are the mode shapes (Figure 3.5), which show the leading edge being stabilised (and eventually pinned down) by the tension variation in transverse modes but destabilised in torsional modes. These results indicate that lengthening the trailing edge more than the cutting edge improves the relative stiffness of the cut-

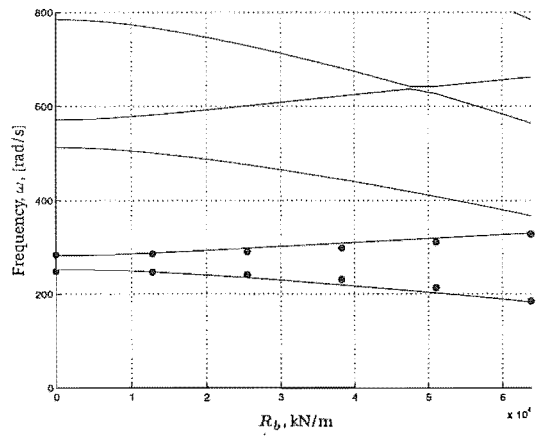

Figure 3.4: *Effect of varying the linear stress variation across the width of the plate, with results compared with Lengoc (1990).* $\ell = 0.948m$, $b = 0.235m$, $h = 1.4mm$, $R_o = 63.8kN/m$

ting edge for transverse vibrations but impairs it for torsional ones. Also, the shift in nodal lines shown in Figure 3.5 shows that the tensioning of the blade affects choice of actuator and sensor positions.

For a translating plate the trends shown in Figure 3.4 are the same but all frequencies are reduced because of the blade translation.

3.3 CUTTING FORCES

The pointwise forces treated in the previous chapter are not useful in wide bandsaw applications, as the workpiece usually encompasses a significant span of the blade length ℓ. However, distributed loads are feasible and may be formulated in a method analogous to that in Chapter 2, so that the entire *cutting edge*, (defined by $0 \leq x \leq \ell$, $y = b$) is under cutting influences. This method was presented by Lengoc and McCallion (1995c), and is reformulated below with some extensions. The work done and results presented by Lengoc and McCallion is huge, and only results for the extensions are presented. Another, more realistic representation of the cutting forces is to treat the saw blade to be made up of a cutting span which is encompassed by the workpiece with noncutting spans on either side. This novel method is also presented and results compared with those of the full cutting span.

3.3.1 Full span cutting

Considering a distributed follower force acting along the entire cutting edge, the out of plane component enters the motion equations via the virtual work done, while the inplane component enters via Airy's stress function and (3.3). Considering firstly the out of plane action, an exogenous force of

$$f_{ex} = -\left[k_s w + k_d \frac{\partial w}{\partial t} + k_f \frac{\partial w}{\partial x}\right] \bar{\delta}(y - b) + u(t)\bar{\delta}(x - x_a, y - y_a) \tag{3.8}$$

results, where $u(t)$ is still a pointwise control or disturbing force. Lengoc and McCallion (1995a) considered spatially constant forces per unit length to act along the

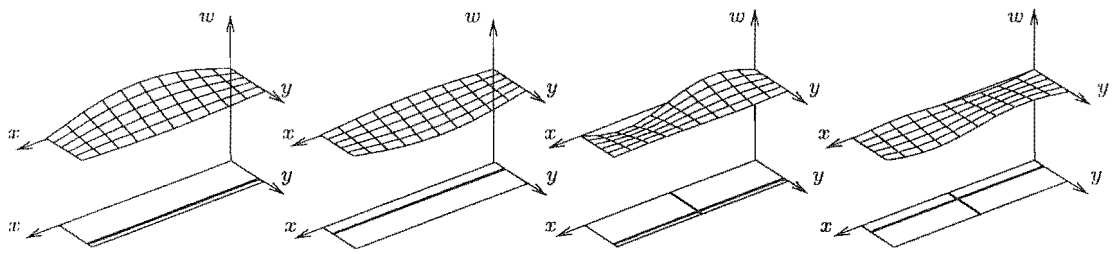

Figure 3.5: *Modal forms and nodal lines for the first four modes for the tensioned stationary plate in Figure 3.4 with* $R_b = \frac{3}{4}R_o$.

cutting span, without the edge damping and stiffness. The resulting stress functions N_x, N_{xy}, N_y can then be superimposed with those from the tensioning effects already mentioned. For a constant distributed cutting load the shear stress along the cutting edge must be a constant, and along the trailing edge it must be zero. Furthermore, N_y must be zero along both the cutting and trailing edges but N_x is unrestricted. The boundary conditions on the other two edges ($x = 0$, $0 \leq y \leq b$, and $x = \ell$, $0 \leq y \leq b$) are unrestricted in terms of N_y and N_{xy}, however N_x depends upon the tension mechanism of the bandmill (see Section 2.1.3). Again using the variable ι such that ($0 \leq \iota \leq 1$), a stress function satisfying the above boundary conditions is

$$\Phi = \frac{k_f}{3b^2}(x - \iota\ell)y^3, \tag{3.9}$$

which gives

$$N_x = \frac{2k_f}{b^2}(x - \iota\ell)y$$
$$N_{xy} = k_f(\frac{y}{b})^2$$
$$N_y = 0,$$

where $\iota = 0$ represents the counterweight mechanism and $\iota \neq 0$ represents systems with finite stiffness. N_x and N_{xy} are plotted in Figure 3.6, for $\iota = 0.0$ and $\iota = 0.5$ (which Lengoc and McCallion (1995a) proposed). There is no compelling reason to enforce $\iota = 0.5$ so it is considered more general to allow for this variation.

Figure 3.7(a) shows the effects of the upstream boundary condition and the size

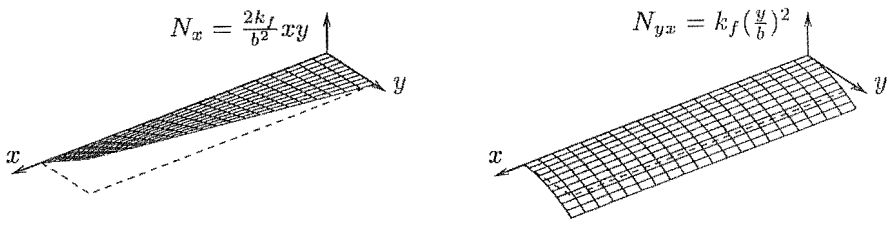

(a) Simulation of a counterweight mechanism ($\iota = 0$), whereby the stress at the $x = 0$ boundary must remain constant.

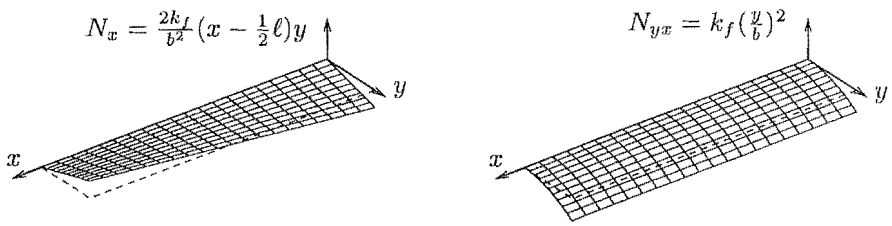

(b) The stress state used in Lengoc and McCallion (1995a) ($\iota = 0.5$).

Figure 3.6: *N_x and N_{xy} for a constant cutting load.*

of the tangential load on the first natural frequency. Results for six values of ι are shown, and of note is the initial stiffening for $\iota \leq 0.4$ followed by destiffening and finally buckling as the cutting load increases. This makes sense as for $\iota = 0$ the stress at the upstream boundary ($x = 0$) remains constant, and the cutting load increases N_x throughout the plate. For $\iota = 1$ the boundary at $x = 0$ is reacting all of the cutting force, so that the tension N_x throughout the plate is decreased from the noncutting state. As the cutting force increases divergent buckling occurs. (Except where otherwise mentioned, the plate parameters used in the results for this chapter are listed in Table 3.2 so that comparison with the results of Lengoc and McCallion (1995a,b,c) may be made.)

Figure 3.7(b) shows the same effect but for the first six natural frequencies. Again, the blade is stiffened for $\iota = 0$ but de-stiffened for $\iota = 1$. Also of interest is the way that the torsional modes do not suffer buckling in the way that the transverse ones do (shown by the way two eigenvalue curves approach each other and then diverge again — the mode of vibration is essentially "swapped" between the curves, and the torsional frequencies remain comparatively unaffected). The modal forms of the first three modes are shown in Figure 3.8, for $k_f = 15\text{kN}$ and $\iota = 0.0, 0.5$, showing that the tangential component couples the transverse and torsional modes.

If the lateral component of the follower force is introduced, the flutter instability mentioned in Section 2.3.2.1 occurs, as is shown in Figure 3.9(a). The first transverse mode has stiffened in comparison to Figure 3.7(a), and the first torsional and second transverse modes coalesce around $k_f = 20\text{kN/m}$. The higher frequencies also coalesce around this load, with the torsional mode always being stiffened and the transverse destiffened prior to instability. Figure 3.9(b) shows the effect of altering ι, showing the apparent stiffening of all modes when $\iota = 0$, and the flutter instabilities for $\iota = 1$ (for which the flutter loads are lower than when $\iota = 0.5$). Figure 3.9(c) shows the first three modes of vibration for $k_f = 15\text{kN/m}$ and $\iota = 0.0, 0.5$.

3.3.2 Partial span cutting and feed loads

In real applications the cutting edge is not in contact with the workpiece along the entire length. To model this situation a formulation that affords the application of cutting and feed forces that act only over a part of the leading edge is required. Such a form of cutting load is shown in Figure 3.10. The cutting load is a biased sinusoid,

Table 3.2: *Nominal parameters for results of Chapter 3.*

ℓ	b	h	E	R_o	R_b	m	n	η	ν	ι
1m	275mm	1.65mm	205GPa	45kN/m	0	8	6	0	0.3	1

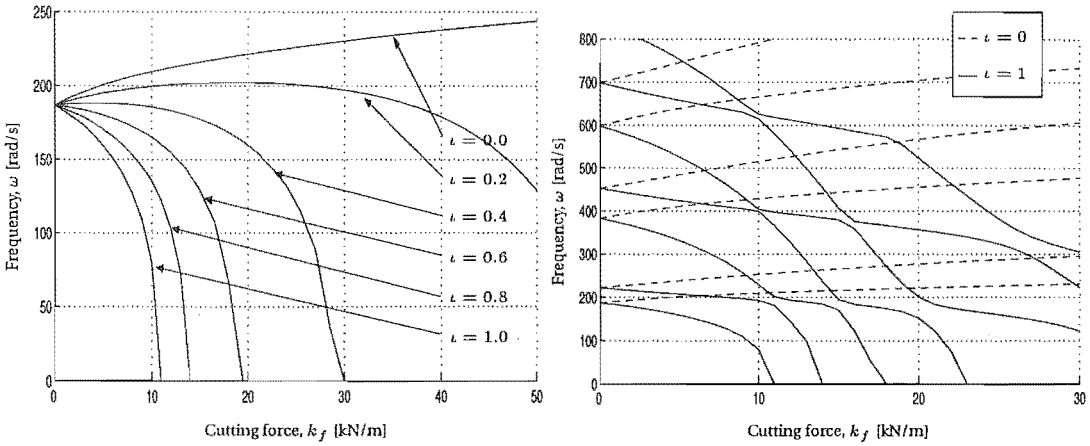

(a) Effect on the first vibration mode.

(b) Effect on the first seven modes of vibration.

Figure 3.7: *Effect of in-plane component of the distributed follower force on the stationary plate.*

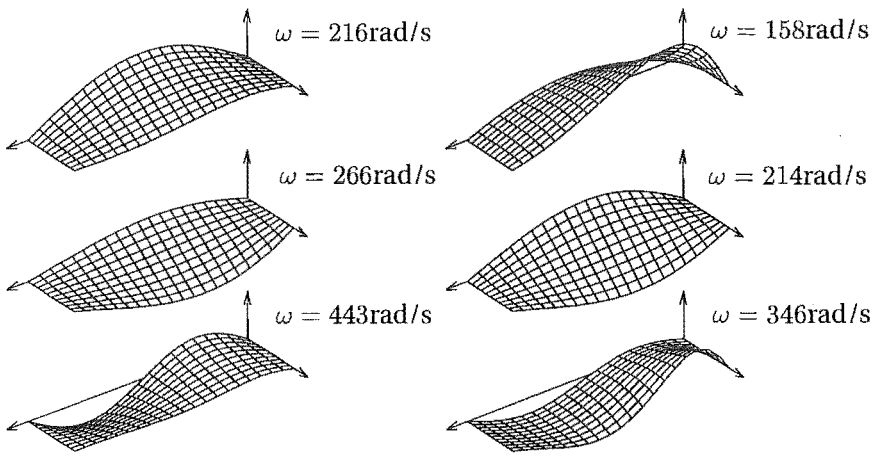

(a) $\iota = 0.0$.

(b) $\iota = 0.5$.

Figure 3.8: *Mode shapes for tangential component of full-span follower load,* $k_f = 15kN/m$.

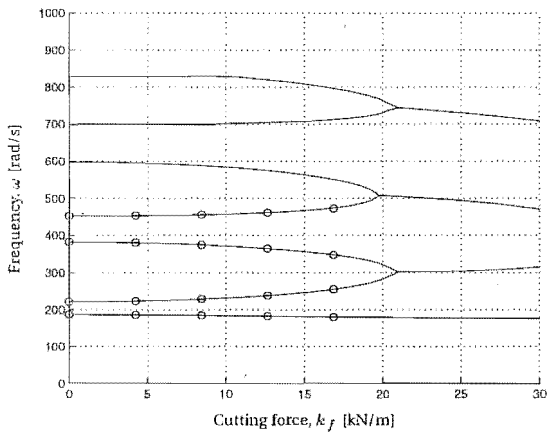

(a) Comparison with Lengoc and McCallion (1995c), ie. $\iota = 0.5$.

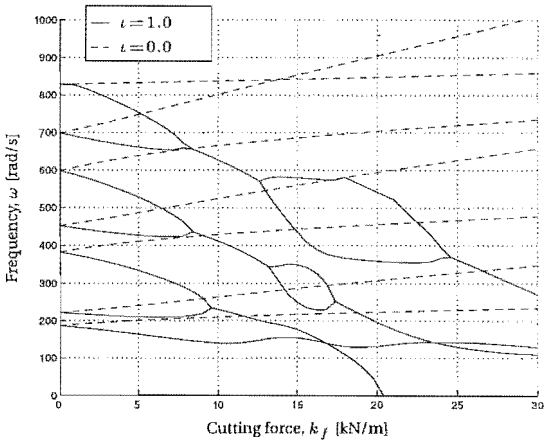

(b) Changing the stress state at the $x = 0$ boundary.

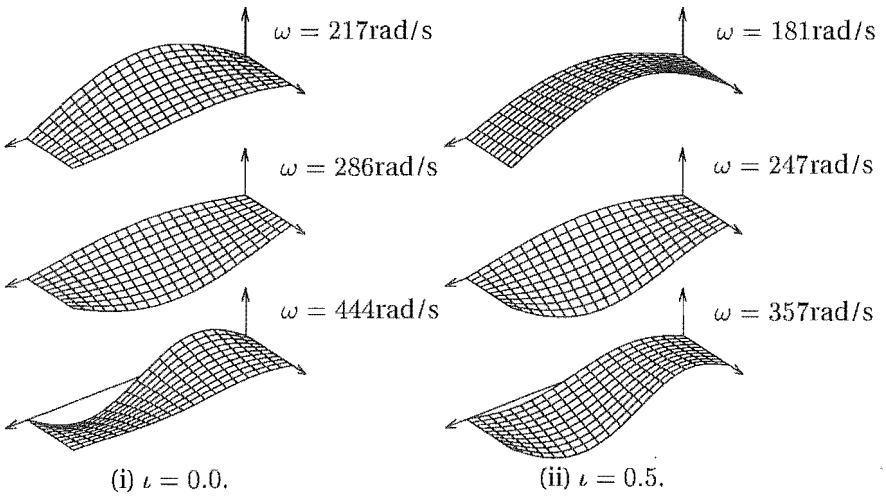

(i) $\iota = 0.0$. (ii) $\iota = 0.5$.

(c) Mode shapes for full-span follower force, $k_f = 15kN/m$.

Figure 3.9: *Change in imaginary parts of eigenvalues for increasing full-span cutting load.*

and a feed load exists that is spatially similar but smaller in magnitude. Therefore,

$$k_f(x,t) = \begin{cases} 0, & 0 \le x < s_u \\ \Lambda_c(t) + A_c(t)\sin\left(\frac{i\pi x}{p}\right), & s_u \le x \le \ell - s_l \\ 0, & \ell - s_l < x \le \ell, \end{cases} \tag{3.10}$$

where s_u and s_l represent (respectively) the lengths of the upstream and downstream noncutting spans. Between these spans the workpiece envelopes the blade. The diameter of logs, density, hardness and other properties naturally change throughout the log length, so the parameters Λ_c, A_c, s_u and s_l are considered to vary with time.

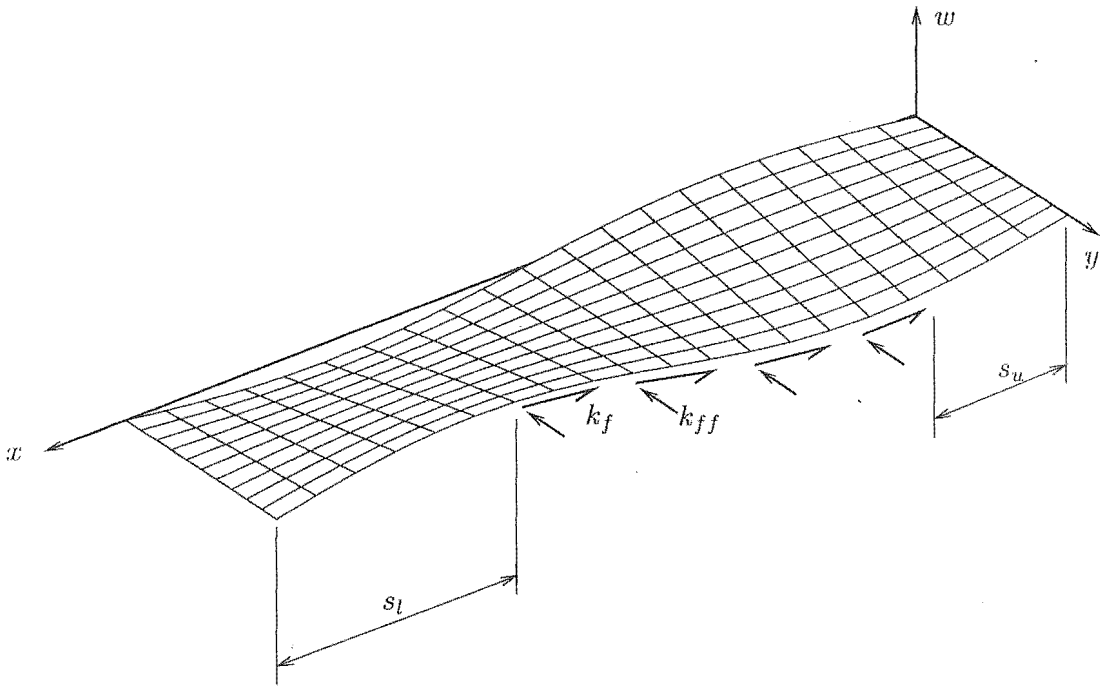

Figure 3.10: *Form of partial cutting load, showing tangential follower force and normal feed force.*

The form depicted in Figure 3.10 and (3.10) may be approximated using Fourier sine series with time varying coefficients. A biased sinusoid rather than a constant load is used in an attempt to model individual teeth loading. Considering for now the cutting load only, the Fourier sine series may be written as

$$k_f(x,t) = \sum_{i=1}^{I} B_{fi}(t) sin(\frac{i\pi x}{\ell}), \tag{3.11}$$

where

$$B_{fi}(t) = \frac{2}{\ell} \int_o^{\ell} k_f \sin(\frac{i\pi x}{\ell}) dx. \tag{3.12}$$

Because the cutting force equals zero either side of the workpiece the integral limits of (3.12) become $x = s_u$ and $x = s_l$, with $k_f = \Lambda_c + A_c \sin(2\pi x/\ell)$ over this

range. From this the following Fourier coefficients may be found:

$$B_{fi} = \begin{cases} \frac{A_c p}{\pi \ell}\left[\cos\left(\frac{2\pi s_u}{p}\right)\sin\left(\frac{i\pi s_u}{\ell}\right) - \cos\left(\frac{2\pi(\ell - s_l)}{p}\right)\sin\left(\frac{i\pi(\ell - s_l)}{\ell}\right)\right] \\ \quad + \frac{2A_c}{i\pi}\left[\sin\left(\frac{2\pi s_u}{p}\right)\cos\left(\frac{i\pi s_u}{\ell}\right) - \sin\left(\frac{2\pi(\ell - s_l)}{p}\right)\cos\left(\frac{i\pi(\ell - s_l)}{\ell}\right)\right] \\ \quad - \frac{2\Lambda_c}{i\pi}\left[\cos\left(\frac{i\pi(\ell - s_l)}{\ell}\right) - \cos\left(\frac{i\pi s_u}{\ell}\right)\right] & , \text{for} \frac{2}{p} \neq \frac{i}{\ell} \\ \frac{A_c \ell}{2}\left[\ell - s_l - s_u\right] - \frac{A_c \ell}{\pi\left(\frac{2}{p} + \frac{i}{\ell}\right)}\left[\sin\left(\pi\left(\frac{2}{p} + \frac{i}{\ell}\right)(\ell - s_l)\right) - \sin\left(\pi\left(\frac{2}{p} + \frac{i}{\ell}\right)s_u\right)\right] \\ \quad - \frac{2\Lambda_c}{i\pi}\left[\cos\left(\frac{i\pi(\ell - s_l)}{\ell}\right) - \cos\left(\frac{i\pi s_u}{\ell}\right)\right] & , \text{for} \frac{2}{p} = \frac{i}{\ell}. \end{cases}$$

For each of the $i = 1, 2, \ldots, I$ functions in (3.11) the in-plane stress distributions $N_{ci,x}$, $N_{ci,xy}$ and $N_{ci,y}$ must be found. Consider the cutting edge of the plate loaded with a tangential force given by the i'th term of (3.11), *i.e.*, $q_{fi}(x) = B_{fi}\sin(\gamma_i x)$, where $\gamma_i = i\pi/\ell$. Again, the Airy stress function may be used to find the stresses throughout the plate. Assuming $\Phi_{fi} = \cos(\gamma_i x) f_{fi}(y)$ and substituting it into (3.4) yields

$$\gamma_i^4 f_{fi}(y) - 2\gamma_i^2 f''_{fi}(y) + f''''_{fi}(y) = 0, \tag{3.13}$$

the general solution of which is

$$f_{fi}(y) = C_{1,fi}\cosh(\gamma_i y) + C_{2,fi}\sinh(\gamma_i y) + C_{3,fi} y\cosh(\gamma_i y) + C_{4,fi} y\sinh(\gamma_i y).$$

Substituting this into (3.5) provides expressions for the in-plane stresses:

$$\begin{aligned} N_{fi,x} = \frac{\partial^2 \Phi_{fi}}{\partial y^2} = {} & \gamma_i\cos(\gamma_i x)\left[C_{1,fi}\gamma_i\cosh(\gamma_i y) + C_{2,fi}\gamma_i\sinh(\gamma_i y)\right. \\ & + C_{3,fi}\left(2\sinh(\gamma_i y) + \gamma_i y\cosh(\gamma_i y)\right) \\ & \left. + C_{4,fi}\left(2\cosh(\gamma_i y) + \gamma_i y\sinh(\gamma_i y)\right)\right], \\ N_{fi,xy} = -\frac{\partial^2 \Phi_{fi}}{\partial x \partial y} = {} & \gamma_i\sin(\gamma_i x)\left[C_{1,fi}\gamma_i\sinh(\gamma_i y) + C_{2,fi}\gamma_i\cosh(\gamma_i y)\right. \\ & + C_{3,fi}\left(\cosh(\gamma_i y) + \gamma_i y\sinh(\gamma_i y)\right) \\ & \left. + C_{4,fi}\left(\sinh(\gamma_i y) + \gamma_i y\cosh(\gamma_i y)\right)\right], \\ N_{fi,y} = \frac{\partial^2 \Phi_{fi}}{\partial x^2} = {} & -\gamma_i^2\cos(\gamma_i x)\left[C_{1,fi}\cosh(\gamma_i y) + C_{2,fi}\sinh(\gamma_i y)\right. \\ & \left. + C_{3,fi} y\cosh(\gamma_i y) + C_{4,fi} y\sinh(\gamma_i y)\right]. \end{aligned} \tag{3.14}$$

Using the boundary conditions $N_{fi,y}(x,0) = N_{fi,y}(x,b) = N_{fi,xy}(x,0) = 0$ and $N_{fi,xy}(x,b) =$

$B_{fi}\sin\left(\frac{i\pi x}{\ell}\right)$, the constants $C_{1,fi}\ldots C_{4,fi}$ are found to be

$$\begin{aligned}
C_{1,fi} &= 0,\\
C_{2,fi} &= B_{fi}\frac{b\sinh(\gamma_i b)}{\gamma_i\left(\sinh^2(\gamma_i b)-(\gamma_i b)^2\right)},\\
C_{3,fi} &= -B_{fi}\frac{b\sinh(\gamma_i b)}{\sinh^2(\gamma_i b)-(\gamma_i b)^2},\\
C_{4,fi} &= B_{fi}\frac{\gamma_i b\cosh(\gamma_i b)-\sinh(\gamma_i b)}{\gamma_i\left(\sinh^2(\gamma_i b)-(\gamma_i b)^2\right)}.
\end{aligned}$$

A similar procedure may used to find the in-plane forces due to each of the $i = 1,2,\ldots,I$ sinusoids that make up the feed force. The assumed solution of the Airy stress function is now $\Phi_{ffi} = \sin(\gamma_i x) f_{ffi}(y)$ but (3.13) and (3.14) remain valid with subscripts 'f' replaced with 'ff'. The final form of the stress functions becomes

$$\begin{aligned}
N_{ffi,x} = \tfrac{\partial^2\Phi_{ffi}}{\partial y^2} &= \gamma_i\sin(\gamma_i x)\left[C_{1,ffi}\gamma_i\cosh(\gamma_i y)+C_{2,ffi}\gamma_i\sinh(\gamma_i y)\right.\\
&\quad +C_{3,ffi}\left(2\sinh(\gamma_i y)+\gamma_i y\cosh(\gamma_i y)\right)\\
&\quad \left.+C_{4,ffi}\left(2\cosh(\gamma_i y)+\gamma_i y\sinh(\gamma_i y)\right)\right],\\
N_{ffi,xy} = -\tfrac{\partial^2\Phi_{ffi}}{\partial x\partial y} &= -\gamma_i\cos(\gamma_i x)\left[C_{1,ffi}\gamma_i\sinh(\gamma_i y)+C_{2,ffi}\gamma_i\cosh(\gamma_i y)\right.\\
&\quad +C_{3,ffi}\left(\cosh(\gamma_i y)+\gamma_i y\sinh(\gamma_i y)\right)\\
&\quad \left.+C_{4,ffi}\left(\sinh(\gamma_i y)+\gamma_i y\cosh(\gamma_i y)\right)\right],\\
N_{ffi,y} = \tfrac{\partial^2\Phi_{ffi}}{\partial x^2} &= -\gamma_i^2\sin(\gamma_i x)\left[C_{1,ffi}\cosh(\gamma_i y)+C_{2,ffi}\sinh(\gamma_i y)\right.\\
&\quad \left.+C_{3,ffi}y\cosh(\gamma_i y)+C_{4,ffi}y\sinh(\gamma_i y)\right],
\end{aligned}\tag{3.15}$$

and the constants $C_{1,ffi}\ldots C_{4,ffi}$ are

$$\begin{aligned}
C_{1,ffi} &= 0,\\
C_{2,ffi} &= B_{ffi}\frac{\sinh(\gamma_i b)+\gamma_i b\cosh(\gamma_i b)}{\gamma_i^2\left(\sinh^2(\gamma_i b)-(\gamma_i b)^2\right)},\\
C_{3,ffi} &= -B_{ffi}\frac{\sinh(\gamma_i b)+\gamma_i b\cosh(\gamma_i b)}{\gamma_i\left(\sinh^2(\gamma_i b)-(\gamma_i b)^2\right)},\\
C_{4,ffi} &= B_{ffi}\frac{b\sinh(\gamma_i b)}{\left(\sinh^2(\gamma_i b)-(\gamma_i b)^2\right)}.
\end{aligned}$$

Thus each of the $i = 1,2,\ldots,I$ components of the cutting and feed forces produce stress functions which alter the strain energy of the system via (3.3). Calculating the terms of each stiffness matrix requires integration of products of polynomials and trigonometric or hyperbolic functions, for which recursive methods may be employed.

Figure 3.11 shows the stress distributions for a plate which has noncutting spans

of $s_u = 0.3\ell$ and $s_l = 0.2\ell$, with 15 sine series in the approximation of k_f, where k_f is a bias of 10kN/m with no sinusoidal nature. Considering Figure 3.11 the specified boundary conditions for N_{xy} and N_y, have been satisfied. Gibbs phenomenon can be seen in N_{xy} along the cutting edge at the edges of the workpiece, and N_{xy} is seen to vary about the bias between $x = s_u$ and $x = \ell - s_l$. Naturally, more sine functions in the approximation would yield a more accurate representation of k_f, although Gibbs phenomenon would be exacerbated.

To compare the partial-span formulation with the full-span one, the entire length may be taken as the cutting span ($s_u = s_l = 0$), which results in the stress distributions shown in Figure 3.12. In comparison with the full-span formulation (see Figure 3.6), the stress distribution N_x is nonzero along the trailing edge, however it is otherwise similar to the previous method for $\iota = 0.5$. The reason for this disparity is that the partial-span formulation prescribes zero shearing stress along the pinned boundaries, thus requiring N_x alone to maintain the equilibrium of the plate. In the full-span method the shear forces along these boundaries react the moment caused by the cutting load, and thereby maintain rotational equilibrium. The outcome is that the normal stress N_x within the plate is much larger (in both tension and compression) in the partial-span formulation.

These disparities make comparison of the methods difficult. However Figure 3.13

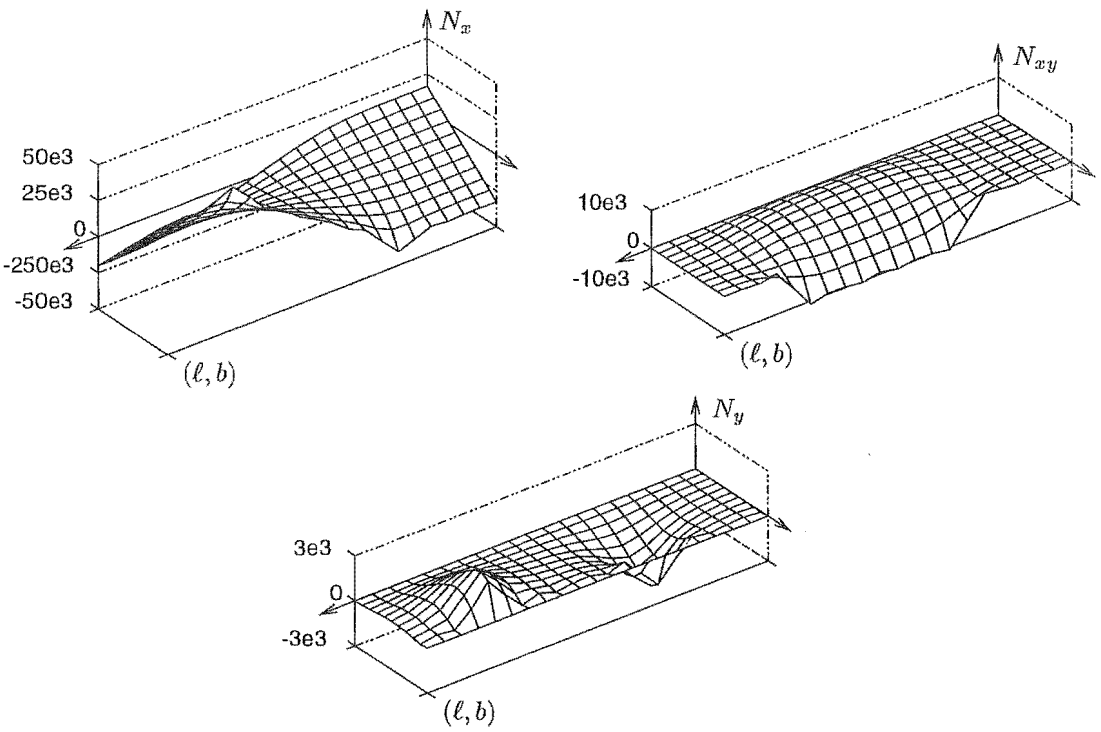

Figure 3.11: *N_x, N_{xy}, N_y for a constant cutting load acting along a partial span of the leading edge ($s_u = 0.3\ell, s_l = 0.2\ell$).*

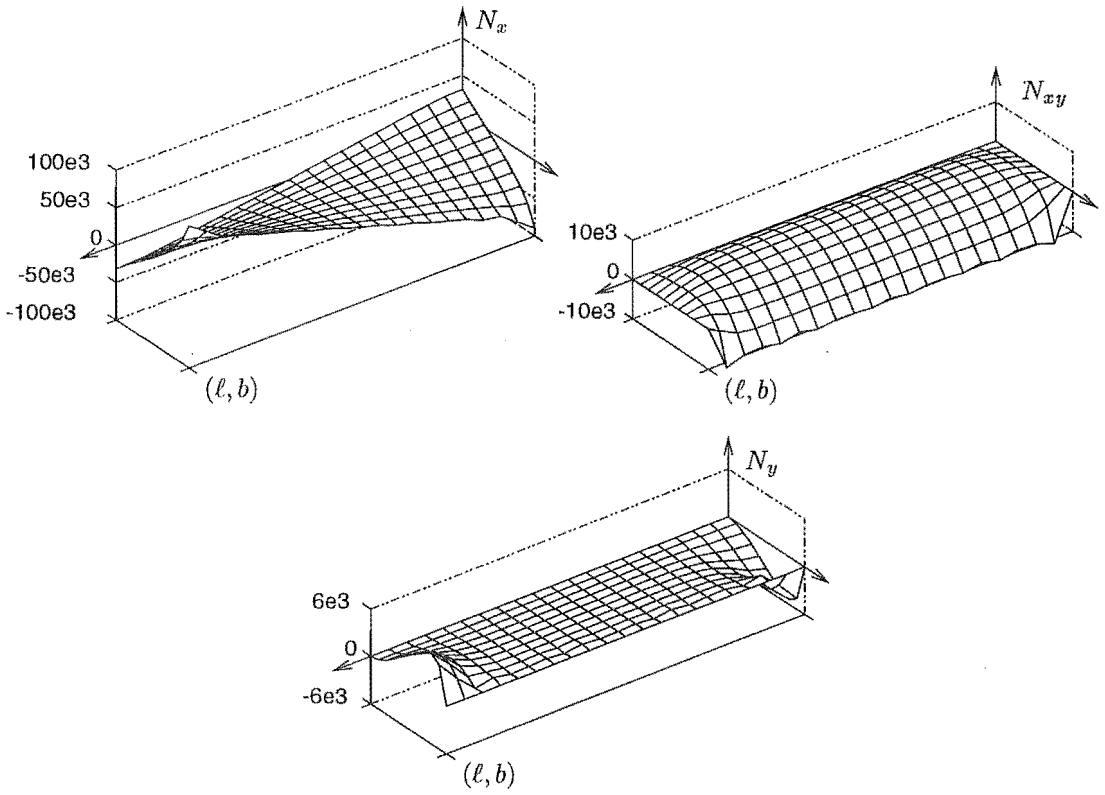

Figure 3.12: *N_x, N_{xy}, N_y for a constant cutting load acting along the entire length of the leading edge ($s_u = 0, s_l = 0$).*

depicts the modal forms of the first three modes for the partial-span formulation, showing that the behaviour is similar in form to the previous formulation. Figure 3.14(a) shows the effect of increasing cutting load upon vibration frequencies, for increasing numbers of Fourier terms.

Figure 3.14(b) adds the lateral component of the follower force, which may be compared with the results of Figure 3.9(a)). One significant result here is the apparent flutter induced for low numbers of functions describing the cutting load, but not for more accurate descriptions. The large values of N_x cause the divergent buckling of the fundamental mode instead of the flutter noted in the full-span formulation, however flutter continues to occur between the fourth and fifth modes independent of the number of Fourier terms.

Each of these cutting formulations have their pitfalls, the major one that threatens both is that the results for the stress conditions near the plate boundaries are often incorrect, especially if the boundary conditions are not accurately described. In the case of a bandmill with crowned and tilted wheels which is cutting timber with unknown and variable qualities, it is hard to imagine the boundary conditions prescribed by either formulation being even close to accurate. Having said this however, it is worth considering the condition of shear at the $x = 0$ and $x = \ell$ boundaries.

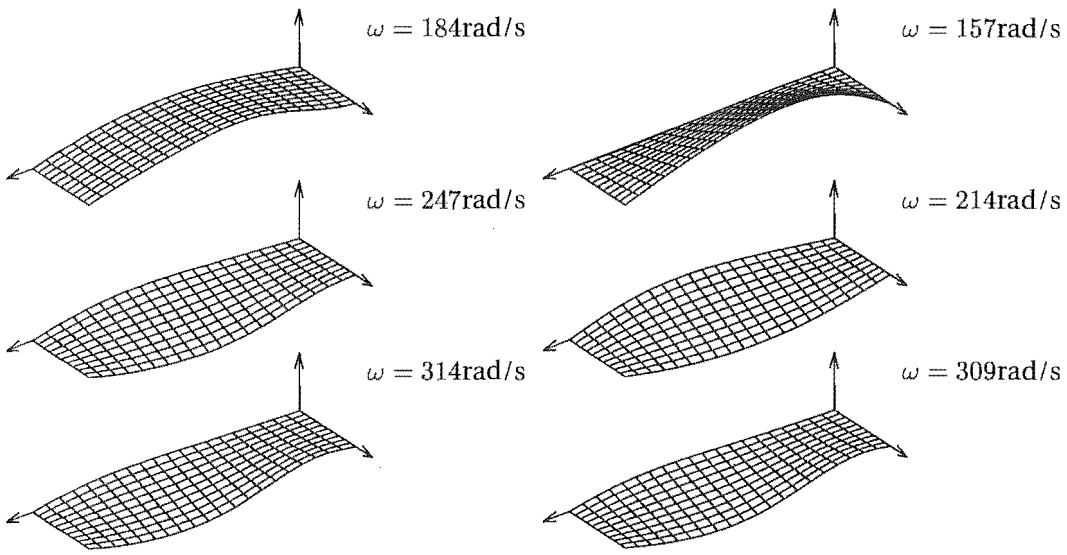

(a) $I = 1$. (b) $I = 15$.

Figure 3.13: *Modal forms using partial cutting formulation for cutting along the entire leading edge.* $k_f = 15kN/m$

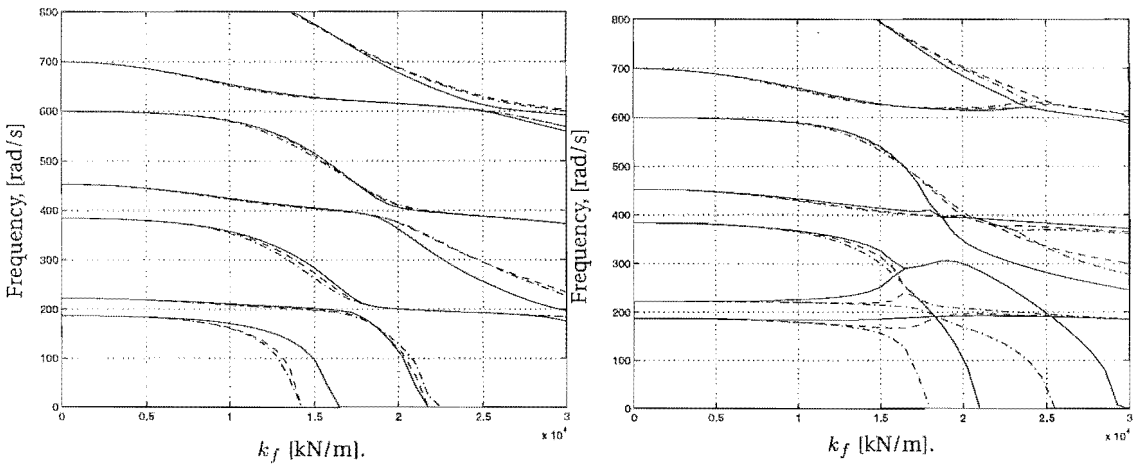

(a) Tangential component of follower force. (b) Full follower force.

Figure 3.14: *The effect of increasing the number of terms in the Fourier representation of the cutting load (which is applied along the entire cutting edge). Figure 3.14(b) may be compared to the full-span results shown in Figure 3.9(a). KEY:* — $I = 1$, - - $I = 5$, -·- $I = 15$.

Such a shear must be either be reacted by the shearing stress between the wheels and the blade or by a movement of the blade that alters the tension so that the cutting load is countered by the longitudinal stress alone. This corresponds to the boundary conditions of the partial-span formulation, while the assumption of shear at the upstream and downstream boundaries corresponds to the full span method.

3.4 PARTIAL SPRING FORCE, DAMPING FORCE, LATERAL FOLLOWER FORCE AND ADDED MASS

In a manner similar to that in Section 2.3.2.1 the spring, damping and follower forces may be accounted for by using the virtual work done by these forces,

$$\delta W_{ex,sd} = \int_0^b \int_0^\ell f_{ex,sd} \delta w dx dy, \tag{3.16}$$

where

$$f_{ex,sd} = \begin{cases} 0, & 0 \leq x < s_u \\ -(k_s w + k_d \frac{\partial w}{\partial t} + k_f \frac{\partial w}{\partial x}) \bar{\delta}(y-b), & s_u \leq x \leq \ell - s_l \\ 0, & \ell - s_l < x \leq \ell. \end{cases} \tag{3.17}$$

Combining these equations gives

$$\delta W_{ex,sd} = -\int_0^b \int_{s_u}^{\ell - s_l} (k_s w + k_d \frac{\partial w}{\partial t} + k_f \frac{\partial w}{\partial x}) \bar{\delta}(y-b)) dx dy, \tag{3.18}$$

so that distributed damping, spring stiffness and the lateral component of the follower load is applied along the partial span of the cutting edge.

Figure 3.15(a) shows the monotonic increase in frequency of all modes with increasing spring stiffness on the cutting edge. Of interest is the way the torsional modes are increased more than the transverse ones. The mode shapes are illustrated in Figure 3.15(b), and noticeable is the leading edge being "pinned" down more in the transverse modes than the torsional ones. The torsional ones are overall smaller due to the stiffening. At very high stiffnesses the third mode (which originally was the first torsional mode) develops length-wise nodes along the leading edge and near the trailing edge.

3.5 MODELLING THE EFFECT OF SAW GUIDES

In industrial saws, guides are positioned either side of the workpiece to aid saw stability and hence tracking. Guides used to be made from dense varieties of wood but

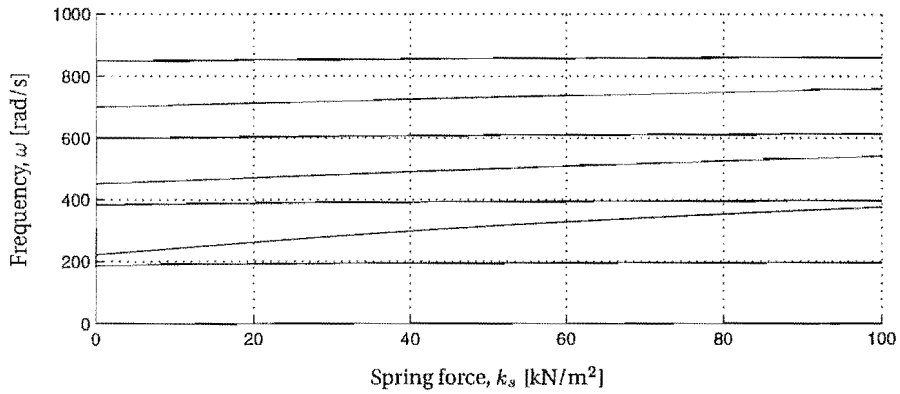

(a) Variation of frequency with spring stiffness on leading edge.

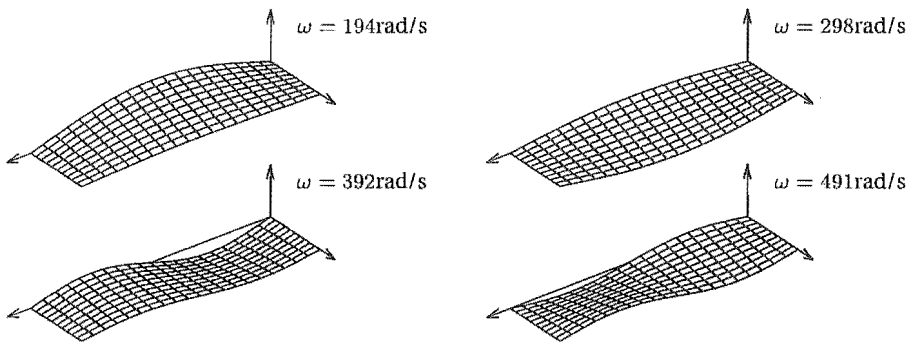

(b) Modal forms for $k_s = 40\text{kN/m}^2$.

Figure 3.15: *Effect of distributed cutting edge stiffness on vibration frequencies for the moving plate.*

are now made from polymers, resins or synthetic composites, sometimes with lubricating fluid to cool the blade and reduce friction between the guides and blade. The guides are either fitted on one side of the blade and maintain an offset pressure on the blade, so that the cutting surface is in a different plane to that joining the wheel rims, or on both sides with a defined pressure. The top guide position is often reset for each cut to further increase blade stiffness. These increases in blade stiffness are what improves the cutting accuracy.

Previous contributors have either ignored the guides or only modelled the span of the bandsaw between the saw guides. Lengoc (1990) showed that the inter-span coupling that exists in a three span beam (pinned at each end and at two mid points) reduces with increasing tension, thus justifying the approach of modelling just the central span.

For lateral control action, there must be enough space to position an actuator, for which there are four alternatives. These are:

(a) In the span between the band wheel and the upstream guide,

(b) In the corresponding span downstream of the lower guide,

(c) On the span on the opposite side of the bandmill, ie. the *return* span of the blade,

(d) The guide positions, so that the actuators are actually part of or a replacement for the current guide system.

All of these methods require a more complex model than what has been presented thus far; for example option (c) requires the modelling of the entire bandsaw instead of a linear span (Mote and Wu, 1985, Mote and Wang, 1986). The other options require a model of the guides themselves, which is the content of this section.

What follows are two methods for simply modelling such guides. The first uses singular value decomposition to find the null space of the basis function space comprising the plate deflection, and the second uses "regions of stiffness", or a restitutive pressure, that restricts the deflection throughout the region.

3.5.1 Singular value decomposition

Consider a point $(x, y) = (x_i, y_i)$ on the plate surface that is required to be constrained to the undeflected plane, so that

$$w(x_i, y_i, t) = 0. \tag{3.19}$$

Substituting w for the Ritz discretisation, a matrix equation may be formed from (3.19):

$$w(x_i, y_i, t) = \sum_{\alpha}^{m} \sum_{\beta}^{n} \phi_\alpha(x_i)\psi_\beta(y_i)q_{\alpha\beta}(t) = 0,$$

$$= \begin{bmatrix} \phi_1(x_i)\psi_1(y_i) & \phi_1(x_i)\psi_2(y_i) & \dots & \phi_m(x_i)\psi_n(y_i) \end{bmatrix} \underbrace{\begin{bmatrix} q_{11}(t) \\ q_{12}(t) \\ \vdots \\ q_{mn}(t) \end{bmatrix}}_{\mathbf{q}}. \tag{3.20}$$

If more than one point is to be pinned to the xy-plane, (3.20) becomes

$$col\{w(x_i, y_i, t)\} = \mathbf{W}\mathbf{q} = \mathbf{O}, \tag{3.21}$$

where $dim\{W\} = J \times mn$, J being the number of pinned points. The problem is now a question of finding the set of vectors that satisfy (3.21), and limiting the eigenproblem to this set. Such a problem may be solved using singular value decomposition, which decomposes the matrix $\mathbf{W}$ into three matrices $\mathbf{U}$, $\mathbf{\Sigma}$ and $\mathbf{V}$ such that

$$\mathbf{W} = \mathbf{U}\mathbf{\Sigma}\mathbf{V}^T, \tag{3.22}$$

where $\mathbf{\Sigma}$ has the structure

$$\mathbf{\Sigma} = \begin{bmatrix} \mathbf{\Sigma}_1 & \mathbf{O} \\ \mathbf{O} & \mathbf{O} \end{bmatrix}, \tag{3.23}$$

with $\mathbf{\Sigma}_1$ being diagonal and the diagonal terms being the singular values of $\mathbf{W}$. The matrices $\mathbf{U}$ and $\mathbf{V}$ are orthogonal and comprise spans of the four fundamental spaces corresponding to the mapping of $\mathbf{W}$. By partitioning matrices $\mathbf{U}$ and $\mathbf{V}$ so that

$$\mathbf{W} = \begin{bmatrix} \mathbf{U}_1 & \mathbf{U}_2 \end{bmatrix} \begin{bmatrix} \mathbf{\Sigma}_1 & \mathbf{O} \\ \mathbf{O} & \mathbf{O} \end{bmatrix} \begin{bmatrix} \mathbf{V}_1^T \\ \mathbf{V}_2^T \end{bmatrix}, \tag{3.24}$$

and post-multiplying both sides by $\mathbf{V}$ we find that,

$$\mathbf{W}\mathbf{V}_2 = \mathbf{O} \tag{3.25}$$

which means that $\mathbf{V}_2$ provides a basis for the null-space of the mapping $\mathbf{W}$. Therefore, in solving the vibration problem, we must admit only eigenvectors that come from this null-space. This may be done by replacing $\mathbf{q}$ in the equations of motion by $\mathbf{V}_2\mathbf{z}$, and also pre-multiplying by $\mathbf{V}_2^T$, so that the equation of motion (for the stan-

dard **MGK** system) becomes

$$\mathbf{V}_2^T\mathbf{M}\mathbf{V}_2\ddot{\mathbf{z}} + \mathbf{V}_2^T\mathbf{G}\mathbf{V}_2\dot{\mathbf{z}} + \mathbf{V}_2^T\mathbf{K}\mathbf{V}_2\mathbf{z} = \mathbf{V}_2^T\mathbf{B}u(t). \tag{3.26}$$

Once this system is solved the original coordinates are returned by $\mathbf{q} = \mathbf{V}_2\mathbf{z}$. The size of $\mathbf{q}$ is reduced by the number of restrained points, hence reducing the number of degrees of freedom of the system.

The number of constrained points alters the results of this formulation markedly, and so for this application where a reasonable area is to be constrained by a relatively small number of points this method is not suitable. Another method of describing the guides is shown below.

3.5.2 Regions of springs

Consider a rectangular area of the plate that is acted upon by a distributed restitutive pressure that is in proportion to but opposes the plate deflection throughout the area. If the area is bounded by $x_{g1} \leq x \leq x_{g2}$, $0 \leq y \leq b$, then the virtual work done on the plate is

$$\delta W_{ex} = -\int_0^b \int_{x_{g1}}^{x_{g2}} k_g w \delta w dx dy, \tag{3.27}$$

where k_g is the pressure generated for a unit deflection. As k_g becomes large, the results approach those of the singular value decomposition method, as shown in Figure 3.16. The singular value method does not model the third mode of the spring formulation, but produces almost identical mode shapes for the other modes. The stiffness method has the advantage that it may be "tuned" to model more accurately different guide materials, and also it does not reduce the number of basis functions in the model. A more complete guide model would include damping and the change in band tension caused by the friction opposing the translation of the saw; essentially a distributed version of the mass-spring-damper arrangement of Chapter 2.

Partial cutting examination. Figure 3.17 shows the effect of the partial loading in comparison to the full length loading. The workpiece is assumed to be located in mid-span and to act over one half of the blade length ℓ, which is now 2m in length (twice that of Figure 3.14(b)). Guides are placed either side of the cutting length, with widths of 0.01m and stiffnesses of $k_g = 1 \times 10^8 \mathrm{N/m}^2$. Results for the short span ($\ell = 1$m) are also shown for this number of basis functions. The first mode to destabilise in the three span blade vibrates primarily in the upstream span. The second mode to be destabilised vibrates predominantly in the central span, and compares reasonably well with the single span result. The modal forms of this mode are shown

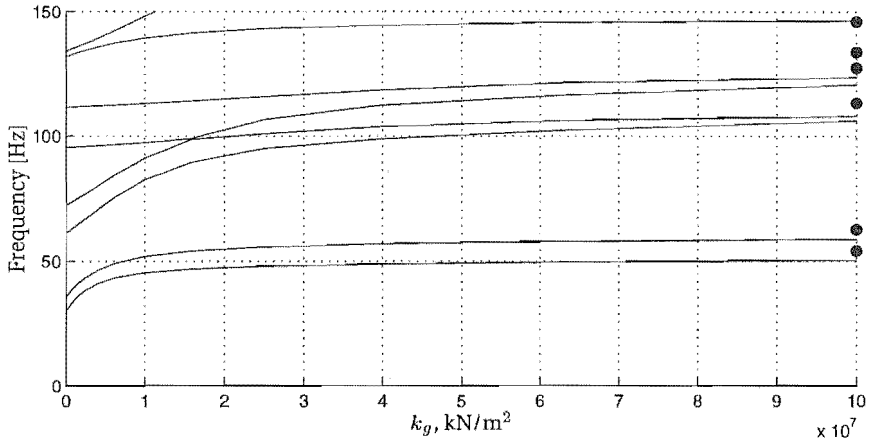

Figure 3.16: *Modelling guides by areas of restitutive pressure.* $x_{g1} = 0.3\ell$, $x_{g2} = 0.4\ell$. *KEY:* — *Spring like formulation,* • *Singular value method, with six constrained points (arranged in two lines of three across the width of the blade).*

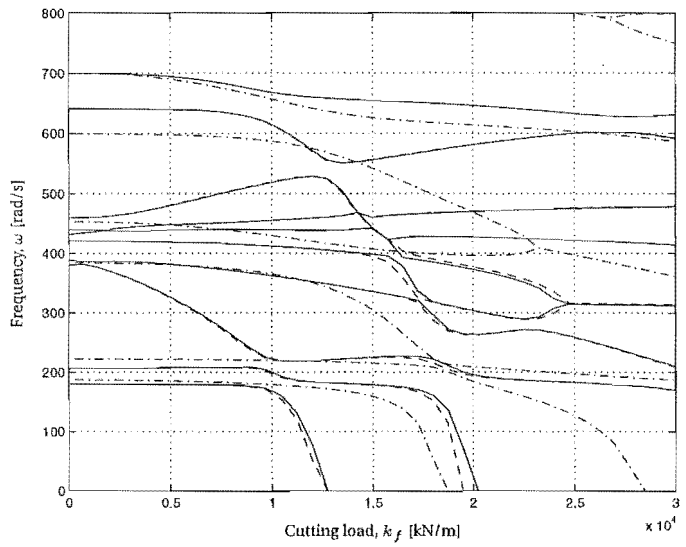

Figure 3.17: *The effect on vibration frequency of the cutting span length.* $m = 7$, $n = 5$. *KEY:* — *Long span,* $I = 5$, - - *Long span,* $I = 15$, -·- *Short span,* $I = 10$.

for $k_f = 17\text{kN/m}$ in Figure 3.18. The small vertical lines on the multispan plots show the borders of the central span. The final multispan blade with higher guide stiffness and more terms in the cutting load produces a form very close to the single span result, however the frequency is still similar to the previous multispan system.

3.6 FURTHER DAMPING

The damping of the previous section models the damping inherent in the cutting process, and thus acts along the cutting edge. However, stationary and idling blades are also damped, and this damping may be modelled in a similar way to the former. The only difference is that the damping force exists over the entire blade surface, so the damping force becomes

$$f_{ex} = -k_{ds}\frac{\partial w}{\partial t}. \tag{3.28}$$

3.7 BRINGING IT ALL TOGETHER

The large number of effects that comprise this model and the uncertainty in some parameters (k_f and k_s for example) means that a logical examination of the interactions of each of the various parts would be cumbersome, confusing and unenlightening. Such an analysis would also be useless in solving the problem at hand, which is to produce a model of a cutting bandsaw that may be used to implement effective model-based feedback control. A case study that embodies the modelling thus far presented is given in Chapter 5.

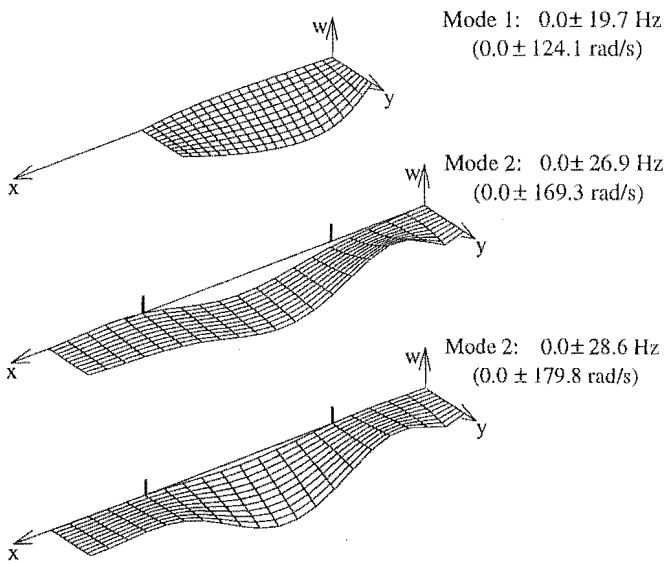

Figure 3.18: *Modal forms of the single and three span blades under loads of* $k_f = 17\,kN/m$.

3.8 CONCLUSION

The single span blade subjected to a follower load has been modelled and successfully compared with the results from Lengoc and McCallion (1995a). Edge damping and stiffness has been added, as well as pointwise disturbance and/or actuation forces.

A multispan model with cutting forces acting along a part of the leading edge has been formulated, with the aim of being used in the investigation of the vibration control of the centre (cutting) span via sensing and actuation of the upstream and downstream spans. The feed load was also modelled by this method. Damping, stiffness and the lateral component of the follower load were applied to the cutting region of the leading edge. Guides were modelled upstream and downstream of the cutting region, creating a multispan blade. The partial cutting formulation prescribes different boundary stresses to the full length one, making the two methods difficult to compare. Also, the lack of orthonormality of higher order basis functions limits the number that may be successfully employed in this technique. In fact, this is a limitation to using polynomials generated by the modified Gram-Schmidt process for the single span work also, but is more problematical in the partial cutting formulation because of integrands involving higher order polynomials multiplied by trigonometric and hyperbolic functions.

In both formulations, an attempt is made to allow for the effect of the strain mechanism on the longitudinal stress of the cutting saw. This has a large affect on the saw behaviour, and real data is required to find the correct change in boundary strain with increasing cutting load.

Another addition to the model would be the out of plane component of the feed force. Rather than being proportional to $\frac{\partial w}{\partial x}$ as the cutting force is, this would be proportional to $-\frac{\partial w}{\partial y}$. So, while the feed forces are smaller than the cutting ones, the addition of the follower nature to the feed force may add some interesting dynamics.

Chapter 4

EXPERIMENTAL APPARATUS AND CALIBRATION

This chapter details the experimental rig developed and used to compare a real system with the modelling of Chapters 2 and 3. The rig is a simplified bandsaw, simple enough to reduce unwanted or spurious effects in more complex bandmills but complete enough to embody the nature of axially moving continua and more specifically bandsaws. Also, a collocated magnetic actuator-sensor pair is developed, tested and used in the validation of the models of the previous two chapters.

Electromagnets are an attractive (excuse the pun) means of actuation as they can exert a noncontacting force on the blade, minimising heat production and therefore blade wear. If such electromagnetic actuators are good enough, they may in time replace current guides, providing noncontacting damped stiffness and control of the blade, without the wear and continual replacement associated with conventional guides.

A potential spin-off from considering lateral control of distributed bodies (such as plates) using electromagnets is the possible application to other industries, such as plate levitation and vibration suppression in the steel making industry and noncontacting forced vibration analysis.

4.1 EXPERIMENTAL RIG

The bandsaw rig used throughout this work is pictured in Figures 4.1 and 4.2. The bottom wheel is fixed while the top is borne eccentrically on a shaft to which is attached a weighted lever. The torque applied by the lever on the shaft is reacted by the saw tension acting at the eccentric distance. This mechanism provides the simple counterweight strain mechanism, and may be locked in position or left free. The wheels are aluminium, and the top wheel is not crowned while the bottom has the minimum crown required for good tracking of the saw. The motor is a single phase induction machine driven by a variable frequency current driver, thus providing variable transport speed. The blade speed is monitored using an optical circuit that is switched once every wheel revolution. A safety cage is used in case of band

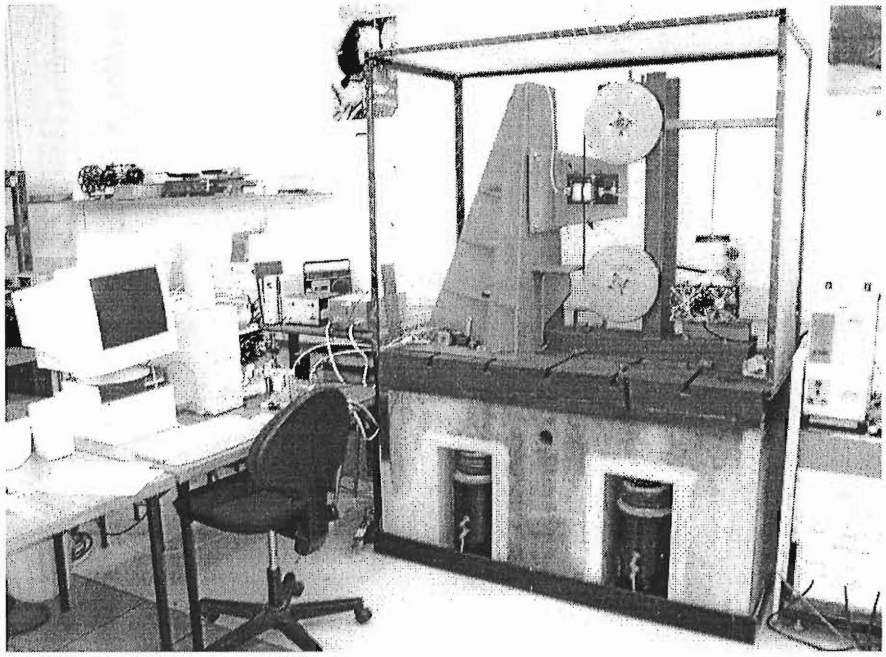

Figure 4.1: *Bandsaw rig and associated hardware.*

failure, and the main bracket to the left of the rig is used to support the actuating magnets and other hardware. A PC is used to capture signals such as the band speed via an analog to digital converter, and actuation signals are made using pulse width modulated signals output by a digital to analog converter on board the computer, and converted to a winding current in the electromagnets via a 150V current driver. Basic specifications are listed in Table 4.1, and Appendix B provides more details.

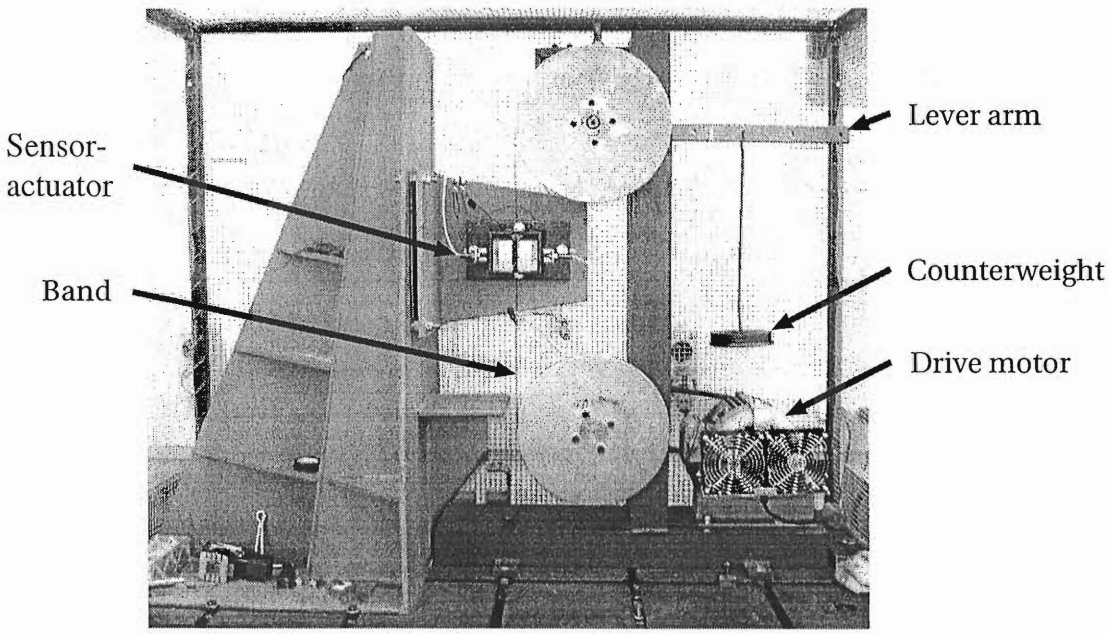

Figure 4.2: *Bandsaw rig - elevation.*

Table 4.1: *Bandsaw rig specifications*

Wheel diameter	300mm
Nominal wheel centre distance, ℓ	600mm
Wheel thickness	30mm
Blade width, b	22mm
Blade thickness, h	0.6mm
Blade Young's modulus, E	205GPa
Blade density, ρ	7800kg/m^3

4.2 ELECTROMAGNETIC ACTUATION

4.2.1 Basic theory

This section provides a brief overview of electromagnetism as it applies to this work. The literature includes many treatments of the subject, and the reader is directed there for more detailed accounts.

Magnetic fields are measured by the *flux*, ϕ, measured in *Webers* (Wb), and the *flux density*, B, which is measured in Wb/m^2, or equivalently in *Tesla*, (T). One Tesla is present if a 1 Coulomb charge moving at 1m/s experiences a force of 1N. The flux passing through a certain area is calculated by integrating the component of the flux density that is orthogonal to the area. The *field intensity*, H, of units A/m, is related to the flux density by $B = \mu H$, where μ is the *permeability* of the material containing the field. The permeability of free space is $\mu_o = 4\pi \times 10^{-7}$H/m, and other materials are specified by their *relative permeability*, a dimensionless quantity that relates the material permeability to that of free space. A material with a high relative permeability produces high flux densities, concentrating or magnifying the magnetic field. Such materials are *ferromagnetic*, examples being iron, cobalt and nickel.

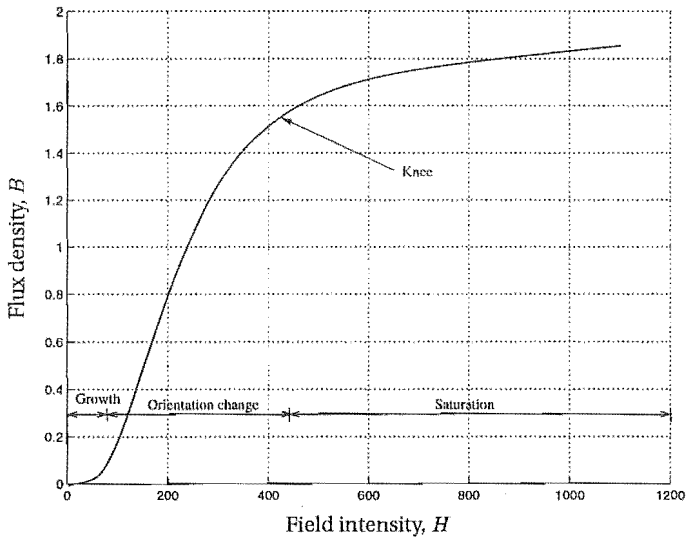

Figure 4.3: *Generic B-H curve for ferromagnetic material.*

If a magnetic field is applied near a ferromagnetic material, the material actually changes so that the flux density is greater than that expected from free space. This change is the formation and growth of magnetic *domains* within the material, with these domains being defined by the constituting atoms having a common alignment of their magnetic polarity. As the applied field increases, domains already in-line with the field grow, and the others rotate to align their polarity with the applied field. Once all domains are aligned the rate of increase in flux density with the applied field strength resembles that of free space, and the material is said to be *magnetically saturated.* This process is shown on a B-H curve in Figure 4.3, where the initial part of the curve is the (reversible) growth of the initially aligned domains, the steep portion is the (irreversible) re-alignment of the other domains, and the last portion is where the material has become saturated. The generic shape of the curve holds for all ferromagnetic materials but the steepness and saturation levels change with material composition and processing.

If the applied magnetic field is then reduced (after the material has been saturated), the domains within the material maintain their state until the applied field decreases enough to start actively reversing their orientation (region "A", Figure 4.4). If the applied field is oscillatory with large enough amplitude to saturate the material the *hysteresis loop* shown in Figure 4.4 results.

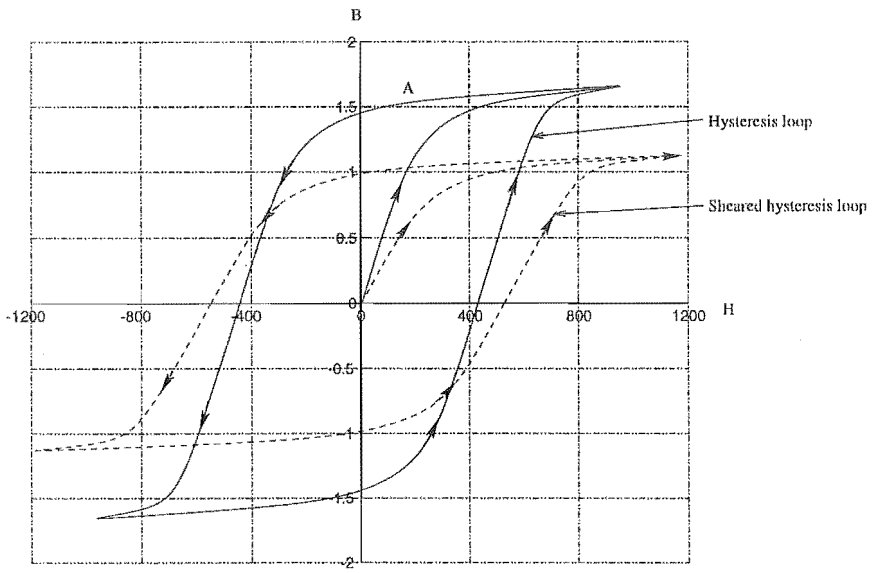

Figure 4.4: *Generic hysteresis loop for ferromagnetic material.*

A magnetic field is usually pictured by lines of flux, which must form a closed loop. The closeness of these lines depicts flux density. The closed loop of flux lines constitutes a *magnetic circuit,* which is analogous to the electric circuit. Appendix 4.2.3 discusses and uses the magnetic circuit in calibrating the electromagnets, however it is worth mentioning here the effects of shearing of the B-H curve and magnetic

fringing. Both effects are due to air gaps in the magnetic circuit, where the flux must traverse a gap of relatively low permeability (in relation to the other, probably ferromagnetic parts of the circuit). Such gaps reduce the overall permeability of the circuit, producing the "sheared" B-H also curve shown in Figure 4.4. Fringing occurs when the lines of flux "bulge" out across a gap, so that the area relating the flux to the flux density becomes unknown, reducing the effectiveness of the magnetic circuit laws.

4.2.2 Electromagnet specification

Electromagnets with E-type laminated steel cores are used in this work. This is acceptable for proof of concept however graphite cores are superior in high frequency applications, and for simulating the point loads modelled in Chapters 2 and 3 concentric cylinders would be a better core geometry. Table 4.2 lists the specifications of the electromagnets, and Figure 4.5 provides an accompanying sketch. The calibration and specification of the eddy current sensors to be used in tandem with these electromagnets are detailed in Appendix B.2.

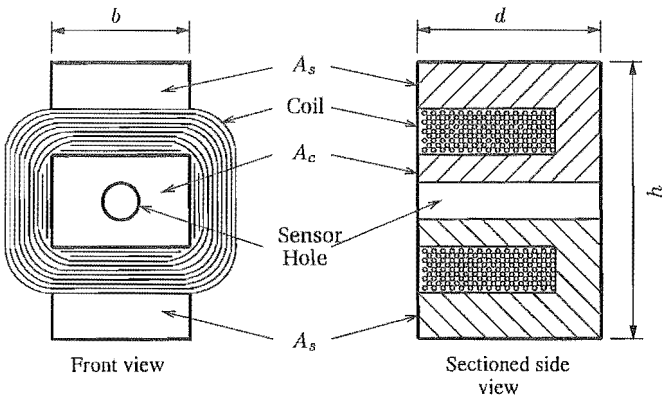

Figure 4.5: *E-type electromagnet, showing the core area, A_c, and side areas, A_s, of the face.*

Table 4.2: *Electromagnet specification*

Dimensions	$h \times b \times d = 58 \times 28 \times 38$mm
Core area, A_c	4.20×10^{-4}m^2
Side area, A_s	2.42×10^{-4}m^2
Core material	Laminated steel
Core type	E-type
Coil material	0.26mm diameter copper wire
Coil resistance	94.5 Ω
Number of turns in coil	2200
Coil inductance (without core)	102.1 mH
Coil inductance (with core)	760 mH

4.2.3 Calibration

The goal of this calibration is to be able to specify a winding current in the magnet coil that will enact a certain required force in a target that is a known distance from the magnet face. According to standard magnetic theory the force induced in the target should be proportional to the square of the winding current and the inverse square of the separating distance; however, the effects mentioned in Section 4.2.1 compromise this relationship. The extent of and solutions for this compromise are detailed in Appendix B.1, however the main result is that excellent agreement between theory and experiment can be achieved for the blade if the saturation of the B-H curve in Figure 4.3 is accounted for. The reader is directed to the Appendices for the detail of this work.

4.3 MODEL VALIDATION

This section compares the aforementioned bandsaw rig with the models of Chapters 2 and 3. An informative method of identifying the physical system is to produce experimental frequency responses and compare these with Bode plots of the theoretical models. The correlation method discussed and used in Appendix B.1 (Ljung, 1999) is used again here. Figure 4.6 shows the frequency response of a stationary blade over a frequency range of 10-400Hz using 2Hz intervals, with a higher resolution inset that encompasses the first mode. The sensor-actuator pair is positioned at $x = 0.4\ell, y = b/2$. The important points in Figure 4.6 are the modal points (where the magnitude becomes large), the zero points (small magnitude) and the corresponding shifts in phase at these points. The band tension R_o may be found by equalising the moment of the hanging weights with the band tension, and this along with the other physical parameters may be used to produce a theoretical Bode plot using the beam model of Chapter 2. This theoretical response is compared with the experimental data in Figure 4.7. The DC gain is correct and the vibration frequencies match well throughout the entire spectrum, although the theoretical gain at high frequency is slightly larger than the experimental. Also, the disparity in the phase curves increases with frequency, with the experimental output lagging the theoretical. The DC gain matches because of the work in Appendix B.1, although the forcing field is only marginally strong enough to saturate the blade and so the saturated analysis does not affect this gain significantly. However, the matching of gains near the modal points is afforded by the saturated analysis as the deflections are large and hence the gap distances small. The theoretical gain is higher than the experimental at high frequency because there is no damping in the theoretical model, whereas the actual blade will naturally be subject to windage and material damping. Another factor contributing to this incongruence is the actuator bandwidth discussed in Sec-

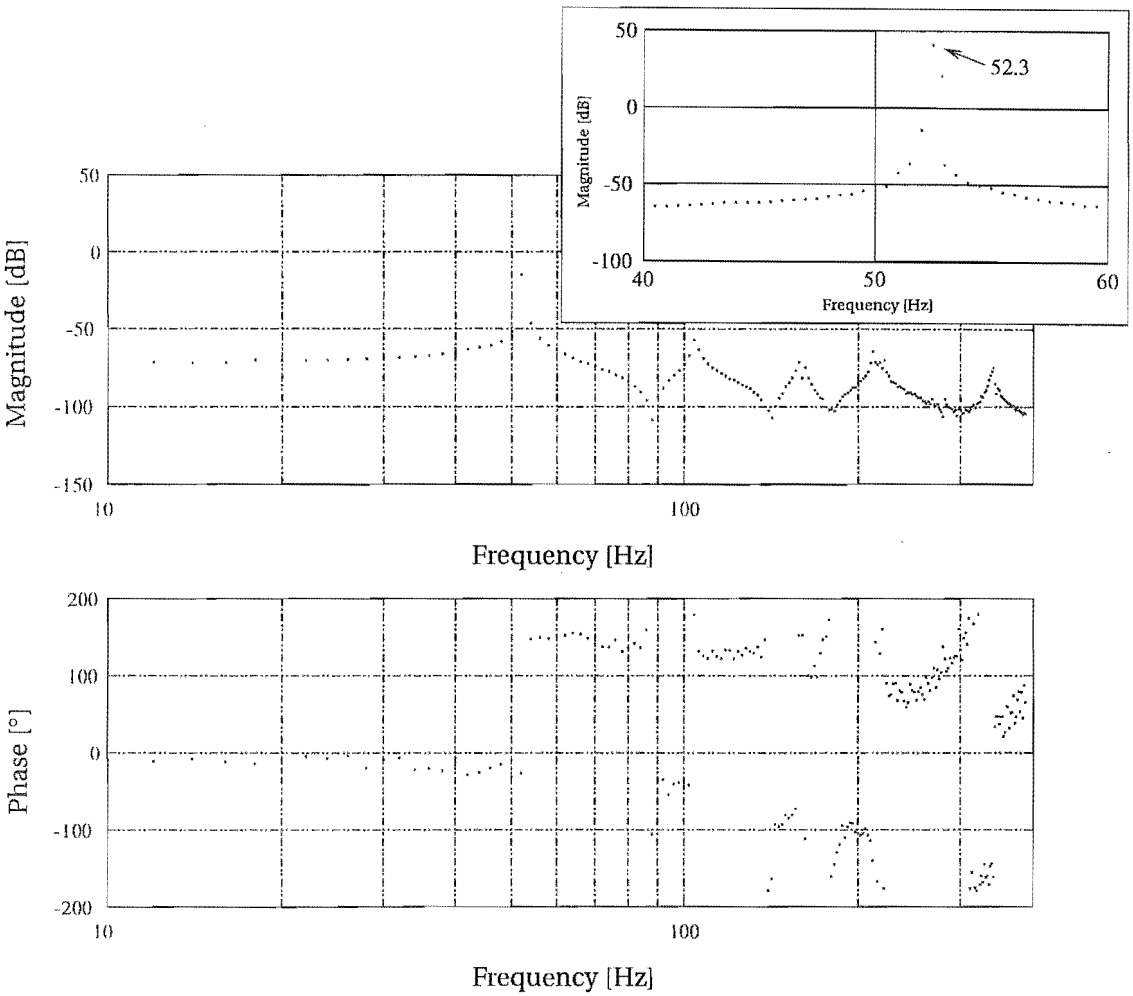

Figure 4.6: *Experimental frequency response of stationary beam.*

tion B.1 (see Figures B.5 and B.6). This also contributes to the experimental phase deviating from the theoretical.

4.3.1 Blade tension

The accuracy of the model regarding bandmill strain is shown for three different strains in Figure 4.8. The experimental points are found graphically using the experimental frequency responses, and therefore the accuracy is at best ±1Hz, (as all frequency response data is taken at 2Hz intervals). The agreement between theory and practice improves with tension, essentially because curvature of the band is removed and the blade approaches the straight beam assumed in theory.

4.3.2 The moving beam

Figure 4.9 shows the experimental frequency response for the blade travelling at $c = 15\text{m/s}$, and compares this data with theoretical responses for both the station-

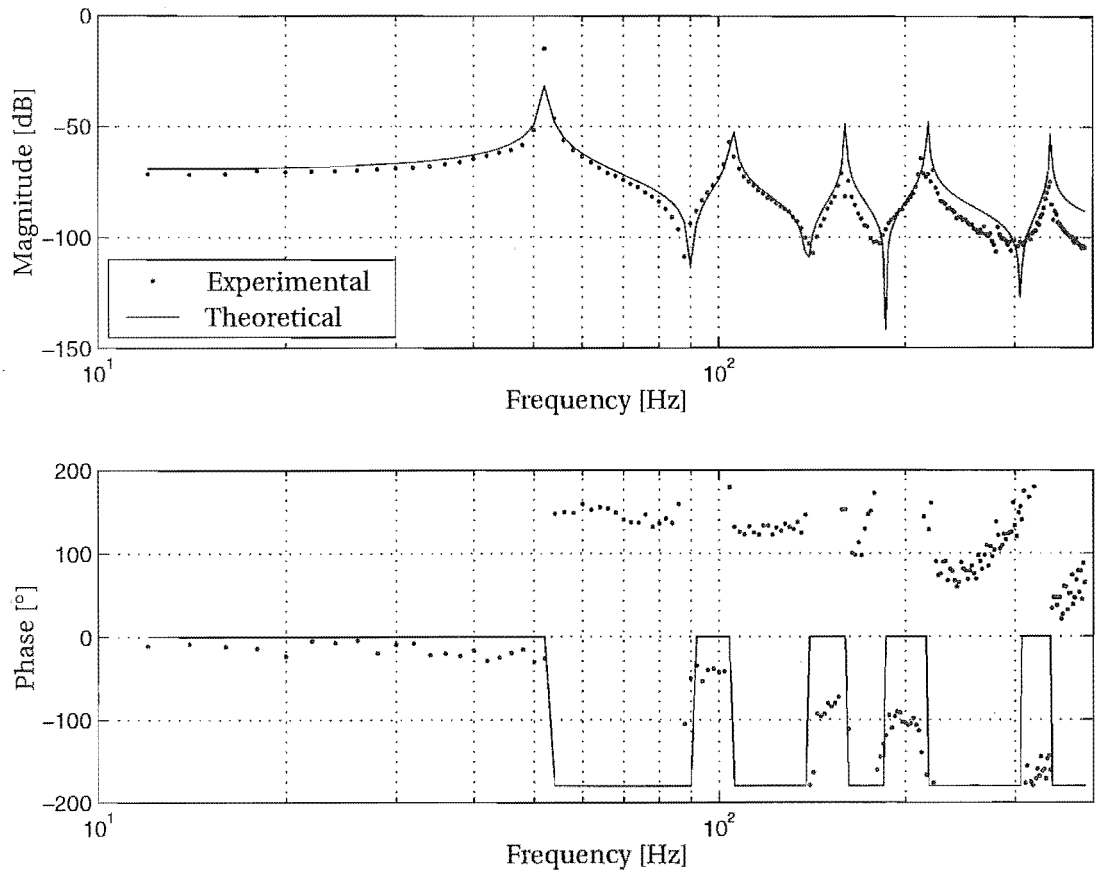

Figure 4.7: *Experimental and theoretical frequency responses of a stationary beam.* $R_o = 403N, m = 6.$

Tension [N]	Forced vibration frequency [Hz (Exp.) / Hz (The.)]				
168	34.8	68.1	101.7	147.6	235.2
	33.9	69.1	106.8	148.2	245.5
285	45.6	87.6	137.0	184.6	294.1
	44.0	89.0	136.1	186.0	297.8
403	52.0	104.6	159.1	212.3	341.4
	52.3	105.4	160.2	217.6	342.5

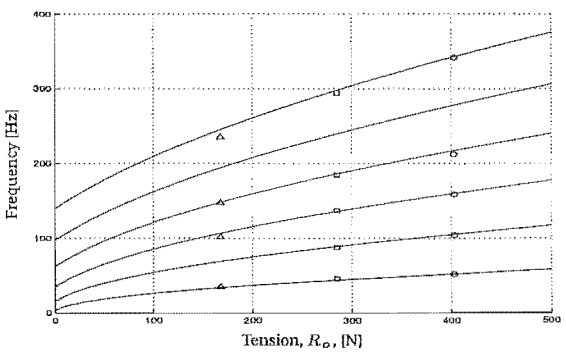

Figure 4.8: *The effect of blade tension on experimental and theoretical frequencies. The table compares experiment and theory at specific tensions, while the graph shows how well the experimental values compare against the theoretical continuum of frequency with respect to tension.*

ary and moving blades. The translating model fits the experimental data better than the stationary both in the vibration frequencies and in the form of the response. The translation has also had the effect of scattering the phase plot at high frequencies, and to reduce the sharpness of the modal peaks. To summarize the effect of speed the modal points were graphically found for a number of different speeds at each of the three tensions in Figure 4.8. Figure 4.10 shows these results for the first four modes of vibration. The theory matches experiment well for the first three modes but not for the fourth, and in fact the fifth mode (shown in Figure 4.7 near 340Hz) is impossible to pick from the experimental magnitude plots when $c \neq 0$. This mode is in fact the sixth natural mode of vibration, as the fifth does not appear in the frequency responses as the sensor-actuator position ($x_a = x_s = 0.4\ell$) is a nodal point of this mode (a small jump near 280Hz in the translating theoretical plot can be seen). Figure 4.10 is for $\eta = 1$, corresponding to a free top wheel assembly. From theory a fixed wheel assembly should produce larger decreases in vibration frequencies for a certain speed, however the axles on the current rig deflect to a degree that the strain on the saw remains reasonably constant with speed, and therefore a similar situation to the free top wheel exists.

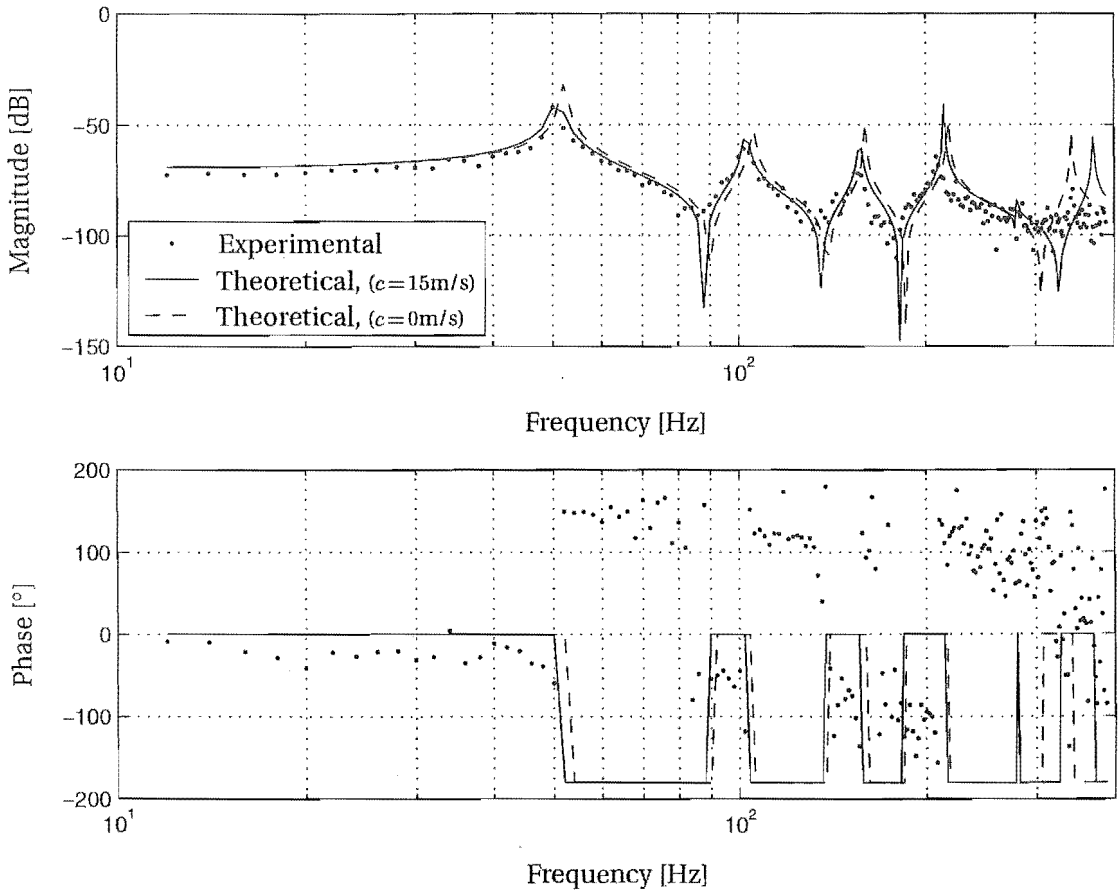

Figure 4.9: *Experimental and theoretical Bode plots of a moving beam.* $\eta = 1, c = 15 m/s$.

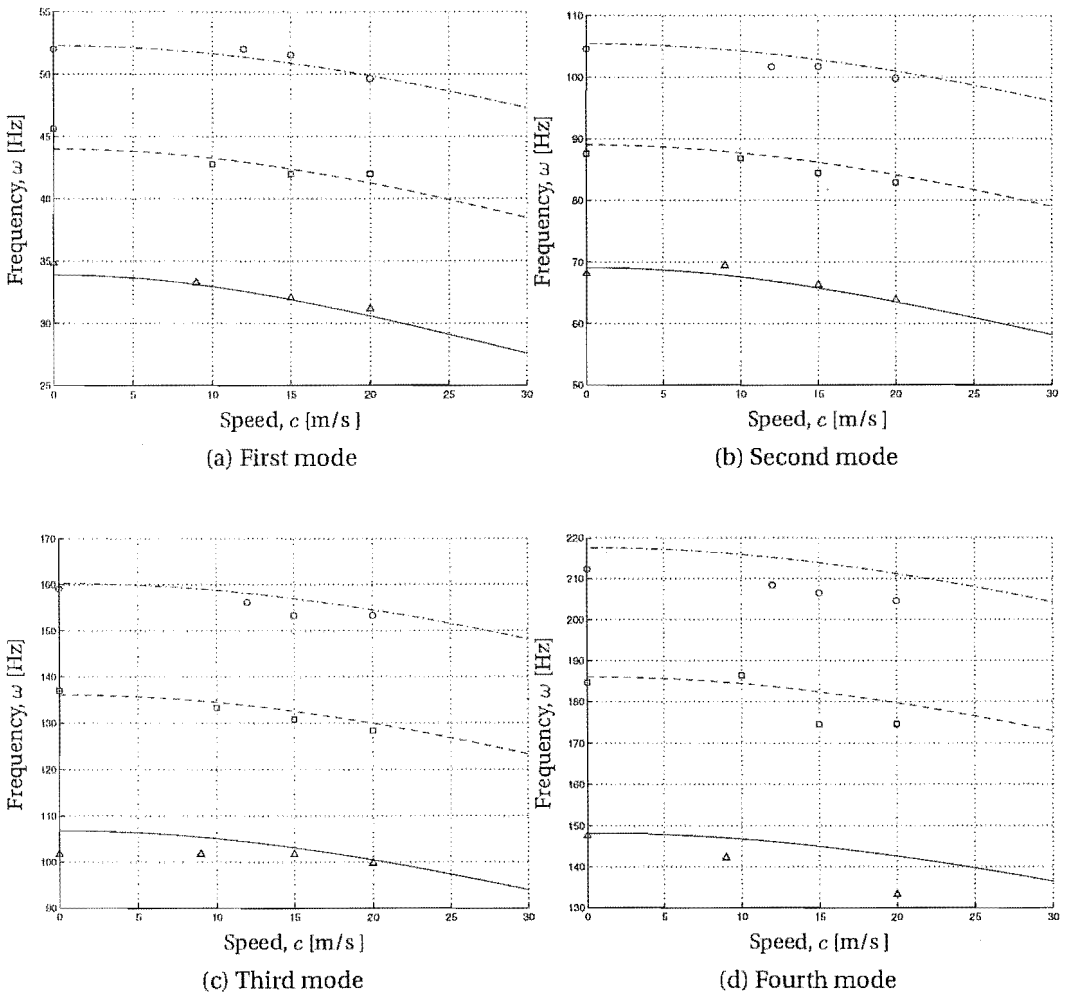

Figure 4.10: *Comparing the effect of blade speed on experimental and theoretical frequencies. Key:* — , ▵ $R_o = 168N$; — , □ $R_o = 285N$; - - , ○ $R_o = 403N$.

4.3.3 Actuator location

As shown in Figures 4.6-4.9, sensor placement at a nodal point completely reduces the observability of this mode (even if it is being excited by the actuator or some other influence, the sensor will not register any movement). The effects of changing the sensor-actuator position from $x_s = x_a = 0.4\ell$ to $x_s = x_a = 0.3\ell$ is shown in Figure 4.11. The fifth mode is now obvious but the transmittance of the third mode is greatly reduced because the sensor-actuator pair is now near a nodal point of that mode.

4.3.4 Plates

If the sensor-actuator pair is positioned at $(x_a, y_a) = (x_s, y_s) = (0.4\ell, 0.25b)$, so that torsional modes are also excited and measured (in fact the magnetic relationship means that these modes will be excited even when the magnets are placed in the middle of the blade but the sensor will not register movement). Figure 4.12 shows the magnitudes of the frequency responses for both the stationary and translating cases, and compares this data with both the beam and plate models. Considering

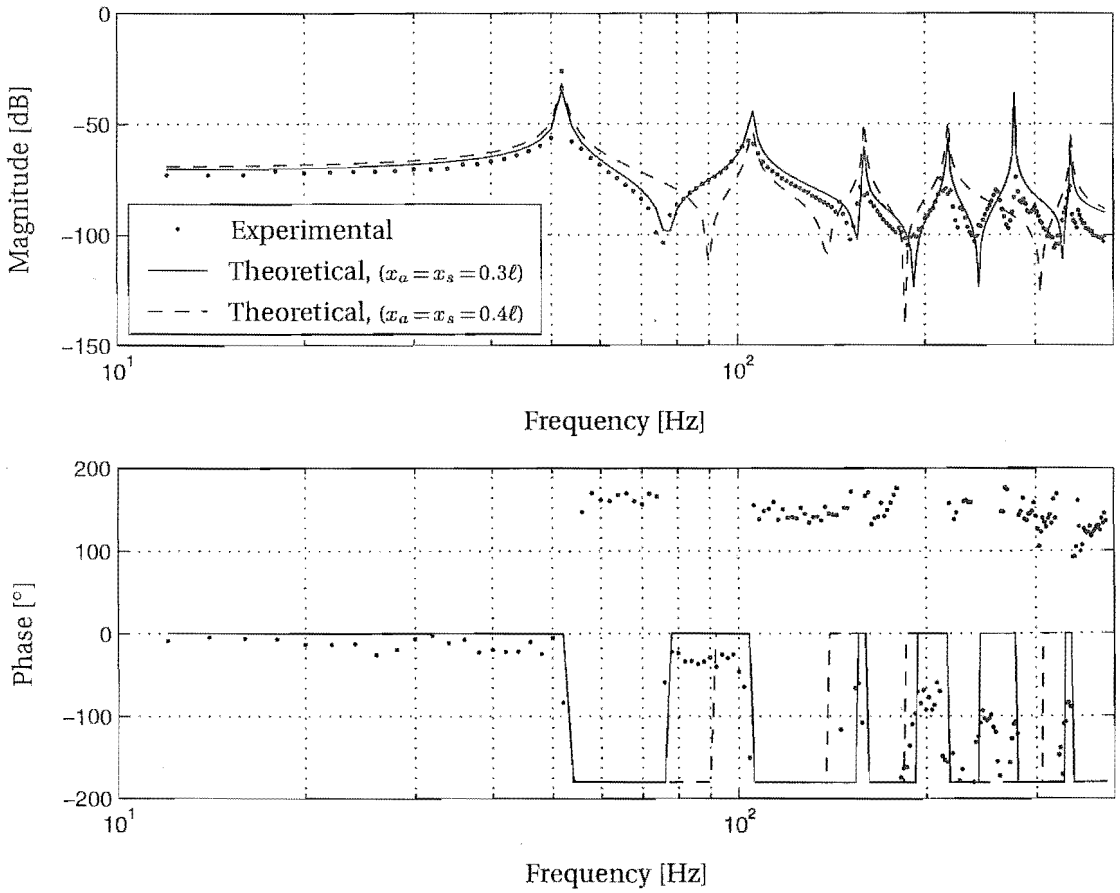

Figure 4.11: *The effect of sensor-actuator position on stationary blade dynamics.*

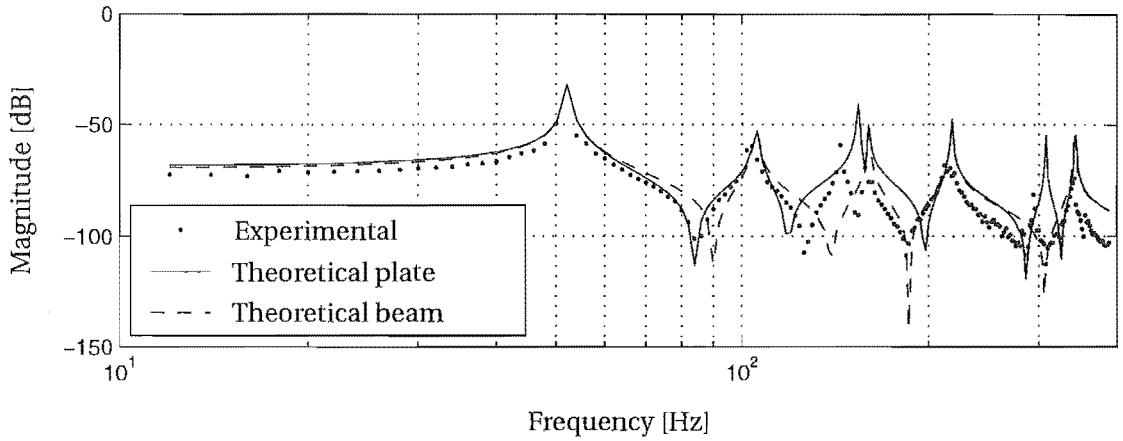

(a) Stationary case. (The gain at 52Hz is higher than 0dB, and hence is not shown.)

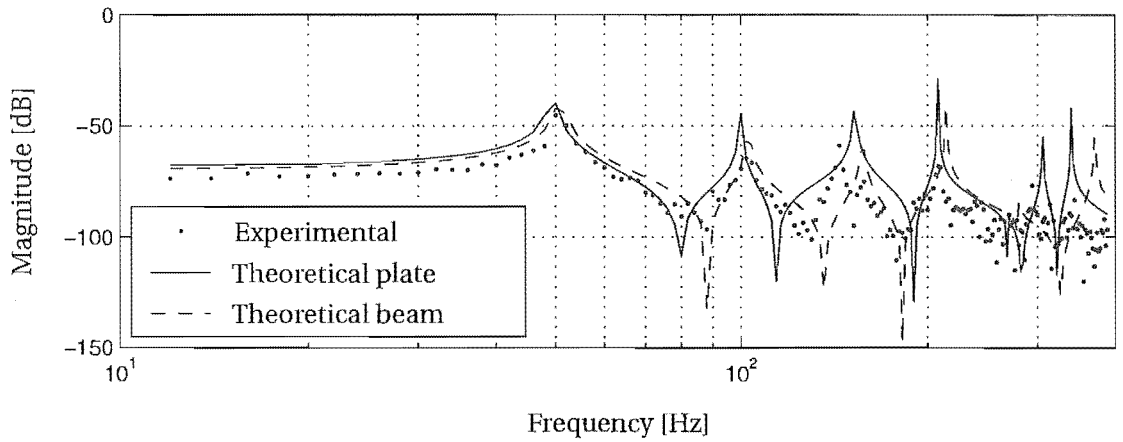

(b) Translating case ($c = 15m/s$).

Figure 4.12: *Experimental and theoretical frequency responses of a plate.*

the stationary case, the plate theory overestimates the torsional vibration frequencies, while the transverse modes remain as accurate as those predicted by the beam theory. Also of interest is the accurate prediction of the first system zero, but inaccurate prediction of the second and third zeros. However, with the inaccurate prediction of the torsional frequencies, it is unreasonable to expect accurate modelling of the nearby zeros. The sensor position is accurate to within ±3mm, which is small in comparison to the length, but significant in terms of the width. In the translating case, the same comments apply although the experimental data is made unclear by the blade translation.

4.4 DAMPING

Figure 4.13 shows that adding a small level of distributed damping in the theoretical model serves to reduce the sharpness of the peaks and troughs but otherwise does not alter the theoretical response. The damping mechanism is that proposed in Chapter 2, where the damping force is proportional to $-(\partial w/\partial t)$, rather than $-(c\partial w/\partial x + \partial w/\partial t)$ which has also been presented as a model of natural damping (Ulsoy and Mote, 1982). Using this formulation does not change the frequency response at all, because the translation speed is not high and the damping coefficient k_d is low.

4.5 ADDING ACTUATOR DYNAMICS

From Figures 4.7 and B.5 the electromagnet may be represented by a second order system with a natural frequency of 200Hz and a damping ratio of ζ =0.6. Such a system will add no gain at low frequencies but appreciable attenuation at higher frequencies and a phase lag of 90° at 200Hz and 160° at 600Hz. Figure 4.14 compares the experimental frequency response with the theoretical plot where the actuator dynamics have been included in the beam model. The damping is distributed with $k_d = 0.5\text{N}\cdot\text{s/m}^2$, and the phase has been unwrapped for clarity. The comparison with experiment is excellent and this actuator model will be used in the control strategies of the following chapter.

4.6 CONCLUSION

The collocated sensor-actuator and current driver worked very well in the validation work. Also, empirically modelling the actuator by simple second order dynamics was effective.

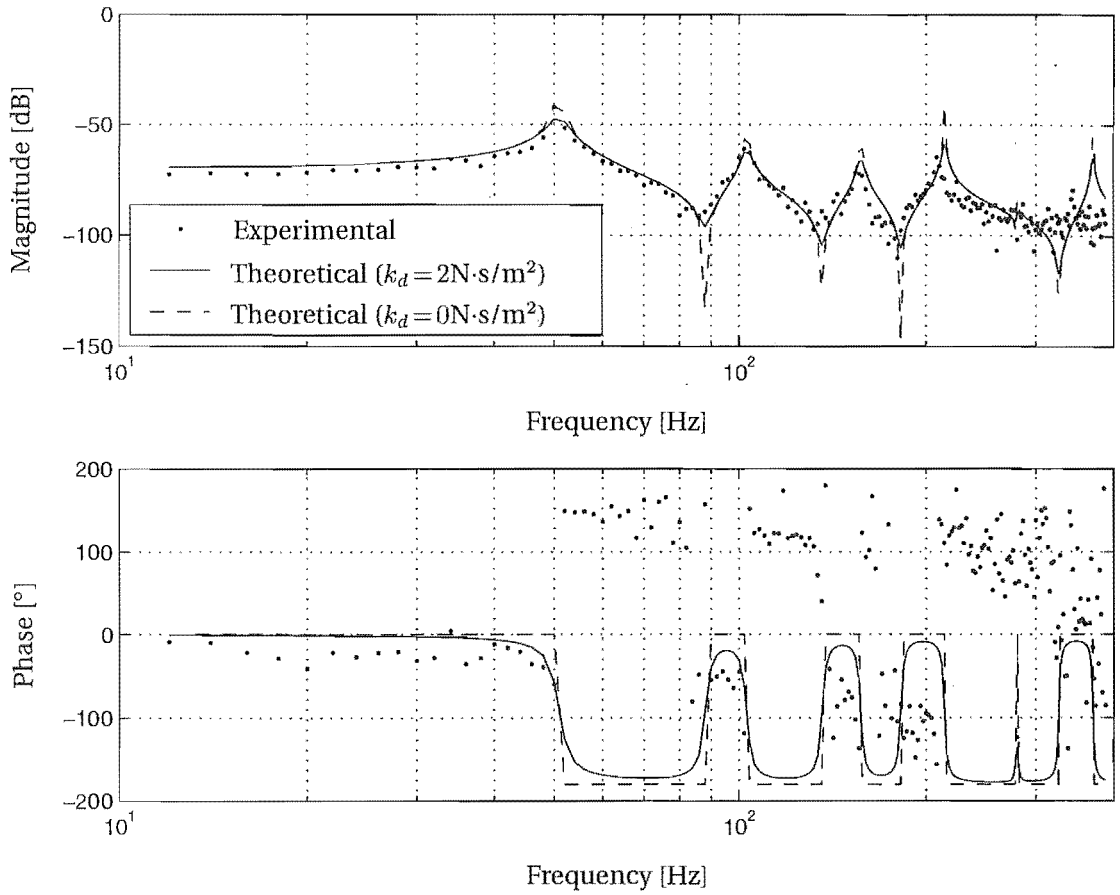

Figure 4.13: *Experimental plant compared with damped theoretical plant.* $\eta = 1, c = 15 m/s$.

The saturated force-current-distance linearisation produced excellent agreement between theoretical and practical deflections, statically and dynamically. However, accurately detailing the saturation levels is time consuming and differs with blade material. Therefore, if adequate control is possible without considering electromagnetic saturation then only the linear portion of the B-H curve should be used.

Prediction of transverse frequencies with respect to blade tension and speed were very good. However, prediction of the torsional frequencies and neighbouring zeros was less accurate. This has been noted by other contributors, and required some more investigation. Also, flexure of the top wheel shaft prohibited a true fixed wheel bandsaw.

Introduction of distributed damping and the simple modelling of the actuator dynamics resulted in very good agreement in the high frequency magnitude and phase. The physical apparatus and its modelling will be used in the ensuing control work.

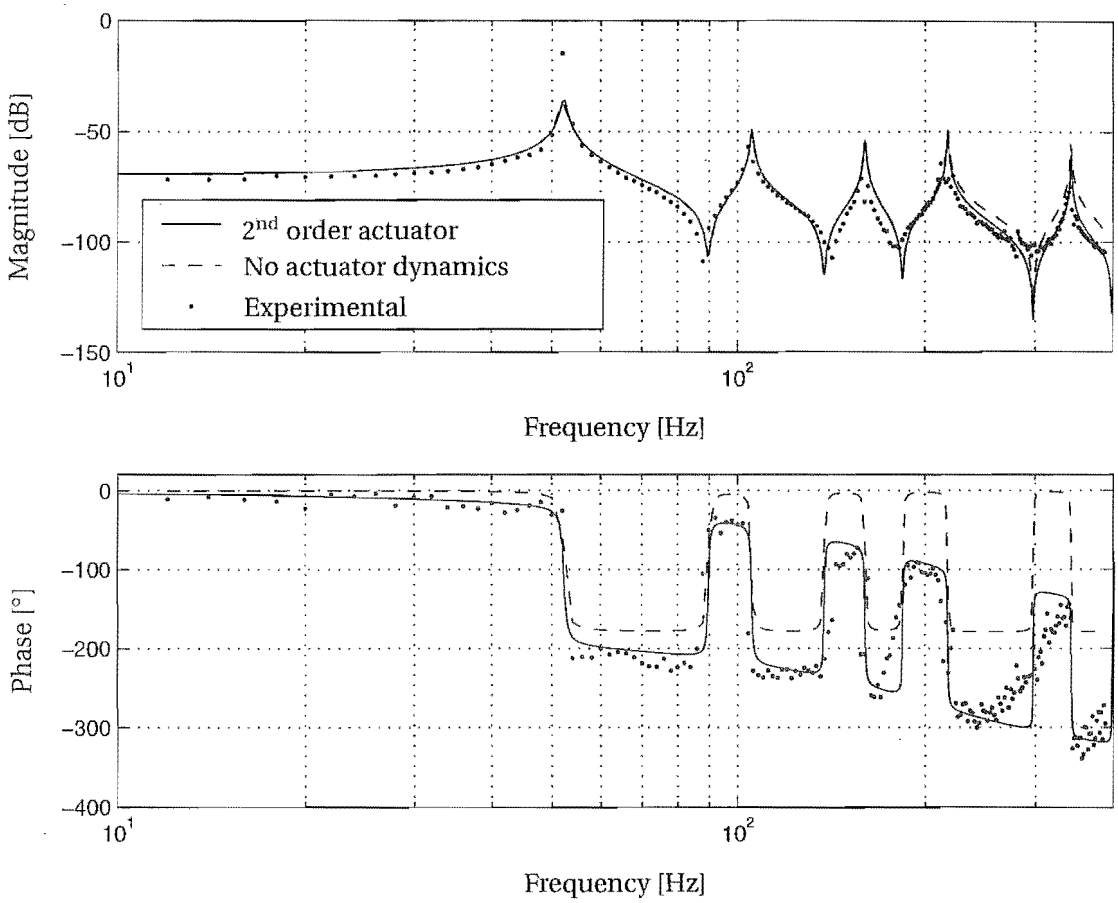

Figure 4.14: *Experimental plant compared with theoretical plant augmented with second order actuator dynamics.*

Chapter 5

CONTROL

The main hypothesis of this work is that active feedback control of a bandsaw blade can improve the performance of the bandmilling process. Such improvement can be made in a number of areas. Firstly, active stiffening and dampening of the sawblade means that, for the same performance, less damping and stiffness is required from passive sources such as the blade material, the blade geometry, the bandmill strain and the current guides. Secondly, phenomena such as washboarding, wedging and snaking, which are partially mitigated by existing bandmill designs, may be further reduced or entirely overcome by active control.

This chapter tests the above hypothesis using the beam and plate models presented in Chapters 2 and 3, coupled with the actuator and sensor dynamics of Chapter 4. Firstly a summary of the literature is given, after which classical and optimal control are introduced, with attention to the bandsaw problem. The work on signals and systems in Appendix C is requisite to this work. A comprehensive theoretical and experimental robustness study of the controlled moving beam is then presented, with the aims of gaining confidence in the theoretical simulation and gaining an accurate assessment of the potential improvements in nominal and robust performance. Finally, theoretical control of the cutting wide bandsaw is considered, leveraging on the lessons learnt in the noncutting control, and considering the more complex uncertainties inherent in the sawmilling process. Both single and multispan control are researched. In the multispan system the upstream and downstream spans are sensed and actuated, with the aim of attenuating the vibrations in the central span.

5.1 THE CURRENT STATE OF AFFAIRS

The active suppression of bandsaw vibration falls into two main categories; the active control of system parameters such as blade tension *(parametric control)*, and the active application of one or more transverse forces to the blade itself. Both methods require measurement of, among other things, the blade deflection and/or its veloc-

ity. As already mentioned, this work concentrates on the application of transverse loads. This method of controlling axially moving continua has been researched over the past decade, and this research is summarised below.

Mote and Yang (1991b) considered the controllability and observability of distributed gyric systems using the system eigenfunctions. They related controllability and observability to the system eigenvectors in the normal way, so that the minimum number of sensors and actuators required is the highest *multiplicity* of the system (assuming the sensors and actuators are not placed on nodal points or lines). The system multiplicity is the highest number of modes having common eigenvalues. In a companion paper (Mote and Yang, 1991c) these authors considered the frequency domain control of distributed gyric systems, using the root locus and generalised Nyquist methods to find controller gain limits with respect to system stability. Positive feedback of a pointwise deflection measurement was assumed. The authors presented controller gain limits for three special cases, one with collocation of the sensor and actuator with no time delay, one with collocation and time delay, and a third without collocation or time delay. It was found that for collocation and zero time delay any gyric distributed system is stable under the feedback law given by

$$H(s) = \mu \frac{N(s)}{D(s)},$$

where $\Im(\frac{N(j\omega)}{D(j\omega)}) \leq 0$ for $\omega > 0$, and μ is a real positive constant. This is equivalent to the condition for a Strictly Positive Real (SPR) controller, which for positive position feedback is that $-\Re\{\frac{1}{j\omega}\frac{N(j\omega)}{D(j\omega)}\} > 0, \forall\omega > 0$. Mote and Yang concluded that both of the other controllers produce an unstable closed-loop, and cited spillover as the cause of instability.

In the same year, Mote and Yang (1991a) focussed their attention to the active control of an axially moving string, and presented similar results to their more general works (Mote and Yang, 1991b,c). This work focuses on velocity feedback, using to advantage the closed-loop eigenvalue-loci curves and their rates of change with controller gain to prove stability with respect to collocation and time delay. One of the most interesting results is the destabilisation of the moving string when using dislocated control without time delay, but stabilisation when using a specific time delay, T_s, and symmetric dislocation about the midpoint of the string. This time delay is dependent on the translational band speed and the sensor and actuator positions, and given by

$$T_s = \frac{1}{a - \frac{c^2}{a}}\left[\ell + \frac{c}{a}(x_s - x_a)\right],$$

where $a = \sqrt{R_o/\rho A}$. Stability was guaranteed using the controllers for the collo-

cated case without time delay, but with 180° phase difference. Also, an upper stability bound was placed on the controller gain.

Yang (1994) considered the control of gyroscopic systems via direct velocity feedback using finite dimensional models rather than the infinite dimensional ones in Mote and Yang (1991b,c). Yang used the same root locus arguments of the previous works to generate an index of the damping introduced in each mode. A specific example of the moving string was again shown, but with no attempt to optimise the controller gains.

Moving away from mid-span actuators and sensors, Lee and Mote (1996) considered the boundary control of the travelling string. The control laws were based on the material velocity such that

$$u(t) = \left[k_1 c\frac{\partial w}{\partial x} + k_2\frac{\partial w}{\partial t}\right]\Bigg|_{x\in 0,\ell},$$

and expressions for the energy of the string including the flux across the boundaries were found and used to find the optimal control gains. Each boundary was considered individually and the optimal control gains for $(k_1 \neq 0, k_2 = 0)$, $(k_1 = 0, k_2 \neq 0)$, $(k_1 = k_2 \neq 0)$ were found by minimising the energy reflected at the controlled boundary. Asymptotic stability was proven for both boundaries and exponential stability proven for any downstream controller. Finally a numerical example compared control at either end with no control and control at both ends. The same authors produced a similar treatment for the translating beam (Lee and Mote, 1999).

Ying and Tan (1996) presented midspan control of the string using the curious notion of *space feedforward* and *space feedback* controllers. Here, the space feedforward controller used two deflection measurements taken upstream of the actuator position to quell vibrations downstream of the actuator. The space feedback controller used a single downstream deflection measurement to counter externally excited vibrations in the downstream span. The space feedback control law was a simple low pass filter, and the space feedforward control law was constructed by cancelling the forward propagating waves, with the assumption that such cancellation removes vibration in the downstream span and therefore no waves can be reflected back upstream by the downstream boundary. Simulations of the proposed control were presented with perfect vibration attenuation in the downstream span as soon as control was applied.

Wang and Mote (1996) discussed the formulation and design optimisation of hybrid bearings coupled to an axially moving beam. These bearings are a hybridisation of lubricated guides with active feedback control. The feedback comprises the sensing of both the blade deflection and its rate at the guide position, and the actuation of the guide fluid pressure. Passive control was also considered and increased flow of

lubricating fluid through the bearing was shown to increase the critical translation speed, with the position offering maximum translation speed being $x_a = 0.5\ell$. The problem was solved analytically for a single bearing, with multiple bearings left for future investigation.

A series of three papers (Fung and Tseng, 1999, Fung et al., 1999a,b) tackled the control problem by replacing the downstream boundary with a mass supported by a spring and dashpot, with the mass subjected to a control force. Linear control via velocity feedback at $x = \ell$ was considered by Fung et al. (1999a), and exponential stability of the linear string-mass system shown. Fung et al. (1999b) considered linear and nonlinear feedback for the nonlinear string-mass system, and showed that asymptotic stability was achieved using linear control but exponential stability could only be achieved by nonlinear control. Fung and Tseng (1999) approached the problem using the Lyapunov function used by Lee and Mote (1996) but with the mass-spring-damper energy added. A nonlinear model was presented and *variable structure control* applied, with the string deflection, slope and instantaneous velocity at the downstream boundary being required for control. Again asymptotic stability was proven and in special cases exponential.

de Queiroz et al. (1999) presented the adaptive control of an axially moving string, and compared this to a model-based controller. The control actuator was a sleeve encasing a portion of the string part way along the length, to which a lateral force and a couple could be imparted. Required for the model-based control were the string slopes and time rates of change at either side of the actuator sleeve and lateral position and orientation of the sleeve. The adaptive law also required these measurements but compensated for parametric uncertainty by adaptively estimating other parameters of the system.

Damaren and Le-Ngoc (2000) considered the feedback control of the cutting plate model presented in Lengoc and McCallion (1995a). A model-based approach was applied, with controllers formulated from $\mathcal{H}_2$ and $\mathcal{H}_\infty$ perspectives. Plant uncertainty was described in terms of the cutting load and band speed. Four controllers that satisfied performance and stability criteria were presented using a single actuator with collocated rate measurement.

Where from here. The above works provide a variety of control solutions to the translating continua problem. Many are highly theoretical works which assume and rely on physically unrealisable signals such as perfect rate measurement and/or unrealistic means of actuation. The last few contributions consider the practicalities of control implementation on a limited degree, but remain in the theoretical domain. The present work attempts to bridge the theory-practice gap, focusing attention to the non-contacting, multispan, multi-input multi-output feedback control of cut-

ting bandsaw blades. Classical and modern controllers are considered, and implementation issues kept in high regard throughout.

5.2 SAWMILLING - THE REAL WORLD

The work of Chapter 4 showed the limitations of the theoretical models for a simple bandmill without cutting influences. Such disparities can only increase during milling, where cutting influences, heating and other unmodelled effects come into play. Table 5.1 lists the major uncertainties present in the sawing process; some are

Table 5.1: *Bandmilling uncertainties*

Uncertainty	Description	Model parameters
Blade temperature	The cutting process heats the leading edge of the blade, altering the tension variation across the width.	R_o, R_b
Guide position	Often the top guide is repositioned for each cut, minimising the free span between the top guide and the workpiece.	x_g
Depth of cut	As the log diameter changes the length of saw encompassed by the workpiece changes.	s_u, s_l
Cutting force	The load on the saw teeth changes in both direction and magnitude due to changes in the depth of cut, timber type and age, moisture content, irregularities such as knots, and blade wear.	k_f, A_c, β
Blade speed	Timber variability also affects motor load and hence sawblade speed.	c
Finite dimensional modelling	Controller synthesis and simulation is performed using finite dimensional models. Either inaccuracies in higher modes or the omission of high modes can cause instabilities.	m, n, N_d
Nonlinearities	At high frequency and high band speeds nonlinearities increase, reducing the accuracy of the linear modelling.	

specific to the bandmilling of logs, but others apply to more general circumstances. The modelling proposed in Chapter 3 allows for some of the effects listed, although some heretofore constant parameters must be made time dependent. Where appropriate, the third column of Table 5.1 lists the model parameters pertinent to each uncertainty. Suitable controllers must provide stability and improved performance for any system that is described within physically feasible bounds of these parameters.

5.3 CONTROLLER FORMULATION

This section introduces classical and modern control, using the moving string model of Chapter 2 in examples. The string model is kept simple, using only two or four terms in the discretisation of the deflection surface; however, the sensor and actuator dynamics are considered throughout. The major steps and results of each controller development are shown without proof; references containing such proofs are given. The discussion is intended to give the layperson an idea of the mechanics behind each controller, as well as satisfying the control technician that the steps

being taken are correct and the underlying assumptions are satisfied. These goals do not require the treatment to be rigorous and therefore it is not. The merits and failings of each control strategy are discussed, leading to the somewhat predictable progression from classical to $\mathcal{H}_2$-optimal and finally $\mathcal{H}_\infty$-optimal control.

The control problem. The Single Input Single Output (SISO) feedback problem is shown graphically in Figure 5.1, where the translating continua is part of the feedback loop. All signals are assumed to be affected by noise, and the measured deflection is filtered prior to digital conversion. There is also an exogenous disturbance to the system that acts at $x = x_d$. Figure 5.2 shows the equivalent system in block

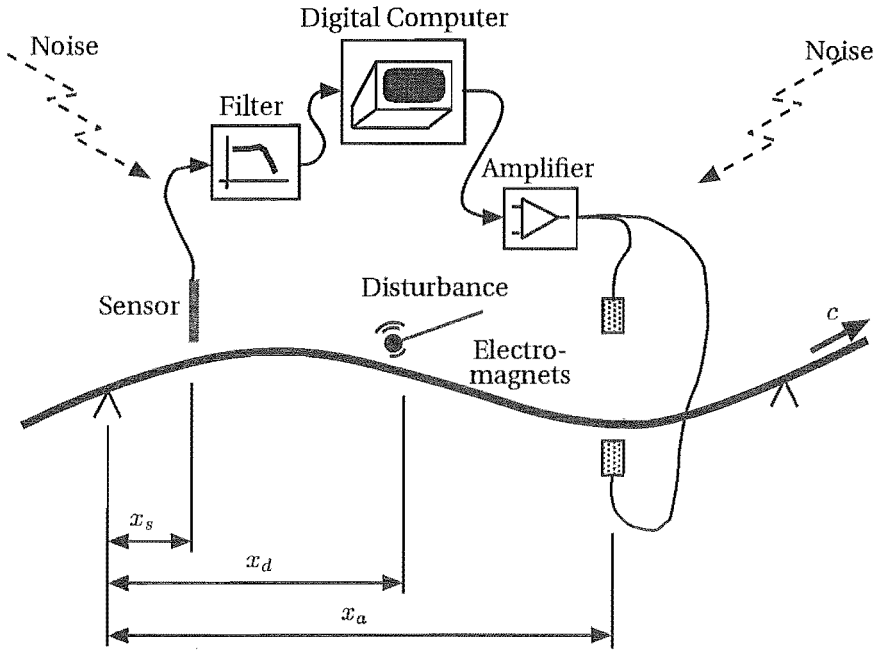

Figure 5.1: *SISO electromagnetic feedback control of translating continua.*

diagram form, where each block denotes a dynamic system such that (for example)

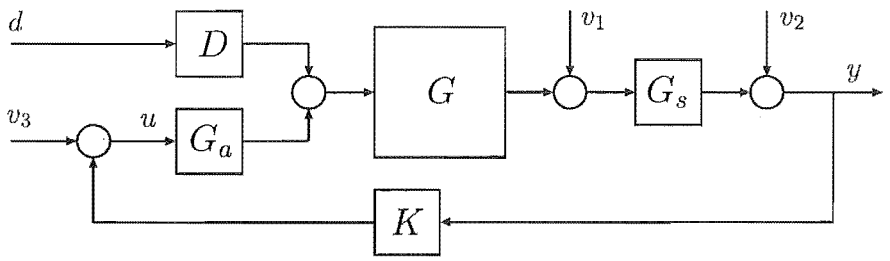

Figure 5.2: *General block diagram of SISO feedback control. In this and other block diagrams, signals entering summing junctions are assumed positive unless labelled otherwise.*

$$G \equiv G(s) = \left[\begin{array}{c|c} \mathbf{A}_G & \mathbf{B}_G \\ \hline \mathbf{C}_G & \mathbf{D}_G \end{array}\right], \tag{5.1}$$

where $\mathbf{A}_G, \mathbf{B}_G, \mathbf{C}_G, \mathbf{D}_G$ are the standard state-space matrices describing the system. Section C.1.1 describes this format as well as block partitioning and (matrix) transfer function descriptions.

The systems in Figure 5.2 are the plant itself, $G(s)$, the actuator $G_a(s)$, the sensor and any associated filtering $G_s(s)$, the disturbance dynamics $D(s)$, and the controller $K(s)$. Also shown are four exogenous inputs, three are noise inputs; $v_1(t)$ degrades the states of the plant, $v_2(t)$ the sensed position and $v_3(t)$ the control effort. The fourth input, $d(t)$, is a disturbance to the plant that may or may not be related to the actuator. It is assumed henceforth that the three noise inputs may be expressed by a single input $\tilde{v}(t)$ that is injected in place of $v_2(t)$, so that $v_1 = v_3 = 0$, $v_2(t) = \tilde{v}(t)$.

To fix ideas, recall the first order description of the original plant defined in Chapter 2,

$$\dot{\mathbf{x}}_m = \mathbf{A}_m \mathbf{x}_m + \mathbf{B}_m u \tag{5.2}$$

$$y_m = \mathbf{C}_m \mathbf{x}_m, \tag{5.3}$$

or in the new parlance

$$G_m(s) = \left[\begin{array}{c|c} \mathbf{A}_m & \mathbf{B}_m \\ \hline \mathbf{C}_m & \mathbf{O} \end{array}\right], \tag{5.4}$$

where the subscript "m" indicates that the terms are associated with the original model of the plant. Because the actuator and sensor in Figure 5.2 are dynamical systems in their own right, $G(s)$, may defined as

$$G(s) = \left[\begin{array}{c|c} \mathbf{A}_m & \mathbf{I} \\ \hline \mathbf{I} & \mathbf{O} \end{array}\right], \tag{5.5}$$

the actuator as

$$G_a(s) = \left[\begin{array}{c|c} \mathbf{A}_a & \mathbf{B}_a \\ \hline \mathbf{B}_m \mathbf{C}_a & \mathbf{O} \end{array}\right], \tag{5.6}$$

and the sensor as

$$G_s(s) = \left[\begin{array}{c|cc} \mathbf{A}_s & \mathbf{B}_s \mathbf{C}_m & \mathbf{O} \\ \hline \mathbf{C}_s & \mathbf{O} & \mathbf{W}_v \end{array}\right], \tag{5.7}$$

where the input to the sensor is assumed to be $\left[\mathbf{x}_m^T \quad v\right]^T$, and $\mathbf{W}_v$ is an arbitrary

weighting function on the sensor noise, so that $\tilde{v} = \mathbf{W}_v v$. The disturbance system $D(s)$ is assumed (at this stage) to be a static system defined by $D(s) = \mathbf{B}_d \mathbf{W}_d$, where $\mathbf{B}_d$ maps a pointwise force positioned at $(x, y) = (x_d, y_d)$ into the generalised coordinates of the original plant in the same way that $\mathbf{B}_m$ does. $\mathbf{W}_d$ is another arbitrary weighting matrix. Such arbitrary weighting matrices will be used extensively throughout this chapter, and are used by the control designer to make signals of different units or ranges of magnitude more comparable, or, when frequency dependent, to filter signals when some frequencies are considered more important to the control problem than others. It is worth noting that there may be multiple sensors, actuators and disturbances, so that the systems above are multi-input multi-output (MIMO) systems.

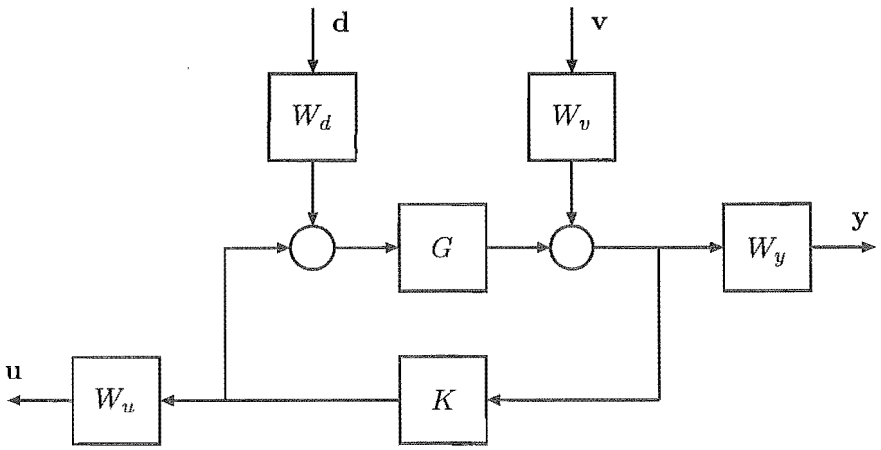

Figure 5.3: *General feedback problem.*

Closed-loop performance specifications. The feedback problem shown in Figure 5.2 is akin to the more general one shown in Figure (5.3). The only differences are that the control effort is considered as a system output and both this and y are subject to weightings. Also, the signals are now vectors and the systems are multiple-input, multi-output. Considering this more general problem we can write that

$$\mathbf{u} = W_u K(I - GK)^{-1} G W_d \mathbf{d} + W_u K(I - GK)^{-1} W_v \mathbf{v}, \tag{5.8}$$

$$\mathbf{y} = W_y(I - GK)^{-1} G W_d \mathbf{d} + W_y(I - GK)^{-1} W_v \mathbf{v} \tag{5.9}$$

or, in matrix form,

$$\begin{bmatrix} \mathbf{y} \\ \mathbf{u} \end{bmatrix} = \begin{bmatrix} W_y \\ W_u K \end{bmatrix} (I - GK)^{-1} \begin{bmatrix} W_v & GW_d \end{bmatrix} \begin{bmatrix} \mathbf{v} \\ \mathbf{d} \end{bmatrix}. \tag{5.10}$$

Equation (5.10) is the so called *four block problem*, as each of the four transfer functions give different performance and/or robustness specifications. For instance, the 1-1 block given by $W_y(I-GK)^{-1}W_v$ prescribes how the output disturbance $\mathbf{v}$ affects the output $\mathbf{y}$. This transfer function is therefore critical to the *sensitivity* of the sensed output to noise on the sensing device. In fact, the transfer function $(I-GK)^{-1}$ is known as the *sensitivity function*. Table 5.2 lists these transfer functions and their input-output relationships. All of the weighting functions are frequency dependent

Table 5.2: *Closed-loop performance specifications*

Function	-Interpretation
$W_y(I-GK)^{-1}GW_d$	-gain from plant input disturbance to plant output
$W_y(I-GK)^{-1}W_v$	-gain from plant output disturbance to plant output
$W_uK(I-GK)^{-1}GW_d$	-gain from plant input disturbance to control signal
$W_uK(I-GK)^{-1}W_v$	-gain from plant output disturbance to control signal

and chosen by the designer to satisfy and/or prescribe the requirements of each performance measure.

Linear fractional transformations. The feedback loop in Figure 5.3 may be composed as a *lower linear fractional transformation* (LLFT) system (see Glover and McFarlane, 1990). Defining the states of the new system to be $\mathbf{x} = \begin{bmatrix}\mathbf{x}_s^T & \mathbf{x}_m^T & \mathbf{x}_a^T\end{bmatrix}^T$, the inputs to be $\mathbf{w} = \begin{bmatrix}d & v\end{bmatrix}^T$ and u, and the outputs to be $\mathbf{z} = \begin{bmatrix}y & u\end{bmatrix}^T$ and y, the feedback system can be reduced to that shown in Figure 5.4. The *generalised* plant $P(s)$

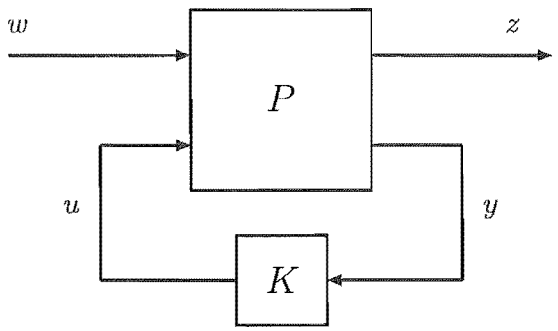

Figure 5.4: *Lower LFT diagram of feedback control.*

is given by the LFT arrangement

$$P(s) = \left[\begin{array}{ccc|cc:c} \mathbf{A}_s & \mathbf{B}_s\mathbf{C}_m & \mathbf{O} & \mathbf{O} & \mathbf{O} & \mathbf{O} \\ \mathbf{O} & \mathbf{A}_m & \mathbf{B}_m\mathbf{C}_a & \mathbf{B}_d\mathbf{W}_d & \mathbf{O} & \mathbf{O} \\ \mathbf{O} & \mathbf{O} & \mathbf{A}_a & \mathbf{O} & \mathbf{O} & \mathbf{B}_a \\ \hline \mathbf{C}_s & \mathbf{O} & \mathbf{O} & \mathbf{O} & \mathbf{W}_v & \mathbf{O} \\ \mathbf{O} & \mathbf{O} & \mathbf{O} & \mathbf{O} & \mathbf{O} & \mathbf{I} \\ \hdashline \mathbf{C}_s & \mathbf{O} & \mathbf{O} & \mathbf{O} & \mathbf{W}_v & \mathbf{O} \end{array}\right] \tag{5.11}$$

which is more amenable to the subsequent controller synthesis.

5.3.1 Classical control

An initial solution to the control problem is simple rate control. A proper, first order rate feedback controller may be expressed as

$$K_{c1}(s) = \frac{s}{2\pi f_1 s + 1} = -K(s) \tag{5.12}$$

where the variable f_1 gives the corner frequency of the controller. Partitioning the plant $P(s)$ so that

$$P(s) = \left[\begin{array}{c:c} P_{zw} & P_{zu} \\ \hdashline P_{yw} & P_{yu} \end{array}\right], \tag{5.13}$$

the Bode plot of the system $P_{yu}(s)K_{c1}(s)$ may be considered. Figure 5.5 shows this for a string with the parameters listed in Table 5.3 and the controller in (5.12) with $f_1 = 1500$Hz. The sensor and actuator dynamics are as per Chapter 4. Figure 5.5

Table 5.3: *String parameters.*

$\ell = 1$m	$A = \pi(\frac{2\times10^{-3}}{2})^2$m^2	$R_o = 500$N	$\rho = 7800$kg/m^3
$x_s = \frac{5}{12}\ell$	$x_a = \frac{5}{12}\ell$	$x_d = \frac{7}{10}\ell$	$k_d = 0.05$N·s/m^2

shows a stable closed-loop system, which is borne out in the impulse response plot of Figure 5.6. The disturbance is a 5N burst lasting 0.005s. The 2 mode assumption is of course misleading, as there are more modes in a real vibrating string. Figure 5.7 shows the open loop Bode plot of the same controller in feedback with a plant constructed from a four term discretisation of the deflection. At unity gain the fourth mode is unstable, and reduction in gain to the point of stability of this mode will produce great performance degradation in the lower modes.

The second order lag of the actuator is causing the closed-loop instability, and may be counteracted by a second order lead in the controller. Such a controller may

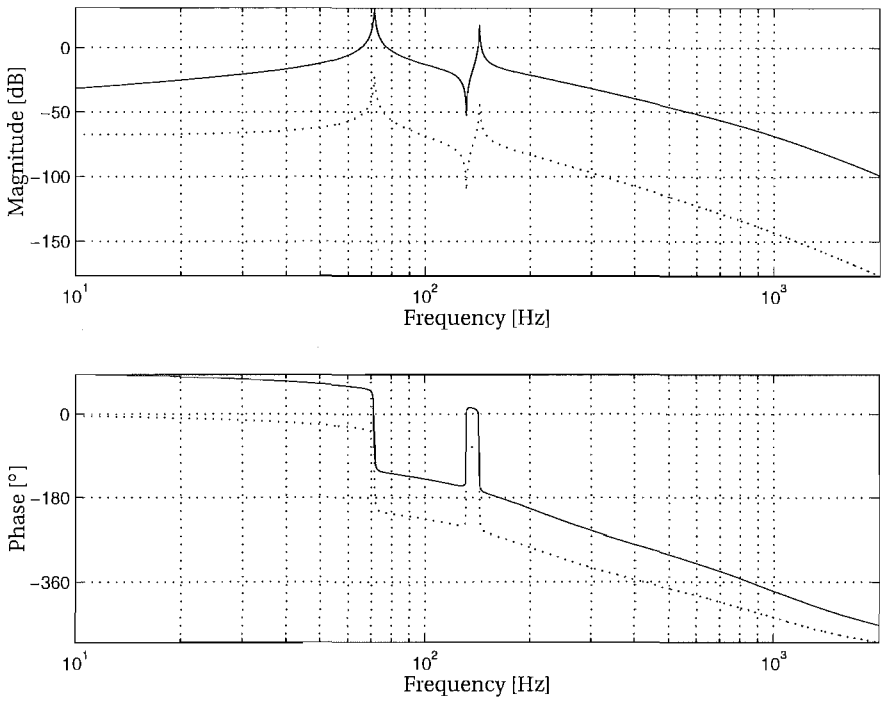

Figure 5.5: *Bode plot of simple rate feedback controller in series with 2 mode string model. KEY: — Simple controller, ····· Uncompensated system.*

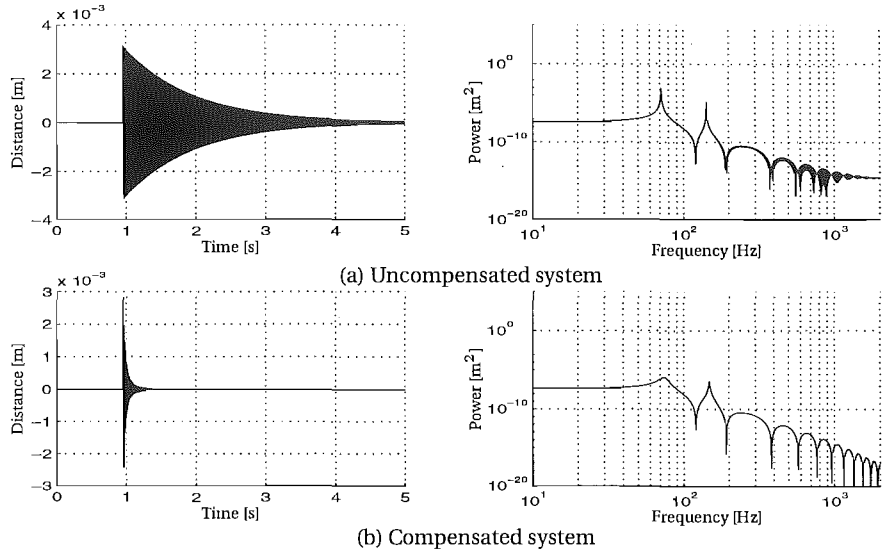

Figure 5.6: *Impulse response of closed loop with simple rate feedback controller,* $K(s) = -K_{c1}(s)$*, in feedback with the 2 mode string model.*

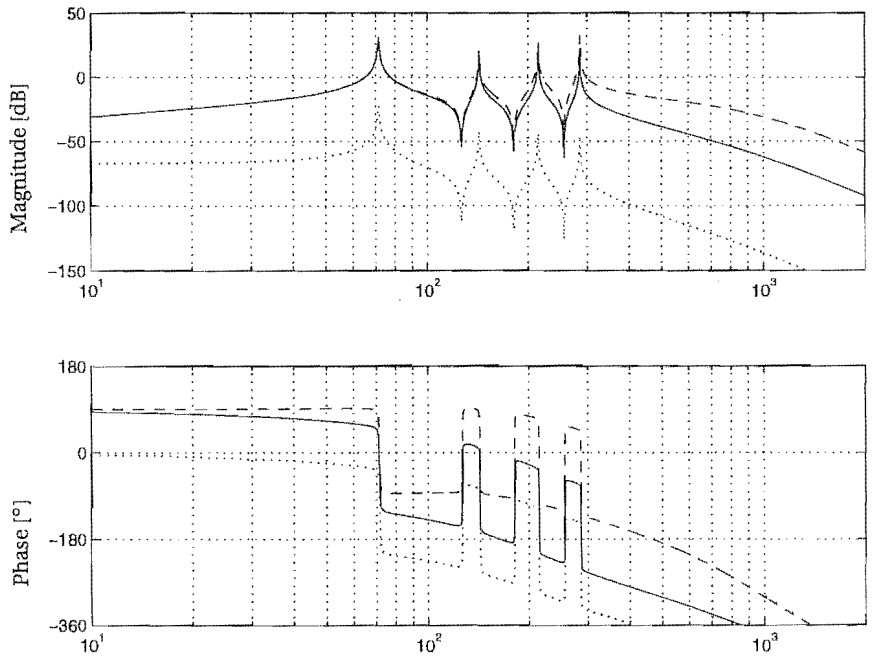

Figure 5.7: *Bode plot of simple rate feedback controller in series with 4 mode string model. KEY:— Simple controller, - - Lead controller, ····· Uncompensated system.*

be written as

$$K_{c2}(s) = \frac{s}{(2\pi f_1 s + 1)} \frac{(s^2 + 4\pi\zeta_1 f_2 s + (2\pi f_2)^2)}{(s^2 + 4\pi\zeta_2 f_3 s + (2\pi f_3)^2)} = -K(s), \tag{5.14}$$

which, for $f_1 = 1500$Hz, $f_2 = 140$Hz, $f_3 = 1000$Hz, $\zeta_1 = \zeta_2 = \sqrt{1/2}$, gives the open loop Bode plot shown by the dashed curves in Figure 5.7, which show that the fourth mode is now stable. In fact, in this example the fifth and sixth mode are also stable and attenuated well, but the seventh is destabilised. This is an example of controller *spillover*, where the controller stabilises a finite number of the modes (known as controlled modes) but destabilises others (called residual modes). In distributed systems such as this spillover is a major problem, complicated by the way neighbouring modal frequencies become closer together with increasing frequency.

Noise sensitivity. Figure 5.8 shows the Bode plots of the two classical controllers considered thus far. The more complex controller was required to improve the phase of the open loop system, but as shown this is at the expense of large controller gain at high frequencies. Figure 5.9 shows the output y and the required control force u for the closed loop system for each controller, where white noise has now been added to the sensor signal. Of note is that even though the control force is very noisy

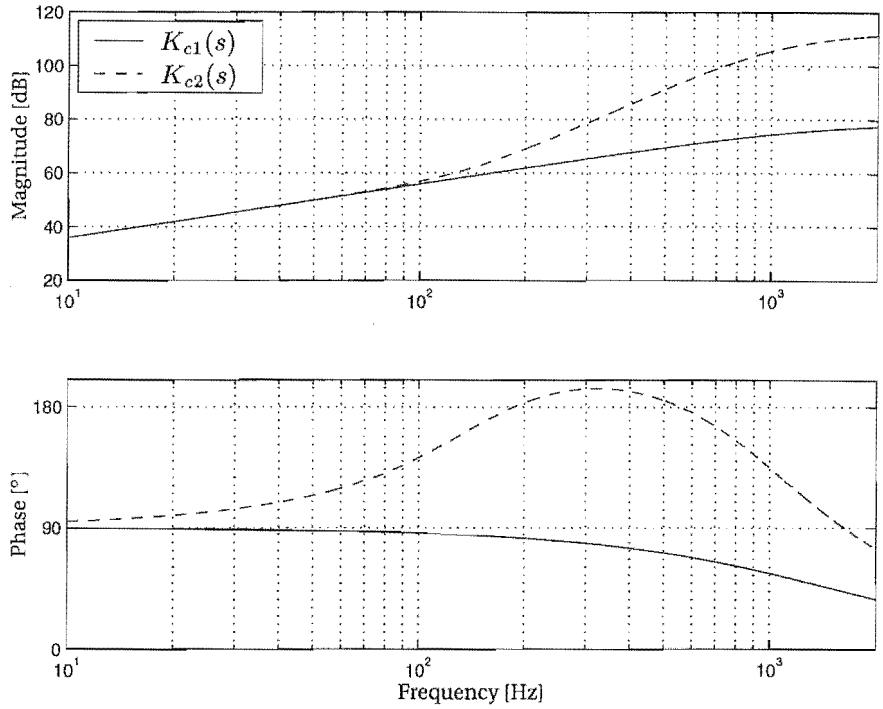

Figure 5.8: *Bode plots of rate feedback controllers.*

(resulting from the differentiation of the deflection) the vibration is still attenuated. However, the control effort is unreasonably large, especially for K_{c2}.

Model uncertainty. As the classical controller is not model-based, it is extremely robust (insensitive) to the parametric uncertainties mentioned in Table 5.1. However, the continual destabilisation of high frequency modes and amplification of noise reduces the applicability of such control (a real example is given in the experimental work below).

5.3.2 LQG and $\mathcal{H}_2$ control

Linear Quadratic Gaussian (LQG) control is an example of *model-based* control, where the controller is a state-space dynamical system with similar dynamics to the plant model. An LQG controller consists of an optimal state-feedback controller, which requires the system state vector, and a Kalman-Bucy filter which provides an estimate of this state vector from noisy measurements. The controller synthesis relies upon the constrained minimisation of a linear quadratic cost function that is dependent on the plant states and the control effort, with the constraint being the satisfaction of the plant dynamics. The estimator synthesis is dual to this and uses statistical information about the system noise and disturbance signals to optimally estimate the

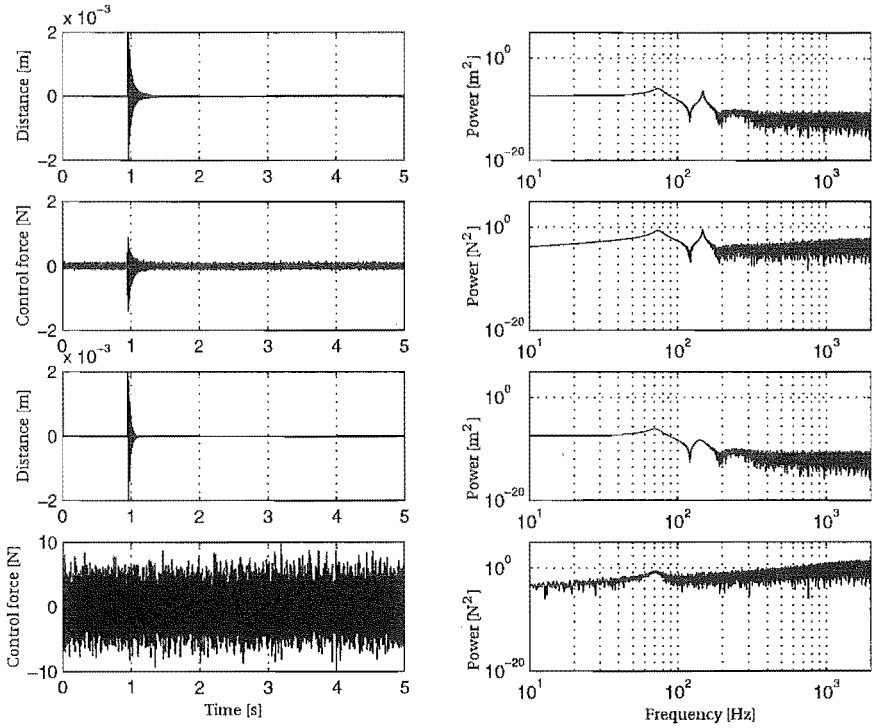

Figure 5.9: *Noise sensitivity of two classical controllers. Upper four plots are for the controller given by $K_{c1}(s)$, (Eqn. 5.12), lower four are for the $K_{c2}(s)$, (Eqn. 5.14).*

system state vector given inaccurate measurements. Formulation of each part is outlined below; for a detailed treatment the reader is directed to Kwakernaak and Sivan (1972). Also, generation of a similar controller via the minimisation of the $\mathcal{H}_2$-norm of a closed-loop transfer function is given, and shown to be equivalent to the LQG formulation. A full exposition of $\mathcal{H}_2$ optimal control is given in Doyle et al. (1989).

It is worth recalling here the standard state space equations describing a Linear Finite Dimensional Time Invariant (FDLTI) system, with the addition of sensor noise and state disturbance.

$$\begin{aligned} \dot{\mathbf{x}}(t) &= \mathbf{A}\mathbf{x}(t) + \mathbf{B}\mathbf{u}(t) + \mathbf{d}(t), \quad \mathbf{x}(0) = \mathbf{O} \\ \mathbf{y}(t) &= \mathbf{C}\mathbf{x}(t) + \mathbf{v}(t), \end{aligned} \tag{5.15}$$

where $\mathbf{v}(t)$ and $\mathbf{d}(t)$ are the sensor noise and state disturbance signals, which are further introduced below. For now this description should be considered to be unrelated to the matrices of Section 5.3. Throughout this and the $\mathcal{H}_\infty$ section positive state feedback is assumed, so we can add the equation

$$\mathbf{u}(t) = \mathbf{F}\mathbf{x}(t). \tag{5.16}$$

Optimal state-feedback. The cost function to be minimised is

$$J = \frac{1}{2}\int_0^\infty \left(\mathbf{x}^T\mathbf{Q}\mathbf{x} + \mathbf{u}^T\mathbf{R}\mathbf{u}\right) dt, \tag{5.17}$$

where the weighting matrices $\mathbf{Q}$ and $\mathbf{R}$ are chosen by the designer. The minimisation of this function (subject to the constraint of the plant dynamics) leads to the solution of an *algebraic matrix Riccati equation* of the form

$$\mathbf{A}^T\mathbf{X}_{LQG} + \mathbf{X}_{LQG}\mathbf{A} - \mathbf{X}_{LQG}\mathbf{B}\mathbf{R}^{-1}\mathbf{B}^T\mathbf{X}_{LQG} + \mathbf{Q} = \mathbf{O}, \tag{5.18}$$

the solution of which gives the optimal controller gain matrix, such that

$$\mathbf{F}_{LQG} = -\mathbf{R}^{-1}\mathbf{B}^T\mathbf{X}_{LQG}. \tag{5.19}$$

Numerical methods for solving Riccati equations are readily available in proprietary and free code. This work uses routines from the Fortran library SLICOT[1] to solve algebraic Riccati equations.

The weighting matrices $\mathbf{Q}$ and $\mathbf{R}$ are chosen through experience; both are often diagonal to weight each state and control signal individually. In a distributed mechanical problem such as the original string/beam/plate dynamics, where the system is described in modal coordinates η (see Section 2.1.6), diagonal entries in $\mathbf{Q}$ penalise the strain energy (via the $q_{ii}\eta_{ii}^2$ terms) and the kinetic energy (via the $q_{ii}\dot{\eta}_{ii}^2$ terms) in each mode of vibration. The $\mathbf{R}$ matrix penalises the energy of the control signals, allowing the designer to avoid actuator saturation and control signals larger than the plant can sustain. An obvious constraint on $\mathbf{R}$ is that it is positive definite, so that the inverses in (5.18) and (5.19) exist. In fact, in SISO systems $\mathbf{R}$ is often set to unity. Furthermore, $\mathbf{Q}$ must be positive semidefinite and for the closed loop to be asymptotically stable the plant must be controllable and the pair $(\mathbf{C}_p, \mathbf{A})$, where $\mathbf{Q} = \mathbf{C}_p^T\mathbf{C}_p$, must be observable. Controllability of the plant means that the state vector, given any starting value $\mathbf{x}(0)$, can be driven to any desired value $\mathbf{x}(t_f)$ via state feedback, where $t_f < \infty$. For a system to be controllable its controllability grammian, $\mathbf{P}$, shown in (5.20) below, must be positive definite. A weaker concept is stabilisability, which requires only that the *unstable* modes are controllable.

$$\mathbf{P} := \int_0^\infty e^{\mathbf{A}t}\mathbf{B}\mathbf{B}^T e^{\mathbf{A}^T t} dt. \tag{5.20}$$

Dual to controllability is *observability*. A state space system is observable if the entire state vector can, in finite time, be reconstructed from the measured output $\mathbf{y}$. The weaker notion is detectability, where only the unstable states are required to be

[1] See `http://www.win.tue.nl/niconet/NIC2/slicot.html`

reconstructible. The observability grammian, $\mathbf{Q}$, is given by

$$\mathbf{Q} := \int_0^\infty e^{\mathbf{A}^T t}\mathbf{C}^T\mathbf{C}e^{\mathbf{A}t}dt, \tag{5.21}$$

and G is observable if $\mathbf{Q} > 0$.

Estimating the state vector. In many control problems (and indeed this one) the sensed variables are not the states themselves, so an estimate of the state vector is required to enable state feedback. The problem is further complicated by noisy sensor data. The Kalman-Bucy filter is a dynamic system that uses information about the plant, the sensor noises and the plant disturbances to provide an optimal state estimate. Given the plant description (5.15), the estimator takes the form

$$\dot{\hat{\mathbf{x}}}(t) = \mathbf{A}\hat{\mathbf{x}}(t) + \mathbf{B}\mathbf{u}(t) - \mathbf{L}_{LQG}\big(\mathbf{y}(t) - \mathbf{C}\hat{\mathbf{x}}(t)\big), \tag{5.22}$$

where $\hat{\mathbf{x}}$ is the estimated state vector, and $\mathbf{L}_{LQG}$ is the estimator gain matrix. Substituting the control law $\mathbf{u} = \mathbf{F}_{LQG}\mathbf{x}$ into (5.22) gives

$$\dot{\hat{\mathbf{x}}}(t) = (\mathbf{A} + \mathbf{B}\mathbf{F}_{LQG} + \mathbf{L}_{LQG}\mathbf{C})\hat{\mathbf{x}}(t) - \mathbf{L}_{LQG}\mathbf{y}(t). \tag{5.23}$$

So, when the estimated output is similar to the actual output, the estimator behaves exactly as the plant description. When the outputs differ, the error drives the estimator via the gain matrix $\mathbf{L}_{LQG}$, so as to remove the difference. The choice of this matrix is made via an optimisation process, as described below.

Both $\mathbf{d}(t)$ and $\mathbf{v}(t)$ are assumed to be stationary (zero mean) white noise processes, with covariances equal to

$$E[\mathbf{d}^T(t)\mathbf{d}(\tau)] = \mathbf{V}_d\delta(t-\tau) \tag{5.24}$$

$$E[\mathbf{v}^T(t)\mathbf{v}(\tau)] = \mathbf{V}_v\delta(t-\tau). \tag{5.25}$$

Each component of $\mathbf{d}(t)$ is assumed to be uncorrelated with each component of $\mathbf{v}(t)$. $\mathbf{V}_d$ and $\mathbf{V}_v$ may be found from their power spectral density matrices, which are known *a priori* or can be found experimentally. A new dynamical system may be generated which has the state estimation error $\mathbf{e}(t) = \mathbf{x}(t) - \hat{\mathbf{x}}(t)$ as the state vector, and the stochastic signals $\begin{bmatrix}\mathbf{d}\\ \mathbf{v}\end{bmatrix}$ as inputs:

$$\dot{\hat{\mathbf{e}}}(t) = \dot{\mathbf{x}}(t) - \dot{\hat{\mathbf{x}}}(t) = (\mathbf{A} + \mathbf{L}_{LQG}\mathbf{C})\hat{\mathbf{e}}(t) + \begin{bmatrix}\mathbf{I} & \mathbf{L}_{LQG}\end{bmatrix}\begin{bmatrix}\mathbf{d}\\ \mathbf{v}\end{bmatrix}. \tag{5.26}$$

Because the inputs to (5.26) are stochastic, so too is the estimation error $\mathbf{e}(t)$. The mean square of this error is the quantity to be minimised, subject to the satisfaction

of (5.26). This optimisation leads to the solution of another Riccati equation, of the form

$$\mathbf{A}\mathbf{Z}_{LQG} + \mathbf{Z}_{LQG}\mathbf{A}^T - \mathbf{Z}_{LQG}\mathbf{C}^T\mathbf{V}_v^{-1}\mathbf{C}\mathbf{Z}_{LQG} + \mathbf{V}_d = 0, \tag{5.27}$$

from which is found the optimal estimator gain matrix:

$$\mathbf{L}_{LQG} = -\mathbf{Z}_{LQG}\mathbf{C}^T\mathbf{V}_v^{-1}. \tag{5.28}$$

The resulting controller may be expressed as

$$K(s) = \left[\begin{array}{c|c} \mathbf{A} + \mathbf{B}\mathbf{F}_{LQG} + \mathbf{L}_{LQG}\mathbf{C} & -\mathbf{L}_{LQG} \\ \hline \mathbf{F}_{LQG} & \mathbf{O} \end{array}\right]. \tag{5.29}$$

The measurements $\mathbf{y}(t)$ are all assumed to be corrupted, so the covariance matrix $\mathbf{V}_v$ is assumed to be positive definite. Also $\mathbf{V}_d$ must be positive semidefinite. As they are both covariance matrices they are by definition positive semi-definite. The assumption that $\mathbf{V}_v > 0$ guarantees the existence of $\mathbf{V}_v^{-1}$. The relative sizes of $\mathbf{V}_d$ and $\mathbf{V}_v$ are dual to those of $\mathbf{Q}$ and $\mathbf{R}$ in the optimal state feedback formulation. For $\mathbf{V}_v$ small compared to $\mathbf{V}_d$ the filtering of sensor noise has a low priority and the resulting observer quickly and accurately mimics the true state vector, but poorly filters measurement noise. Kwakernaak and Sivan (1972) discusses LQG behaviour with regard to asymptotic values of $\mathbf{Q}$, $\mathbf{R}$, $\mathbf{V}_v$ and $\mathbf{V}_d$. Further to the conditions on $\mathbf{V}_v$ and $\mathbf{V}_d$, the plant must be observable to produce a stable closed loop. While the final controller is guaranteed to be asymptotically stable, the state estimation means that no minimum stability margins can be guaranteed. This is considered in the example below.

Minimising the $\mathcal{H}_2$ norm of the closed loop. An alternative to the LQG formulation above is firstly to add two outputs to the plant dynamics in (5.15), to create the system

$$G(s) = \left[\begin{array}{c|c:c|c} \mathbf{A} & \mathbf{W}_d\mathbf{B}_d & \mathbf{O} & \mathbf{B} \\ \hline \mathbf{W}_x & \mathbf{O} & \mathbf{O} & \mathbf{O} \\ \mathbf{O} & \mathbf{O} & \mathbf{O} & \mathbf{W}_u \\ \hdashline \mathbf{C} & \mathbf{O} & \mathbf{W}_v & \mathbf{O} \end{array}\right] = \left[\begin{array}{c|c:c} \mathbf{A} & \mathbf{B}_1 & \mathbf{B}_2 \\ \hline \mathbf{C}_1 & \mathbf{O} & \mathbf{D}_{12} \\ \hdashline \mathbf{C}_2 & \mathbf{D}_{21} & \mathbf{O} \end{array}\right] \tag{5.30}$$

which has inputs $\begin{bmatrix} \mathbf{w} \\ \mathbf{u} \end{bmatrix}$, where $\mathbf{w} = \begin{bmatrix} \mathbf{d} \\ \mathbf{v} \end{bmatrix}$, and outputs $\begin{bmatrix} \mathbf{z} \\ \mathbf{y} \end{bmatrix}$. Then, this system is considered to be the general plant in the LFT of Figure (5.4), and the $\mathcal{H}_2$-norm of the closed loop system mapping $\mathbf{w}$ to $\mathbf{z}$ (denoted $T_{zw}(s)$) is minimised. This minimisation again reduces to the solution of two algebraic Riccati equations, the Generalised Control Algebraic Riccati Equation (GCARE) and the Generalised Filtering Algebraic

Riccati Equation (GFARE) (see Appendix C.1.2 for details). The optimal $\mathcal{H}_2$ controller is given by

$$K_2(s) = \left[\begin{array}{c|c} \mathbf{A}+\mathbf{B}_2\mathbf{F}_2+\mathbf{L}_2\mathbf{C}_2 & -\mathbf{L}_2 \\ \hline \mathbf{F}_2 & \mathbf{O} \end{array}\right], \tag{5.31}$$

where $\mathbf{L}_2$ and $\mathbf{F}_2$ are the filter and controller gain matrices corresponding to the GFARE and GCARE respectively.

This procedure relies on the following assumptions;

- (i) $(\mathbf{A}, \mathbf{B}_1)$ is stabilisable and $(\mathbf{C}_1, \mathbf{A})$ is detectable.
- (ii) $(\mathbf{A}, \mathbf{B}_2)$ is stabilisable and $(\mathbf{C}_2, \mathbf{A})$ is detectable.
- (iii) $\mathbf{D}_{12}^T \begin{bmatrix} \mathbf{C}_1 & \mathbf{D}_{12} \end{bmatrix} = \begin{bmatrix} \mathbf{O} & \mathbf{I} \end{bmatrix}$.
- (iv) $\begin{bmatrix} \mathbf{B}_1 \\ \mathbf{D}_{21} \end{bmatrix} \mathbf{D}_{21} = \begin{bmatrix} \mathbf{O} \\ \mathbf{I} \end{bmatrix}$.

Assumption (ii) is obvious for any controller to be able to stabilise the system, but together with (i) it also guarantees positive semi-definite solutions to the GCARE and GFARE (in fact, the above formulas are valid even if these assumptions do not hold). Assumption (iii) forces there to be no cross weighting between the state penalisation and the control effort penalisation, as well as forcing the control penalty to be nonsingular and normalised. Assumption (iv) is dual to this and forces the plant disturbance to be independent of the sensor noise, and the sensor weighting to be normalised and nonsingular.

The generalised plant in (5.30), satisfies the orthogonality constraints of (iii) and (iv), but not the normalisation and nonsingularity of the sensor noise and control effort weightings. This may be achieved by the following change of variables,

$$\mathbf{z}_n = \mathbf{Q}_o\mathbf{z}, \quad \mathbf{y}_n = \mathbf{R}_o\mathbf{y}, \tag{5.32}$$

$$\mathbf{u} = \mathbf{R}_i\mathbf{u}_n, \quad \mathbf{w} = \mathbf{Q}_i\mathbf{w}_n, \tag{5.33}$$

such that

$$\mathbf{Q}_o\mathbf{D}_{12}\mathbf{R}_i = \begin{bmatrix} \mathbf{O} \\ \mathbf{I} \end{bmatrix}, \tag{5.34}$$

$$\mathbf{R}_o\mathbf{D}_{21}\mathbf{Q}_i = \begin{bmatrix} \mathbf{O} & \mathbf{I} \end{bmatrix}. \tag{5.35}$$

If an optimal $\mathcal{H}_2$ controller, $\mathbf{K}_n(s)$ is found for the new system mapping $\begin{bmatrix} \mathbf{w}_n \\ \mathbf{u}_n \end{bmatrix}$ to $\begin{bmatrix} \mathbf{z}_n \\ \mathbf{y}_n \end{bmatrix}$, the controller for the original system is given by $\mathbf{K}_2 = \mathbf{R}_i\mathbf{K}_n\mathbf{R}_o$. The matrices defining the change of variables are the standard QR-decomposition matrices of $\mathbf{D}_{12}$ and $\mathbf{D}_{21}$.

Minimising the $\mathcal{H}_2$-norm of $T_{zw}(s)$ is equivalent to minimising the energy of the output $\mathbf{z}$ for impulsive inputs or unit intensity white noise. From (5.30) the $\mathcal{L}_2$-norm[2] of $\mathbf{z}$ is

$$||\mathbf{z}||_2^2 = \int_0^\infty \{\mathbf{x}^T\mathbf{W}_x^T\mathbf{W}_x\mathbf{x} + \mathbf{u}^T\mathbf{W}_u^T\mathbf{W}_u\mathbf{u}\}dt, \tag{5.36}$$

which is obviously similar to the cost function in (5.17).

If the weighting matrices $\mathbf{W}_v$ and $\mathbf{W}_d$ are such that the signals $\mathbf{W}_v\mathbf{v}$ and $\mathbf{W}_d\mathbf{d}$ are (respectively) equivalent to those described by $\mathbf{V}_v$ and $\mathbf{V}_d$ in the LQG formulation, and if $\mathbf{W}_x^T\mathbf{W}_x = \mathbf{Q}$ and $\mathbf{W}_u^T\mathbf{W}_u = \mathbf{R}$, then the $\mathcal{H}_2$ formulation will produce an identical controller to the LQG formulation. Doyle et al. (1989), Zhou (1998) and many others treat the $\mathcal{H}_2$ problem in far more detail, with proofs and discussion.

Applying the $\mathcal{H}_2$ strategy to the bandsaw model The LQG/$\mathcal{H}_2$ formulations were presented using a general state space plant, rather than the bandsaw model presented in (5.11). Essentially, the system $\begin{bmatrix} G_{yd} & G_{yv} & G_{yu} \end{bmatrix}$ in (5.11) comprises the general state space system in (5.15), so that the generalised plant in the LFT framework is given by

$$G(s) = \left[\begin{array}{ccc|c:cc} \mathbf{A}_s & \mathbf{B}_s\mathbf{C}_m & \mathbf{O} & \mathbf{O} & \mathbf{O} & \mathbf{O} \\ \mathbf{O} & \mathbf{A}_m & \mathbf{B}_m\mathbf{C}_a & \mathbf{B}_d\mathbf{W}_d & \mathbf{O} & \mathbf{O} \\ \mathbf{O} & \mathbf{O} & \mathbf{A}_a & \mathbf{O} & \mathbf{O} & \mathbf{B}_a \\ \hline \mathbf{O} & \mathbf{W}_x & \mathbf{O} & \mathbf{O} & \mathbf{O} & \mathbf{O} \\ \mathbf{O} & \mathbf{O} & \mathbf{O} & \mathbf{O} & \mathbf{O} & \mathbf{W}_u \\ \hdashline \mathbf{C}_s & \mathbf{O} & \mathbf{O} & \mathbf{O} & \mathbf{W}_v & \mathbf{O} \end{array}\right] = \left[\begin{array}{c|c:c} \mathbf{A} & \mathbf{B}_1 & \mathbf{B}_2 \\ \hline \mathbf{C}_1 & \mathbf{O} & \mathbf{D}_{12} \\ \hdashline \mathbf{C}_2 & \mathbf{D}_{21} & \mathbf{O} \end{array}\right]. \tag{5.37}$$

Note that the weighting matrix $\mathbf{W}_x$ has only been applied to the flexible modes of the model, not the actuator and sensor states.

Examples. For the two mode string, Figure 5.10 compares an LQG/$\mathcal{H}_2$ controller with the classical controllers previously examined. We have selected $\mathbf{Q} = diag\{0, 0, 500, 250\}$, $\mathbf{R} = 1$. This choice of $\mathbf{Q}$ penalises the kinetic energy of each mode of vibration, placing particular importance on the fundamental mode. In the LQG/$\mathcal{H}_2$ formulation $V_v = 1 \times 10^{-11}$ (from section B.2) and $V_d = 1 \times 10^{-5}$. Of interest in terms of magnitude is the comparatively fast roll-off of the LQG controller at high frequencies and the fact that gains are only high at the natural frequencies of the plant. In terms of phase the LQG controller matches (at the natural frequencies) the more sophisticated classical controller.

[2] In this work the $\mathcal{L}_2$-norm and the $\mathcal{H}_2$-norm of a signal are considered identical and will be used interchangeably. For simulation and experimental results the truncated norm is used.

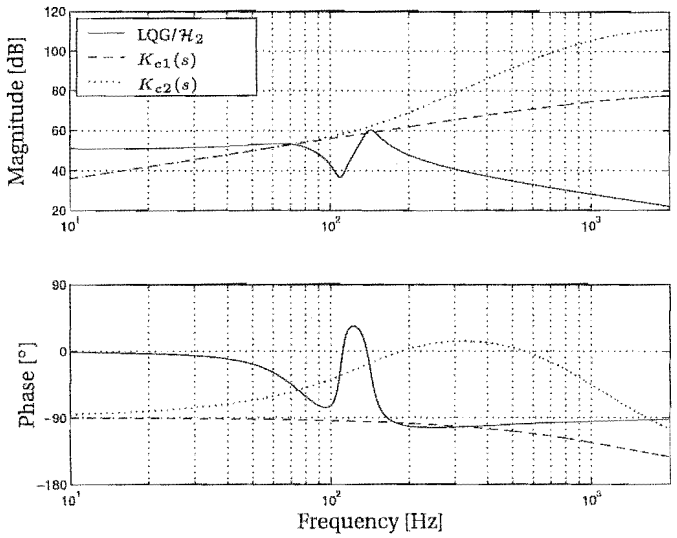

Figure 5.10: *Bode plots of LQG/$\mathcal{H}_2$ and classical controllers.*

Performance. Figure 5.11 shows the impulse response for the optimal LQG controller. For similar attenuation this controller is far less sensitive to noise than the classical controllers, which is expected due to the fast roll-off in magnitude shown in Figure 5.10. This roll-off also reduces spillover instabilities.

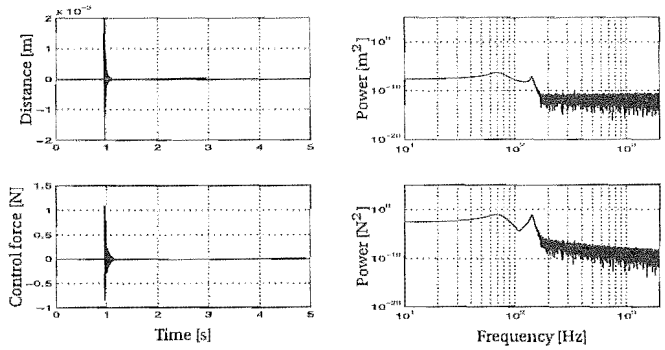

Figure 5.11: *Noisy impulse response for 2 mode string model in feedback with LQG/$\mathcal{H}_2$ controller (parameters defined in Table 5.3).*

Robustness. Figure 5.12 shows results for a controller designed from a four mode plant. Figure 5.12(a) shows results when the *nominal* plant is in the feedback loop, and Figure 5.12(b) shows results for the controller in feedback with a *perturbed* plant. The perturbed string is under 90% of the tension of the nominal, and as shown the controller is destabilising. If such a perturbation is feasible in a real application then this controller is obviously unacceptable. While this example is fictitious it exemplifies the lack of robustness that is a hallmark of LQG controllers. Discussion of more robust controllers and methods of describing system uncertainties is covered in the

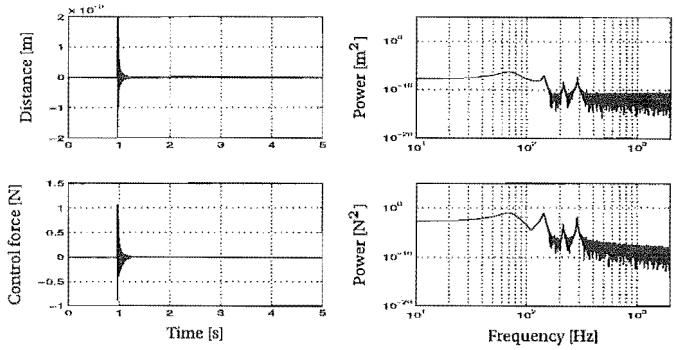

(a) Nominal plant model.

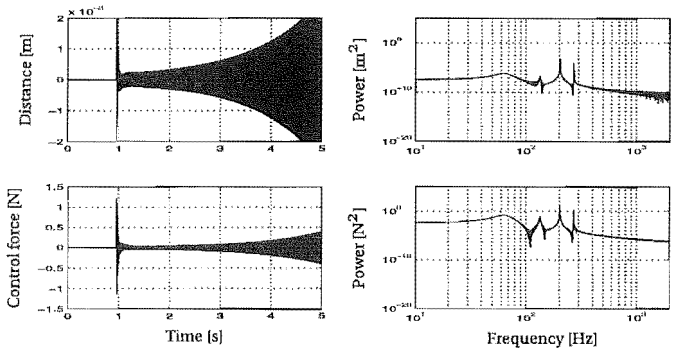

(b) Perturbed plant model. $R_{o,pert.} = 0.9R_{o,nom.}$

Figure 5.12: *Noisy impulse responses for LQG/$\mathcal{H}_2$ control of nominal and perturbed stationary string. The controller is designed using a four mode model as defined by Table 5.3.* $\mathbf{Q} = diag\{0, 0, 0, 0, 500, 250, 100, 50\}$.

following section.

5.3.3 Robust control

As discussed in the previous section, LQG/$\mathcal{H}_2$ controllers are designed with regard to a very small class of disturbances, and are often sensitive to unmodelled effects and erroneous models. These traits have limited the successful deployment of optimal LQG/$\mathcal{H}_2$ controllers in real applications, and much work throughout the late 1970s and 1980s focussed on developing what is now called *robust control*. The aim of robust control is to provide stability and performance for a *set* of plants, where this set includes a *nominal* plant and all plants that are "close" to it. Zames (1981) produced the seminal work which considered the stabilisation and sensitivity reduction (via feedback) of uncertain systems, where the uncertainty was considered to be a *ball* of plants surrounding the nominal one. This work was further developed by various researchers; the reader is directed to the excellent review of the formation of $\mathcal{H}_\infty$ control in Doyle and Francis (1987), as well as Zhou et al. (1996) and Zhou

(1998). An $\mathcal{H}_\infty$ loop shaping technique was given in Glover and McFarlane (1992), and this method is used throughout this work. Also, this work uses the *gap metric* (Zames and El-Sakkary, 1980) and the *ν-gap metric* (Vinnicombe, 1993a) to measure the "closeness" of two plants. Central to all of the above references is the small gain theorem (Zames, 1966), which states that if the product of the maximum singular values of the components comprising a feedback loop is less than unity for all frequency, then the feedback loop is internally stable. A more conservative statement of this is that the system is internally stable if the product of the $\mathcal{H}_\infty$-norms of each component is less than unity. The following paragraphs consider mathematical descriptions of uncertainty, $\mathcal{H}_\infty$ optimality and the loop shaping method. Not all concepts are discussed in the text; the reader is at times directed to Appendix C.

Uncertainty descriptions. Finding uncertainty descriptions that have a physical basis as well as being mathematically tractable is achieved using either a *structured* approach, where uncertainty is described in terms of the parameters comprising the model, or using an *unstructured* approach, where the uncertainty is measured by the "size" of an uncertainty system Δ. The structured approach allows some of the model parameters to vary within prescribed limits, and the nominal model is that given by the nominal set of parameters. This method is appealing in its physical basis, but accurately prescribing these bounds for many parameters in a complex process is difficult. Also, manipulating these perturbations into a separate system (specifically the LFT arrangement of Figure 5.14 below) becomes very challenging as system complexity increases. Furthermore, no allowance is made for model errors that cannot be described parametrically, such as errors caused by finite dimensional modelling and nonlinear effects. Unstructured uncertainty descriptions do make allowances for such phenomena, but lack the clear physical basis of the parametric perturbation. Three common unstructured descriptions are additive, multiplicative and coprime factor uncertainty, which are depicted in Figure 5.13. In Figure 5.13(c) $\tilde{M}$ and $\tilde{M}$ are *normalised left coprime factors* of G (see Section C.1.2), meaning that $G = \tilde{M}^{-1}\tilde{N}$ and $\tilde{M}\tilde{M}^T + \tilde{N}\tilde{N}^T = I$. Furthermore, $\tilde{M}_\Delta = (\tilde{M} + \Delta_{\tilde{M}})$ and $\tilde{N}_\Delta = (N + \Delta_{\tilde{N}})$ are left coprime factors of G_Δ.

Additive and multiplicative uncertainties are useful in describing effects such as sensor noise and unmodelled high frequency dynamics. For these effects the gain of Δ is small at low frequencies (where FDLTI models are often accurate), and large at high frequencies (where signal-to-noise ratios are relatively high and models are often inaccurate). The MIMO equivalent of this is that the maximum singular value $\bar{\sigma}(\Delta)(s)$ is bounded from above at low frequencies and the minimum singular value $\underline{\sigma}(\Delta)$ is bounded from below at high frequencies. The coprime factor approach is useful for these effects as well as low frequency modelling errors, which are often caused by parameter errors. Inspecting the additive uncertainty description in Fig-

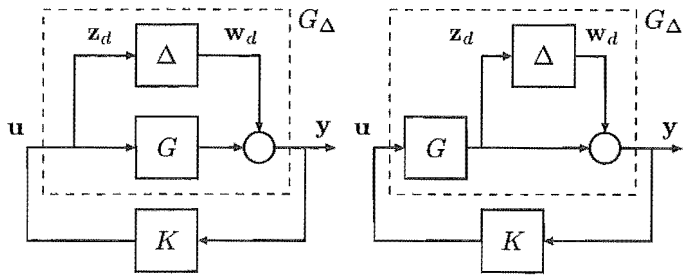

(a) Additive uncertainty, $G_\Delta = G + \Delta$.

(b) Multiplicative uncertainty, $G_\Delta = (1 + \Delta)G$

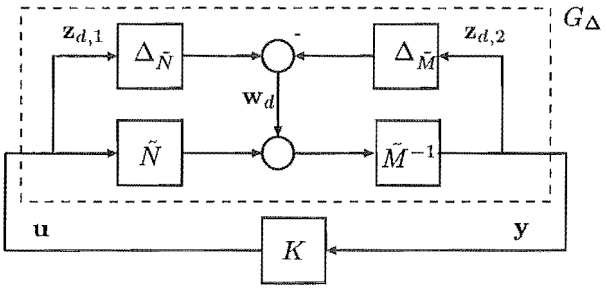

(c) Coprime factor uncertainty, $G_\Delta = (\tilde{M} + \Delta_{\tilde{M}})^{-1}(N + \Delta_{\tilde{N}})$

Figure 5.13: *Unstructured uncertainty descriptions.*

ure 5.13(a) we find for the transfer function from disturbance $\mathbf{w}_d$ to output $\mathbf{z}_d$

$$\mathbf{z}_d = K(I - GK)^{-1}\mathbf{w}_d,$$

so that the function

$$\frac{1}{\overline{\sigma}(K(I - GK)^{-1})}$$

is, by Zames' small gain theorem, the maximum allowable size of the additive uncertainty $\Delta(s)$, for stability of the closed loop to be guaranteed. Similarly, the transfer function for the multiplicative case (Figure 5.13(b)) is

$$\mathbf{z}_d = GK(I - GK)^{-1}\mathbf{w}_d,$$

so that the function

$$\frac{1}{\overline{\sigma}(GK(I - GK)^{-1})}$$

is the maximum allowable size of the multiplicative uncertainty $\Delta(s)$, for guaran-

teed stability of the closed loop. These functions can be considered alongside the closed-loop performance specifications in Table 5.2. The coprime factor approach also offers advantages in terms of controller synthesis, as shown below.

$\mathcal{H}_\infty$ optimality using coprime factors. Any of the uncertainty descriptions described above may be presented in the LFT arrangement of Figure 5.14. In this framework

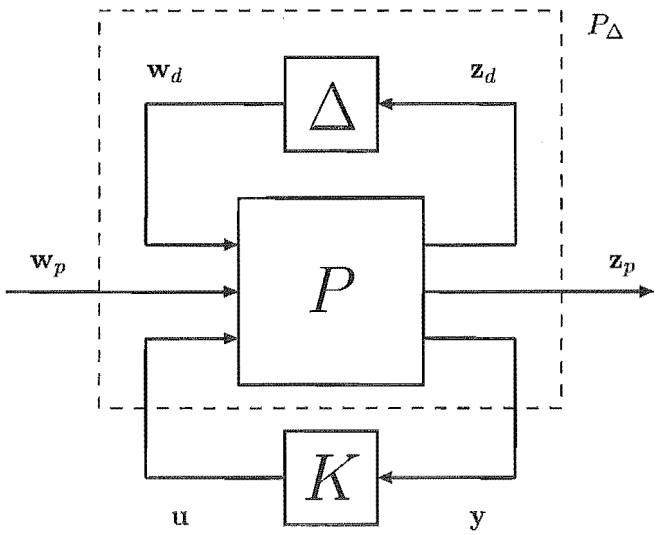

Figure 5.14: *LFT showing uncertainty block, plant and controller.*

the $\mathcal{H}_\infty$ control problem is to minimise the $\mathcal{H}_\infty$-norm of the system mapping $\mathbf{w} = \begin{bmatrix} \mathbf{w}_\Delta \\ \mathbf{w}_p \end{bmatrix}$ to $\mathbf{z} = \begin{bmatrix} \mathbf{z}_\Delta \\ \mathbf{z}_p \end{bmatrix}$, that is $T_{zw}(s)$. If appropriate weighting functions are applied, then both stability with respect to the uncertainty as well as input-output performance may be achieved, all from an $\mathcal{H}_\infty$ perspective. The reason for using this perspective becomes clear by considering that the $\mathcal{H}_\infty$-norm is the induced norm on $\mathbb{R}\mathcal{H}_2$, so the minimisation of $||T_{zw}||_\infty$ minimises the worst case ratio of the $\mathcal{L}_2$-norm of the output $\mathbf{z}$ to the $\mathcal{L}_2$-norm of the input $\mathbf{w}$. This minimisation holds for all input functions in $\mathcal{H}_2$, which is obviously a larger class than that of the LQG/$\mathcal{H}_2$ formulation. However, the general optimal $\mathcal{H}_\infty$ solution cannot be directly calculated; rather, a *sub-optimal* problem that can be directly calculated is solved repeatedly. The mechanics of this are not covered here, but suffice it to say that a stabilising controller is found such that $||T_{zw}(s)||_\infty < \gamma$, where $\gamma \in (0, \infty)$. The number γ is logically reduced until no stabilising solutions can be found, and the last stabilising one becomes the sub-optimal $\mathcal{H}_\infty$ controller. The smaller γ becomes the larger $||\Delta||_\infty$ can be while still guaranteeing internal stability of the closed loop. This means that G_Δ includes a larger class of plants for small values of γ, and hence the robustness of the closed loop should be better. In practice γ is less than ten, and often greater than two.

The computationally intensive process of finding γ_{min} is eliminated if G is de-

scribed by its coprime factors. In this situation γ_{min} may be found directly, and is given (Glover and McFarlane, 1989, see Theorem 4.2) by

$$\gamma_{min} = \left(1 - \left\|\begin{bmatrix}\tilde{N} & \tilde{M}\end{bmatrix}\right\|_H^2\right)^{-\frac{1}{2}}, \tag{5.38}$$

where $||\cdot||_H$ denotes the Hankel norm. So, as the size of $\begin{bmatrix}\tilde{N} & \tilde{M}\end{bmatrix}$ increases (in terms of its Hankel norm), the optimal value γ_{min} increases. But $\gamma_{min} = ||T_{zw}||_\infty$ so, by the small gain theorem, as γ_{min} increases the allowable size (such that internal stability is still guaranteed) of the uncertainty block Δ decreases. Equation (5.38) is an important result, as it allows the optimal stability margin, $b_{opt} = \gamma_{min}^{-1}$ to be found directly. Also, in comparison to additive and multiplicative uncertainties the coprime factor description encompasses a larger class of systems that are admissible in the $\mathcal{H}_\infty$ synthesis (Glover and McFarlane, 1990), as both factors are always stable, regardless of plant stability.

Once γ_{min} is found, a value $\gamma > \gamma_{min}$ may be used and the controller satisfying

$$\left\|T_{z_d w_d}\right\|_\infty = \left\|\begin{bmatrix}K_\infty \\ I\end{bmatrix}(I - GK_\infty)^{-1}\tilde{M}^{-1}\right\|_\infty \leq \gamma, \tag{5.39}$$

can be calculated directly. The expanded form of $T_{z_d w_d}$ in (5.39) can be found from examining 5.13(c), or firstly converting this figure to the LFT arrangement, for which the generalised plant P is

$$P = \left[\begin{array}{c|c} 0 & I \\ \tilde{M}^{-1} & G \\ \hline \tilde{M}^{-1} & G \end{array}\right], \tag{5.40}$$

and the Δ block is given by

$$\Delta = \begin{bmatrix}\Delta_N & -\Delta_M\end{bmatrix}. \tag{5.41}$$

The controller satisfying (5.39) is given (Glover and McFarlane, 1989, see Corollary 5.1) by

$$K_\infty(s) = \left[\begin{array}{c|c} \mathbf{A} + \mathbf{BF} + \gamma^2\mathbf{W}_1^{-T}\mathbf{ZC}^T(\mathbf{C} + \mathbf{DF}) & \gamma^2\mathbf{W}_1^{-T}\mathbf{ZC}^T \\ \hline \mathbf{B}^T\mathbf{X} & -\mathbf{D}^T \end{array}\right], \tag{5.42}$$

where $\mathbf{W}_1 = \mathbf{I} + (\mathbf{XZ} - \gamma^2\mathbf{I})$. $\mathbf{X}$ and $\mathbf{Z}$ are the standard solutions to the GCARE and GFARE, and $\mathbf{F}$ is the control gain matrix corresponding to the GCARE. Naturally the requirements for unique, positive semi-definite solutions to the Riccati equations must be satisfied.

As shown in Appendix C, (5.39) can be restated as

$$\left\|T_{z_d w_d}\right\|_\infty^{-1} = \left\| \begin{bmatrix} K_\infty \\ I \end{bmatrix} (I - GK_\infty)^{-1} \begin{bmatrix} I & G \end{bmatrix} \right\|_\infty^{-1} \leq \gamma^{-1} = b, \tag{5.43}$$

where b is called the robust stability margin, as any $||\Delta||_\infty$ that is less than this value produces a G_Δ that is guaranteed to be stabilised by K_∞. It is shown in Georgiou and Smith (1990, Thm. 4) that this interpretation of b is identical to saying that any G_1 such that $\delta_g(G, G_1) < b$ is also guaranteed to be stabilised by K_∞, where δ_g is the *gap metric*, as defined in Zames and El-Sakkary (1980). This metric is specific to input-output systems that are in feedback loops, and it and another such metric, the δ_ν-gap (Vinnicombe, 1993a) are further detailed in Section C.1.3. The δ_ν-gap will be used in the experimental work to compare plants with different parameters such as translation speeds and bandmill tension.

5.3.4 $\mathcal{H}_\infty$ loop shaping using coprime factorisations

Recall the system P_{yu} defined in (5.11), and denote it by G, that is

$$P_{yu}(s) = \left[\begin{array}{ccc|c} \mathbf{A}_s & \mathbf{B}_s\mathbf{C}_m & \mathbf{O} & \mathbf{O} \\ \mathbf{O} & \mathbf{A}_m & \mathbf{B}_m\mathbf{C}_a & \mathbf{O} \\ \mathbf{O} & \mathbf{O} & \mathbf{A}_a & \mathbf{B}_a \\ \hline \mathbf{C}_s & \mathbf{O} & \mathbf{O} & \mathbf{O} \end{array}\right] = G(s) = \left[\begin{array}{c|c} \mathbf{A} & \mathbf{B} \\ \hline \mathbf{C} & \mathbf{O} \end{array}\right]. \tag{5.44}$$

The $\mathcal{H}_\infty$ loop shaping procedure is in three parts. Firstly the plant $G(s)$ is shaped with pre- and/or post-compensators $W_1(s)$ and $W_2(s)$ to form a desired open loop shape. Then, this modified plant $G_s(s) = W_2(s)G(s)W_1(s)$ is robustly stabilised by the suboptimal $K_\infty(s)$ controller of (5.42). Thirdly, the compensators are applied to this controller to give the final controller $\hat{K}_\infty(s) = W_1(s)K_\infty(s)W_2(s)$.

Of immediate concern is that the desired open loop shape, given by $G_s = W_2GW_1$, is modified by the controller K_∞, to give the actual open loop of $GW_1K_\infty W_2$ (at the plant output). It is shown in Glover and McFarlane (1992) that the deterioration in this loop shape is limited by the value γ. At frequencies corresponding to high loop gain (often where performance is of primary concern), the actual open loop gain will not be smaller than $1/\sqrt{\gamma^2 - 1}$ times the desired gain, as long as $\overline{\sigma}((W_2))/\underline{\sigma}((W_2)) \approx 1$. Also, at frequencies corresponding to low open loop gain, the actual loop gain will not be greater than $\sqrt{\gamma^2 - 1}$ times the desired gain, again with the condition that $\overline{\sigma}((W_2))/\underline{\sigma}((W_2)) \approx 1$.

The reason for using this shaping of the plant is that the shape of the open loop affects the closed-loop performance and robustness. Replacing G in (5.39) with $G_s =$

W_2GW_1 gives

$$\left\| \begin{bmatrix} W_1^{-1}K_\infty \\ W_2 \end{bmatrix} (I - GK_\infty)^{-1} W_2^{-1} \tilde{M}^{-1} \right\|_\infty \leq \gamma \tag{5.45}$$

$$\left\| \begin{bmatrix} W_1^{-1}K_\infty \\ W_2 \end{bmatrix} (I - GK_\infty)^{-1} \begin{bmatrix} W_2^{-1} & GW_1 \end{bmatrix} \right\|_\infty \leq \gamma, \tag{5.46}$$

where the second inequality comes from post multiplying the closed loop function by the unitary matrix $\begin{bmatrix} \tilde{M} & \tilde{N} \end{bmatrix}$ (the $\mathcal{H}_\infty$-norm is invariant under multiplication by unitary matrices). Of note is the similarity between (5.46) and the general 4-block problem in (5.8); however, (5.45) is all that is required to find the following inequalities

$$\begin{aligned}
\overline{\sigma}(K(I - G\hat{K}_\infty)) &= \gamma\overline{\sigma}(\tilde{M}_s)\overline{\sigma}(W_1)\overline{\sigma}(W_2) \\
\overline{\sigma}(K(I - G\hat{K}_\infty)G) &= \gamma\overline{\sigma}(\tilde{N}_s)\overline{\sigma}(W_1)/\underline{\sigma}(W_1) \\
\overline{\sigma}((I - G\hat{K}_\infty)) &= \gamma\overline{\sigma}(\tilde{M}_s)\overline{\sigma}(W_2)/\underline{\sigma}(W_2) \\
\overline{\sigma}((I - G\hat{K}_\infty G)) &= \frac{\gamma\overline{\sigma}(\tilde{N}_s)}{\underline{\sigma}(W_1)\underline{\sigma}(W_2)} \\
\overline{\sigma}((1 - \hat{K}_\infty G)) &= 1 + \gamma\overline{\sigma}(\tilde{N}_s)\overline{\sigma}(W_1)/\underline{\sigma}(W_1) \\
\overline{\sigma}(G(1 - \hat{K}_\infty G)\hat{K}_\infty) &= 1 + \gamma\overline{\sigma}(\tilde{M}_s)\overline{\sigma}(W_2)/\underline{\sigma}(W_2).
\end{aligned}$$

While these are useful, they still rely on the singular values of the coprime factors. It is further shown in Glover and McFarlane (1992) that they may be reduced to the following:

- For frequencies where the open loop gain is high, ($\overline{\sigma}(G_s) \gg 1$), the weighting functions only affect the performance of the closed loop, as described by

$$\overline{\sigma}((I - G\hat{K}_\infty)) \leq \frac{\gamma}{\underline{\sigma}(G)\underline{\sigma}(W_1)\underline{\sigma}(W_2)} \tag{5.47}$$

$$\overline{\sigma}((I - G\hat{K}_\infty)G) \leq \frac{\gamma}{\underline{\sigma}(W_1)\underline{\sigma}(W_2)}, \tag{5.48}$$

  which means that $\underline{\sigma}(W_1)$ and $\underline{\sigma}(W_2)$ should be large in this frequency range.

- For frequencies in regions of low loop gain, ($\overline{\sigma}(G_s) \ll 1$), the weighting functions only affect robust stability, as described by

$$\overline{\sigma}(\hat{K}_\infty(I - G\hat{K}_\infty)) \leq \gamma\overline{\sigma}(W_1)\overline{\sigma}(W_2) \tag{5.49}$$

$$\overline{\sigma}(\hat{K}_\infty(I - G\hat{K}_\infty G)G) \leq \gamma\overline{\sigma}(G)\overline{\sigma}(W_1)\overline{\sigma}(W_2), \tag{5.50}$$

  so that $\overline{\sigma}(W_1)$ and $\overline{\sigma}(W_2)$ should be kept small in this frequency range. These bounds essentially require the gains of W_1 and W_2 to be high in the frequency

THE LIBRARY
UNIVERSITY OF CANTERBURY
CHRISTCHURCH, N.Z.

region where good performance is required (typically low frequency), and low where high robustness is required (typically high frequency).

For a *SISO* system, one shaping function, $W = W_1 W_2$, can be used instead of two. Glover and McFarlane (1990, 1992) contain excellent treatments of $\mathcal{H}_\infty$ loop shaping and the reader is directed there for proofs and further results.

Example. The 2 mode string may again be used as an illuminating example. Figure 5.15 shows the open loop shape of the nominal plant G, the shaped plant G_s and the weighting functions W_1 and W_2. The problem in this case is SISO, so only one weighting matrix is required, so we have set $W_1 = 1$. Considering the nominal plant, the open loop gain needs to be increased dramatically to achieve reasonable closed-loop bandwidth. The minimum $\mathcal{H}_\infty$ norm of $T_{z_d w_d}$ is given by $\gamma_{min} = 1.55$.

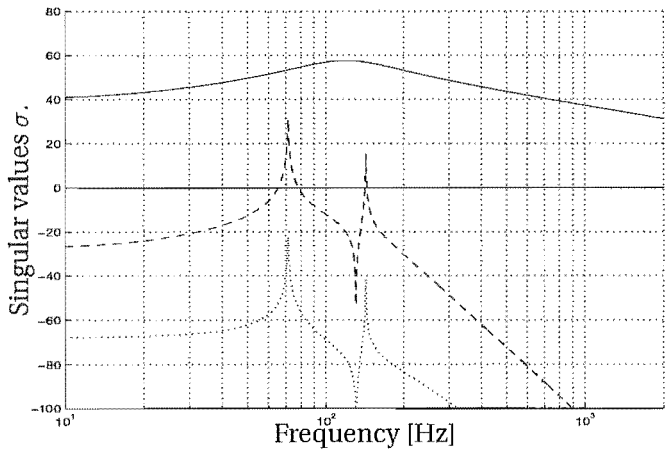

Figure 5.15: *Singular values for shaping function and open loop systems for the string example. KEY:* $\cdots\cdots G, - - G_s, —\ W_1 = 1, —\ W_2 = \frac{100(2\pi 20 s+1)}{s^2+4\pi 0.4(120)s+(2\pi 120)^2}$.

Figure 5.16 shows the impulse response for the controller given by $\gamma = 3$.

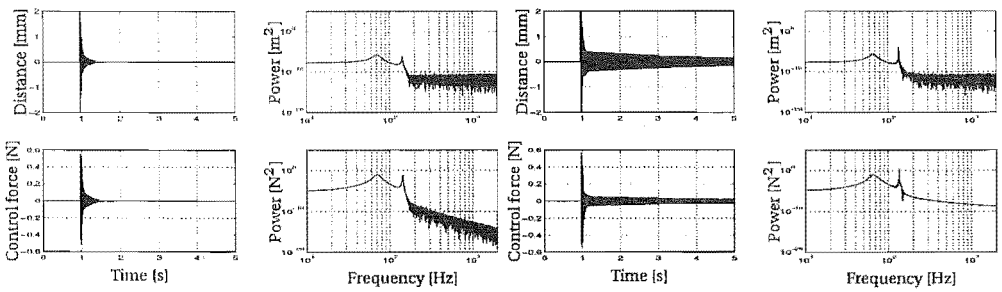

Figure 5.16: *Impulse responses of string in feedback with $\mathcal{H}_\infty$ controller, $\gamma = 3.0$. Nominal plant on left and perturbed plant on right.*

5.3.5 Controller order reduction

The model-based controllers are the same order (or higher in the $\mathcal{H}_\infty$ case) as the plant. For accurate modelling of even low frequency dynamics, higher order plant models are required, and using controllers of the same order in real time control can lead to long computation times and hence reduced sampling frequency and increased phase lag. Two options exist; to reduce the order of the plant (without greatly reducing the input-output accuracy of the model) and synthesise a controller from this reduced plant, or to generate a full order controller using the original plant and reduce the order of this controller (without greatly affecting its input-output behaviour). This work takes the former approach, and reduces a *balanced realisation* of the plant, a frequency weighted plant, or a normalised left or right coprime factorisation of the plant to give a reduced plant G_r. We may assume that the full order plant has been partitioned such that

$$\begin{bmatrix} \dot{\mathbf{x}}_c \\ \dot{\mathbf{x}}_r \end{bmatrix} = \begin{bmatrix} \mathbf{A}_{11} & \mathbf{A}_{12} \\ \mathbf{A}_{21} & \mathbf{A}_{22} \end{bmatrix} \begin{bmatrix} \mathbf{x}_c \\ \mathbf{x}_r \end{bmatrix} + \begin{bmatrix} \mathbf{B}_1 \\ \mathbf{B}_2 \end{bmatrix} \mathbf{u}, \tag{5.51}$$

and from this produce a reduced order system with the same number of states as $\mathbf{x}_c$. Depending on the procedure this system may or not be dependent on the $\mathbf{A}_{12}$, $\mathbf{A}_{21}$, $\mathbf{A}_{22}$, $\mathbf{B}_2$ and $\mathbf{C}_2$ matrices. The ordering and partitioning of the system is done by finding its Hankel singular values, and rearranging it so that the Hankel singular vector of the newly ordered system is ordered in a descending fashion.

Either the LQG/$\mathcal{H}_2$ or $\mathcal{H}_\infty$ loop shaping procedures can then be used to find a controller K_r, which is then used to control the original full order plant (or, in reality, the actual system). Again the SLICOT library is used for these reductions.

5.3.6 Summary of controller syntheses

Classical controllers are simple in synthesis and can offer good robustness but amplify high frequency noise and are susceptible to spillover. LQG/$\mathcal{H}_2$ optimal control can provide excellent performance and noise insensitivity, but requires a well known plant. Robust controllers can provide robustness to plant variations without great loss in performance, but the $\mathcal{H}_\infty$ loop shaping method, while simple to implement, is a simplification of the full 4-block system. Furthermore, and particularly for translating plants, model reduction produces far more effective controllers.

5.4 CONTROL IMPLEMENTATION

The controllers so far presented must be converted into difference equations for digital implementation. This is done using a bilinear approximation, and unless other-

wise noted the sampling frequency is 6033Hz. Other control implementation issues are discussed in Section B.4.

In the experimental system the actuator $G_a(s)$ includes the linearisation of the electromagnetic circuit, which requires the deflection as an input as well as the desired control force. Both saturated and unsaturated analyses are used, and compared in the first few experiments. The output of the linearisation and the actuator dynamics is the actual force applied to the blade, and errors between this and the desired force are the kind of modelling error that the unstructured uncertainty descriptions should take care of.

Investigations of the sensor noise intensity are given in Section B.2, and the results therein are used in the following work.

5.5 MOVING BEAM ROBUSTNESS STUDY: THEORY AND EXPERIMENT

This section considers the control of the translating beam of Chapter 4. The outcomes of this study are to provide a robustness study of the controlled system with respect to translation speed and bandmill tension, to assess the effectiveness of the non-contacting actuator-sensor pair, and to learn about the strengths and weaknesses of simulation results via comparison with experiment. The work is split into two groups; in the first $\eta = 1$, so that the band strain mechanism is supposed to be a freely hanging weight, and in the second $\eta = 0$, modelling rigid band wheels. Experimental results are provided in the first group.

5.5.1 Hanging counterweight study

5.5.1.1 Controller specifications

Seven controllers were applied to the beam model, two classical, two LQG/$\mathcal{H}_2$ and three $\mathcal{H}_\infty$ loop shaping controllers. The beam specifications are as per Table 4.1. The controller gains/weightings were chosen to give comparable $\mathcal{L}_2$-norms of the output y when applied to the nominal stationary model. The specifics are shown Table 5.4. It is worth considering the closed-loop performance specifications listed in Table 5.2 (refer to page 81 and also (5.8)), as shown in Figure 5.17 for the classical controllers, Figure 5.18 for the $\mathcal{H}_2$ controllers and Figure 5.19 for the $\mathcal{H}_\infty$ ones. Consider firstly the sensitivity function, $(I - GK)^{-1}$), for each type of controller, recalling that this is a measure of how sensitive the output is to additive noise on the sensor. It is apparent that the classical controllers exhibit low sensitivity at low frequency but high sensitivity at mid and high frequency. The higher gain $\mathcal{H}_2$ controller (LQG2) is more sensitive than the first, as expected. The high gain $\mathcal{H}_\infty$ controller, HINF3, exhibits similar sensitivity to HINF1, while HINF2 is less sensitive at low frequency.

Table 5.4: *Controllers for experimental beam analysis.*

Code	**Specifications**
CLAS1	$f_1 = 1500Hz$
CLAS2	$f_1 = 2000$, $f_2 = 140$, $f_3 = 1000$, $\zeta_1 = \zeta_2 = \sqrt{1/2}$
LQG1	$\mathbf{Q} = diag\{0,0,0,0,100,50,20,10\}$, $\mathbf{R} = 1$
LQG2	$\mathbf{Q} = diag\{0,0,0,0,100,50,20,10\}$, $\mathbf{R} = 0.1$
HINF1	$W_1 = 250$, $W_2 = 1$, $\gamma = 1.02\gamma_{min} \approx 1.45$
HINF2	$W_1 = 250$, $W_2 = 1$, $\gamma = 2\gamma_{min} \approx 2.84$
HINF3	$W_1 = 500$, $W_2 = 1$, $\gamma = 2$

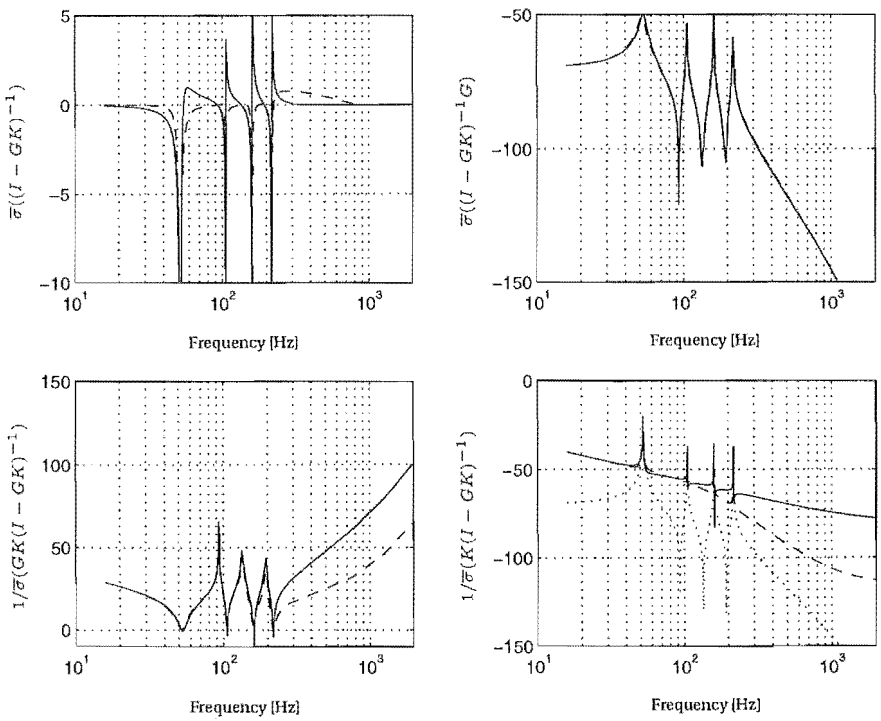

Figure 5.17: *Performance specifications for classical controllers. KEY: — CLAS1, - - CLAS2, ····· Plant.*

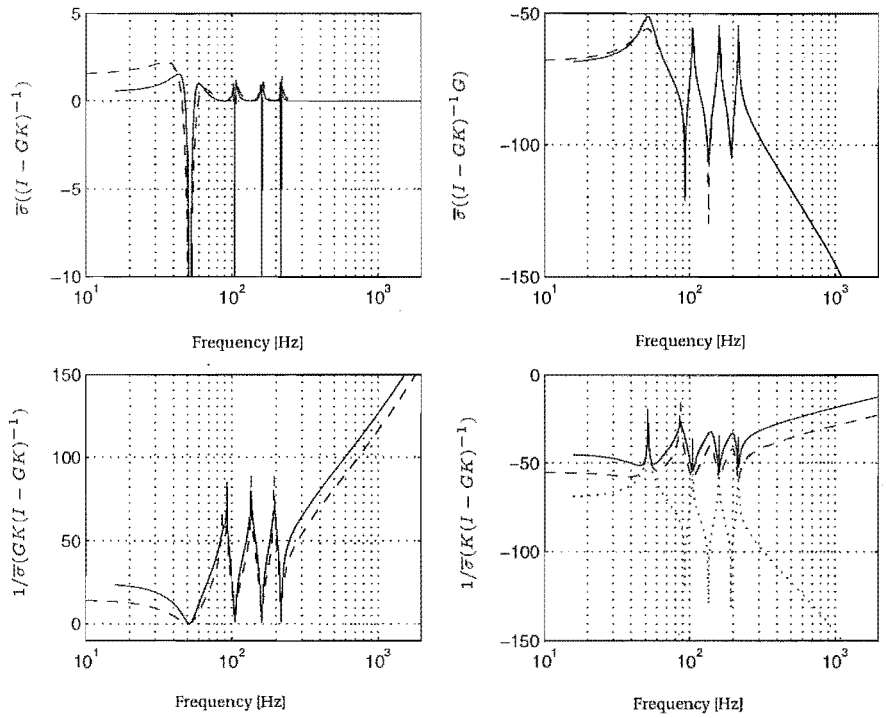

Figure 5.18: *Performance specifications for $\mathcal{H}_2$ controllers. KEY: — LQG1, - - LQG2, ····· Plant.*

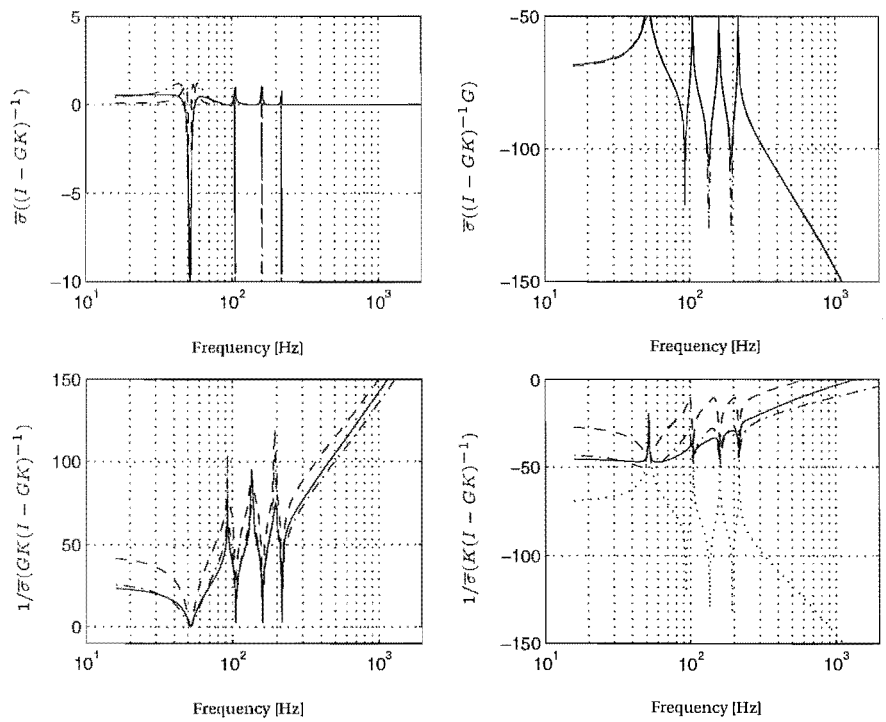

Figure 5.19: *Performance specifications for $\mathcal{H}_\infty$ controllers. KEY: — HINF1, - - HINF2, -·- HINF3, ····· Plant.*

The effect of the input disturbance upon the output is very similar for all controllers, and essentially follows the maximum singular value of the plant.

The robustness measures are however quite dissimilar. The classical solutions provide, in comparison to the modern controllers, similar robustness to additive and multiplicative uncertainties at low frequency, but markedly less at high frequency. The $\mathcal{H}_\infty$ controllers provide better robustness than the $\mathcal{H}_2$ controllers, both at high and low frequencies. The natural roll-off of the plant model has allowed the superior high frequency robustness to be achieved by the constant weighting functions. As expected the high gain controllers produce less robustness than the others. Of interest is the similar performance of HINF1 and HINF3, as is the high robustness of HINF2, considering that it guarantees a smaller stability margin than HINF1.

5.5.1.2 Preliminary stationary results

Figures 5.20 and 5.21 shows the free decay of the beam, in both simulation and practice, as well as the controlled responses of the stationary system in feedback with each of the controllers. The disturbance in each case is an impulse of 5N force and 0.006s duration, acting at $x_d = \frac{5}{12}\ell$. The modelled damping is assumed to be distributed with k_d=0.1Ns/m^2, (this value has been chosen to match roughly the theoretical free decay with the experimental). The low frequency envelope in the experimental free decay is the transfer of energy from one span to the other, a completely unmodelled effect. Considering the frequency spectra, the real system exhibits many modes of vibration, whereas the theoretical is of course limited to the number of basis functions comprising the beam deflection. Throughout this work the simulated plant is described using six basis functions. The $\mathcal{L}_2$-norms for each output are shown in each sub-caption.

From Figures 5.20(c) and 5.20(d), the simple rate controller produces an unstable closed-loop. The distance spectra show different modes as the offenders but this is only because of the finite dimension of the model and its ability to deflect linearly without bound. The more sophisticated classical controller is stable but at the expense of large control effort in the theoretical case. In the experimental case, large control effort is required and the attenuation is inferior to the uncontrolled decay.

The model-based controllers provide far better control, largely due to the noise insensitivity shown in Figures 5.18 and 5.19. The main difference in the distance spectra of the $\mathcal{H}_2$ controllers is that the control effort spectra is higher over the entire frequency range in the high gain case. The difference is more noticeable in the time domain signals, where the high gain case exhibits a much faster attenuation, both in theory and experiment. Also, the control effort is much greater. The experimental output differs from the theoretical in the low amplitude vibration after the initial transience has been attenuated. This is primarily due to the torsional and

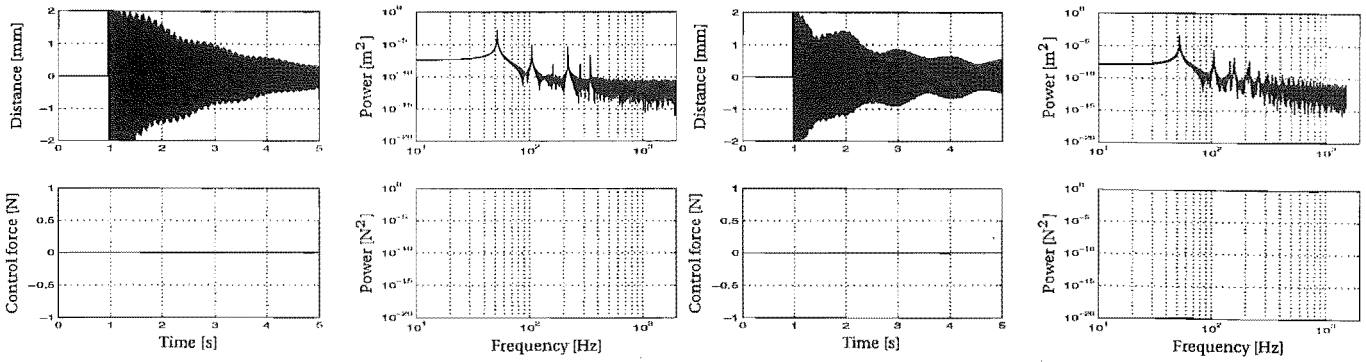

(a) Free response, $||y||_2 = 1.71 \times 10^{-3}$.

(b) Free response, $||y||_2 = 1.25 \times 10^{-3}$.

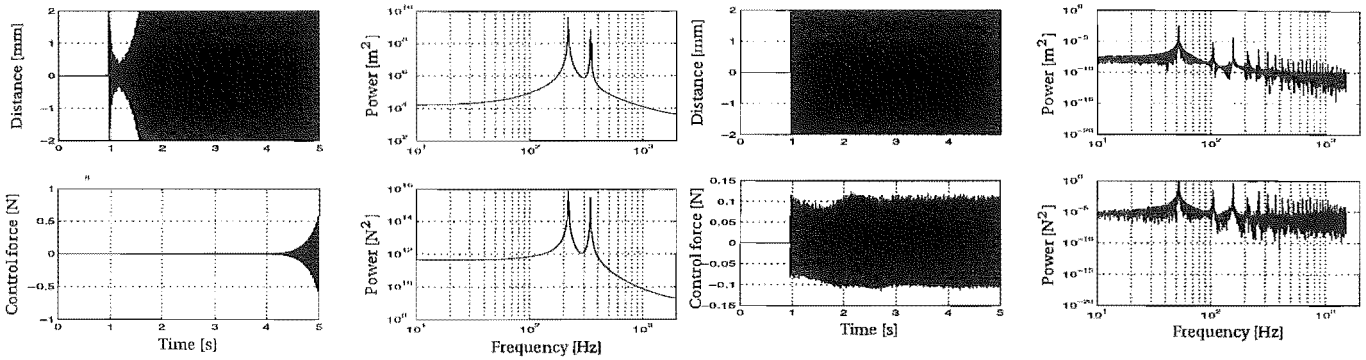

(c) CLAS1, $||y||_2 = 7753$.

(d) CLAS1, $||y||_2 = 3.45 \times 10^{-3}$.

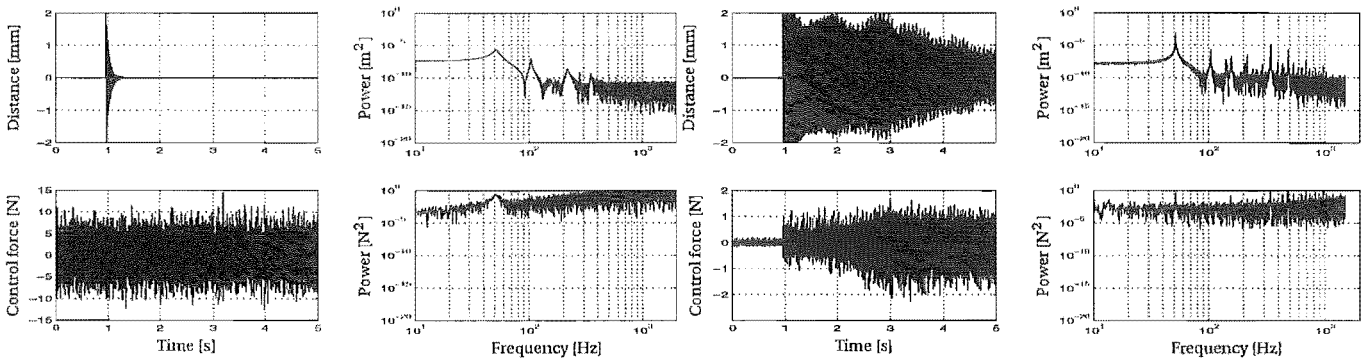

(e) CLAS2, $||y||_2 = 0.309 \times 10^{-3}$.

(f) CLAS2, $||y||_2 = 1.94 \times 10^{-3}$.

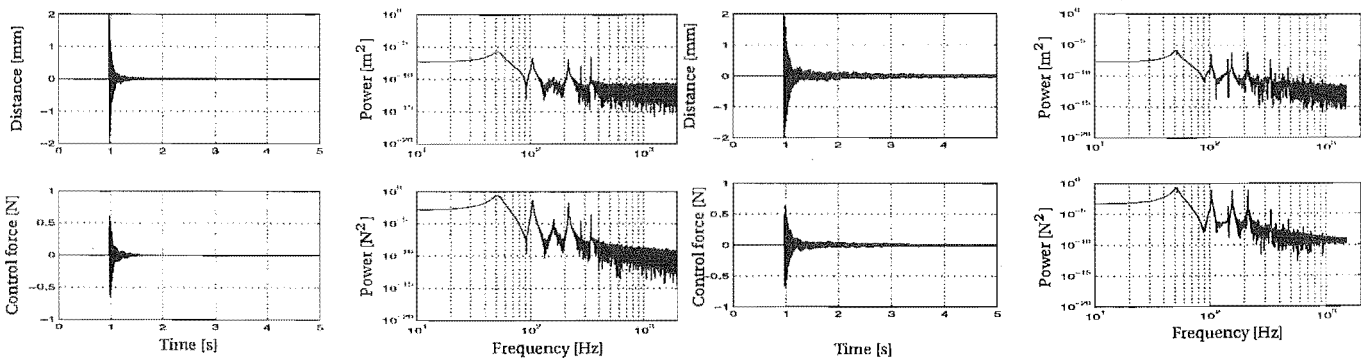

(g) $LQG1$, $||y||_2 = 0.337 \times 10^{-3}$.

(h) $LQG1$, $||y||_2 = 0.361 \times 10^{-3}$.

Figure 5.20: *Controlled impulse responses of stationary beam (First plot). Theoretical results are on the left, experimental ones on the right. The theoretical results use a 6 mode plant model in analysis, and all model based controllers are synthesised using a 4 mode plant model.*

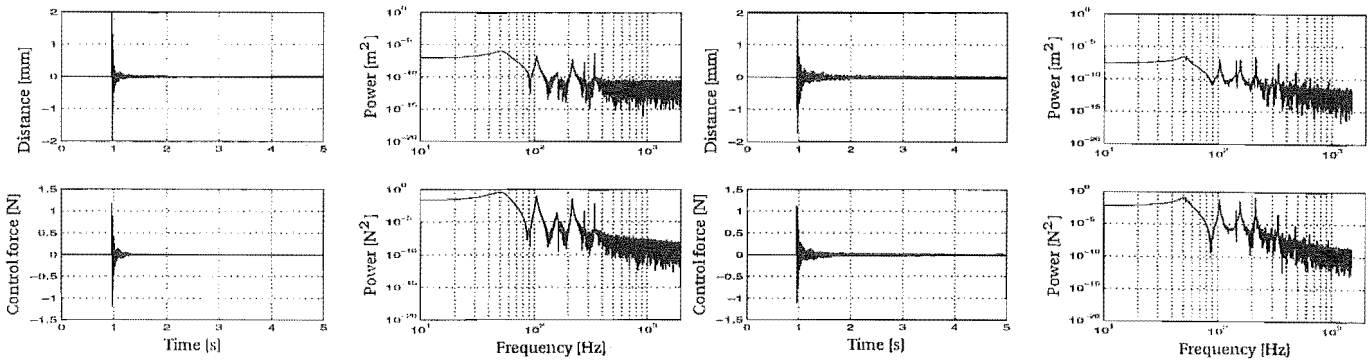

(a) LQG2, $||y||_2 = 0.271 \times 10^{-3}$.

(b) LQG2, $||y||_2 = 0.267 \times 10^{-3}$.

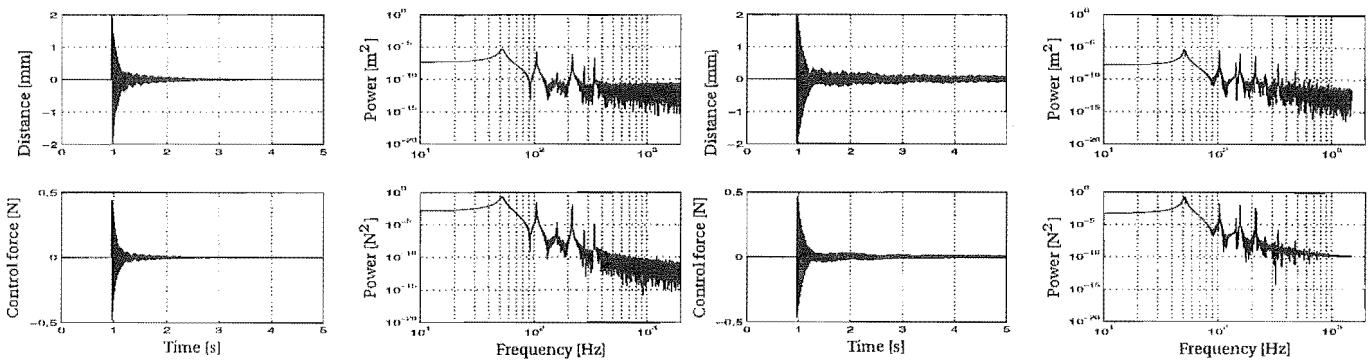

(c) $HINF1$, $||y||_2 = 0.393 \times 10^{-3}$.

(d) $HINF1$, $||y||_2 = 0.458 \times 10^{-3}$.

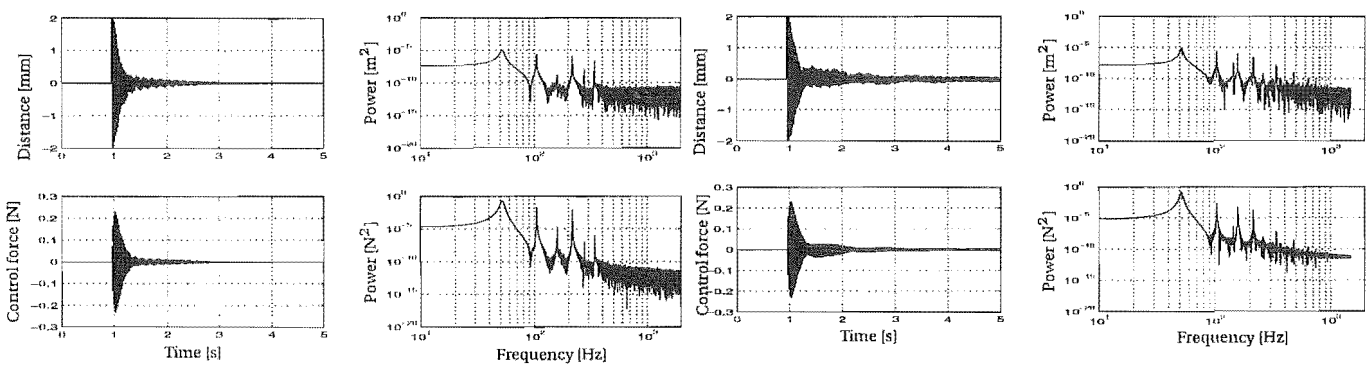

(e) $HINF2$, $||y||_2 = 0.525 \times 10^{-3}$.

(f) $HINF2$, $||y||_2 = 0.502 \times 10^{-3}$.

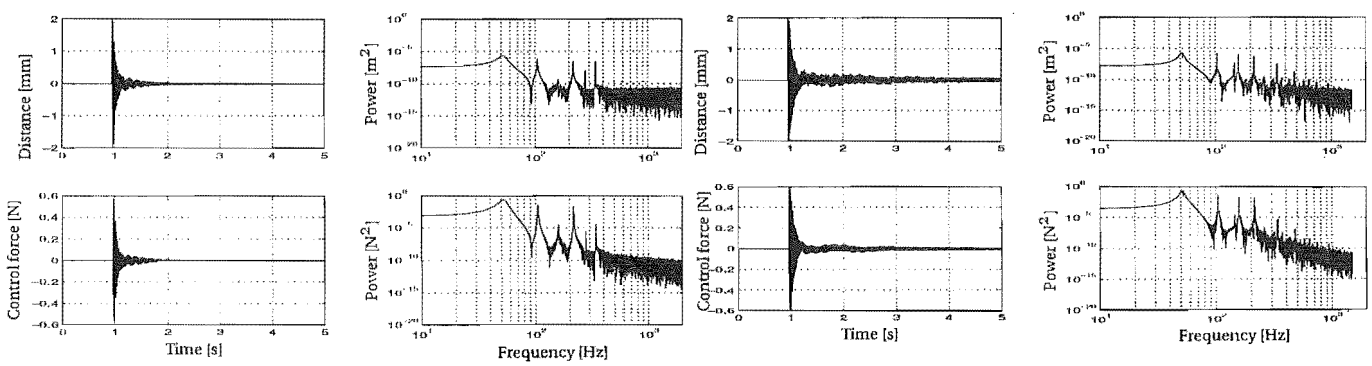

(g) $HINF3$, $||y||_2 = 0.352 \times 10^{-3}$.

(h) $HINF3$, $||y||_2 = 0.383 \times 10^{-3}$.

Figure 5.21: *Controlled impulse responses of stationary beam (Second plot). Theoretical results are on the left, expe mental ones on the right. The theoretical results use a 6 mode plant model in analysis, and all model based controll are synthesised using a 4 mode plant model.*

other unmodelled modes of the real plant, and secondarily due to vibration of the bandmill assembly and interaction with the return span. The low gain, near optimal, $\mathcal{H}_\infty$ controller HINF1 applies more control effort than HINF2, and produces correspondingly faster attenuation. The higher gain controller HINF3 produces even faster attenuation. All of these outputs are effectively related by the $\mathcal{L}_2$-norms of the outputs, and this is used in the ensuing work as an overall performance measure.

All of the results above use the saturated linearisation analysis presented in Chapter 4 in the calculation of PWM duty cycle for a required actuation force. The saturated analysis is used throughout, and produces responses that are 2—5% greater (in the 2-norm) than in the unsaturated analysis.

5.5.1.3 Robustness study

As mentioned in the introduction, any controller in an environment such as sawmilling must be robust to fluctuations in parameters such as bandmill tension, band speed, cutting forces and other effects. The results below detail the robustness of the five model-based controllers with respect to blade speed and tension, in theory and experiment, to see whether a single controller can provide enough robust performance to be used in an application such as sawmilling. The experimental results are not as comprehensive as the theoretical, but do serve the outcomes listed at the start of this section.

The gap metric. It is of interest to consider the "distance" between the plants as translation speed and tension changes, as shown in Tables 5.5 and 5.6. The synthesis

Table 5.5: *δ_ν metric for beam model as translation speed changes from $c = 0m/s$ to $c = 60m/s$.*

		Speed, c, in plant used in analysis				
	c	**0**	**15**	**30**	**45**	**60**
Speed, c, in plant used for synthesis	**0**	0.01	0.10	0.11	0.12	0.13
	15	0.10	0.02	0.11	0.12	0.13
	30	0.11	0.11	0.05	0.12	0.13
	45	0.12	0.12	0.12	0.11	0.13
	60	0.13	0.13	0.13	0.13	0.13

plants use four terms in the deflection discretisation, while the analysis plants use six. This is done to better simulate the actual plant by the analysis plant, and causes the non-zero diagonal terms, which would normally be expected to be zero. It is interesting that these diagonal terms are comparatively small for tension variation, but large for speed variation. Table 5.7 shows similar results to Table 5.5, but for a synthesis plant that has been generated using 8 basis functions (16 states) and then

Table 5.6: *δ_ν metric for beam model as blade tension changes from $R_o = 160N$ to $R_o = 400N$.*

		Tension, R_o, in plant used in analysis				
	R_o	**160**	**220**	**280**	**340**	**400**
Tension, R_o, in plant used for synthesis	**160**	0.01	0.15	0.15	0.15	0.15
	220	0.15	0.01	0.13	0.13	0.13
	280	0.15	0.13	0.01	0.11	0.11
	340	0.15	0.13	0.11	0.01	0.10
	400	0.15	0.13	0.11	0.10	0.01

reduced using the modal reduction method of Chapter 2 to a model with 8 states, after which the actuator and sensor dynamics are added. The off diagonal terms are

Table 5.7: *δ_ν metric for beam model as translation speed changes from $c = 0m/s$ to $c = 60m/s$.*

		Speed, c, in plant used in analysis				
	c	**0**	**15**	**30**	**45**	**60**
Speed, c, in plant used for synthesis	**0**	0.01	0.10	0.11	0.12	0.13
	15	0.10	0.02	0.11	0.12	0.13
	30	0.11	0.11	0.02	0.12	0.13
	45	0.12	0.12	0.12	0.03	0.13
	60	0.13	0.13	0.13	0.13	0.06

almost identical to those in the previous results, but the diagonal entries are greatly reduced.

Speed variation A reasonable method of analysing the robust stability and performance of the model-based controllers shown in Figures 5.20 and 5.21 is to use each one to control plants that are translating at different speeds. If the speed of the plant upon which the controller is designed is also changed, and used to control the various plants, a comprehensive picture of robustness can be created. The plant upon which a controller is designed is called the *synthesis* plant, and the plant to be controlled is the *analysis* plant. Furthermore, the closed-loop system given by synthesis and analysis plants of identical transport speed is known as the *nominal controlled system* and produces the *nominal controlled response.*

The robustness picture becomes more detailed if each closed loop is subjected to different disturbances. For each controller four disturbances were applied; the impulse of Figures 5.20 and 5.21, a random excitation, and two sinusoids. The first three disturbances act at $x_d = \frac{5}{12}\ell$, while the second sinusoid acts at $x_d = \frac{7}{12}\ell$. The random force has an intensity of 0.5N^2, and the sinusoids have an amplitude of 2N and fre-

quency of 150Hz. For the first three disturbances the real system is perturbed by the sensor-actuator and also controlled by it, and for the fourth disturbance there are no experimental results. Figure 5.22 shows the free responses to the four disturbances with respect to transport speed. Considering the theoretical results, the energy in the

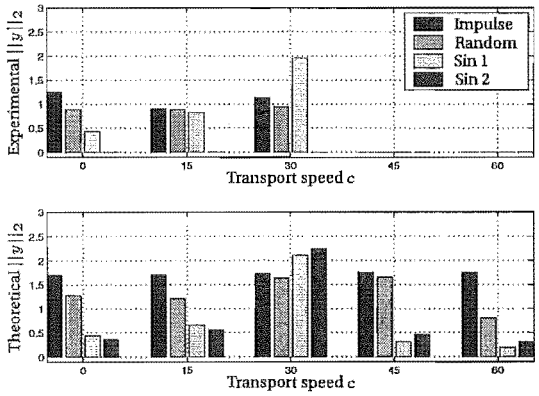

Figure 5.22: *Free responses of moving beam, subject to four disturbances. Sin 1 acts at* $x_d = \frac{5}{12}\ell$ *and Sin 2 at* $x_d = \frac{7}{12}\ell$

impulse response remains constant with speed, while the random response changes slightly. The sinusoidal responses show marked increases at $c = 30$m/s, for which the third mode vibrates at 159Hz, close to the 150Hz forcing frequency. For the stationary case, the experimental results are slightly lower than the theoretical, in fact this is true for the impulse and random responses throughout the speed range. The sinusoidal responses also exhibit the peak at $c = 30$. There are no experimental data for the fourth disturbance (Sin 2) because only one actuator-sensor arrangement was produced, and the lack of experimental data for the speeds of 45m/s and 60m/s is caused by limitations to the experimental rig.

Because the raw data from these experiments is rather uninformative, such bar graphs are the main representation of the robustness studies. For each test the $\mathcal{H}_2$-norm of the output is used as a measure of the closed-loop performance. For unstable systems the $\mathcal{H}_2$-norm is still used but the entry is flagged to indicate the instability. The graphical results have also been normalised such that the $\mathcal{H}_2$-norm of a certain synthesis-analysis combination is normalised with respect to the nominal controlled response corresponding to the **analysis** speed. This normalisation serves two purposes. Firstly, it removes effects of the real rig such as vibration caused by wheel rotation and the weld passing on and off the band wheels. Such exogenous effects cannot be ignored in a real situation but do detract from these robustness studies. Secondly, normalising the data with respect to the nominal controlled response (rather than the free response of the analysis plant) means that the robustness of controllers of the same type but designed for different speeds can be accurately and easily compared.

To fix ideas, consider the results for the impulse response of controller LQG1, as shown in Table 5.8. The experimental results only exist for speeds not exceeding 30m/s, simply because of the physical limitations of the experimental plant. Figure 5.23 plots the raw and normalised results for the model-based controllers

Table 5.8: *Effectiveness of LQG1 controller with respect to variations in the band speed used in synthesis and analysis, as measured by* $||y||_2 \times 10^8$.

		Speed, c, in plant used in analysis				
	c	0 The:Exp	15 The:Exp	30 The:Exp	45 The:Exp	60 The:Exp
Speed, c, in plant used for synthesis	0	*0.337:0.361*	0.345:0.556	0.397:.983	0.454:-	0.499:-
	15	0.357:0.368	*0.358:0.521*	0.388:0.919	0.450:-	0.504:-
	30	0.409:0.425	0.392:0.586	*0.364:0.927*	0.422:-	0.492:-
	45	0.580:0.593	0.526:0.765	0.424:0.954	*0.375*:-	0.455:-
	60	1.17:0.950	0.961:0.969	0.646:1.16	0.452:-	*0.396*:-

and an impulse disturbance (excluding LQG2, which is considered subsequently). Each group of bars comprises the five analysis speeds, according to the legend in Figure 5.23(a). Considering the raw data (the left column of graphs), it is immediately apparent that the experimental output energy increases with speed regardless of control action but the simulation energy does not. This effect is swamping the experimental data, which becomes very close to the theoretical when the normalised results are used (right column of graphs). All of these results are stable, and as would be expected and in keeping with the gaps between the plants, the nominal controlled response is always lower than other responses. Considering LQG1, the controllers designed on a stationary plant are much more robust to plant speed variation than are controllers designed using high speed plants. For HINF1 this is still the case, but the high speed controllers are more robust than those of LQG1. However, the nominal outputs are larger in the $\mathcal{H}_\infty$ case. HINF2 is more sensitive than both LQG1 and HINF1. In fact, the low speed controllers are also very sensitive to the speed variation. This is counter to the robust performance specifications in Figure 5.19. Also, the nominal values for HINF2 are larger than HINF1. HINF3 produces very similar results to LQG1.

The random excitation responses (see Figure 5.24) produce very similar results to the impulse ones. However, the sinusoidally disturbed systems (see Figure 5.25) all show very little sensitivity with regard to speed variation (note that the raw $\mathcal{H}_2$-norms have been used here). Considering the free response norms shown in Figure 5.22 and the raw data of the controlled sinusoidal responses the feedback control has had little effect on the system, in fact HINF1 adds energy to the output. This was foreseen in the second sensitivity plot of the performance specifications in Fig-

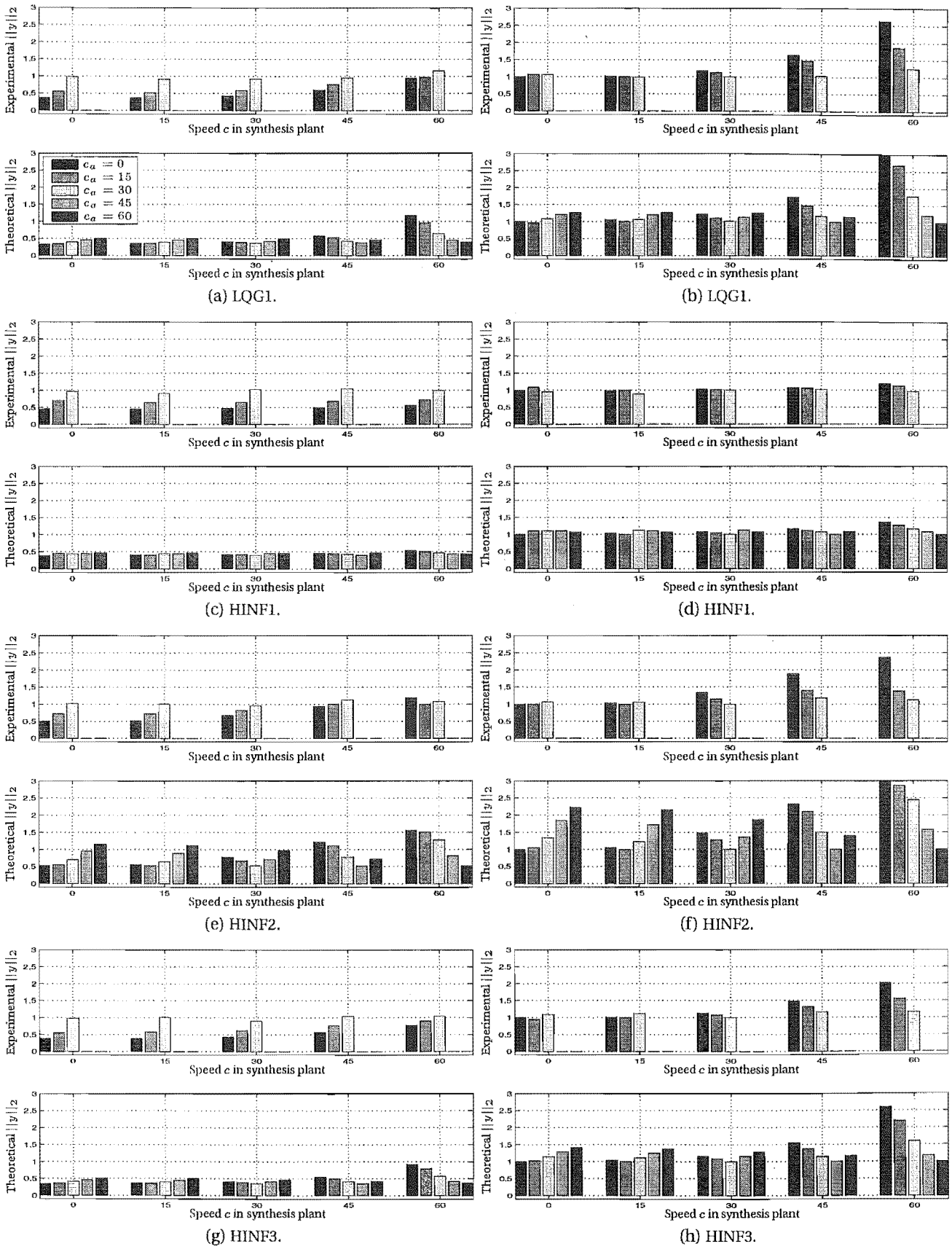

(a) LQG1. (b) LQG1.

(c) HINF1. (d) HINF1.

(e) HINF2. (f) HINF2.

(g) HINF3. (h) HINF3.

Figure 5.23: *Speed robustness of controlled responses of LQG1, HINF1, HINF2, HINF3 for the impulsive disturbance. Raw data comprises the left column and normalised data the right.*

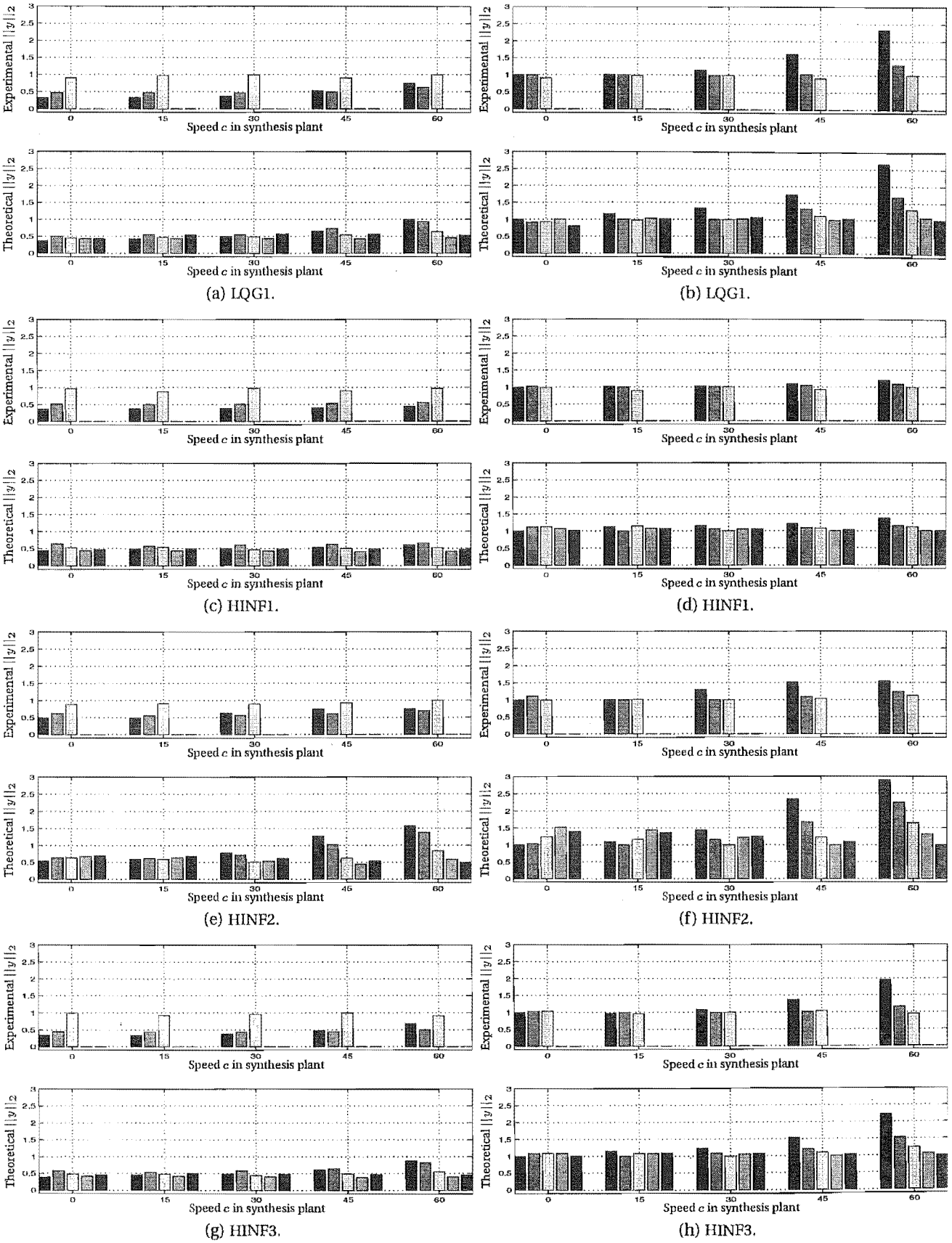

(a) LQG1. (b) LQG1.

(c) HINF1. (d) HINF1.

(e) HINF2. (f) HINF2.

(g) HINF3. (h) HINF3.

Figure 5.24: *Speed robustness of controlled responses of LQG1, HINF1, HINF2, HINF3 for the random disturban Raw data comprises the left column and normalised data the right.*

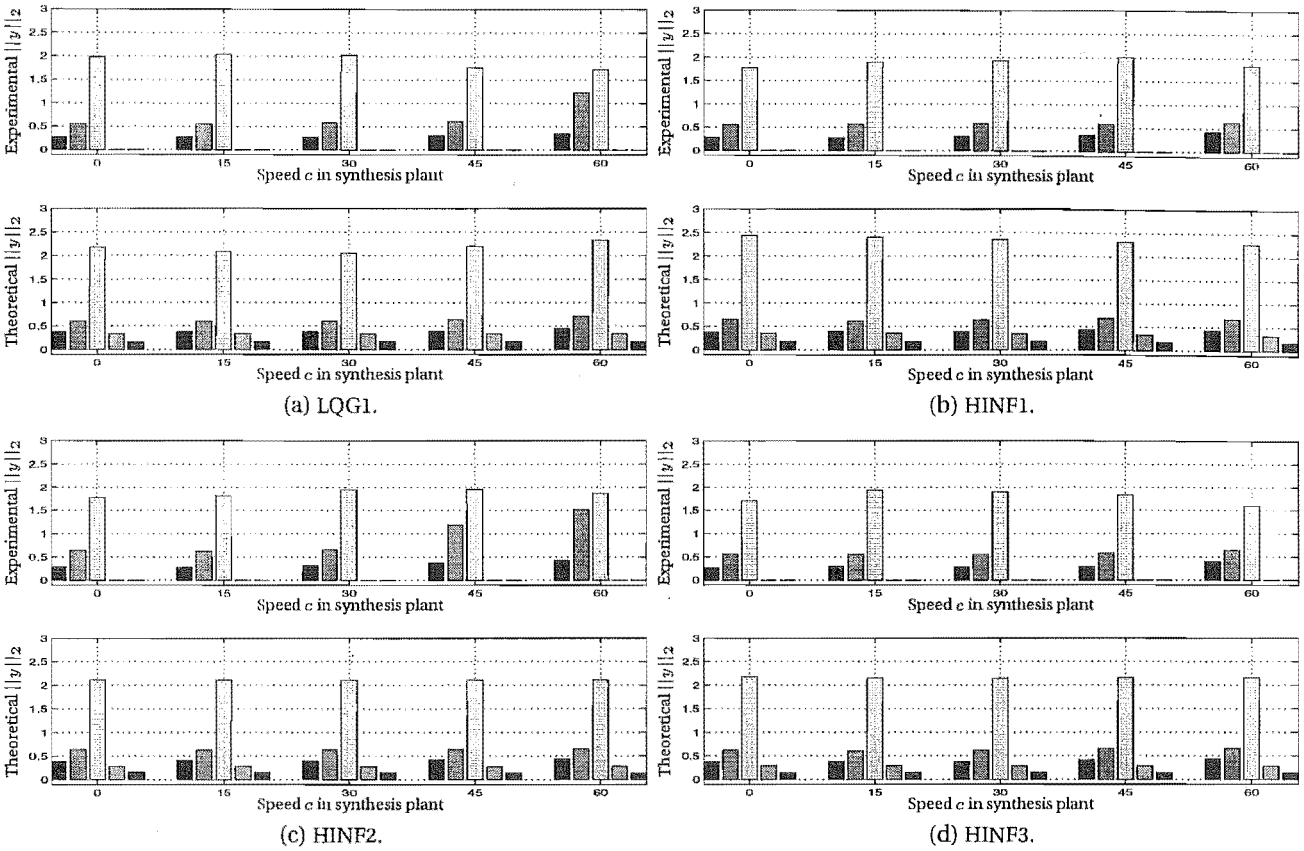

Figure 5.25: *Speed robustness of controlled responses of LQG1, HINF1, HINF2, HINF3 for sinusoidal disturbance. All results are raw $\mathcal{H}_2$-norms.*

ures 5.18 and 5.19, where the sensitivity of the output to plant input disturbances essentially follows the plant description.

LQG2 results. The high gain LQG controller LQG2 is very sensitive to parameter variation as well as spillover, as shown in Figure 5.26(a)[3]. Applying the model reduction procedure of Section 5.3.5 so that an 8 state plant is produced from a 16 state one (prior to adding actuator and sensor dynamics), the results of Figure 5.26(b) emerge.

Tension variation In a similar manner to the results of the speed analysis, the robustness with respect to tension variation may be considered. Table 5.9 shows $||y||_2$ when using LQG1 as synthesis and analysis plant tensions are varied. The variation in tension is the same as that used in the validation work of Chapter 4, and the robustness is considered at three speeds.

Figure 5.27 plots the normalised impulse response norms for the four controllers. Considering LQG1 the experimental and theoretical responses again match well, al-

[3]A bar with a small negative component indicates an unstable output.
[†]Unstable output.

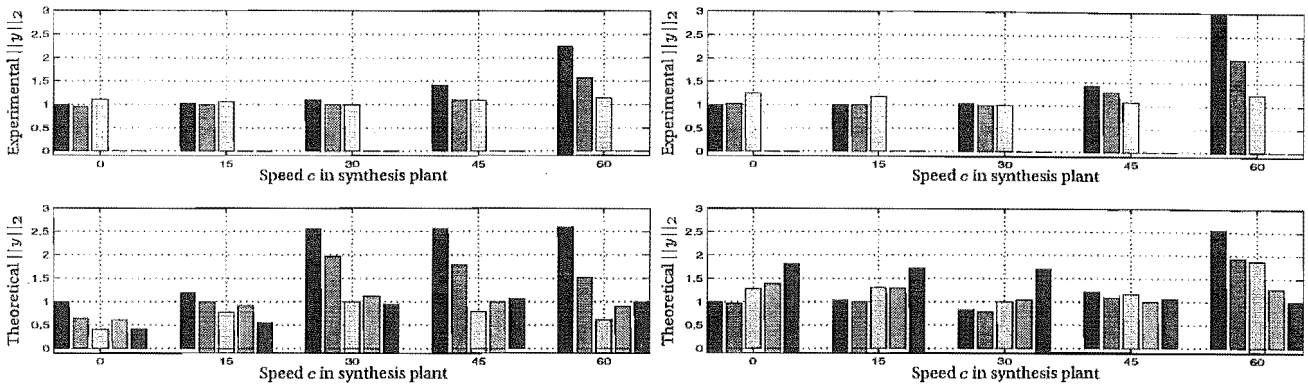

(a) LQG2. (b) LQG2b.

Figure 5.26: *Speed robustness of normalised controlled impulse responses of LQG2 and LQG2b. All results a normalised.*

Table 5.9: *Effectiveness of LQG1 controller with respect to variations in the band tension used in synthesis and analysis, as measured by* $||y||_2 \times 10^3$.

		R_o	R_o, (analysis) 160 The:Exp	280 The:Exp	400 The:Exp
$c = 0$	R_o, (syn.)	160	*0.594*:*0.418*	0.734:0.656	†66.8:†3.31
		280	0.847:0.458	*0.418*:*0.380*	0.458:0.490
		400	0.905:0.524	0.554:0.422	*0.337*:*0.361*
$c = 15$	R_o, (syn.)	160	*0.624*:*0.708*	0.870:0.944	†629:1.17
		280	0.855:0.815	*0.425*:*0.629*	0.475:0.734
		400	0.927:0.864	0.565:0.715	*0.358*:*0.521*
$c = 30$	R_o, (syn.)	160	*0.857*:-	1.81:-	†1321:1.26
		280	0.874:-	*0.456*:-	0.543:1.04
		400	0.972:-	0.599:-	*0.364*:*0.927*

though the theoretically unstable combination given by $R_{o,s} = 160$, $R_{o,a} = 400$ is only mirrored experimentally in the stationary case. HINF1 has even more unstable combinations, of particular interest are the unstable nominal responses occurring at $c = 15$m/s and $c = 30$m/s. Where the unstable nominal response also has large energy, the results that are normalised with respect to it become very small, as seen by the small entries for $R_{o,a} = \{280, 400\}$N. Aside from these values the theoretical and experimental results match very well (the experimental results do not have the normalisation problem as there are no nominally unstable experimental responses). Also, HINF1 is experimentally more robust than LQG1. HINF2 offers less robust performance than LQG1 and HINF1, both experimentally and theoretically, but is robustly stable throughout the entire range. HINF3 offers worse theoretical robust stability than all other controllers, and similar robust performance to LQG1 (although the theoretical results are altered in the same way as those in HINF1). So in this light the $\mathcal{H}_2$ optimal controller offers the best mix of robust stability and nominal and robust performance.

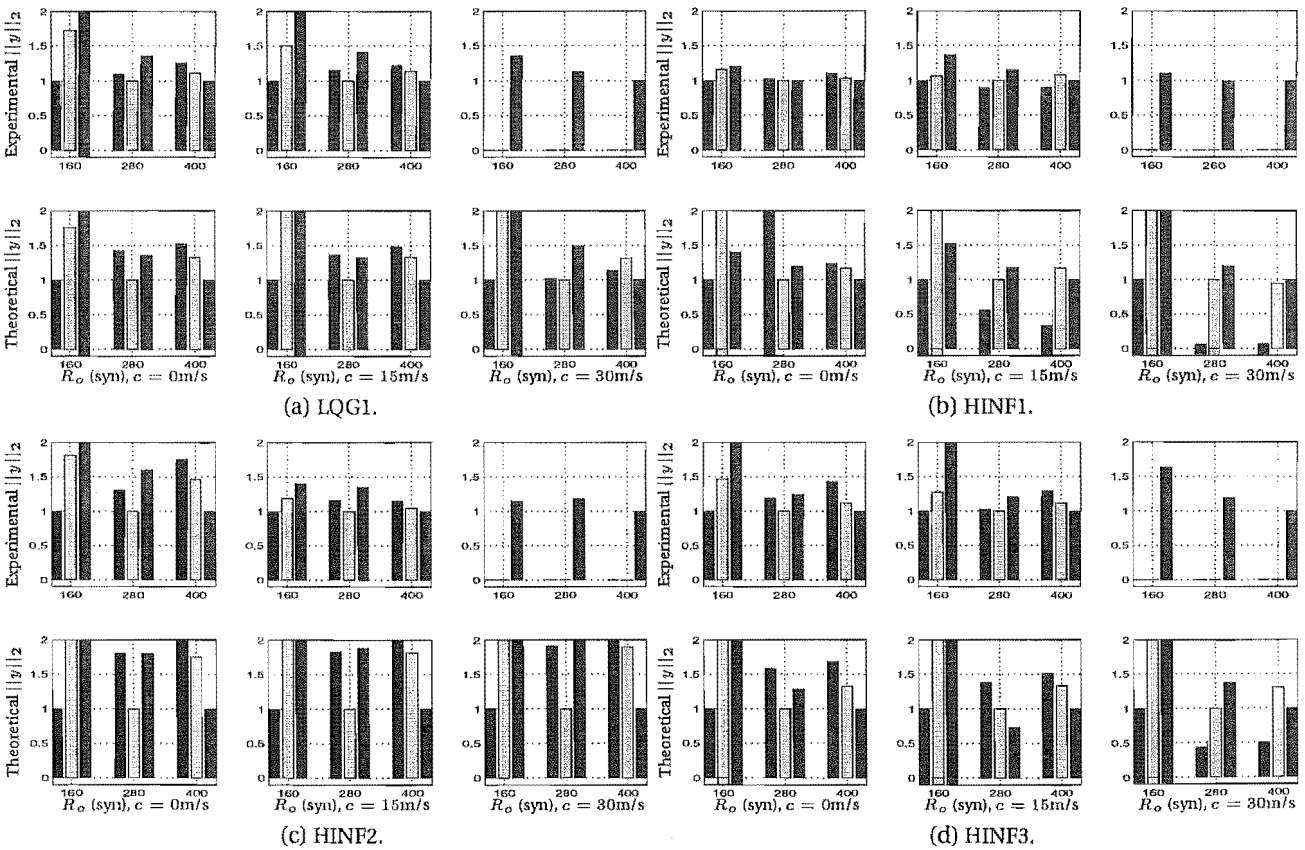

Figure 5.27: *Tension robustness of controlled responses of LQG1, HINF1, HINF2, HINF3 with impulse disturbance. All results are normalised, and each group of bars corresponds to analysis plants with R_o (ana) = $[160, 280, 400]N$.*

Figure 5.28 shows the same results for the sinusoidal disturbance (the random results are omitted), with raw results. The large values for plants with $R_{o,a} = 400$N at

$c = 30\text{m/s}$ are caused by the third mode being excited by the disturbance, while the large values for $R_{o,a} = 160\text{N}$ at $c = 0$ are caused by the fourth mode being excited. The experimental results match the theoretical very well, with the constant exception of the experimental values for $R_{o,a} = 280\text{N}$, $c = 15\text{m/s}$ being higher than the theoretical. The robust stability is very similar to the impulse results and it is hard to distinguish the controllers by robust performance, as was the case in the sinusoidally forced speed robustness tests.

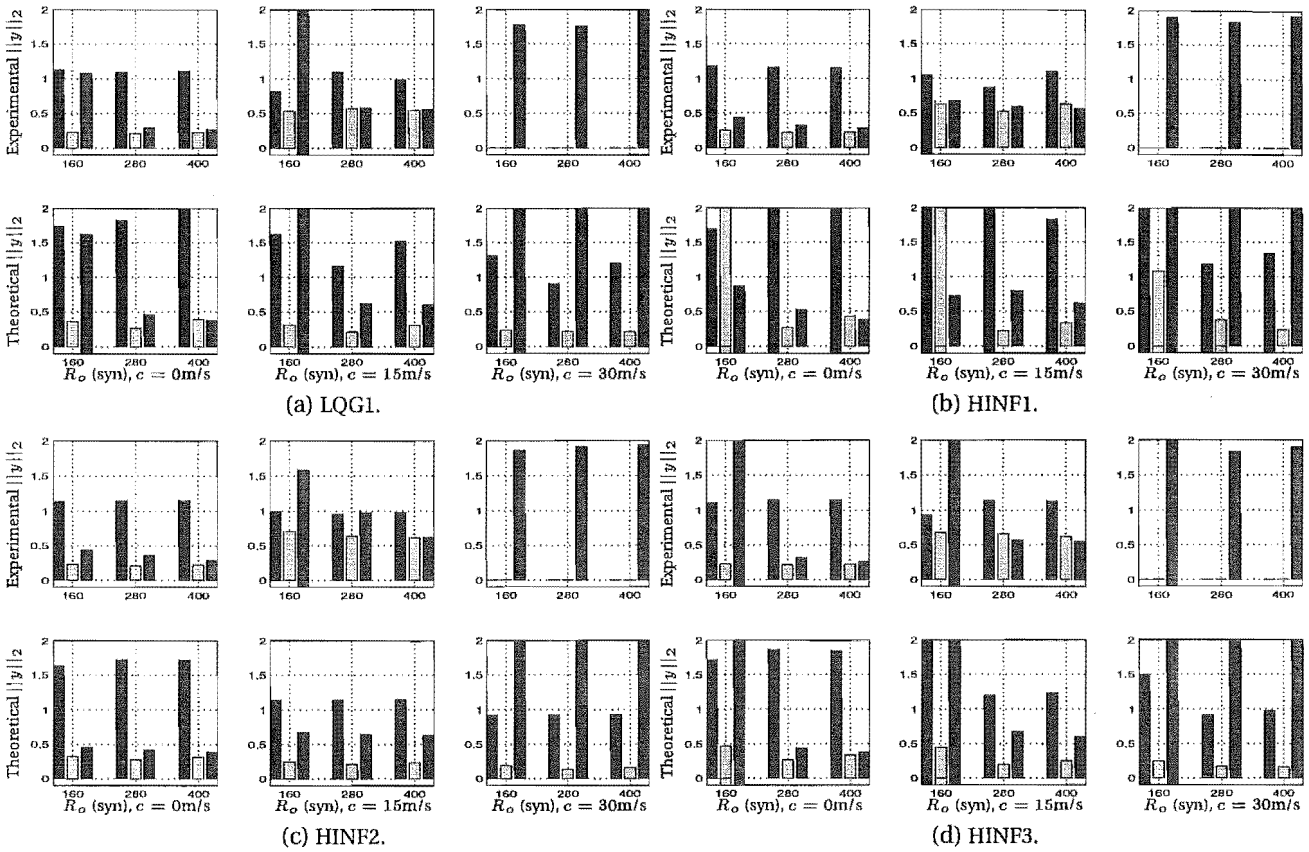

(a) LQG1. (b) HINF1.

(c) HINF2. (d) HINF3.

Figure 5.28: *Tension robustness of controlled responses of LQG1, HINF1, HINF2, HINF3 with sinusoidal distu bance. All results are raw $\mathcal{H}_2$-norms.*

5.5.1.4 Miscellaneous results

Noncollocated disturbance. The results so far consider the disturbance signal to act at the same position as the actuation and sensing, essentially because this allows the comparison with the experimental work. Figure 5.29 compares the theoretical normalised $\mathcal{H}_2$-norms of the outputs for the sinusoidal disturbance at $x_d = \frac{5}{12}\ell$ with the those for the disturbance acting at $x_d = \frac{7}{12}\ell$. With the exception of the LQG1 controller synthesised using a plant with $c = 60m/s$, the results are very similar.

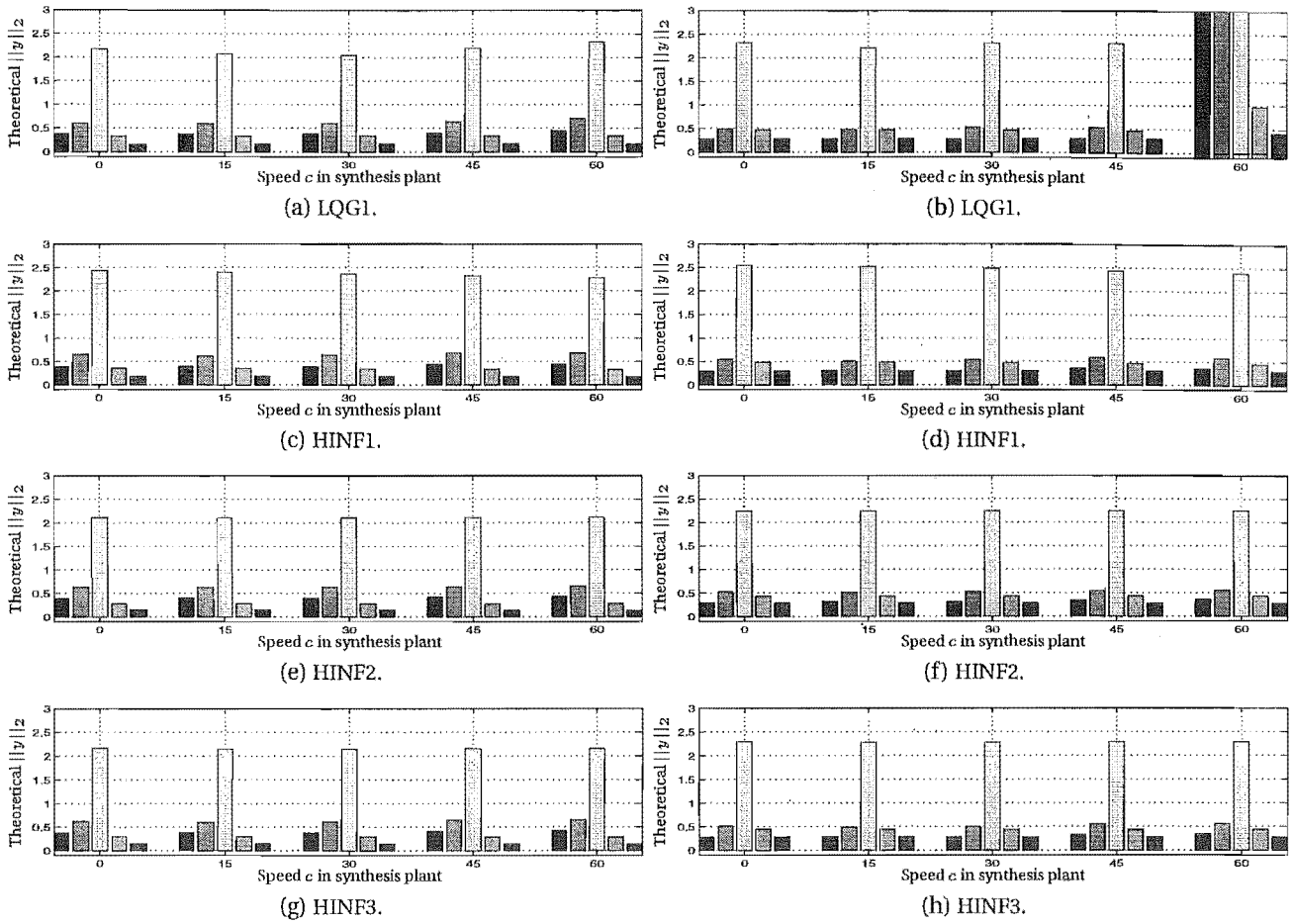

Figure 5.29: *Comparing the position of the sinusoidal disturbance on the performance of LQG1, HINF1, HINF2, HINF3. All results are raw $\mathcal{H}_2$-norms.*

Effect of actuator dynamics on disturbance input. The experimental system is disturbed by the actuator, and so the disturbance signal does not have the same spectra as the theoretical disturbance, which has no actuator dynamics built in. Figure 5.30 redisplays the normalised random speed robustness results (Figure 5.24(b)), and compares it with results where the theoretical actuator dynamics have been assumed part of the disturbance. Very little difference is noticeable, and in fact the impulse and sinusoidally disturbed systems show even less change.

5.5.2 Fixed band wheel study

Figure 5.31 shows the $\mathcal{H}_2$-norms of the free forced responses to the impulsive, random and sinusoidal loads. Only one sinusoidal disturbance acting at $x_d = \frac{7}{12}\ell$ is examined. In contrast to the corresponding results for $\eta = 1$, the impulse response energy increases with transport speed, essentially because the speed (now reaching the critical speed) markedly affects band tension and hence the high speed plants lack the stationary stiffness. It is to be remembered that the linear plant description does not model high speed phenomena accurately. This does not necessarily mean

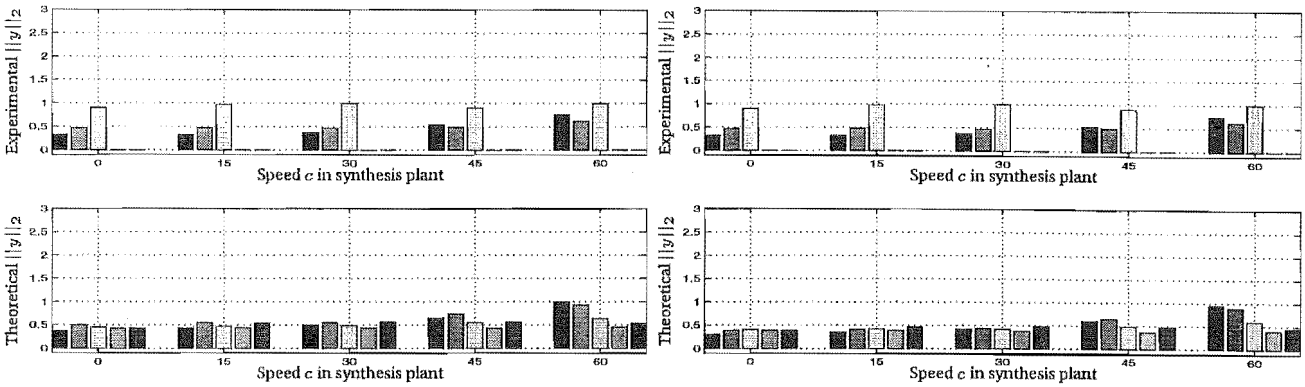

(a) LQG1. (b) LQG1a.

Figure 5.30: *Speed robustness of normalised controlled random responses of LQG1 and LQG1a. All results are ra $\mathcal{H}_2$-norms.*

that the linear controllers presented here will not stabilise a more accurate description of the plant (for example the plants within the maximum stability radius in the $\mathcal{H}_\infty$ formulation are not restricted to be linear), but that the analysis plants in the robustness work below should be represented by a nonlinear model. For these reasons the work is kept brief, and is considered an avenue for future work. In any case the sawmilling application restricts attention to subcritical speeds.

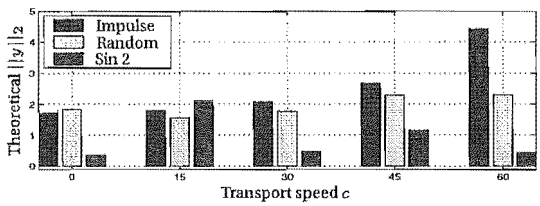

Figure 5.31: *Free responses of moving beam, subject to three disturbances.*

Figure 5.32 plots the speed robustness results for the LQG1, HINF1 and HINF3 controllers. Both synthesis and analysis plants describe fixed band wheels (ie. $\eta = 0$), and the left column represents systems where the analysis plant is of the same dimension as the synthesis one, so that spillover instabilities are eliminated. Considering firstly the left column of results, the low speed controllers are more robust than the high speed one. This effect was also noticed in the hanging counterweight experiment. Here, nominal stability is achieved everywhere except for HINF3 at $c = 60\text{m/s}$. For the higher order analysis plant spillover causes more unstable combinations, but the same robustness trends.

Figure 5.33 depicts closed-loop systems with six mode analysis plants and reduced order four mode synthesis models. These synthesis models are reduced from eight mode models. The results are superior to those with no model reduction, but not as good as those for $m_a = 4$. Without a physical plant to compare the theoretical

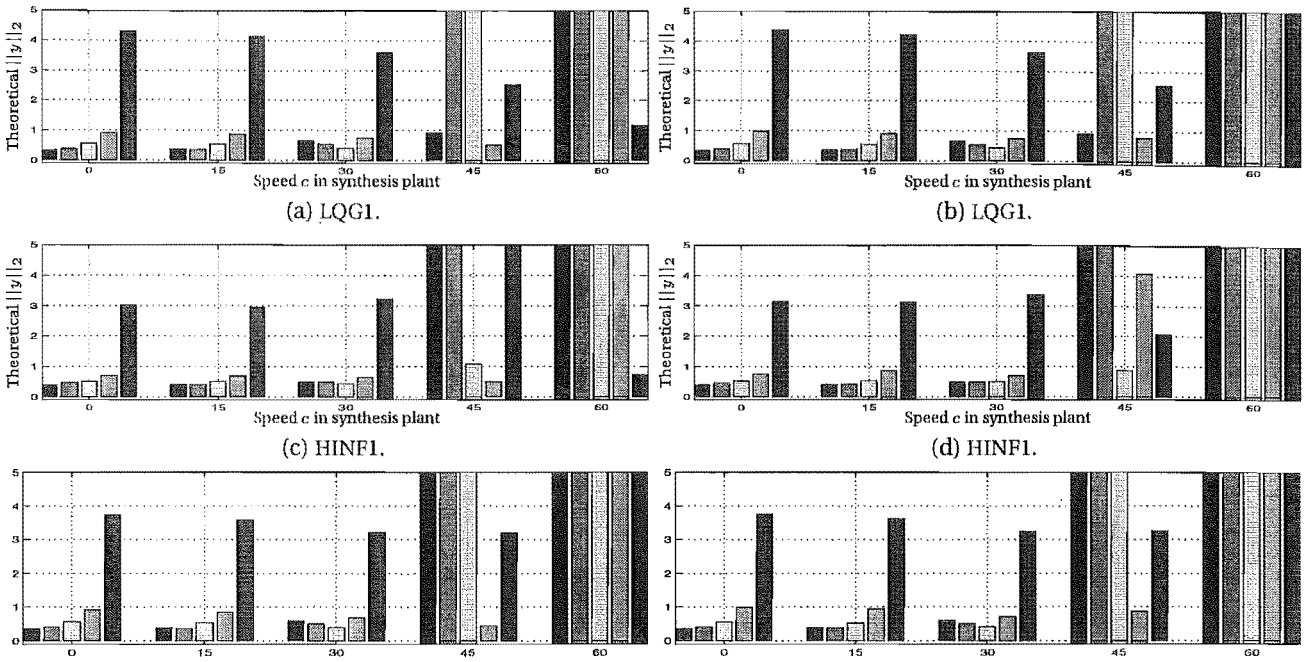

Figure 5.32: *Speed robustness of constrained wheel problem, controlled responses of LQG1, HINF1 and HINF3 for the impulsive disturbance are shown. All results are raw $\mathcal{H}_2$-norms. The left column shows results where $m_s = m_a = 4$, while the right column shows results where $m_s = 4, m_a = 6$.*

model it is imprudent to continue further, and this avenue is hereby closed.

5.5.3 Moving beam conclusions

Considering the desired outcomes of these robustness studies we may make the following comments:

- The noncontacting electromagnetic actuator and collocated eddy current sensor arrangement was shown to be effective in the active control of the moving beam.
- The theoretical and experimental data and trends were very close, especially where normalised results are used. This further validates the theoretical modelling and indeed the control formulation, allowing confidence in more complex theoretical analysis.
- Unstable theoretical closed-loop systems were not always matched with unstable experimental counterparts. The level of damping in the model is considered the cause of this, and is either too low or simply incorrect.
- Large variability in controller robustness was found, with the near optimal $\mathcal{H}_\infty$ loop shaping controller giving the best overall robust performance with regard

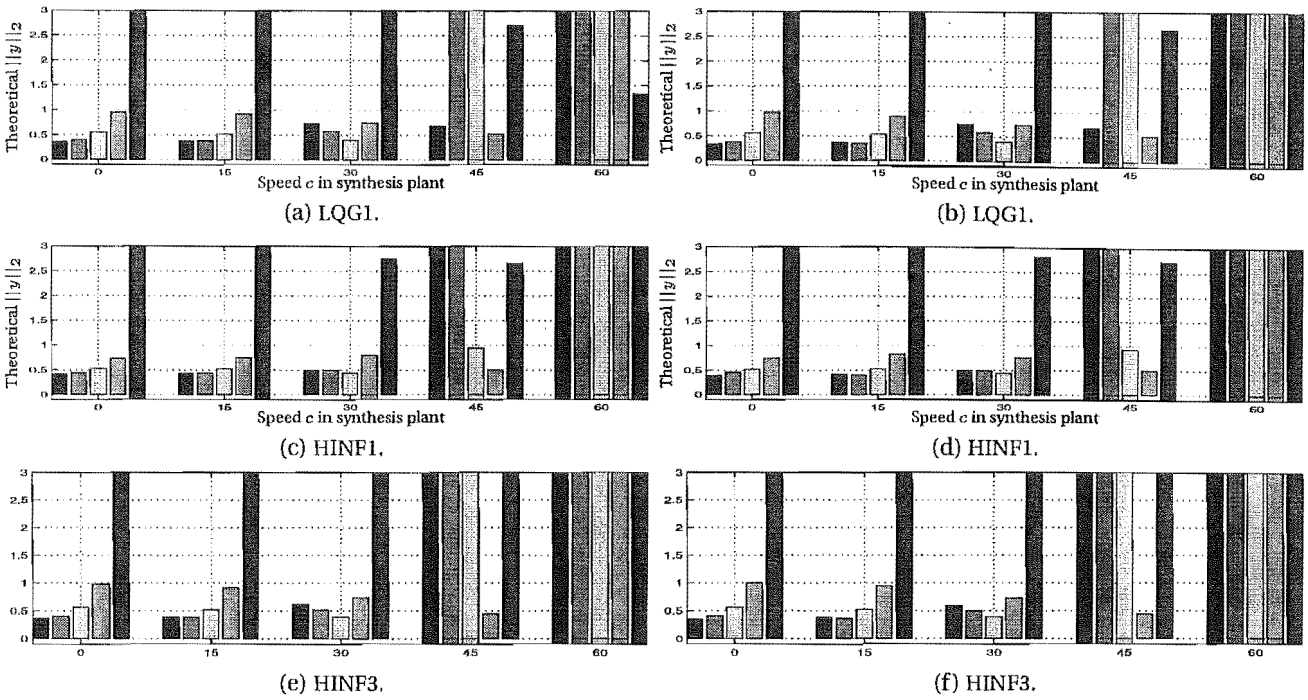

(a) LQG1. (b) LQG1.

(c) HINF1. (d) HINF1.

(e) HINF3. (f) HINF3.

Figure 5.33: *Speed robustness of constrained wheel problem, controlled responses of reduced versions of LQG HINF1 and HINF3 for the impulsive disturbance are shown. The left (right) column shows results where the reduction has been done before (after) combining the actuator and sensor models with the beam description.*

to speed variation, and the low gain $\mathcal{H}_2$ controller giving slightly superior robust performance with regard to tension variation. From these tests the near optimal $\mathcal{H}_\infty$ controller is considered the best single option.

- Controllers designed using low speed plants were often more robust than those designed using high speed plants.
- None of the controllers provided good attenuation to sinusoidal disturbances that were near natural frequencies of the plant, but did attenuate responses to other excitation frequencies.
- For the fixed band wheel system, where the speed variation is a much larger proportion of the critical speed, robust stability cannot be achieved over the entire speed range. Model reduction improves the situation to a limited extent, but without physical corroboration this work is left for the future.

5.6 MOVING PLATE ROBUSTNESS STUDY

The five controllers of the previous sections are theoretically examined from a robust stability standpoint in Figure 5.34. The beam models are generated using four basis functions in both the synthesis and analysis plants. The synthesis and analysis

plants for the plate models are the same dimension as the beam ones, having been modally reduced from ones generated using four basis functions along the length and two across the breadth. The synthesis and analysis models are of the same dimension to more accurately compare the beam and plate systems. The actuator and sensor are located at $x_a = x_s = \frac{5}{12}\ell$, $y_a = y_s = \frac{1}{4}b$, and the disturbance is located at $x_d = \frac{5}{12}\ell$, $y_d = b$. The damping in the plate case is distributed over the entire length, and $k_{ds} = 5Ns/m^3$ so it is equivalent to the beam damping. Considering

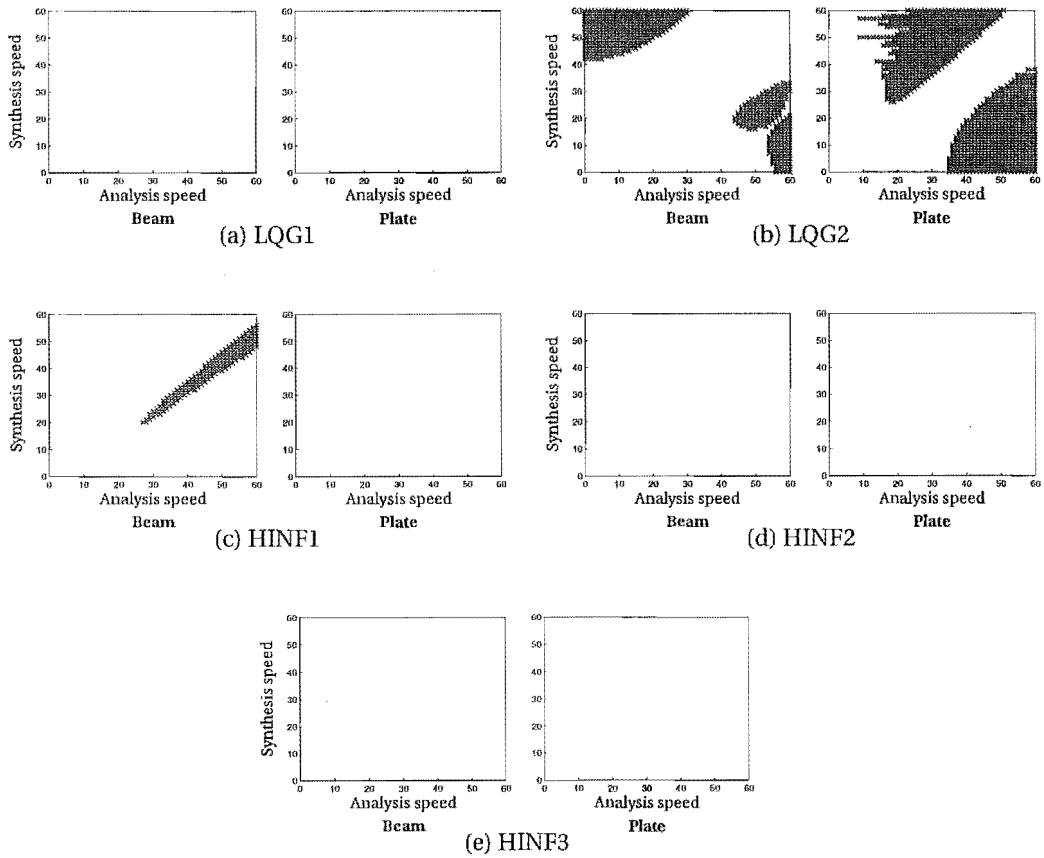

Figure 5.34: *Robust stability for $\eta = 1$ with respect to speed, for both the beam and plate problems. Locations marked by a × indicate unstable synthesis-analysis combinations.*

Figure 5.34 it is clear that the plate problem exhibits larger stable regions than the beam, although the regions of instability are similar, as exemplified in Figures 5.34(b) and 5.34(c). The results for LQG2 fit well with the δ_ν-gaps of Table 5.5, in that the unstable regions start (shown in the plate results) at the corners of the domain and finally encroach upon the nominal low speed combinations. Also of interest is the superior robust stability of HINF2 and HINF3 over HINF1, especially since the experimental results showed that HINF1 gave far better robust performance than the others. The superior robust performance is shown if the actual $\mathcal{H}_2$-norms are plotted over the domain, as shown in Figure 5.35. So while HINF2 (and HINF3) offer

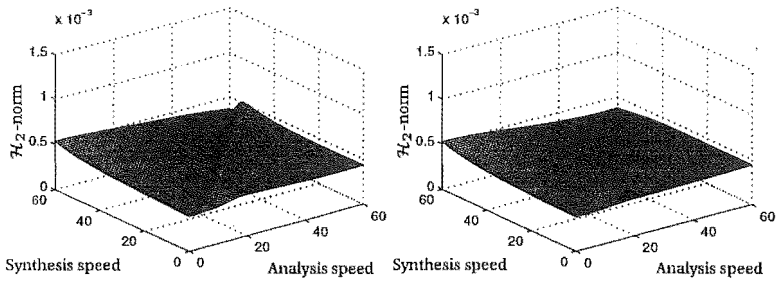

(a) HINF1

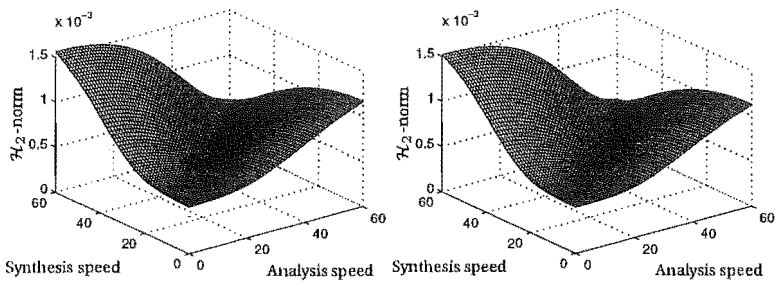

(b) HINF2

Figure 5.35: *Robust performance for HINF1 and HINF2. Beam models on left, plate ones on right.*

excellent robust stability, it is at the expense of robust performance. The flatness of Figure 5.35(a) also indicates why the instabilities in Figure 5.34(c) did not produce unstable outputs in the experimental work.

5.7 THE CUTTING SYSTEM

This section is presented as a case study of a wide bandsaw. It considers the control of a single span cutting saw initially and then, using the partial cutting and guide formulations of Chapter 3, a multispan saw. Firstly the cutting plate is modelled as per Damaren and Le-Ngoc (2000) and control results compared with this work. Then, the performance and robustness of the single span control with respect to parametric variations is researched. Lastly, the plate is extended in length and guides added, sensor and actuator positions moved to the noncutting spans and partial cutting applied. A similar robustness study to the single span case is performed.

5.7.1 Single span system.

Modelling. As mentioned in the literature summary, Damaren and Le-Ngoc (2000) considers the follower load to be distributed along the entire length of the cutting

edge, and assumes a single pointwise actuator with collocated rate measurement. This work contained a numerical example with the parameters as shown in Figure 5.36. Here, $N_{d,s}$ and $N_{d,a}$ are the number of modes of (respectively) the synthe-

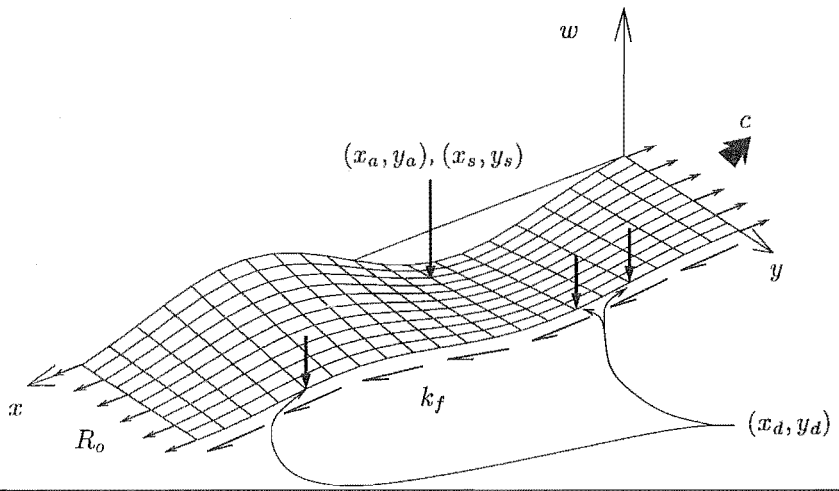

$\ell = 0.8\text{m}$	$b = 0.22\text{m}^2$	$h = 1.65\text{mm}$	$R_o = 15\text{kN}$	$\rho = 8200\text{kg/m}^3$
$x_s = x_a = \frac{5}{12}\ell$	$y_s = y_a = 0.2b$	$x_d = [0.2\ell, 0.3\ell, 0.8\ell]$	$y_d = [1b, 1b, 1b]$	$\zeta = 0.05$
$m = 10$	$n = 5$	$N_{d,s} = 5$	$N_{d,a} = 10$	$c = -40\text{m/s}$
$k_f = -7.5\text{kN/m}$				

Figure 5.36: *Sketch of plate model proposed in Damaren and Le-Ngoc (2000).*

sis and analysis models after transformation and truncation to modal coordinates (Damaren and Le-Ngoc (2000) used the procedure outlined in Section 2.1.6). Modal damping is also assumed, with the damping matrix (the plate corollary of $k_d \mathbf{E}^T \mathbf{D}_d \mathbf{E}$ in (2.31)) given by $diag\{2\zeta_{0i}\omega_{0i}\}$, where ω_{0i} and ζ_{0i} are the natural frequency and the damping coefficient of the ith stationary mode. Figure 5.37 shows the system root loci as the cutting force increases from $k_f = 0$ to $k_f = -50\text{kN/m}$, as well as digitised data from Fig. 2 in Damaren and Le-Ngoc (2000).

The root loci are, as expected, almost identical to Damaren and Le-Ngoc (2000), with the fifth and tenth modes being destabilised by the follower load. Figure 5.38 shows the responses under a idling and cutting conditions ($k_f = -7.5\text{kN/m}$). Considering the decay envelope of the idling system and the experimental results of the previous chapter, this level of damping is considered to be rather high for an idling saw (other damping models are considered below). The increased attenuation of the cutting response shows the added damping of the predominant modes by the cutting load.

However, the model reduction technique used by Damaren and Le-Ngoc (henceforth called the modal model reduction) produces credible but misleading results. Figure 5.39(a) shows the root-locus plot for the first ten modes of the full order system. These loci are compared with the reduced model results of Figure 5.37, and a

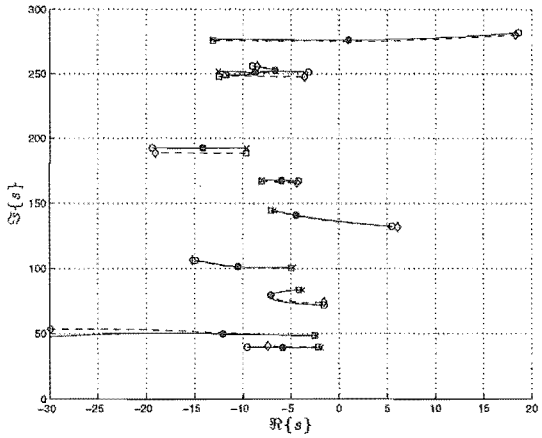

Figure 5.37: *Root loci as full length follower load varies from $k_f = 0$ to $k_f = -50kN/m$. Modal damping with $\zeta_{0i} = 0.05$ is used, and N_d=10. KEY: — Current model, - - Damaren and Le-Ngoc's model. × , □ indicate roots where $k_f = 0$, ● indicates roots where $k_f = -25kN/m$ and ○ , ◇ indicate roots where $k_f = -50kN/m$.*

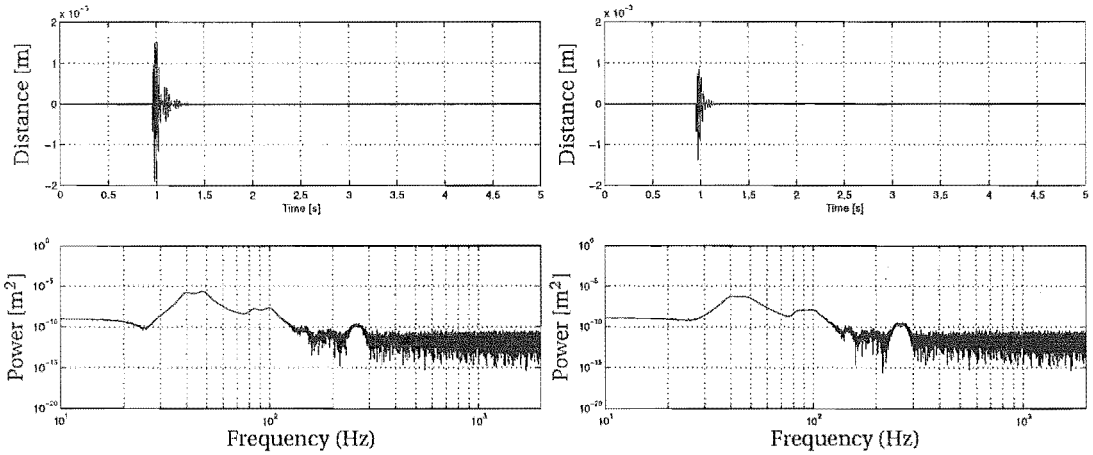

(a) Impulse response for $k_f = 0$.

(b) Impulse response for $k_f = -7.5$kN/m.

Figure 5.38: *Impulse response under cutting conditions.*

Bode plot providing a snapshot at $k_f = -7.5$kN/m is shown in Figure 5.39(b). Considering the root loci plot, the loci are similar for the two models for some modes but very dissimilar for others. In fact, the sixth mode is stabilised in the full order model but destabilised in the reduced case. Higher modes are also misrepresented, even at idle. Furthermore, the full order model is stable up to a cutting load of nearly

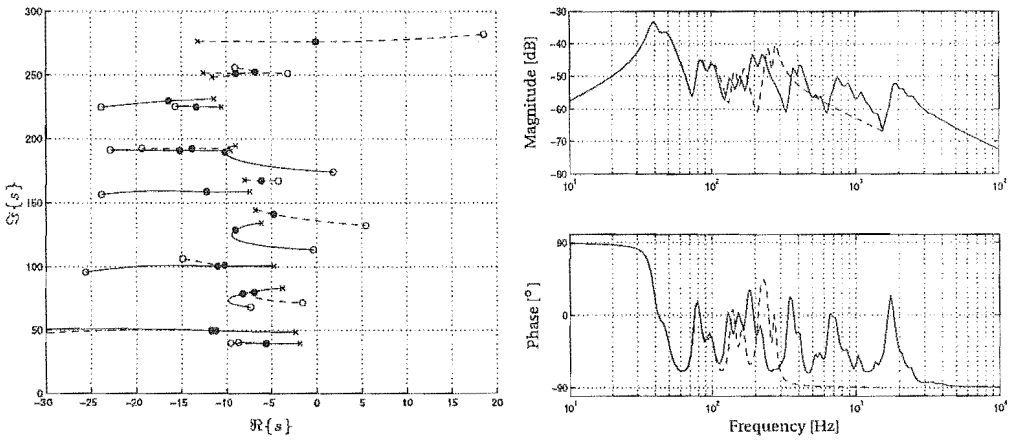

(a) Root loci as full length follower load varies from $k_f = 0$ to $k_f = -50$kN/m.
KEY: × indicates roots where $k_f = 0$, ● indicates roots where $k_f = -25$kN/m and ○ indicates roots where $k_f = -50$kN/m.

(b) Bode plots at $k_f = -7.5$kN/m.

Figure 5.39: *Root loci of the first ten modes of the full order model with respect to cutting load. Modal damping with $\zeta_{0i} = 0.05$ is used. KEY: — $N_d = 50$, - - $N_d = 10$ (ie. as per Damaren and Le-Ngoc (2000)).*

$k_f = -48$kN/m, and only one mode of the first ten is destabilised. There are of course higher modes that are not shown in the figure, but the level of modal damping means that none of these are destabilised for this cutting range. The Bode plot shows that even at relatively low cutting loads the modal approximation deviates considerably from the full model at fifth and higher modes, although accurately describes the first four. The modal truncation procedure is compared with other model reduction techniques below.

Control. Damaren and Le-Ngoc presented four controllers; two based on nominal closed-loop performance, the first being measured with a $\mathcal{H}_2$ performance criterion and the second with a $\mathcal{H}_\infty$ one, and two "robust" controllers, the first based on robust stability objectives and the second on robust performance. Figure 5.40 compares the open loop singular values of $-G(s)K(s)$ with results from Damaren and Le-Ngoc (2000), where both plant and controller are 5 mode models (the plant has been modally reduced from the full 50 mode plant). The controller is the standard $\mathcal{H}_2$ one formulated in Section 5.3.2 with the gains used in Damaren and Le-Ngoc

(2000). The results are in reasonable agreement, the most major differences being

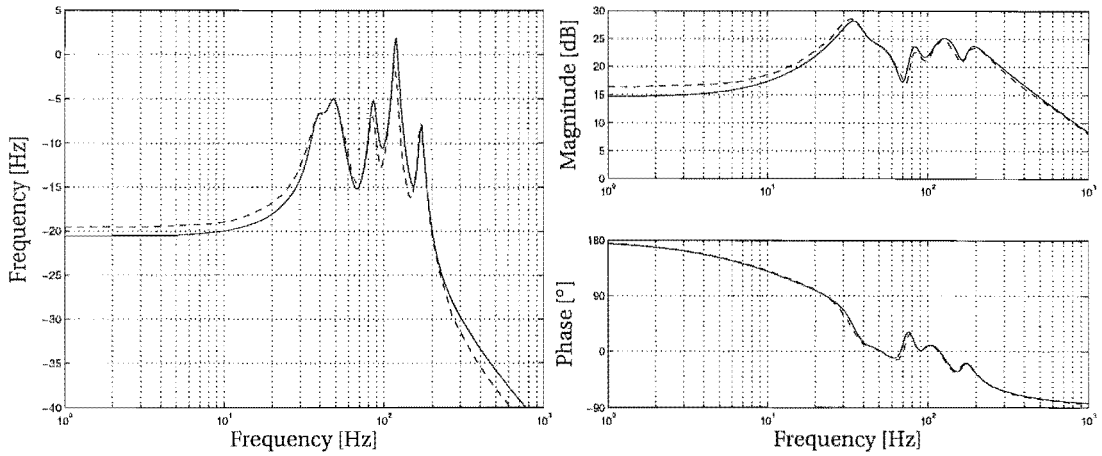

(a) Maximum singular value plot of open loop ($\overline{\sigma}(G(s)K(s))$).

(b) Bode plot of LQG controller ($-K(s)$).

Figure 5.40: *Bode and maximum singular value plots of LQG controller compared with Figures 5 and 10 from Damaren and Le-Ngoc (2000). KEY: — Current model, - - Damaren and Le-Ngoc*

the DC and high frequency gains. These comparisons with Damaren and Le-Ngoc (2000) further validate this plate formulation, as well as the $\mathcal{H}_2$ control formulation. More corroboration could be done but is considered unnecessary; it is time to learn from the above comparisons and consider the partial span cutting formulation and guide models of Chapter 3, as well as the actuator and sensor dynamics of Chapter 4, so that a more realistic system is considered.

Model reduction. The balanced truncation of the plant or its coprime factorisation as detailed in section 5.3.5 is considered herein. As already mentioned, the coprime factor approach has the advantage that unstable plants may be reduced. The reduction routines of the SLICOT library are used, as they produce superior results to the standard MATLAB routines. Figure 5.41 compares six different reduced models with the full order model, including that produced by the modal reduction method. Table 5.10 briefly describes each reduction method used. In each case the full model has been generated using the same 50 modes previously used (*ie.* 100 states), and the reduced systems all have 20 states. The simple, modal damping with $k_{dm} = 0.05$ is used throughout. The unweighted methods give similar results, with the reduction scheme ignoring the torsional frequencies at large cutting loads as they have been well damped and hence do not contribute much to the input-output behaviour. However, the loci for higher modes seem at times random, especially in terms of the damping level. This is also shown in the bode plots of Figure 5.42, where even at

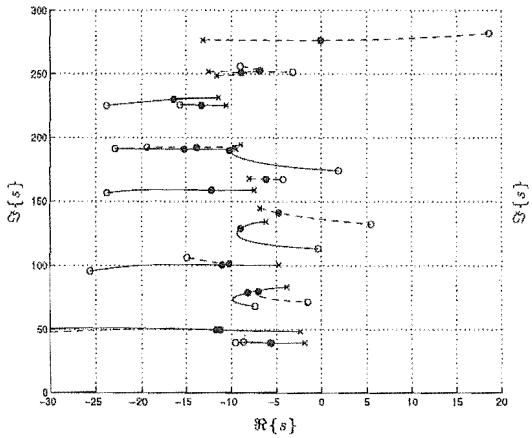

(a) MR.

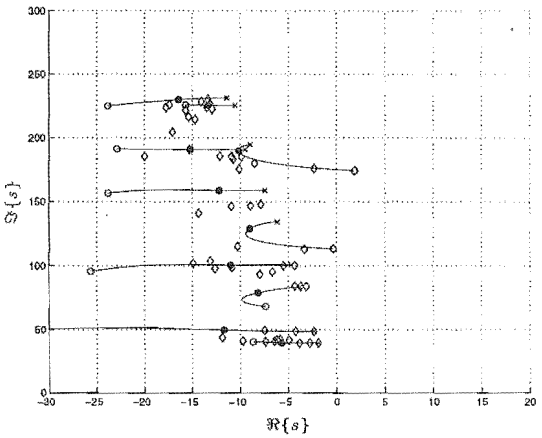

(b) B&T.

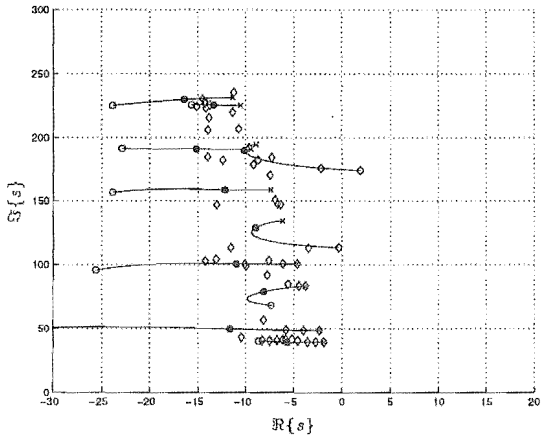

(c) SPA.

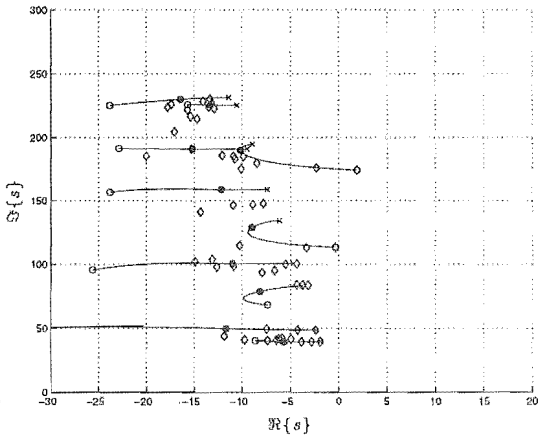

(d) B&T-RCF.

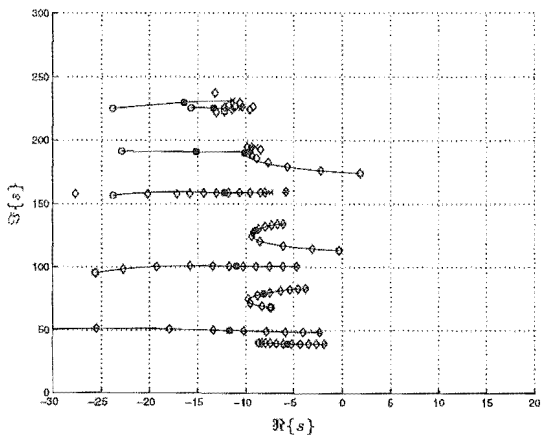

(e) FWB&T $W(s) = \frac{1}{(s^2+2\zeta\omega+\omega^2)^4}\mathbf{I}, \zeta = 0.2, \omega = 2\pi 50; V(s) = \mathbf{I}$.

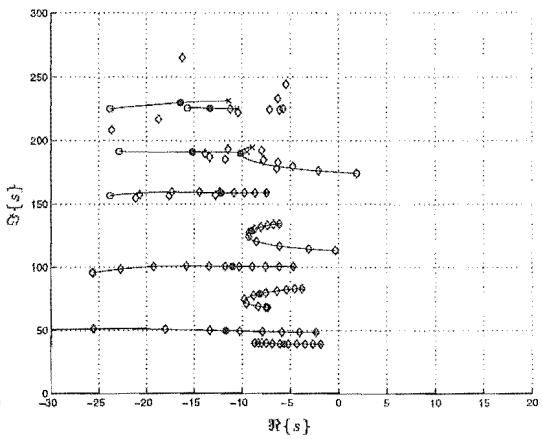

(f) FWB&T $W(s) = \frac{1}{(s^2+2\zeta\omega+\omega^2)^4}\mathbf{I}, \zeta = 0.2, \omega = 2\pi 50; V(s) = \frac{1}{(s^2+2\zeta\omega+\omega^2)^4}\mathbf{I}, \zeta = 0.2, \omega = 2\pi 100$.

Figure 5.41: *Root loci of plants produced by various reduction procedures.* $k_{dm} = 0.05$. *KEY:* × *indicates roots where* $k_f = 0$, • *indicates roots where* $k_f = -25kN/m$ *and* ○ *indicates roots where* $k_f = -50kN/m$, ◇ *Reduced system.*

Table 5.10: *Model reduction schemes used in plate analysis.*

Name	Description
MR	Modal reduction. See Chapter 2.
B&T	Balance and Truncate. The Hankel singular values of the stable part of the system are used to order the modes. The system is then truncated in a similar way to the modal reduction technique. If the system is unstable then it is first separated into stable and unstable parts, such that $G = G_{stab.} + G_{unstab.}$, and only the stable part is reduced.
SPA	Singular Perturbation Approximation. Again the Hankel singular values provide the ordering, but the matrices of the reduced system include combinations of $\mathbf{A}_{12}$, $\mathbf{A}_{21}$, $\mathbf{A}_{22}$, $\mathbf{B}_2$ and $\mathbf{C}_2$.
B&T-RCF	Balance and Truncation of Right Coprime Factorisation. Instead of the additive separation of the stable and unstable parts, an unstable system is separated into right coprime factors, and each of these (which are guaranteed to be stable) are reduced.
FWB&T	Frequency Weighted Balance and Truncate. This differs from the B&T method in that the system is first weighted, so that the Hankel singular values at some frequencies are effectively increased by the designer. The reduction procedure then follows and finally the weightings are removed from the reduced system.

$k_f = -7.5$kN/m the sharpness of the magnitude peaks (an indication of the modal damping) is quite different in the reduced systems. The weighted methods produce excellent root loci, especially for low modes. Considering the Bode plots, the simple weighted methods produce excellent results for the lower modes with a little deviation at higher modes However, the introduction of a filter on the input causes sharp spikes in the magnitude plot and correspondingly large phase changes.

Damping models. Damping in a complex system such as the cutting saw is very difficult to accurately model, and is quite crucial to system stability. Figure 5.43(a) shows the impulse response for a distributed surface damping of $k_{ds} = 15\text{N·s/m}^3$. The decay more closely resembles those in the experimental work than does the damping used in Damaren and Le-Ngoc (2000). However, while this distributed surface damping may accurately reflect an idling saw, it does not accurately describe the cutting system (even low cutting loads destabilise high modes). This may in part be explained by taking into account the lateral restraint provided by the workpiece. Consider the case where the workpiece feed is stopped part way through a cut. Assuming that the kerf thickness means the flank of the blade does not touch the sawn surfaces, the only interaction between the blade and the workpiece will be the restriction to lateral movement of the cutting edge. The simple models presented for this in Chapter 3 were the distributed mass-spring-damping forces. Figure 5.43(b) shows results for the surface damping previously used as well as distributed damping and spring forces along the cutting edge (where $k_d = 5\text{N·s/m}^2$

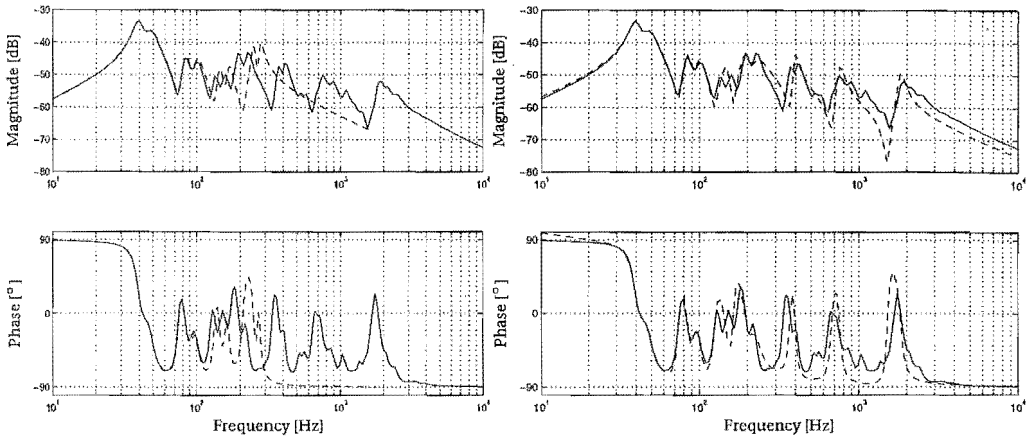

(a) MR. (b) B&T.

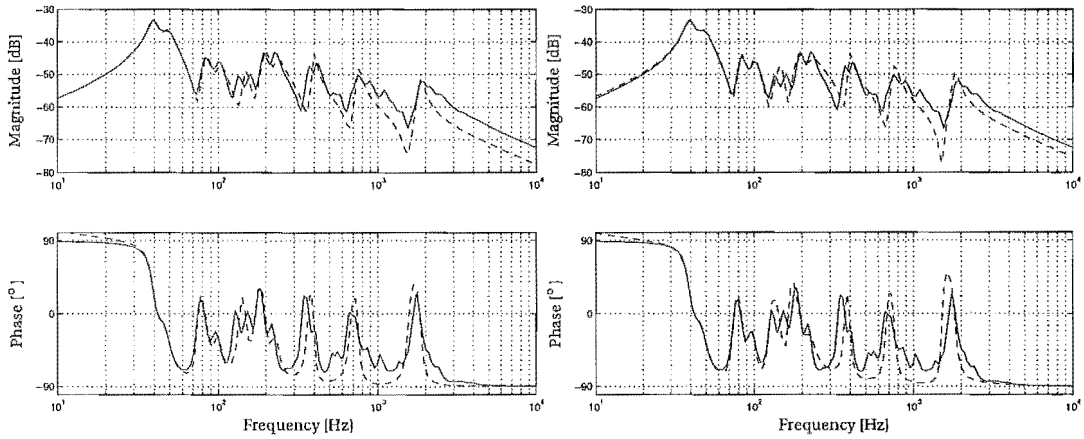

(c) SPA. (d) B&T-RCF.

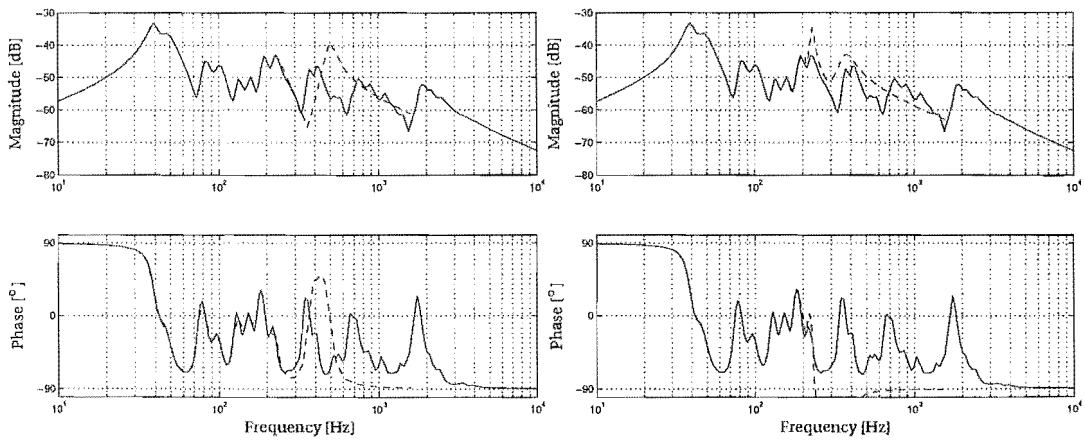

(e) FWB&T $W(s) = \frac{1}{(s^2+2\zeta\omega+\omega^2)^4}\mathbf{I}, \zeta = 0.2, \omega = 2\pi 50$; $V(s) = \mathbf{I}$.

(f) FWB&T $W(s) = \frac{1}{(s^2+2\zeta\omega+\omega^2)^4}\mathbf{I}, \zeta = 0.2, \omega = 2\pi 50$; $V(s) = \frac{1}{(s^2+2\zeta\omega+\omega^2)^4}\mathbf{I}, \zeta = 0.2, \omega = 2\pi 100$.

Figure 5.42: *Bode plots of plants produced by various reduction procedures.* $k_{dm} = 0.05$. — *N=50,* - - *Reduced system.*

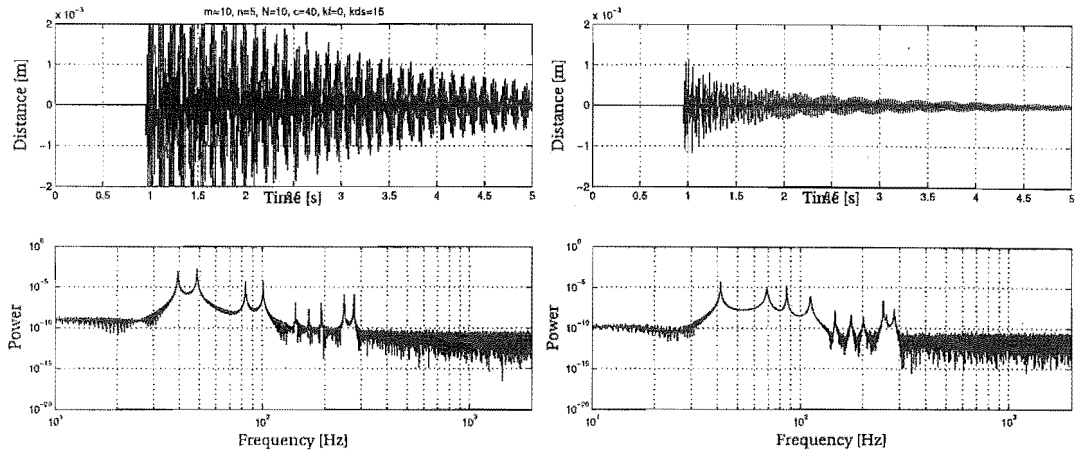

(a) Distributed damping only.

(b) Distributed damping and edge restraint. $k_d = 5\text{N}\cdot\text{s/m}^2$, $k_s = 100\text{kN/m}^2$.

Figure 5.43: *Impulse responses for an idling saw, showing the effect of the restraint of the cutting edge.* $k_{ds} = 15N\cdot s/m^3$ *in each case.* $N_d = 10$.

and $k_s = 100\text{kN/m}^2$). The torsional frequencies are affected most by the increase in lateral stiffness of the cutting edge.

However, even with this added damping low cutting loads destabilise the saw. The final alternative is to consider a model that uses both types of damping; the modal damping to ensure that very high modes are well damped, and the functional damping terms to allow the damping of the lower modes to be directly related to the bandsaw problem. Figure 5.44 shows the root loci for the full order model with the previous values of k_{ds}, k_d and k_s, and $k_{dm} = 0.005$, one tenth of the previous value. Also shown are the loci for the reduced system, where the frequency weighted reduction scheme of Figure 5.42(f) has been used. The root loci are not so well mimicked for the lower modes, essentially because higher modes become more important from an input-output perspective, and with high enough cutting load are destabilised. These unstable modes, although within the cutting range considered, are higher than 300Hz and hence not shown. Both the full and reduced systems are destabilised around k_f =8.8kN/m. Of interest is that because of the lateral stiffness the third mode is not destabilised at all.

Figures 5.45 and 5.46 show the modal forms and the impulse responses for this system. The pinning of the cutting edge is evident in the transverse modes, and is also the reason for the relatively small amplitude of the torsional modes. The impulse responses simply corroborate the initial effect of the follower force, which is to dampen the system. Of interest is the high damping of first two torsional modes by the follower load. This is also seen by their "fast" leftward movement in the complex plane with increasing follower load (Figure 5.44).

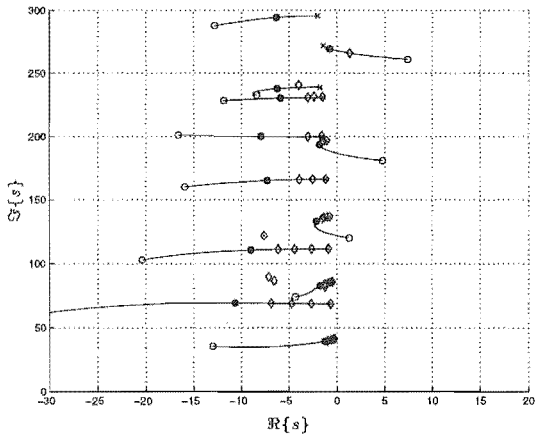

Figure 5.44: *Root loci for complex damping formulation. KEY: — N=50, ⋄ Reduced system.*

It is worth noting that these damping models are only "best guesses", both in terms of the mechanisms and corresponding coefficients. However, the mechanisms do give consideration to the cutting problem, and the coefficients are at least in part derived from experimental behaviour. More work is required to validate experimentally the models presented for each of the three situations considered in Figure 5.46. This is not a minor task, as even if the models can provide accurate damping, the coefficients will vary with saw blades, temperatures, wood species, moisture contents and many other variables.

Actuator and sensor dynamics. The electromagnetic non-contacting actuation and collocated position measurement used in the experimental work is again assumed here. The same simple models for the actuator and sensor are used for each control input and sensed output. The change to position measurement and the increased phase from the sensor and actuator dynamics mean that the plant is no longer passive.

5.7.1.1 Performance of closed-loop single-span system

Consider the control of the single span blade of 5.36 with the new modal damping as well as distributed damping and edge stiffness and damping. The plant is reduced after the sensor and actuator dynamics have been added, and $m = 7$, $n = 5$, $x_s = x_a = \frac{5}{12}\ell$ and $y_s = y_a = 0.8b$. The decrease in number of basis functions in the x-direction is required for numerical stability of the partial cutting formulation. Furthermore, introduce the point $(x_p, y_p) = (0.375\ell, 0.8\ell)$, and let the $\mathbf{C}$ vector mapping the states into the velocity at this point provide the information for the state penalisation in the $\mathcal{H}_2$ formulation. Note that this does not represent a sensor, it is used only in controller synthesis and more will be said about its position in the multispan

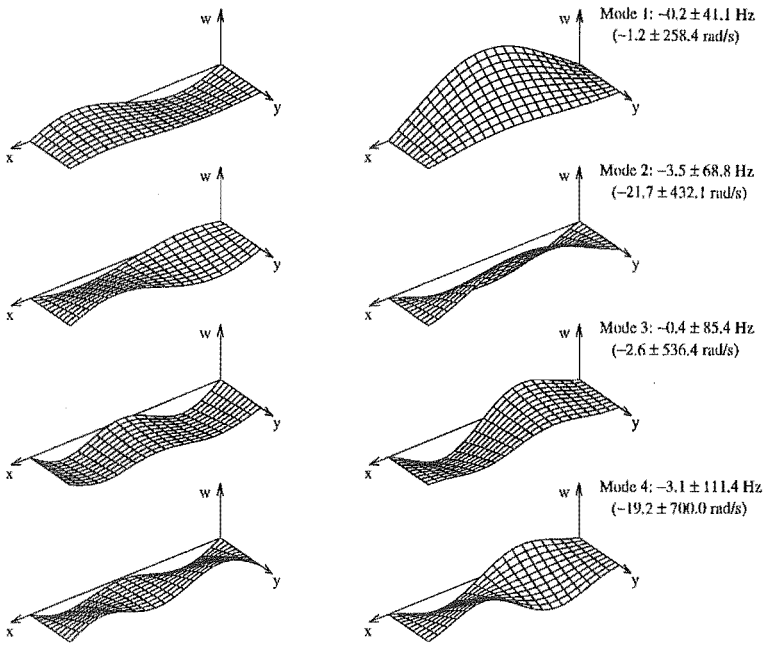

(a) Modes 1 to 4.

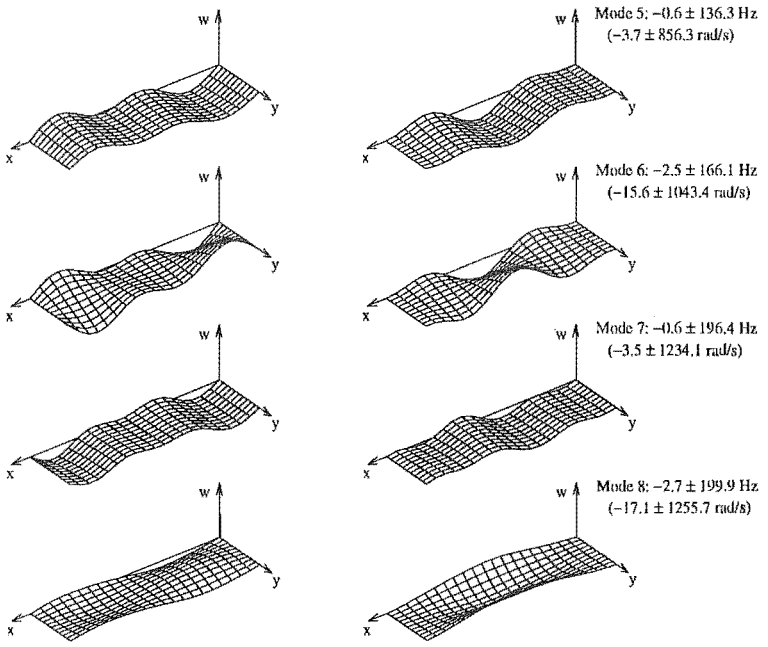

(b) Modes 5 to 8.

Figure 5.45: *Modal forms of complex damping model. "Real" components are on the left and "imaginary" on the right. Full model, $k_f = -7.5 kN/m$.*

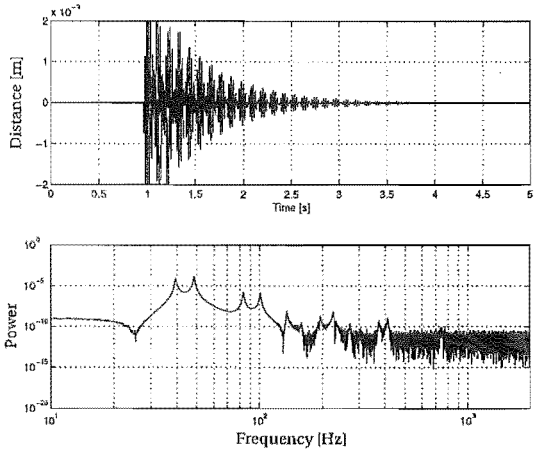

(a) Idling. $k_{dm} = 0.005$, $k_{ds} = 15\text{N}\cdot\text{s/m}^3$, $k_s = k_d = k_f = 0$.

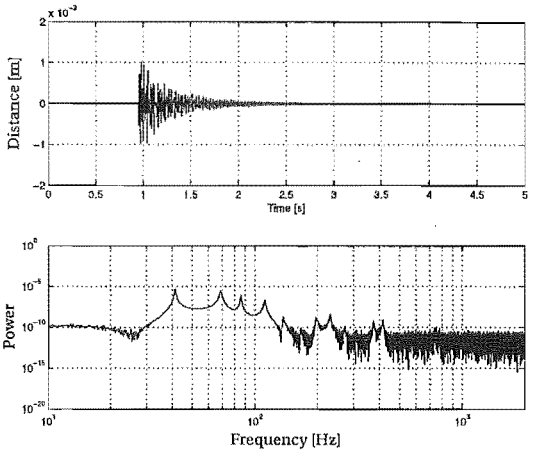

(b) Idling in workpiece. $k_{dm} = 0.005$, $k_{ds} = 15\text{N}\cdot\text{s/m}^3$, $k_s = 100\text{kN/m}^2$, $k_d = 5\text{N}\cdot\text{s/m}^2$, $k_f = 0$.

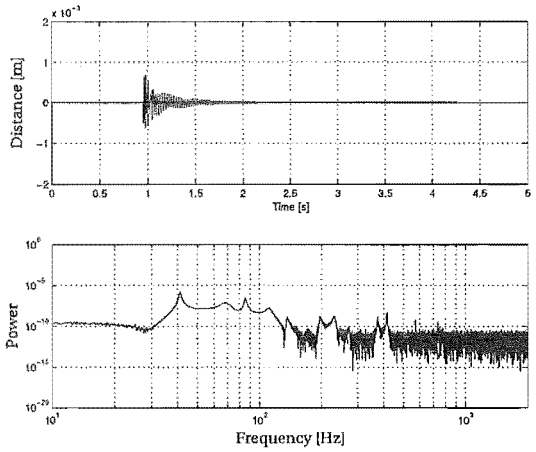

(c) Cutting. $k_{dm} = 0.005$, $k_{ds} = 15\text{N}\cdot\text{s/m}^3$, $k_s = 100\text{kN/m}^2$, $k_d = 5\text{N}\cdot\text{s/m}^2$, $k_f = -7.5\text{kN/m}$.

Figure 5.46: *Idling and cutting impulse responses for complex damping model. Full model.*

case. The $\mathcal{H}_2$ gains used are $R = 2\times10^{-5}$ with $Q_n = 1 \times 10^{-2}$, $R_n = 1 \times 10^{-11}$. The shaping functions in the $\mathcal{H}_\infty$ loop shaping formulation, which does not provide for the performance output, are

$$W_1(s) = 20\times10^3 \frac{s^2 + 2\zeta_1\omega_1 + \omega_1^2}{s^2 + 2\zeta_2\omega_2 + \omega_2^2}$$
$$W_2(s) = \frac{1}{s^2 + 2\zeta_2\omega_2 + \omega_2^2},$$

where $\zeta_1 = 0.4$, $\omega_1 = 2\pi40$, $\zeta_2 = 0.7$, $\omega_2 = 2\pi100$. Table 5.11 lists the $\mathcal{H}_2$ norms of various controlled and uncontrolled impulse responses. The noise and disturbance signals are generated from Q_n and R_n above, and the impulse inputs are all 50N in size and last for 0.006s. The output energy has been halved by each controller for the

Table 5.11: *$\mathcal{H}_2$-norms for impulse responses of single span blade.*

		$\|\|y\|\|_2$ [$\times10^{-3}$]	$\|\|y_p\|\|_2$ [$\times10^{-3}$]	$\|\|u\|\|_2$
Idle	Uncontrolled	0.894	256	0
	Controlled ($\mathcal{H}_2$)	0.349	87.3	8.80
	Controlled ($\mathcal{H}_\infty$)	0.334	106	4.50
Restr. idle	Uncontrolled	0.357	154	0
	Controlled ($\mathcal{H}_2$)	0.150	64.5	4.07
	Controlled ($\mathcal{H}_\infty$)	0.153	75.3	3.23
Distr. cutting	Uncontrolled cutting	0.212	87.5	0
	Controlled cutting ($\mathcal{H}_2$)	0.142	55.9	3.48
	Controlled cutting ($\mathcal{H}_\infty$)	0.145	61.2	2.50
Partial cutting	Uncontrolled partial cutting	0.222	90.8	0
	Controlled partial cutting ($\mathcal{H}_2$)	0.151	59.3	3.14
	Controlled partial cutting ($\mathcal{H}_\infty$)	0.149	60.4	2.60

noncutting systems and reduced by 30% in the cutting situation. These are significant improvements, and will be used to compare those in the multispan situation. Furthermore, the partial cutting model (applied with $s_u = s_l = 0$) produces very similar results to the full length formulation. These results only show the controller in feedback with the nominal (although higher order) analysis plant; the closed-loop robustness with respect to changes in band speed, tension and cutting force have yet to be tested.

Table 5.12 gives the ranges of stability and performance (defined by those outputs not exceeding 150% of the output energy of the nominal synthesis-analysis combination) for the controllers. So while the $\mathcal{H}_2$ controller shows excellent robustness, the $\mathcal{H}_\infty$ does not. No better $\mathcal{H}_\infty$ controller was found, and considering the reliance on the performance output in the multispan case this lack of robustness is not pursued any further here. Both controllers have very similar closed-loop

Table 5.12: *Performance measures and stability margins for single span.*

	Uncontrolled		$\mathcal{H}_2$		$\mathcal{H}_\infty$	
	Performance range	Stability range	Performance range	Stability range	Performance range	Stability range
Speed, c [m/s]	10—†	0—†	0—†	0—†	32—†	32—†
Tension, R_o [kN]	3.75—†	5.0—†	5.25—†	5.25—†	8—16.5	8—16.5
Cutting load k_f	0—6700	0—6350	0—6700	0—6400	0—6700	0—6350

†Reasonable range exceeded.

performance curves.

Figure 5.52 shows the $\mathcal{H}_2$-norms of the performance output with respect to cutting load and tension. Both forms of control have significantly reduced the energy of the blade near the cutting edge, and each, with the exception of the $\mathcal{H}_\infty$ controller in the tension case, have done so over the entire variable ranges considered. The region of poor performance of the $\mathcal{H}_\infty$ controller between 16 and 17kN (shown in the impulsive forcing) tension is unstable. The partial formulation with ten sinusoids in the Fourier expansion gives very similar results to the distributed formulation.

5.7.2 Guides and partial span cutting

Consider now the multispan blade depicted in Figure 5.48. The midspan is the same length as the length of the single span system, and where applicable other variables are unchanged. The stiffness and damping forces on the cutting edge exist along the same length as the cutting load, which is for simplicity assumed to be the entire midspan. Throughout this multispan work k_f relates to the constant cutting load acting along this span (Λ_c was used in the partial cutting formulation in Chapter 3). The performance position ($(x_p, y_p) = (0.5\ell, 0.8b)$) is such that it is in the same position relative to the middle span as in the single span control previously considered.

The problem is tackled in a similar manner to the single span system, whereby the idling, restrained and cutting saws are considered separately. Figure 5.49 compares the singular value plot of the restrained single span system with that of the multispan one, where the performance output and the first disturbance input are used in the singular value analysis. The guide stiffnesses have been artificially tuned to match what are essentially the first and second torsional modes of the middle span (69Hz and 112Hz). The smaller peaks in the multispan case (those at 55Hz and 64Hz are clearest) indicate vibratory forms that are predominantly in the upstream and/or downstream spans.

Figure 5.50 shows the vibratory forms of the first eight modes. The restraint of the guides and workpiece is evident, as is the span wise coupling of some modes.

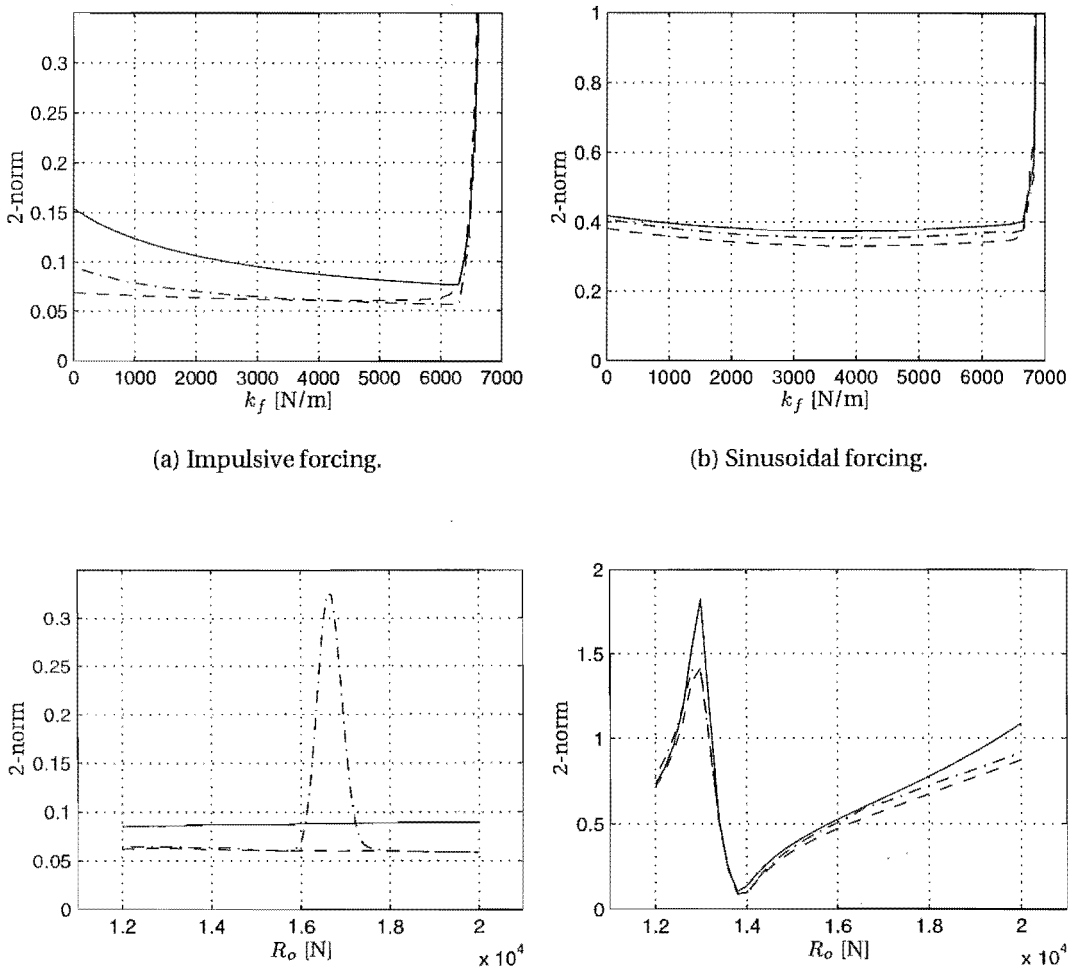

(a) Impulsive forcing.

(b) Sinusoidal forcing.

(c) Impulsive forcing.

(d) Sinusoidal forcing.

Figure 5.47: *$\mathcal{H}_2$-norms of performance output of the single span saw with respect to cutting load and tension. KEY: — Uncontrolled, - - $\mathcal{H}_2$ control, -·- $\mathcal{H}_\infty$ control.*

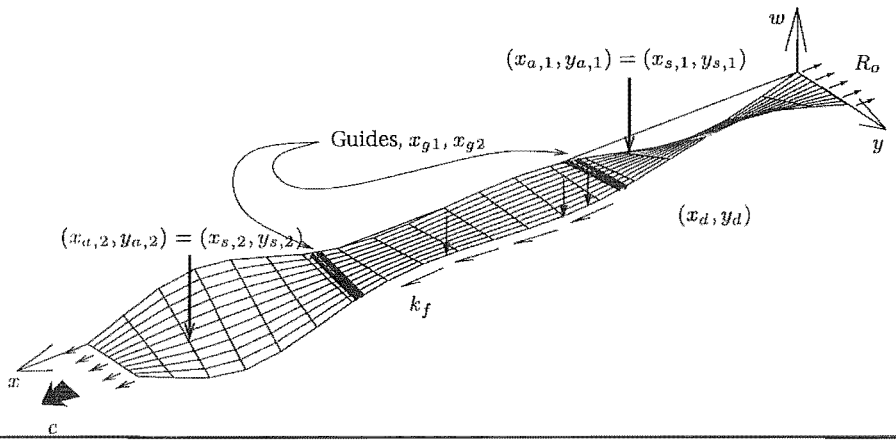

$\ell = 2\text{m}$	$b = 0.22\text{m}^2$	$h = 1.65\text{mm}$	$R_o = 15\text{kN}$	$\rho = 8200\text{kg/m}^3$
$m = 7$	$n = 5$	$N_{d,s} = N_{d,a} = 35$	$dim\{x_{r,s}\} = 15$	$dim\{x_{r,a}\} = 30$
$x_s = x_a = [0.2\ell, 0.8\ell]$	$y_s = y_a = [0.8b, 0.8b]$	$x_d = [0.42\ell, 0.46\ell, 0.64\ell]$	$y_d = [1b, 1b, 1b]$	
$\zeta_{0\alpha} = k_{dm} = 0.05$	$k_{ds} = 15\text{N·s/m}^3$	$k_d = 5\text{N·s/m}^2$	$k_s = 1\times10^5\text{N·s/m}^2$	$k_g = 3\times10^8$
$x_u = 0.35\text{m}$	$x_l = 0.25\text{m}$	$x_{g1} = 0.3\ell$	$x_{g2} = 0.305\ell$	
Guide width= 0.005m		$c = 40\text{m/s}$	$(x_p, y_p) = (0.5\ell, 0.8b)$	

Figure 5.48: *Sketch of multi-span plate model.*

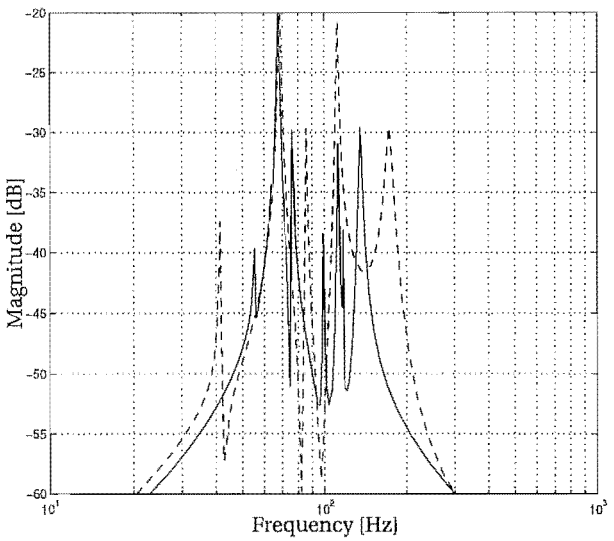

Figure 5.49: *Maximum singular value plots of LQG controller. KEY: — Single span, - - Multispan.*

It is this coupling that is required for any control action applied in the upstream or downstream span to affect the middle one. For completeness the stress state caused by the tangential part of the follower load is shown in Figure 5.51. Ten sinusoids were used in the approximation.

Both the modal forms and the singular value plot indicate that the simple guide formulation is effective in modelling the middle span as well as the upper and lower ones; it remains now to consider the control via these spans. Table 5.13 shows results for a number of tests using $\mathcal{H}_2$ control (R, R_n, Q_n are unchanged). The $\mathcal{H}_2$-norms of the sensed outputs as well as the performance output are performance indicators. Considering the idling situation, the upstream control gives little improvement but the downstream gives good attenuation. Both dislocated controllers give reasonable improvement however the MIMO control is comparatively poor. This is somewhat remedied in the restrained case where the MIMO control gives slightly better attenuation than the downstream control alone, which is in turn significantly better than all other combinations. When the cutting load is introduced the upstream and MIMO controllers destabilise the closed loop via spillover, and the downstream controller produces the best attenuation.

Table 5.13: *$\mathcal{H}_2$-norms of impulse responses for $\mathcal{H}_2$ controlled multispan blade.*

		$\|\|y_u\|\|_2$ [$\times 10^{-3}$]	$\|\|y_d\|\|_2$ [$\times 10^{-3}$]	$\|\|y_p\|\|_2$ [$\times 10^{-3}$]	$\|\|u_u\|\|_2$	$\|\|u_d\|\|_2$
Idle	Uncontrolled	0.175	0.163	294	0	0
	Upstream control	0.084	-	276	3.69	-
	Downstream control	-	0.155	186	-	13.62
	Upstream sen, downstream act.	0.149	-	227	-	15.3
	Downstream sen, upstream act.	-	0.129	213	7.2	-
	Both. MIMO control	0.189	0.115	252	4.34	2.93
Restr. idle	Uncontrolled	0.092	0.180	160	0	0
	Upstream control	0.049	-	153	1.99	-
	Downstream control	-	0.097	116	-	4.56
	Upstream sen, downstream act.	0.139	-	141	-	3.71
	Downstream sen, upstream act.	-	0.156	132	6.91	-
	Both. MIMO control	0.066	0.085	115	3.46	3.45
Cutting	Uncontrolled	0.065	0.108	100	0	0
	Upstream control	0.207†	-	99†	2.01†	-
	Downstream control	-	0.085	94	-	1.72
	Upstream sen, downstream act.	0.062	-	98	-	1.06
	Downstream sen, upstream act.	-	0.103	98	1.84	-
	Both. MIMO control	1.50†	0.183†	124†	11.4†	11.8†

† Destabilised by spillover.

Table 5.14 shows the corresponding results for the $\mathcal{H}_\infty$ controller. In the idling situation the MIMO controller produces mediocre attenuation while the rest perform very poorly. The downstream control introduces spillover. The situation for

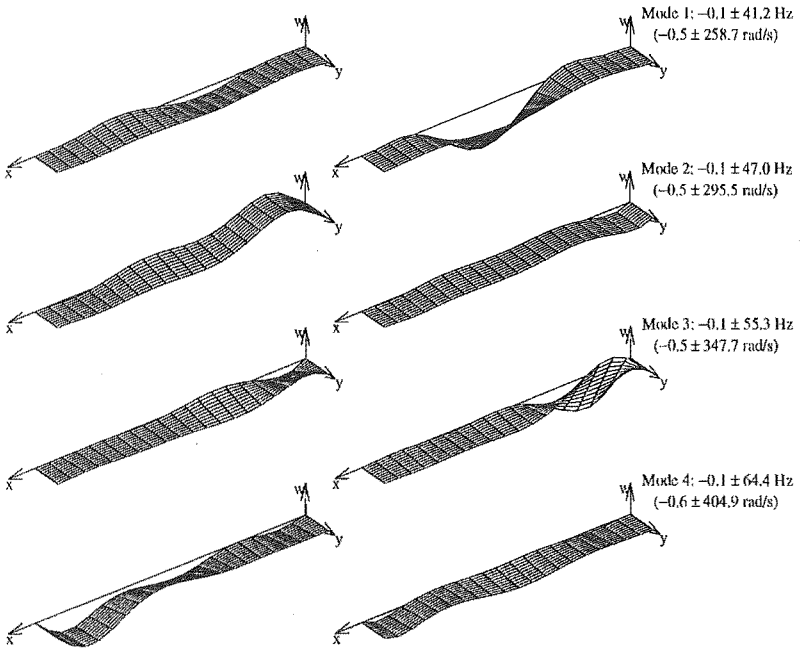

(a) Modes 1 to 4.

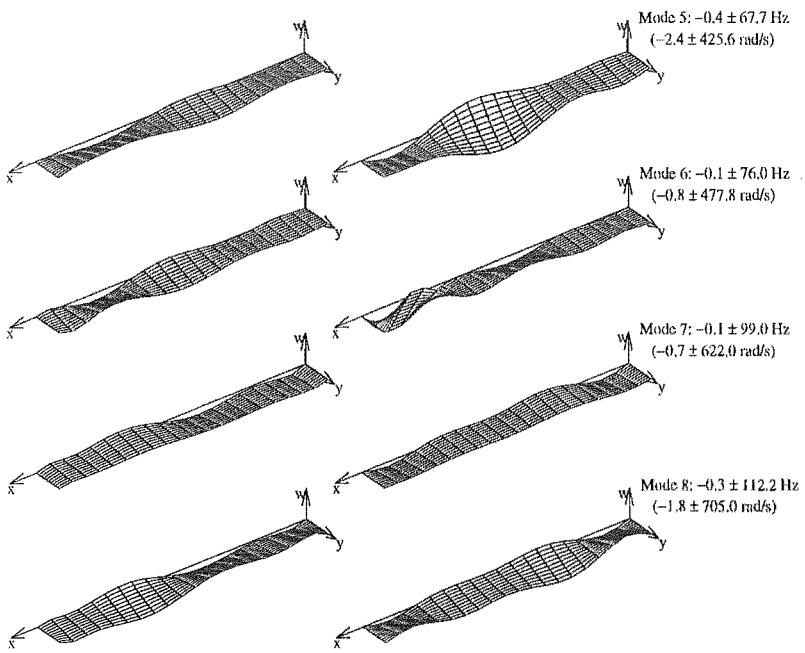

(b) Modes 5 to 8.

Figure 5.50: *Modal forms of restrained but noncutting multispan system. "Real" components are on the left and "imaginary" on the right, and no model reduction has been applied.*

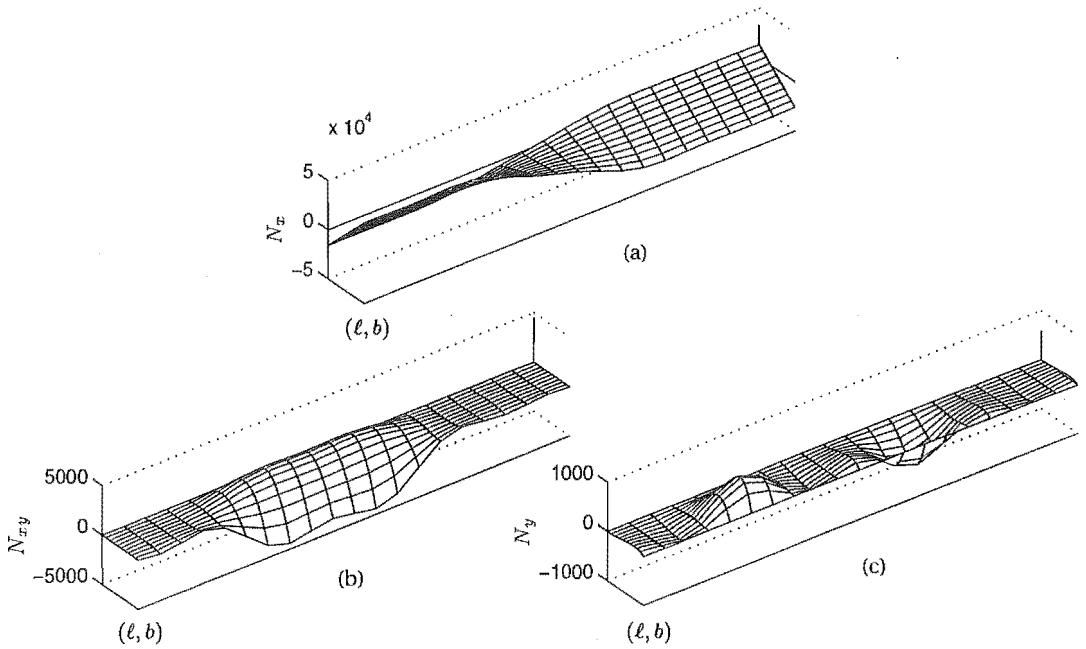

Figure 5.51: *Stress state of multispan blade.*

the restrained case is similar, but the MIMO controller also performs poorly. For the cutting situation the downstream controller is again unstable and all but the MIMO controllers perform poorly.

The spillover noted in the $\mathcal{H}_2$ control may be remedied by moving the upstream actuator toward the trailing edge of the blade. If $y_{s,1} = y_{a,1} = 0.2b$m then the results are as shown in Table 5.15. However, while spillover is avoided (in the $\mathcal{H}_\infty$ case too) the reduction in energy of the middle span is minimal. This is essentially because of the small coupling between the spans.

Figure 5.52 shows the $\mathcal{H}_2$-norms of the performance output with respect to parametric variations in the analysis plant. These variations are cutting load, band tension and the position of the upstream guide (the cutting span remains unchanged). Considering the $\mathcal{H}_2$ control, there is very little attenuation for the impulsively forced system as cutting load increases, however there is a substantial increase in the stablility limit. The sinusoidal response is more markedly reduced and the stability increase remains. The $\mathcal{H}_\infty$ controller does not increase the maximum cutting load as much, but is otherwise similar. Considering the impulsively forced tension variation results, the $\mathcal{H}_2$ controller destabilises low tension plants, and makes a very slight improvement otherwise. The $\mathcal{H}_\infty$ controller also destablises high tension plants. For the sinusoidally forced system both controllers attenuate the response of lower tension plants (even though instability occurs) but degrade the response of higher tension plants. Changes in the upper guide position in the analysis plant do not cause

Table 5.14: *$\mathcal{H}_2$-norms of impulse responses for $\mathcal{H}_\infty$ controlled multispan blade.*

		$\|\|y_u\|\|_2$ [$\times 10^{-3}$]	$\|\|y_d\|\|_2$ [$\times 10^{-3}$]	$\|\|y_p\|\|_2$ [$\times 10^{-3}$]	$\|\|u_u\|\|_2$	$\|\|u_d\|\|_2$
Idle	Uncontrolled	0.175	0.163	294	0	0
	Upstream control	0.152	-	278	2.30	-
	Downstream control	-	0.188†	283†	-	4.65†
	Upstream sen, downstream act.	0.176	-	294	-	0.126
	Downstream sen, upstream act.	-	0.165	294	1.03	-
	Both. MIMO control	0.159	0.168	270	3.14	3.19
Restr. idle	Uncontrolled	0.092	0.180	160	0	0
	Upstream control	0.046	-	156	0.96	-
	Downstream control	-	0.139	158	-	2.64
	Upstream sen, downstream act.	0.092	-	158	-	0.229
	Downstream sen, upstream act.	-	0.177	160	0.66	-
	Both. MIMO control	0.045	0.137	156	0.98	2.50
Cutting	Uncontrolled	0.065	0.108	100	0	0
	Upstream control	0.052	-	99	0.69	-
	Downstream control	-	0.099†	116†	-	2.74†
	Upstream sen, downstream act.	0.064	-	99	-	0.24
	Downstream sen, upstream act.	-	0.108	99	0.24	-
	Both. MIMO control	0.063	0.085	96	0.56	2.44

† Destabilised by spillover.

Table 5.15: *$\mathcal{H}_2$-norms of impulse responses for $\mathcal{H}_2$ and $\mathcal{H}_\infty$ controlled multispan blade, where the upstream actuator-sensor has been moved to the trailing edge.*

		$\|\|y_u\|\|_2$ [$\times 10^{-3}$]	$\|\|y_d\|\|_2$ [$\times 10^{-3}$]	$\|\|y_p\|\|_2$ [$\times 10^{-3}$]	$\|\|u_u\|\|_2$	$\|\|u_d\|\|_2$
Cutting $\mathcal{H}_2$ control	Uncontrolled	0.075	0.108	100	0	0
	Upstream control	0.043	-	99	0.565	-
	Downstream control	-	0.085	94	-	1.72
	Upstream sen, downstream act.	0.075	-	98	-	0.53
	Downstream sen, upstream act.	-	0.106	97	1.82	-
	Both. MIMO control	0.043	0.092	98	0.88	0.89
Cutting $\mathcal{H}_\infty$ control	Uncontrolled	0.075	0.108	100	0	0
	Upstream control	0.035	-	100	0.703	-
	Downstream control	-	0.099†	116†	-	2.74†
	Upstream sen, downstream act.	0.074	-	99	-	0.13
	Downstream sen, upstream act.	-	0.108	99	0.23	-
	Both. MIMO control	0.037	0.090	97	0.64	1.55

† Destabilised by spillover.

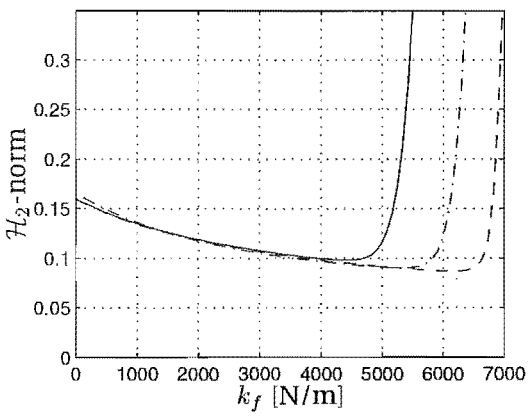

(a) Impulsive forcing.

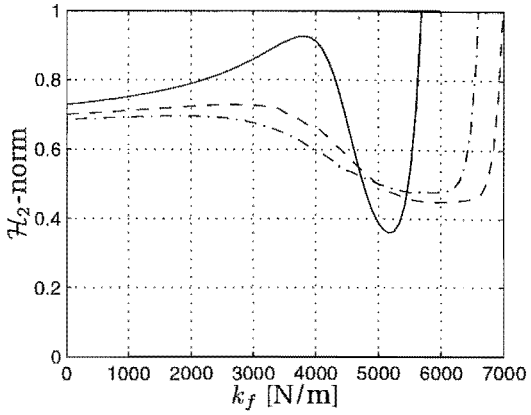

(b) Sinusoidal forcing.

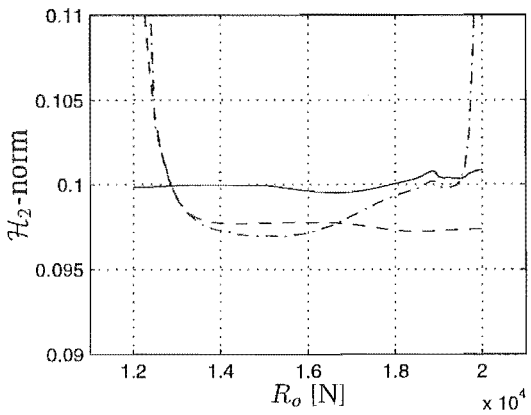

(c) Impulsive forcing.

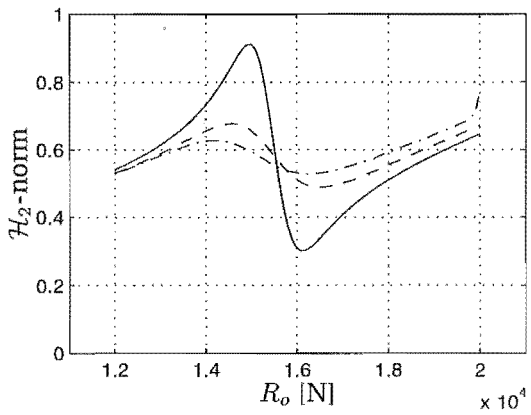

(d) Sinusoidal forcing.

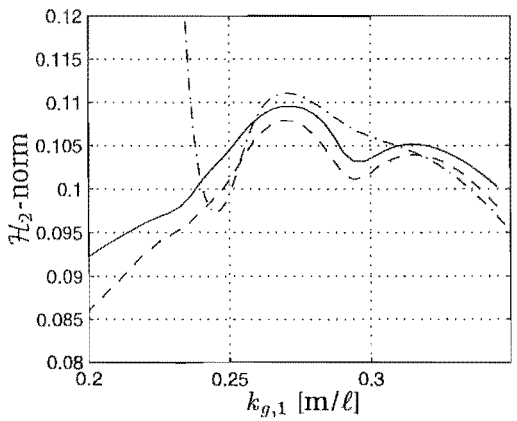

(e) Impulsive forcing.

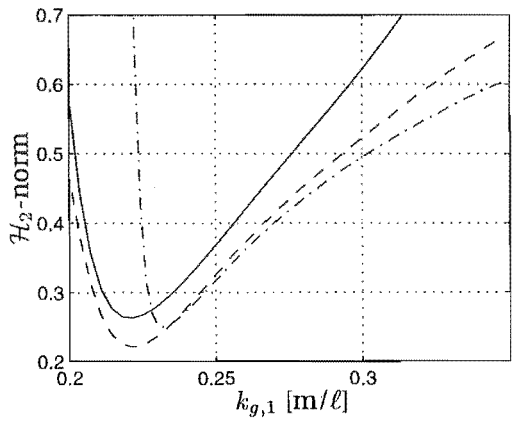

(f) Sinusoidal forcing.

Figure 5.52: *$\mathcal{H}_2$-norms of performance output for the multispan saw with respsect to cutting load and tension. KEY: — Uncontrolled, - - $\mathcal{H}_2$ control, -·- $\mathcal{H}_\infty$ control.*

destabilisation in the $\mathcal{H}_2$ case, in fact reasonable attenuation is achieved for both forced repsonses. The $\mathcal{H}_\infty$ case however destabilises the system as the guide position approaches the sensor-actuator position.

5.8 CONCLUSION

5.8.1 Robustness studies

The agreement between theory and practice for the experimental work was by and large excellent. Although the band speed of the experimental rig was limited, the agreement in trends gives confidence in the high speed theoretical results. With respect to variations in band speed the near optimal $\mathcal{H}_\infty$ controller was found to have superior robust stability and performance. Tension variation was a more difficult problem, but the range considered was large and the variation coarse. The low gain $\mathcal{H}_2$ controller performed marginally better than the others tested. The fixed band wheel problem lacked a physical model with which to compare, due to the limitation of the current rig. Given the increase in importance of nonlinearities at high bandspeed this work is considered preparatory only. The theoretical robustness study of the plate showed similar trends to the beam, but was inherently more stable.

The collocated actuator-sensor worked very well throughout this work, and the same dynamics used in the beam experiments were also used in the plate case studies.

5.8.2 Case study

Single span blade. The controllers formulated in this chapter compared favourably with those of Damaren and Le-Ngoc (2000). However, the damping proposed by them was considered unreasonably high and was therefore replaced by the models presented in Chapter 3. While these damping models embody the bandsaw dynamics, the coefficients of each component will change with sawblades and timber types. Both $\mathcal{H}_2$ and $\mathcal{H}_\infty$ loop shaping controllers were applied with substantial attenuation improvement over the uncontrolled systems. Idling, restrained and cutting systems were all considered. The $\mathcal{H}_2$ controller provided excellent robust stability and performance; with the $\mathcal{H}_\infty$ controller less successful. While work is not comprehensive enough for the relative robustness of each controller to hold for other blade geometries, it does indicate the level of robustness that is possible with such control.

Multispan blade. Tuning the guide stiffnesses allowed accurate modelling of the single span system by the multispan formulation, and even with a limit on the numbers of basis functions the partial cutting formulation gave credible results.

Control of the multispan system did not provide the substantial attenuation of the single span results, essentially because of the weak coupling of the three spans as a results of the actions of the guides. However, the $\mathcal{H}_2$ controller again provided excellent robust performance, including increasing the maximum cutting load by approximately 30%. The $\mathcal{H}_\infty$ controller also increased this load, by around 20%. The $\mathcal{H}_2$ controller also maintained robust performance over large ranges of analysis plant band tension and upper guide position, two highly variable parameters in the sawmilling process. The $\mathcal{H}_\infty$ loop shaping controller was less robust, but this could be remedied by considering the full four-block problem in the $\mathcal{H}_\infty$ setting.

This case study was only a case study, but the results were encouraging and warrant further exploration. A full working model is required for this, and will be considered in future work. Also, the continued successful use of the real actuator and sensor dynamics for the large wide bandsaw bodes well for successful implementation of such actuation.

Damping. Accurately modelling the damping of the cutting blade is fraught with difficulty. Not only is it a complex system, but the fact that the damping plays such an important role in stability means it is crucial to get correct. The models presented in this work allow a great deal of freedom, while remaining in the linear domain. Again, work with real wide bandsaws is required to establish accurately a good model of the system damping. Also, controller robustness with respect to varying levels and types of damping is worthy of investigation.

Miscellany. Initial work suggests that removing the top guide and replacing it with the pointwise actuator-sensor pair can improve performance more markedly than actuating the upper span in conjunction with the top guide. The present model allows for the analysis of such a system, but without corroborating the work so far with real world saws it is unreasonable to pursue this further.

Chapter 6

CONCLUSION

6.1 DISCUSSION AND CONCLUSIONS

6.1.1 Dynamical modelling

The work on moving strings and beams applied a Ritz discretisation to the system energies and non-conservative work, and via Hamilton's principle found the linear set of governing equations. Both sinusoids and polynomials were considered in the discretisation, with sinusoids shown to offer no advantage in terms of accuracy for externally forced axially moving continua.

The application of point and distributed follower forces as well as damping and stiffness terms served to combine and extend the knowledge of the linear modelling of simply supported axially moving strings and beams. Pointwise sensing was also considered in anticipation of the control work and the system cast in a first order state space form. Where applicable, the author's results were shown to compare accuratley with other contributors. Further, the components of the distributed follower force were subjected to the tensioned and untensioned stationary beam, with the in-line component shown to dominate the behaviour in the tensioned case.

The wide single-span cutting bandsaw blade was formulated after Ulsoy and Mote (1982) and Lengoc and McCallion (1995a), and employed the method of Ritz with the polynomial describing functions used in the string and beam work. This method was used to model a multispan blade, which is the major contribution of the modelling component of this work. The blade was modelled as a central cutting span with upstream and downstream noncutting spans. The spans were separated by guides that were modelled using two different methods; a spring-like formulation and a singular value decomposition method. The spring-like method was chosen as the superior method, as it produced a more "tunable" solution that does not affect the solution space to the degree of the singular value method. Inplane cutting and feed forces were applied to a portion of the central span by the superposition of the components of a Fourier series of inplane loads. The lateral component of the cutting load as well as damping and spring forces were also applied over the same por-

tion of the blade length. The full span cutting method used by Lengoc and McCallion (1995a) was modelled and successfully compared, with the aim of testing the partial span formulation. However, the boundary conditions imposed by the two methods are different, making accurate comparisons very difficult. This does not serve to qualify either of the solutions ahead of the other; but it does warrant the investigation of which method prescribes the more realistic set of boundary conditions. Both methods give credible results but each require experimental corroboration. Also, the recursive integration underpinning the solution of the partial span formulation rely heavily on the orthonormality of the basis functions. Attempts were made to improve the quality of these functions, however there still existed a defined limit to the number of basis functions that could successfully be used.

The interaction of the downstream blade tension with cutting load was shown to markedly affect the blade dynamics. A variable with resemblance to the tension mechanism variable was added to allow for "tuning" this effect to different bandmill arrangements.

6.1.2 Experimental apparatus

The simple collocated sensor-actuator and current driver were shown to provide excellent model validation data as well as control of the moving beam and plate. Using a linearisation of the force-current-distance relationship that accounted for the saturation of the blade material provided more accurate results than an unsaturated method. The string, beam and plate models matched the practical rig excellently, with the exception of the torsional modes and nearby zeros of the plate.

The rig itself was very useful in the model verification and control work, with the exception of the fixed wheel system. A lack of stiffness in the top wheel assembly was the cause of this.

6.1.3 Control

Beam work. High frequency noise sensitivity and spillover caused classical controllers to be abandoned in lieu of model-based optimal $\mathcal{H}_2$ and $\mathcal{H}_\infty$ loop shaping designs. Comprehensive experimental and theoretical robustness studies of the translating beam produced the following results:

- Good agreement between theory and experiment, as long as normalised data was used. This agreement, both in trends and often absolute values, substantiated the accuracy and usefulness of theoretical simulations in controller design. The effects removed by the normalisation should be researched and considered in future simulations.

- Robustness with respect to variation in translation speed was considered good, with a $\mathcal{H}_\infty$ controller giving the best mix of robust performance and stability. Robustness with respect to tension was a more difficult problem from a robust stability point of view, but the range considered was large, and the steps in tension coarse.

- One recurring discrepancy between simulation and practice was the way the simulations often predicted unstable closed loops where the practical output was stable. This may be caused by incorrect damping in the model or by excessive differences between the theoretical synthesis and analysis plants (the number of basis functions used to describe each).

Single span control. To corroborate the modelling and control, a $\mathcal{H}_2$ formulation was compared with other contributors. Then, with the same blade geometry but different exogenous influences both $\mathcal{H}_2$ and $\mathcal{H}_\infty$ loop shaping controllers were formulated for the idling, restrained and cutting systems. The cutting system was tested with respect to variations in bandmill tension and cutting force. Substantial vibration suppression was achieved as well as good robust stability and performance. However, only small improvements in parametric stability ranges were possible.

Multispan system. $\mathcal{H}_2$ and $\mathcal{H}_\infty$ controllers were formulated for the idling, restrained and cutting multispan blade, using upstream and downstream control. The guide stiffnesses were tuned so that the central span had similar uncontrolled dynamics to the single span system. The cutting system was again tested with respect to variations in bandmill tension and cutting force, and with the upstream guide position. Excellent robust stability was achievable, and the maximum allowable cutting load was increased by the feedback control. However, the decoupling of the spans via the guides limited the amount of energy transferred to the centre span, and therefore the possible improvement in vibration attenuation.

6.2 FUTURE WORK

Further practical corroboration. The simple rig was useful in assessing the accuracies and inaccuracies of the models. In order to validate the more complicated multispan system a proper cutting bandmill is required. The points of main interest are:

- Damping coefficients. Both the cutting edge and distributed damping coefficients are unknown, and are crucial to closed-loop stability. While these will undoubtedly change with process variations, ball park figures at least are required.

- Stiffness coefficients. The cutting edge and guide stiffnesses.
- Cutting loads. Some work has been done on this, but detailed data is hard to find. This is largely due to expensive experimental requirements and the high variability of the problem. Also, whether the follower load is actually a reasonable model of the cutting process has not been established. Feed load sizes are also required, as even though they are often lower than the cutting loads, badly doctored saws and high feed rates can increase feed forces considerably.
- Interspan coupling. This directly affects the feasibility of controlling the central span via the upstream and downstream ones.

Treating the feed force as a follower load warrants investigation. The importance of this relies on the aforementioned size of the feed force, but is quite simple to model. The work on the change in band strain at the upstream boundary as cutting load increases also requires experimental corroboration, as this markedly affects the theoretical dynamics.

The orthonormality of the describing polynomials in the Ritz expansion has been cited as a limiting factor in the accuracy of this multispan work. It is essentially a numerical issue, caused primarily by the large coefficients of high order normalised polynomials, and exacerbated by the partial span formulation. The numerics of the Gram-Schmidt procedure and the partial span formulation need to be improved to allow more accurate modelling. Alternatively, discretising the plate deflection using the Finite Element method may be an appropriate remedy to this problem.

Guide replacement. Replacing the conventional guides with active, noncontacting electromagnetic actuators is perhaps the holy grail of this work. Instead of each guide, it is imagined that two sensor-actuator pairs are used. With one on either side of the centre-width of the blade both torsional and transverse blade actuation is possible. Such electromagnets would need to be capable of applying large forces, and would result in relatively low bandwidth. It is envisioned that these could control snipe, snake and wedging of the cutting process, while low force, high bandwidth actuators in the noncutting spans may reduce high frequency oscillations and effects such as wash-boarding.

Sensor-actuator development. A higher bandwidth actuator with a smaller face area is required for reducing high frequency blade vibrations. Also, to realise the envisioned future of the previous paragraph, the development of other, high force, low bandwidth actuators is also required.

Appendix A

NOMENCLATURE

The more commonly used symbols used throughout this work are shown below. Often subscripts are added to symbols to more accurately define their meaning.

A	Cross-sectional area of string/beam
A_c	Amplitude of sinusiodal component of partial cutting load
b	Width of bandsaw blade
c	Translational band speed
c^*	Non-dimensional translational band speed, ($c^* = c/((R_o\ell b + D)/(\rho\ell b))$)
c_{cr}	Critical translational speed, defined by $c^* = 1$
D	Plate rigidity ($D = Eh^3/12(1-\nu^2)$)
E	Young's modulus
f_x	In-line loads on string/beam
f_w	Lateral loads on string/beam
$G(s)$	Matrix of transfer functions, or state space equivalent. The letter G usually describes the plant.
h	Plate thickness
$H(t-t_o)$	Heaviside function acting at $t = t_o$
i	Summation variable, or used as a subscipt to denote the i'th variable in Fourier series
I	Number of sinusoids in partial cutting formulation
$\Im\{\cdot\}$	Imaginary part of bracketed term.
k_d	Point wise or distributed lateral damping coefficient
k_ds	Distributed lateral damping coefficient (always acts along full length ℓ
k_s	Point wise or distributed lateral stiffness
k_f	Point wise or distributed follower load
k_g	Guide stiffness (restitutive pressure)
k_m	Point wise or distributed added mass
$K(s)$	Controller (state space or transfer function)
ℓ	Plate length

n Number of basis functions used in y-direction of plate.

N_a Number of retained modes after modal truncation.

N_x Force intensity acting on the middle plane of the plate in the x-direction

N_{xy} Shearing force intensity acting on the middle plane of the plate in the xy-plane

N_y Force intensity acting on the middle plane of the plate in the y-direction

p Tooth pitch

$q_{\alpha\beta}(t)$ The $\alpha\beta$'th function of time in the Ritz discretisation

Rx Band tension as a function of length of string or beam

R_o Nominal band tension for strings and beams (N) or the force per unit length acting in the middlewidth of a plate

R_b Difference between force per unit length at middlewidth and that existing at the leading and trailing edges.

$\Re\{\cdot\}$ Real part of bracketed term.

s_u Length of the span between the workpiece and the upper (upstream) guide or wheel

s_l Length of the span between the workpiece and the lower (downstream) guide or wheel

$\mathcal{T}$ Kinetic energy

$\mathcal{V}_b$ Strain energy due to bending

$\mathcal{V}_s$ Strain energy due to inplane loading

w Deflection

x Co-ordinate spanning $0 \leq x \leq \ell < \infty$

x^* Non-dimensional measure of x ($x* = x/\ell$)

(x_s, y_s) Sensor location

(x_a, y_a) Actuator location

(x_d, y_d) Disturbance location

y Co-ordinate spanning $0 \leq y \leq b < \infty$

y^* Non-dimensional measure of y ($y* = y/b$)

$\mathbf{A}$	State space plant matrix
$\mathbf{B}$	State space input matrix
$\mathbf{C}$	State space output matrix
$\mathbf{d}(t)$	State distubance signal vector
$\mathbf{D}$	State space constant gain matrix
$\mathbf{E}$	Modal transition matrix
$\mathbf{F}$	State feedback control matrix
$\mathbf{G}$	Gyric matrix
$\mathbf{D}$	State space constant gain matrix
$\mathbf{K}$	Stiffness matrix
$\mathbf{L}$	Observer matrix
$\mathbf{M}$	Mass matrix
$\mathbf{P}$	Controllability matrix
$\mathbf{Q}$	Observability matrix
$\mathbf{q}(t)$	$col_\alpha\{col_\beta\{q_{\alpha\beta}(t)\}\}$
$\mathbf{u}(t)$	Control force vector
$\mathbf{v}(t)$	Sensor noise signal vector
$\mathbf{x}$	State space state vector
$\tilde{\mathbf{x}}$	State space estimated state vector
δ_{ij}	Kronecker delta
$\overline{\delta}(x-x_o)$	Delta function acting at x_o
$\delta_{\{\cdot\}}$	Variational operator
η	Strain mechanism variable
η_i	i'th modal coordinate
$\boldsymbol{\eta}$	Modal coordinate vector
ι	Driving motor variable
Λ_c	Constant value of cutting load within workpiece
ν	Poissons ratio
ω_α	Vibration frequency (rad/s) of the αth mode
ω_α^*	Non-dimensional vibration frequency of the αth mode ($\omega_\alpha^* = \omega_\alpha \ell^2 (\rho/D)^{\frac{1}{2}}$)
$\phi_\alpha(x)$	α'th basis function in x-direction
$\psi_i(y)$	i'th basis function in y-direction
$\Phi(x,y)$	Airy stress function throughout plate
$\Phi_c(x,y), \Phi_f(x,y)$	Airy stress functions for cutting and feed forces respectively
ρ	Mass per unit length for strings and beams, and per unit area for plate

Appendix B

EXPERIMENTAL CALIBRATION AND DEVELOPMENT

B.1 CALIBRATION OF ELECTROMAGNETS

The following is a description of the static and dynamic calibration of the electromagnets described in Chapter 4. Effects such as saturation of the blade are accounted for and shown to improve markedly the correlation between theory and practice.

Static characteristics

Figure B.1(a) sketches the magnetic circuit associated with an electromagnet attracting a steel bar, and Figure B.1(b) shows the electrical analog of the magnetic circuit, but with magnetic quantities replacing their electrical counterparts. The *magnetomotive force*, $\mathfrak{F}$, drives flux around the circuit according to $\mathfrak{F} = \phi\mathfrak{R}$, $\mathfrak{R}$ being the combined *reluctance* of the circuit. Considering this relation, magnetomotive force is analogous to the electromotive force or applied voltage in an electrical circuit, and reluctance and flux are analogous to resistance and current respectively. The mag-

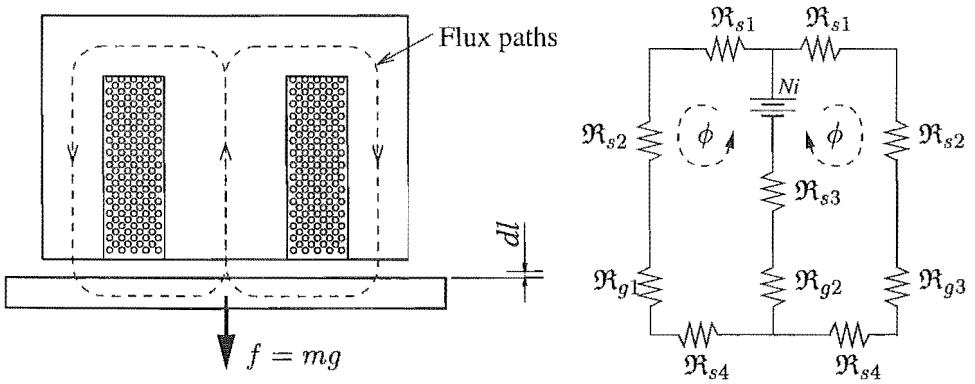

(a) Magnetic circuit.

(b) Electric analog.

Figure B.1: *Static analysis.*

netomotive force is the product of the number of turns in the coil, N, and the current flowing through it, i. The reluctance of a component in the circuit is given by $\Re = \frac{\ell}{\mu A}$, where ℓ is the length of the component, μ $(= \mu_o \mu_r)$ the permeability of the material and A the cross-sectional area. Assuming that no fringing of the magnetic field occurs and that there are no mechanical losses, eddy current losses or hysteresis effects, we can say that for a virtual displacement dl of the suspended bar, the system energy is increased by the electrical energy input $(i^2 R dt)$ and the potential energy gained from the mass being lifted, $(mgdl = fdl)$, and that it is decreased by electrical losses $(i^2 R dt)$ and magnetic losses caused by the reduction of the air gap (of the form $\sum_k \frac{1}{2}\frac{B_k^2 A_k}{\mu_o} dl$, where B_k is the flux density across the k'th air gap, and A_k is the cross sectional area of that gap). Summing these energies gives the energy balance for the system,

$$i^2 R dt + f dl - i^2 R dt - \tfrac{1}{2}\frac{B_{g,1} A_{g,1}}{\mu_0} dl - \tfrac{1}{2}\frac{B_{g,2} A_{g,2}}{\mu_0} dl - \tfrac{1}{2}\frac{B_{g,3} A_{g,3}}{\mu_0} dl = 0$$

which may be reduced to

$$\begin{aligned} f &= \tfrac{1}{2}\frac{B_{g1}^2 A_{g1}}{\mu_0} + \tfrac{1}{2}\frac{B_{g2}^2 A_{g2}}{\mu_0} + \tfrac{1}{2}\frac{B_{g3}^2 A_{g3}}{\mu_0} \\ &= \tfrac{1}{2}\frac{\phi_{g1}^2}{\mu_0 A_{g1}} + \tfrac{1}{2}\frac{\phi_{g2}^2}{\mu_0 A_{g2}} + \tfrac{1}{2}\frac{\phi_{g3}^2}{\mu_0 A_{g3}}. \end{aligned} \tag{B.1}$$

Considering the symmetry of Figure B.1, this equation may be written as

$$f = \frac{\phi^2}{\mu_o A_{g,1}} + 2\frac{\phi^2}{\mu_o A_{g,2}}, \tag{B.2}$$

as $\phi_{g1} = \frac{1}{2}\phi_{g2} = \phi_{g3} = \phi$ and $A_{g,1} = A_{g,2}$. Simple circuit analysis reduces the circuit in Figure B.1(b) to a single loop with a flux equal to 2ϕ. If the reluctances of the core paths and the target are assumed to be negligible in comparison with the air gaps, then the magnetic flux around each loop of Figure B.1(a) is given by

$$\begin{aligned} \phi &= \frac{Ni}{\Re_{g1} + \Re_{g2}} \\ &= \frac{\mu_0 Ni}{d\left(\frac{1}{A_{g1}} + \frac{2}{A_{g2}}\right)} \\ &= \frac{\mu_0 Ni A_{g1} A_{g,2}}{d\left(A_{g,2} + 2A_{g,1}\right)}, \end{aligned} \tag{B.3}$$

which upon substitution into (B.2) yields

$$f = \frac{\mu_o N^2 A_s A_c}{(A_c + 2A_s)}\left(\frac{i}{d}\right)^2. \tag{B.4}$$

To verify (B.4) the setup sketched in Figure B.2 may be used to measure the force produced by the electromagnet at different current levels and distances. The current is controlled via a current drive which converts a PWM signal into winding current, (see Section B.3). Figure B.3 compares these results with those theorised by (B.4), for six gap distances. The results show reasonable agreement between theory and practice, although at high field strength and small distances the agreement deteriorates. This may be due to fringing or saturation effects, or erroneous force measurement. While the load cell is operating within its linear working range, it is sensitive to side loading and torques, which occur when the target block is not parallel to the magnet face. At high currents and low gap distances any initial incongruence is increased, exacerbating the off-axis load and hence the errors in the force measurement.

The actuator bandwidth may be found by sinusoidally driving the winding current throughout a range of frequencies, and comparing the input function with the measured force. Figure B.4 shows such curves at 15Hz and 100Hz. For a linear system the output corresponding to a sinusoid is an amplified and phase shifted sinusoid of the same frequency. However, considering the output in Figure B.4 the nonlinear force-current relationship (B.4) compromises this input-output relationship, with sharp peaks and shallow troughs in the output signal. The gain and phase of such signals may still be found, by firstly assuming the output to be a sinusoid of the same frequency as the input, and secondly correlating it with sine and cosine functions of the same frequency. The relative correlations and the amplitude of the input signal give the gain and phase of the output with respect to the input. This is the "correlation method" discussed in Ljung (1999). Figure B.5 shows the gain and phase plots over the frequency range of 0 to 2000 rad/s. A corner frequency of 55Hz (350rad/s) gives an idea of the bandwidth of the system. The roll-off rate is hard to

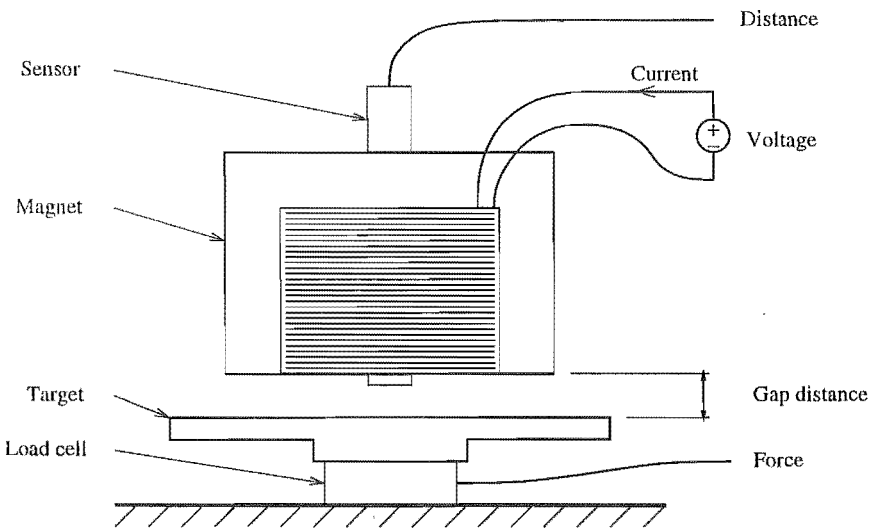

Figure B.2: *Rig for determining magnet force-distance-current relationship.*

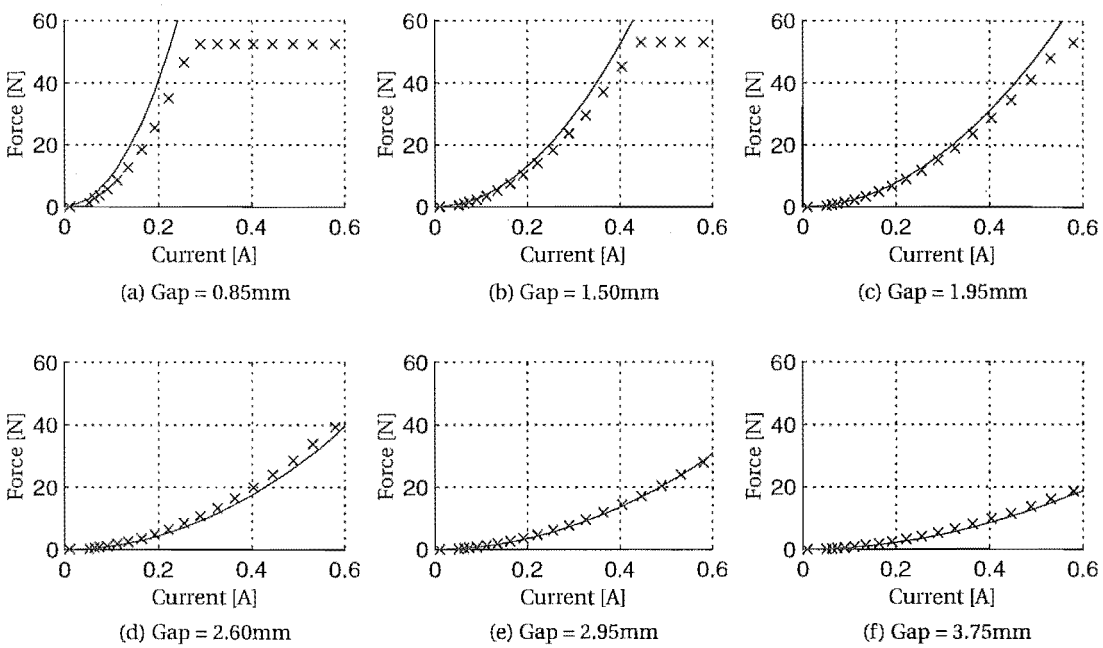

Figure B.3: *Static magnet calibration using steel block as target.*

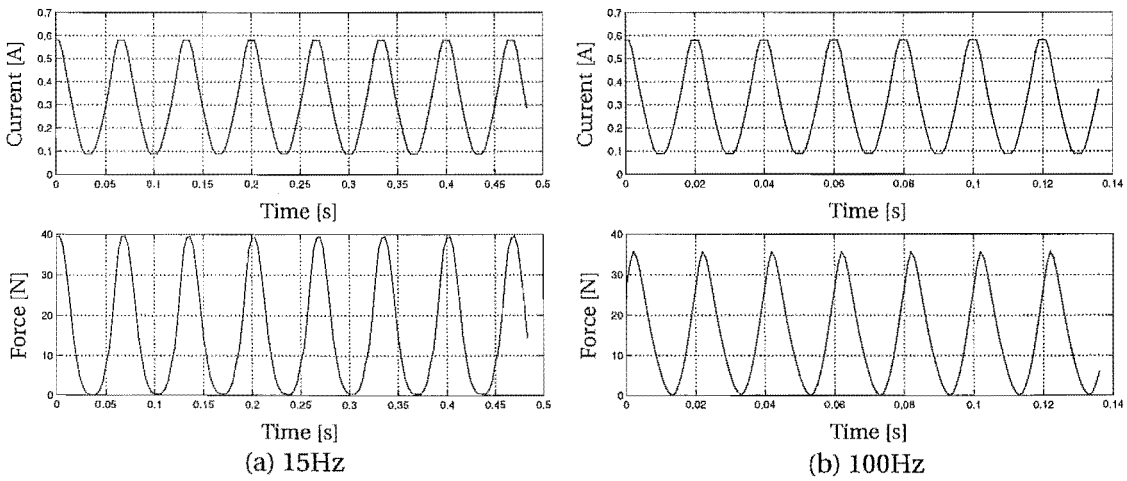

Figure B.4: *Input and output curves for magnet calibration using steel block as target.*

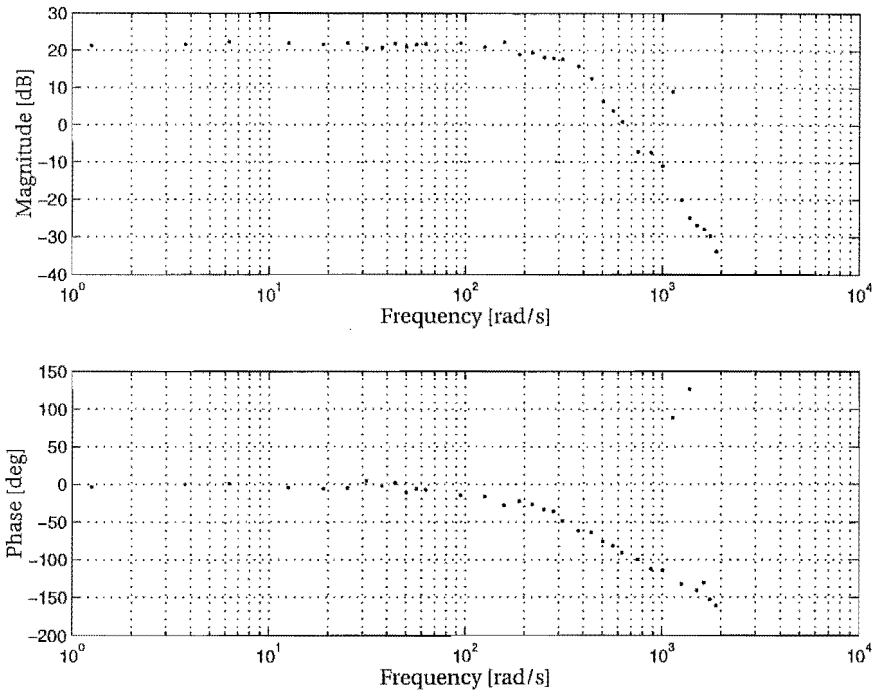

Figure B.5: *Frequency response for electromagnet over 2000 rad/s. Winding current is the input and force as measured by the load-cell arrangement is the output.*

judge with the available data, especially as the load cell dynamics are affecting the results (shown by the peaks in the plots near 180Hz (1125rad/s)). These effects could also be affecting the corner frequency. Figure B.6 plots the winding current against the output force at three different frequencies (with the phase difference between the signals removed), showing the hysteresis effects increasing with frequency and reiterating the attenuation displayed in Figure B.5. All of these curves compare the measured force with points calculated by (B.4), showing a reduction in accuracy of the static theory as frequency increases.

The above agreements between theory and experiment must also be tested with

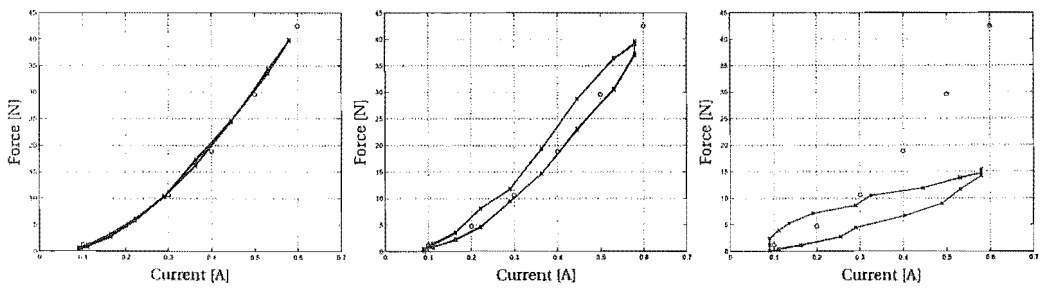

(a) Frequency = 0.2 Hz (1.26 rad/s)

(b) Frequency = 15 Hz (94.3 rad/s)

(c) Frequency = 100 Hz (628 rad/s)

Figure B.6: *Hysteresis curves at different forcing frequencies.*

the blade steel. Instead of using the load cell arrangement the bandsaw rig (Figure 4.1) was used, the deflection of the tensioned beam being used to monitor the force applied to the steel by the electromagnet. Figure B.7 plots the results for one of these experiments where the initial gap distance is 5.55mm. Figure B.7(a) shows the force-current-distance relationship on one plot while the remaining three plots show the various 2-D projections. In all of these plots the upright triangles indicate that the recordings are for increasing current and the upside-down triangles indicate decreasing current. Figure B.7(b) compares the experimental data with results from (B.4), showing correlation at low forces only. For higher forces the magnetic relationship increases nonlinearly, departing from the linear beam theory. This change is also noticeable in Figure B.7(d) where the Current-Distance curve changes from a nonlinear to a linear relationship. Similar tests but at different initial distances and beam tensions show this divergence repeatedly occurs at a flux around $\phi = 1.37 \times 10^{-5} Wb$, which equates by $B = \phi/A$ to a flux density of $B = 1.04T$. The calculations of Section B.1 assume that the target offers no resistance to the magnetic flux circulating around the path of Figure B.1(b). This is accurate for the steel block but inaccurate for the thin band except when the flux is below $1.37 \times 10^{-5} Wb$.

This inaccuracy may be remedied by relaxing the assumption that the target reluctance is insignificant in comparison with the air gaps. Considering the linear part of the B-H curve, we may say that $B = \mu H$ and so the reluctance of the target is given by $\Re = \frac{\ell_t}{\mu_r \mu_o A_t}$, substitution of which into the magnetic circuit equation gives a flux of

$$\phi = \frac{Ni}{\frac{d}{\mu_o}\left(\frac{1}{A_{g1}} + \frac{2}{A_{g2}}\right) + \frac{\ell_t}{\mu_o \mu_r A_t}}. \tag{B.5}$$

If the material is assumed to be approaching the knee of the B-H curve, then the relationship between B and H is better served by $B = B_s + \mu_o \mu_{r,s} H$, where B_s is the saturation flux density and $\mu_{r,s}$ is a permeability that fits the B-H curve above B=1T. The reluctance of the target then becomes

$$\Re = \frac{\mathfrak{F}_t}{\phi} = \frac{H_t \ell_t}{\phi} = \frac{(B_t - B_s)\ell_t}{\mu_o \mu_{r,s} \phi}, \tag{B.6}$$

which, by substituting (B.6) into the magnetic circuit equation and use of $B = \phi/A$ becomes

$$\phi = \frac{\mu_o Ni + \frac{B_s \ell_t}{\mu_r}}{d\left(\frac{1}{A_{g1}} + \frac{2}{A_{g2}}\right) + \frac{\ell_t}{\mu_r A_t}}. \tag{B.7}$$

Values of $\mu_r = 4000$ for $B \leq 1.04T$ and $\mu_{r,s} = 90$ for $B > 1.04T$ improves the accuracy of (B.1) up to $B = 1.52T$, whereupon the theoretical force again diverts from

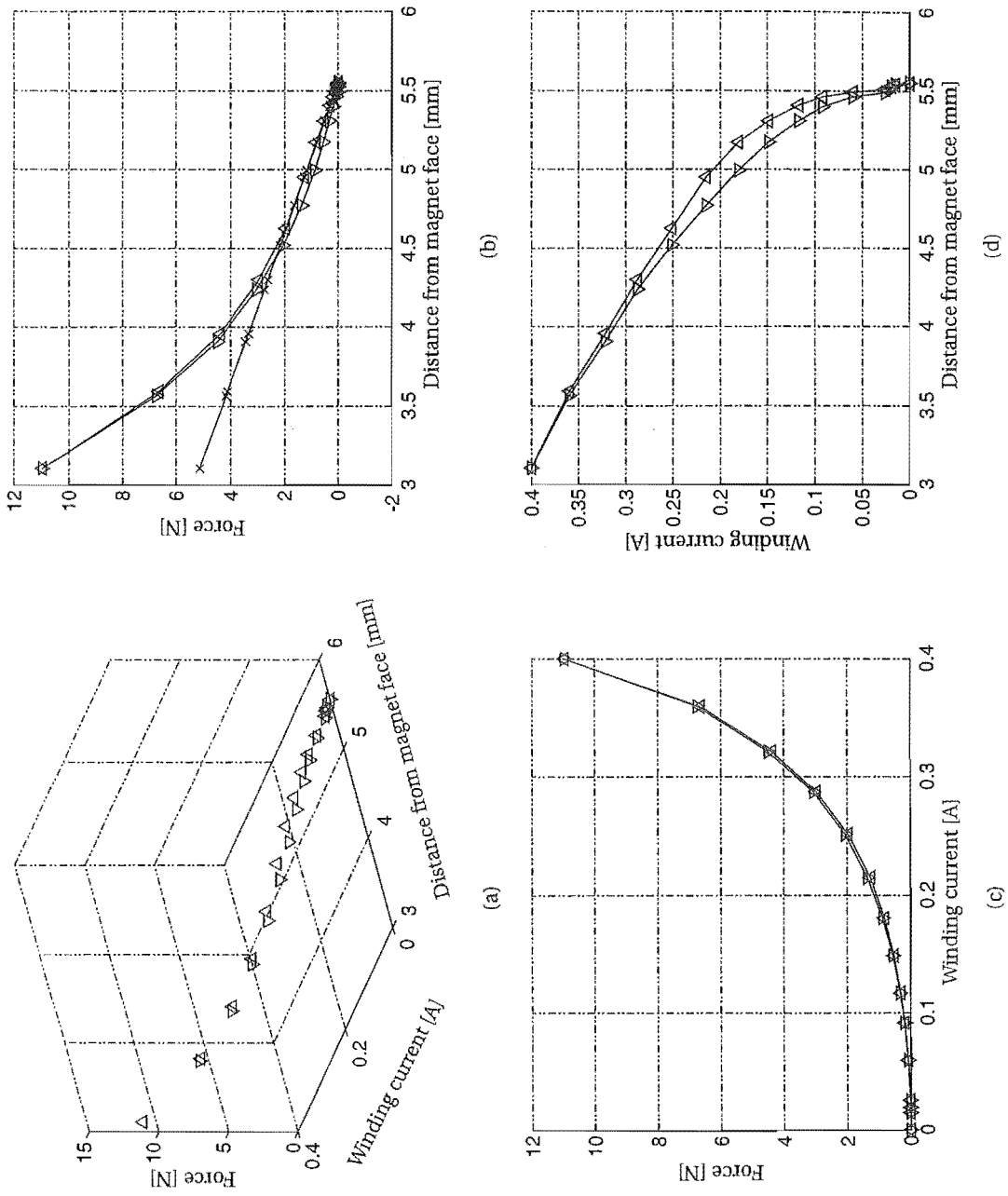

Figure B.7: *Static calibration of electromagnet using tensioned beam.* $R_o = 285N$. *Key* — × — *Beam force,* — ▵ — *Force from (B.4) along increasing current path,* — ▿ — *Force from (B.4) along decreasing current path.*

that measured. Using the same approach for $B_{s2} > 1.52T$ with $\mu_{r,s2} = 30$ gives the force-distance curves shown in Figure B.8. The agreement is excellent and exists for various initial gaps distances (as shown in Figure B.8) and also for other blade tensions.

B.2 SENSING

The aim of a collocated sensor and actuator requires the sensor to be insensitive to the direct effects of the actuator, in this case the magnetic field caused by the electromagnet windings. This section examines this sensitivity with regard to eddy current proximity sensors, which are geometrically favourable for this application and also offer suitable accuracy and range. Standard calibration of the sensors was performed but is not detailed here; suffice to say the sensors were linear within the required range and accurate to within the manufacturer's specifications.

Figure B.9 shows the effect of different magnetic fields at a constant distance, where the relative magnetic field intensities are given by the winding current in the surrounding coil. Interestingly, the sensor disturbance caused by the magnetic field is irrespective of the field strength. The disturbance is only 0.4% of the sensor range. However, the associated noise is more problematical. Figure B.10 shows the effect of magnetic fields varying sinusoidally, again the perturbation is not large but does introduce noise.

Figure B.11 shows the noise signal and corresponding power spectrum when each magnet has a small amount of current flowing through the coils. The power

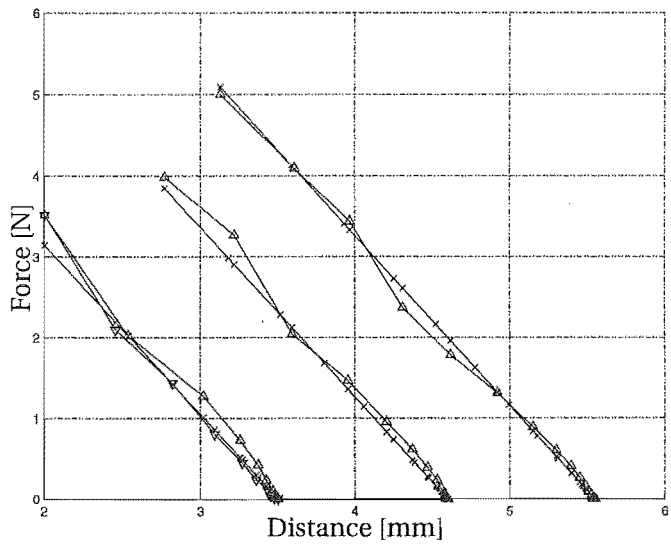

Figure B.8: *Calibration at different nominal distances, using saturated analysis. the curve starting at a gap distance of 5.5mm may be compared with Figure B.7b.*

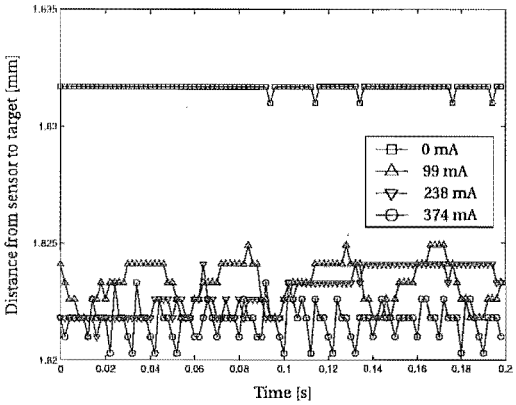

Figure B.9: *The effect on the position measurement due to four different magnetic fields.*

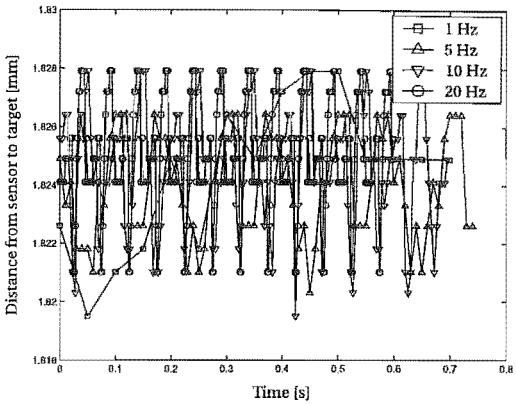

Figure B.10: *The effect on the position measurement due to sinusoidally changing magnetic fields.*

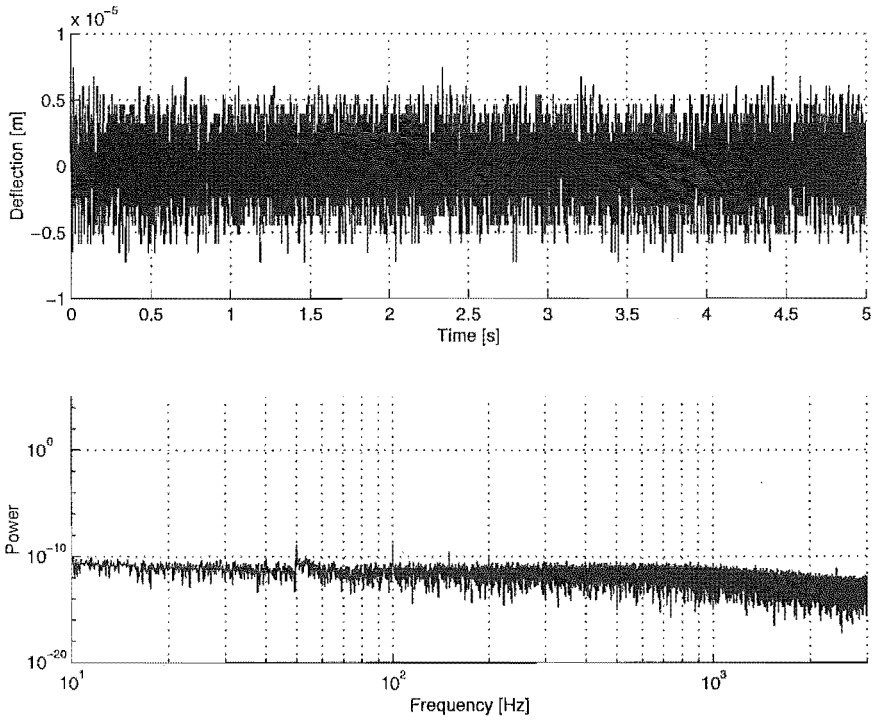

Figure B.11: *Noise signal and corresponding spectra.*

of the distance signal $y(t)$ may be approximated by

$$P = \frac{1}{T}\int_0^T y^2(t)dt \tag{B.8}$$

which for $T = 5$s gives $P = 2.6 \times 10^{-8}\text{m}^2$. Considering that the power spectral density is fairly flat throughout the range $[-1000, 1000]$Hz, we may say that the signal intensity V_y of $y(t)$ is $2.6 \times 10^{-8}/2000 \approx 1 \times 10^{-11}\text{m}^2\text{s}$. For truly white noise the power spectral density is flat over the entire frequency range, and so by definition the power spectral density is equal to the intensity V. This analysis is approximate but will nevertheless be invaluable in the control formulations of Chapter 5.

Filtering. Filtering the sensed deflection of the blade with a 1kHz second order Butterworth filter reduces high frequency noise and the noise caused by interaction between the sensors. This interaction was in fact larger than the affect of the electromagnets on the sensors. Such filtering does not alter the above analysis.

B.3 CURRENT DRIVER SPECIFICATION

Various means of controlling the current in magnet windings were tried, the final and most successful one is briefly discussed.

The basic requirement of the current driver is to control the current in each magnet quickly and accurately. The device therefore has two identical channels, one of which is discussed here. The core of the driver is a 150V supply, connected in series to the magnet coil, a switching transistor and a sense resistor which is tied to ground. The voltage across the sense resistor is proportional to the current flowing through it (and therefore the coil), and this voltage is compared to a reference voltage which is proportional to a PWM signal generated by the PC. If the sensed voltage is higher than the reference or the channel has been turned off then the switching transistor is turned off, so that the voltage is removed from the coil. While this system works well for increasing the current quickly, there is no means of quickly reducing it. When the switching transistor turns off, the source voltage rises, and when this reaches 300V a Zener diode allows current to flow to the gate of another transistor which allows the current also to flow through a load resistor, the coil and back around the loop. This very quickly reduces the current in the coil.

This discussion ignores isolation of the driver from the computer, bias resistors, protection diodes and filtering. The device was designed and built in-house.

B.4 CONTROL IMPLEMENTATION

B.4.1 Hardware

The controller was implemented on 233MHz Pentium II personal computer. A PCL-818L data acquisition card performed the A/D conversion of the filtered and amplified sensor signals and also the generation of PWM signals for the current driver. An in-house Universal Pulse Processor (UPP) card was used for the timing required for calculating the band speed.

B.4.2 Software

The control software was written in C and C++, and run on the Windows NT operating system using the RTX* real-time scheduler. A graphical front end allowed selection of the controller type and gain, test duration, control start times etc, as well as displaying pertinent data as the test ran. Data was then saved and plotted using the MATLAB code developed for the simulation results. New controllers could be developed and simulated using MATLAB and immediately tested on the real system, providing a very fast turn around time.

Real-time computing. The RTX real-time extension of Windows NT was used in this work. This extension provides deterministic control of the OS, reducing interrupt latencies and prioritising certain user-space processes above those of the OS. Also, RTX provides an excellent API, allowing easy interprocess communication and event management. Using this real-time extension the need for dedicated digital signal processors is obviated.

*See `http://www.vci.com/products/vci_products/rtx/rtx_index.html`

Appendix C

SIGNALS AND SYSTEMS

C.1 CONTROL THEORY

The theory below comes almost entirely from Glover and McFarlane (1989, 1992), and Vinnicombe (1993b,a). Boldface capitals represent constant matrices, and normal faced capitals represent linear, finite dimensional (LTI) dynamical systems, either in transfer function matrix or state-space descriptions.

C.1.1 Signals, systems, and spaces thereof

Input-output systems. A system $G = G(s)$ that maps inputs $\left[\begin{smallmatrix}\mathbf{w}\\ \mathbf{u}\end{smallmatrix}\right]$ into outputs $\left[\begin{smallmatrix}\mathbf{z}\\ \mathbf{y}\end{smallmatrix}\right]$ may be block partitioned so that

$$G(s) = \begin{bmatrix} G_{zw} & G_{zu} \\ G_{yw} & G_{yu} \end{bmatrix}, \tag{C.1}$$

where $G_{zw}(s)$ defines the effect of inputs $\mathbf{w}$ upon the outputs $\mathbf{z}$, G_{zu} defines the effect of $\mathbf{u}$ on $\mathbf{z}$, and so on. G may also be expressed in a state-space format, so that

$$G = G(s) = \left[\begin{array}{c|cc} \mathbf{A} & \mathbf{B}_1 & \mathbf{B}_2 \\ \hline \mathbf{C}_1 & \mathbf{D}_{11} & \mathbf{D}_{12} \\ \mathbf{C}_2 & \mathbf{D}_{21} & \mathbf{D}_{22} \end{array}\right] = \left[\begin{array}{c|c} \mathbf{A} & \mathbf{B} \\ \hline \mathbf{C} & \mathbf{D} \end{array}\right] := \mathbf{C}(s\mathbf{I} - \mathbf{A})^{-1}\mathbf{B} + \mathbf{D}, \tag{C.2}$$

and the block partitioning of $\mathbf{B}$, $\mathbf{C}$ and $\mathbf{D}$ are conformal with that of (C.1).

Signal spaces and norms. In this work we shall refer to $\mathcal{L}_{2+}$ as the space of temporal signals with a finite $\mathcal{L}_2$-norm that are identically zero for $t < 0$. The $\mathcal{L}_2$-norm of such a signal (in this case a vector valued signal $\mathbf{u}(t)$) is given by

$$\left\|\mathbf{u}\right\|_2 := \sqrt{\int_0^\infty \mathbf{u}(t)^T\mathbf{u}(t)dt}. \tag{C.3}$$

The Laplace transform maps $\mathcal{L}_{2+}$ onto the space of functions that are analytic in the open right half of the complex plane. This space is denoted $\mathcal{H}_2$ and the associated norm (denoting the Laplace transform of $\mathbf{u}(t)$ by $\tilde{\mathbf{u}}(s)$) is given by

$$\left\|\tilde{\mathbf{u}}\right\|_2 := \sqrt{\sup_{\sigma>0}\left\{\frac{1}{2\pi}\int_{-\infty}^{\infty}\tilde{\mathbf{u}}(\sigma+j\omega)^T\tilde{\mathbf{u}}(\sigma+j\omega)d\omega\right\}}, \tag{C.4}$$

in which the supremum can be shown to be on the boundary of the open right half plane, so that

$$\left\|\tilde{\mathbf{u}}\right\|_2 = \sqrt{\frac{1}{2\pi}\int_{-\infty}^{\infty}\tilde{\mathbf{u}}(j\omega)^T\tilde{\mathbf{u}}(j\omega)d\omega}. \tag{C.5}$$

By Parseval's relation both (C.3) and (C.5) yield identical results. Throughout this work we shall almost always consider signals in $\mathcal{H}_2$ ($\mathcal{L}_{2+}$), and will use $\mathcal{H}_2$ even when discussing temporal signals, except where confusion may arise. For completeness, the space $\mathcal{L}_2(-\infty,\infty)$ includes those functions defined for both positive and negative time, and $\mathcal{L}_2(j\mathbb{R})$ its frequency counterpart. Definitions for the norms on each of these spaces are identical (C.3) and (C.5), with the lower limit of integration in (C.3) replaced with $-\infty$.

Function spaces and norms. We shall also use the spaces $\mathcal{H}_2$, $\mathcal{RH}_2$, $\mathcal{H}_\infty$ and $\mathcal{RH}_\infty$ and the $\mathcal{H}_2$- and $\mathcal{H}_\infty$-norms in the analysis and descriptions of input-output systems. A system $G = G(s)$, described as a matrix of complex-valued functions mapping inputs $\mathbf{u}$ to outputs $\mathbf{y}$, is an element of $\mathcal{H}_2$ if $\left\|G\right\|_2$ is finite, where

$$\left\|G\right\|_2 := \sqrt{\sup_{\sigma>0}\left\{\frac{1}{2\pi}\int_{-\infty}^{\infty}\mathrm{tr}(G(\sigma+j\omega)^TG(\sigma+j\omega))d\omega\right\}}. \tag{C.6}$$

which can again be shown to be equal to

$$\left\|G\right\|_2 = \sqrt{\frac{1}{2\pi}\int_{-\infty}^{\infty}\mathrm{tr}(G(j\omega)^TG(j\omega))d\omega}. \tag{C.7}$$

The subspace of $\mathcal{H}_2$ given by strictly proper rational functions of s with real coefficients is denoted $\mathcal{RH}_2$. The $\mathcal{H}_2$-norm of G may also be found from its state space description (not shown here), as long as G is stable and strictly proper ($D = 0$). In the SISO case $\left\|G\right\|_2$ is equal to the $\mathcal{L}_2$-norm of the impulse response of G, and in the MIMO case it is equal to the $\mathcal{L}_2$-norm of the sum of the responses to impulses in the directions corresponding to each of the basis vectors that span the input space of G.

A system G is an element of $\mathcal{H}_\infty$ if it is analytic in the open right half plane and

$\|G\|_\infty$, defined as

$$\|G\|_\infty := \sup_{\omega \in \mathbb{R} \cup \infty} \overline{\sigma}(G(j\omega)), \tag{C.8}$$

is finite. Using the definition of the maximum singular value, $\overline{\sigma}(\cdot)$, (C.8) becomes

$$\|G\|_\infty = \sup_{\mathbf{u} \in \mathcal{H}_2 \backslash \mathbf{u}=0} \frac{\|G\mathbf{u}\|_2}{\|\mathbf{u}\|_2}, \tag{C.9}$$

and hence $\|G\|_\infty$ can be interpreted as the worst case energy gain of G over all frequency and for all input signals in $\mathcal{H}_2$. This interpretation shows that any system with finite $\mathcal{H}_\infty$-norm is stable (in the bounded input, bounded output sense). The space $\mathcal{RH}_\infty$ is a subspace of $\mathcal{H}_\infty$ and consists of all (stable) proper rational functions of s with real coefficients.

C.1.2 Coprime factors

A Left Coprime Factorisation (LCF) of G is given by $\begin{bmatrix} \tilde{M} & \tilde{N} \end{bmatrix}$ if, and only if, $G = \tilde{M}^{-1}\tilde{N}$, with $\tilde{M}, \tilde{N} \in \mathcal{RH}_\infty$ and

$$\tilde{M}U + \tilde{N}V = I, \tag{C.10}$$

where $U, V \in \mathcal{RH}_\infty$. Furthermore, if $U = \tilde{M}^T$ and $V = \tilde{N}^T$ then $\begin{bmatrix} \tilde{M} & \tilde{N} \end{bmatrix}$ is a *normalised* left coprime factorisation of G. Normalised Right Coprime Factorisations (RCFs), denoted $\begin{bmatrix} N \\ M \end{bmatrix}$, also exist, such that $G = NM^{-1}$, with $M, N \in \mathcal{RH}_\infty$ and $M^TM + N^TN = I$. All properties that hold for LCFs also hold for RCFs. Expressing systems in terms of their coprime factors has several advantages, one being that all RHP poles of G are contained in the zeros of M (or $\tilde{M}$), so that even unstable plants have stable coprime factors.

Definitions for LCFs and RCFs in terms of the state-space matrices of G are given by (Glover and McFarlane, 1989, Zhou, 1998)

$$\begin{bmatrix} \tilde{N} & \tilde{M} \end{bmatrix} := \left[\begin{array}{c|cc} \mathbf{A}+\mathbf{HC} & \mathbf{B}+\mathbf{HD} & \mathbf{H} \\ \hline \mathbf{R}^{-1/2}\mathbf{C} & \mathbf{R}^{-1/2}\mathbf{D} & \mathbf{R}^{-1/2} \end{array}\right], \tag{C.11}$$

and

$$\begin{bmatrix} N \\ M \end{bmatrix} := \left[\begin{array}{c|c} \mathbf{A}+\mathbf{BF} & \mathbf{BS}^{-1/2} \\ \hline \mathbf{C}+\mathbf{DF} & \mathbf{DS}^{-1/2} \\ \mathbf{F} & \mathbf{S}^{-1/2} \end{array}\right], \tag{C.12}$$

where

$$\begin{aligned} \mathbf{S} &= \mathbf{I} + \mathbf{D}^T\mathbf{D}, & \mathbf{R} &= \mathbf{I} + \mathbf{D}\mathbf{D}^T, \\ \mathbf{F} &= -\mathbf{S}^{-1}(\mathbf{D}^T\mathbf{C} + \mathbf{B}^T\mathbf{X}), & \mathbf{H} &= -(\mathbf{B}\mathbf{D}^T + \mathbf{Z}\mathbf{C}^T)\mathbf{R}^{-1}, \end{aligned} \tag{C.13}$$

and $\mathbf{X}$ and $\mathbf{Z}$ are the positive definite solutions of the algebraic Riccati equations

$$\begin{aligned} (\mathbf{A} - \mathbf{B}\mathbf{S}^{-1}\mathbf{D}^T\mathbf{C})^T\mathbf{X} + \mathbf{X}(\mathbf{A} - \mathbf{B}\mathbf{S}^{-1}\mathbf{D}^T\mathbf{C}) - \mathbf{X}\mathbf{B}\mathbf{S}^{-1}\mathbf{B}^T\mathbf{X} \\ + \mathbf{C}^T(\mathbf{I} - \mathbf{D}\mathbf{S}^{-1}\mathbf{D}^T)\mathbf{C} = 0, \end{aligned} \tag{C.14}$$

and

$$\begin{aligned} (\mathbf{A} - \mathbf{B}\mathbf{D}^T\mathbf{R}^{-1}\mathbf{C})\mathbf{Z} + \mathbf{Z}(\mathbf{A} - \mathbf{B}\mathbf{D}^T\mathbf{R}^{-1}\mathbf{C})^T - \mathbf{Z}\mathbf{C}^T\mathbf{R}^{-1}\mathbf{C}\mathbf{Z} \\ + \mathbf{B}(\mathbf{I} - \mathbf{D}^T\mathbf{R}^{-1}\mathbf{D})\mathbf{B}^T = 0, \end{aligned} \tag{C.15}$$

respectively. Equation (C.14) is known as the Generalised Control Algebraic Riccati Equation (GCARE), and (C.15) is known as the Generalised Filtering Algebraic Riccati Equation (GFARE). Solution schemes for solving such Riccati equations are freely and commercially available; however care should be taken in choosing third party solvers.

Using coprime factors to describe plant uncertainty. If a plant G has a LCF such that $G = \tilde{M}^{-1}\tilde{N}$, then we may consider a perturbed plant, G_Δ, such that

$$G_\Delta = (\tilde{M} + \Delta_M)^{-1}(\tilde{N} + \Delta_N), \tag{C.16}$$

where $\tilde{N}_\Delta = \tilde{N} + \Delta_N$ and $\tilde{M}_\Delta = \tilde{M} + \Delta_M$ are left coprime factors of G_Δ. This uncertainty model is presented in feedback with a controller K in Figure C.1. From this figure we find the following equations:

$$\begin{aligned} \mathbf{z}_{d,1} &= \mathbf{u} \\ \mathbf{y} = \mathbf{z}_{d,2} &= \tilde{M}^{-1}\mathbf{w}_d + G\mathbf{u} \\ \mathbf{u} &= K\mathbf{y}, \end{aligned} \tag{C.17}$$

which may be rearranged to give

$$\mathbf{z} = \begin{bmatrix} \mathbf{z}_{d,1} \\ \mathbf{z}_{d,2} \end{bmatrix} = \underbrace{\begin{bmatrix} K \\ I \end{bmatrix}(I - GK)^{-1}\tilde{M}^{-1}}_{T_{zw}}\mathbf{w}, \tag{C.18}$$

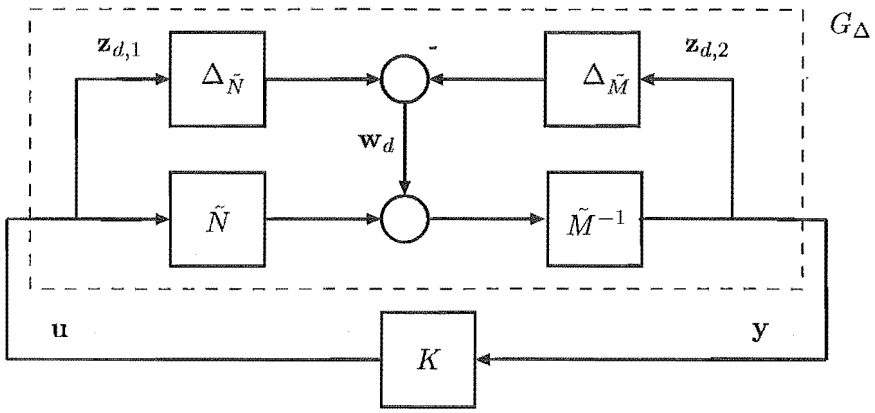

Figure C.1: *Coprime factor uncertainty.*

where $||T_{zw}||_\infty$ is the quantity to be minimised in the optimal $\mathcal{H}_\infty$ control synthesis. Because the ∞-norm is invariant under multiplication by unitary matrices, we may say that

$$\begin{aligned}\left\|T_{zsw}\right\|_\infty &= \left\| \begin{bmatrix} K \\ I \end{bmatrix} (I - GK)^{-1} \tilde{M}^{-1} \right\|_\infty \\ &= \left\| \begin{bmatrix} K \\ I \end{bmatrix} (I - GK)^{-1} \tilde{M}^{-1} \begin{bmatrix} \tilde{M} & \tilde{N} \end{bmatrix} \right\|_\infty \\ &= \left\| \begin{bmatrix} K \\ I \end{bmatrix} (I - GK)^{-1} \begin{bmatrix} I & G \end{bmatrix} \right\|_\infty ,\end{aligned}$$

thereby removing the need to calculate $\tilde{M}^{-1}$.

Furthermore, Figure C.1 may be recast as a *Linear Fractional Transformation* (LFT), as shown in Figure C.2. If we ignore the inputs $\mathbf{w}_p$ and outputs $\mathbf{z}_p$, we can

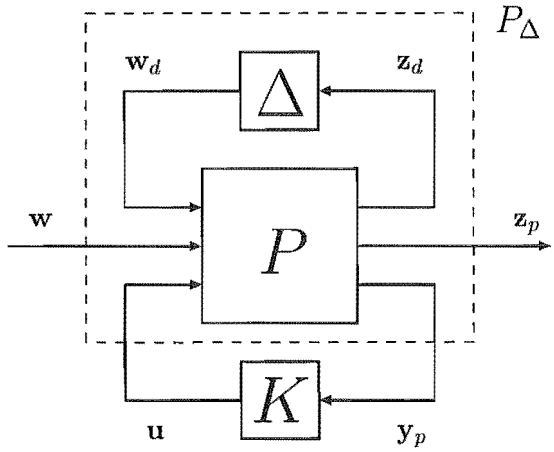

Figure C.2: *LFT showing uncertainty block, plant and controller.*

use (C.17) to find the generalised plant

$$P = \begin{bmatrix} 0 & I \\ \tilde{M}^{-1} & G \\ \tilde{M}^{-1} & G \end{bmatrix}, \tag{C.19}$$

with

$$\Delta = \begin{bmatrix} \Delta_N & -\Delta_M \end{bmatrix}. \tag{C.20}$$

Considering (C.18) as the transfer function combining the controller and the generalised plant in Figure C.2, we have by the small gain theorem that, if $||\Delta||_\infty < 1$, then the closed-loop system is internally stable if, and only if,

$$\left\| \begin{bmatrix} K \\ I \end{bmatrix} (I - GK)^{-1} \tilde{M}^{-1} \right\|_\infty \leq 1. \tag{C.21}$$

C.1.3 Gap metrics and the graph topology: effectively describing uncertainty in feedback systems

The search for a useful *measuring-stick* for comparing stable and/or unstable systems in a feedback loop received a lot of attention throughout the 1980s and early 1990s. The *gap* between two, possibly unstable, systems was introduced to control theory by Zames and El-Sakkary (1980), and it provides a *metric* by which stable and unstable systems can be compared. This metric takes values from zero to unity, and, because it involves minimisation of an $\mathcal{H}_\infty$-norm its computation is an iterative process. The *graph metric* was introduced in Vidyasagar (1984) and provides a more general but computationally more difficult metric. Vinnicombe (1993a) introduced the ν-gap metric, which is directly calculable using coprime factorisations of the two plants, and also has a clear frequency response interpretation that gives more information than the metric alone. Also, it can be extended beyond unity, another advantage over the gap metric. All of these metrics induce the same *topology*, known as the *graph topology*. This subsection discusses the gap metric briefly and the ν-gap more fully. However, prior to launching into these discussions, motivation for such *metrics* is given.

Motivation for feedback specific metrics. Figure C.3 shows two different plants with identical inputs. The output of this system is the difference in the plant outputs, and therefore a reasonable measure of the "difference" between these two plants is the size of the difference of their outputs. Considering signal energy as the measure

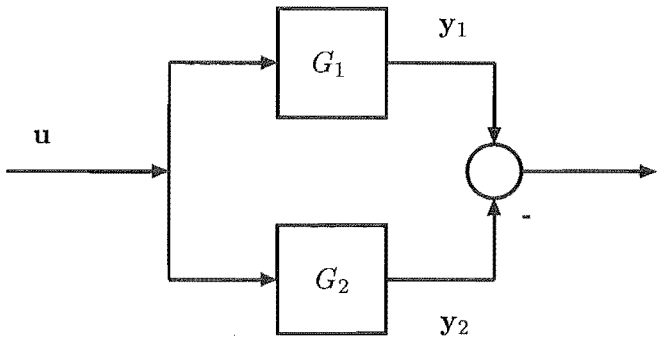

Figure C.3: *Measuring open loop uncertainty.*

of size, we may represent the difference in outputs by

$$\begin{aligned}\delta_n(G_1, G_2) &= \sup_{\mathbf{u}\in\mathcal{H}_2\setminus\mathbf{u}=0} \frac{\left\|G_1\mathbf{u} - G_2\mathbf{u}\right\|_2}{\left\|\mathbf{u}\right\|_2} \\ &= \left\|G_1 - G_2\right\|_\infty \\ &= \sup_{\omega\in\mathbb{R}\cup\infty} \overline{\sigma}(G_1(j\omega) - G_2(j\omega)).\end{aligned} \tag{C.22}$$

So, the difference in energy between the outputs (normalised by the input energy to keep δ_n bounded) is the maximum of the difference between the maximum energy gains of the systems over all frequency. Such a scheme is useful in comparing the open-loop behaviour of two plants, but takes no account of the feedback loop that the plants are about to be part of. Figure C.4 shows the feedback equivalent of Figure C.3, where the two plants are in feedback with the same controller K. Now, for an input $\begin{bmatrix}\mathbf{w}_1\\ \mathbf{w}_2\end{bmatrix}$, both the outputs *and* inputs for each plant will differ, and so a measure of the difference between the plants must take account of both of these quantities. The *directed gap* (Zames and El-Sakkary, 1980) provides such a measure, and is defined as

$$\vec{\delta}_g(G_1, G_2) = \sup_{\begin{bmatrix}\mathbf{y}_1\\ \mathbf{u}_1\end{bmatrix}\in\mathcal{G}_1} \inf_{\begin{bmatrix}\mathbf{y}_2\\ \mathbf{u}_2\end{bmatrix}\in\mathcal{G}_2} \frac{\left\|\begin{bmatrix}\mathbf{y}_1\\ \mathbf{u}_1\end{bmatrix} - \begin{bmatrix}\mathbf{y}_2\\ \mathbf{u}_2\end{bmatrix}\right\|_2}{\left\|\begin{bmatrix}\mathbf{y}_1\\ \mathbf{u}_1\end{bmatrix}\right\|_2}, \tag{C.23}$$

where $\mathcal{G}_i$, called the *graph* of G_i, is defined as the closed subspace of ${\mathcal{H}_2}^{p+q}$ given by all bounded pairs $(\mathbf{u}_i, \mathbf{y}_i)$ such that $\mathbf{y}_i = G_i\mathbf{u}_i$, assuming that G_i has p inputs and q outputs. In this framework, stable systems may be compared to unstable ones as long as the domain of an unstable system is restricted to that for which the range remains in $\mathcal{H}_2$.

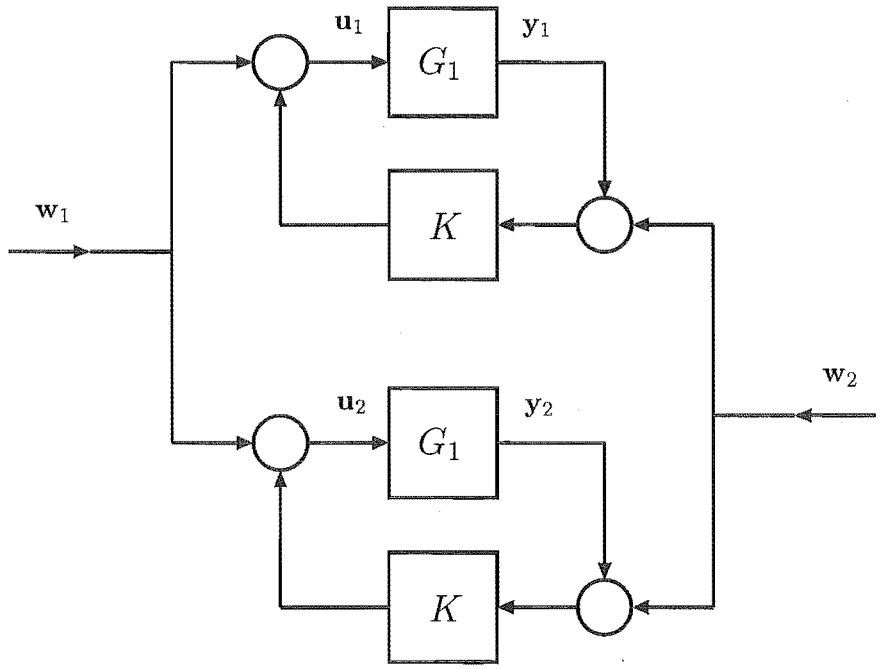

Figure C.4: *Measuring closed-loop uncertainty.*

Equation (C.23) can be made more tractable by defining the following *graph operators*,

$$\mathsf{G}_i := \begin{bmatrix} N_i \\ M_i \end{bmatrix}, \tilde{\mathsf{G}}_i := \begin{bmatrix} -\tilde{M}_i & \tilde{N}_i \end{bmatrix}, \tag{C.24}$$

for which, by Vinnicombe (1993b, Prop. II.5),

$$\begin{aligned} \mathcal{G}_i &= \{ \begin{bmatrix} N_i \\ M_i \end{bmatrix} \mathbf{q} : \mathbf{q} \in \mathcal{H}_2 \} = \mathsf{G}_i \mathcal{H}_2 \\ &= \{ \begin{bmatrix} -\tilde{M}_i & \tilde{N}_i \end{bmatrix} \mathbf{q} : \mathbf{q} \in \mathcal{H}_2 \} = \tilde{\mathsf{G}}_i \mathcal{H}_2, \end{aligned} \tag{C.25}$$

(in fact, by Vidyasagar (1984), these relations hold for unnormalised coprime factors too). It is not obvious that (C.25) are equivalent to the the graph of G_i as defined in the previous paragraph. However, for any $G \in \mathcal{H}_\infty$, a satisfactory right coprime factorisation is $\left[\begin{smallmatrix} M \\ N \end{smallmatrix}\right] = \left[\begin{smallmatrix} I \\ G \end{smallmatrix}\right]$, for which (C.25) is equivalent to the original definition. Vinnicombe (1993b) proves the general case. Using these results (C.23) becomes

$$\vec{\delta}_g(G_1, G_2) = \sup_{\substack{\mathbf{q}_1 \in \mathcal{H}_2, \\ \mathbf{q}_1 \neq 0}} \inf_{\mathbf{q}_2 \in \mathcal{H}_2} \frac{\left\| \mathsf{G}_1 \mathbf{q}_1 - \mathsf{G}_2 \mathbf{q}_2 \right\|_2}{\left\| \mathbf{q}_1 \right\|_2}. \tag{C.26}$$

It is worth noting that this expression is not yet in a computational form, but it is

useful to the exposition and the understanding of the relation between the gap and the graphs of the plants.

The actual gaps. Unfortunately, $\vec{\delta}_g(G_1, G_2)$ is not a metric as it is not symmetric in G_1 and G_2. However, the maximum of $\vec{\delta}_g(G_1, G_2)$ and $\vec{\delta}_g(G_2, G_1)$ is symmetric and indeed is a metric; the *gap metric*. Georgiou (1988) showed that this metric could be calculated by

$$\delta_g(G_1, G_2) = \max\{\inf_{Q\in\mathcal{H}_\infty} \left\|\mathsf{G}_1 - \mathsf{G}_2 Q\right\|_\infty, \inf_{Q\in\mathcal{H}_\infty} \left\|\mathsf{G}_2 - \mathsf{G}_1 Q\right\|_\infty\}, \tag{C.27}$$

which can be solved using iterative techniques to find arbitrarily close but not exact values for the infima. The ν-gap however, introduced in Vinnicombe (1993b,a) can be calculated directly. This metric equals the $\mathcal{L}_2$ gap between the plants if a winding number constraint on ${\mathsf{G}_2}^T\mathsf{G}_1$ is satisfied, and equals 1 if the winding constraint is not satisfied. The $\mathcal{L}_2$ gap is much easier to calculate than the $\mathcal{H}_2$ gap, and may be expressed as

$$\begin{aligned}
\vec{\delta}_{\mathcal{L}_2}(G_1, G_2) &= gap(\mathcal{M}_1, \mathcal{M}_2) && \text{(C.28)}\\
&= \left\|\tilde{\mathsf{G}}_2\mathsf{G}_1\right\|_\infty && \text{(C.29)}\\
&= \left\|(I + G_2G_2^T)^{-1/2}(G_2 - G_1)(I + G_1^TG_1)^{-1/2}\right\|_\infty . && \text{(C.30)}
\end{aligned}$$

In (C.28), $\mathcal{M}_1$ and $\mathcal{M}_2$ are the $\mathcal{L}_{2+}$ equivalents of (C.25). The step from (C.28) to (C.29) involves rather more mathematics than discussed so far, but is briefly covered in Vinnicombe (1993a). (C.30) follows from (C.29) by the definitions of the graph operators in (C.24), and because $\tilde{\mathsf{G}}_2\mathsf{G}_1 = \tilde{M}_2(G_2 - G_1)M_1$ and $(I + G_2G_2^T)^{-1} = \tilde{M}_2^T\tilde{M}_2$, $(I + G_1^TG_1)^{-1} = \tilde{M}_1\tilde{M}_1^T$. Also, $\vec{\delta}_{\mathcal{L}_2}(G_1, G_2) = \vec{\delta}_{\mathcal{L}_2}(G_2, G_1)$, and so the symmetry problem of $\vec{\delta}_g(G_1, G_2)$ does not exist. The following statement defines the ν-gap metric, along with the winding number constraint:

$$\delta_\nu(G_1, G_2) := \begin{cases} \left\|\tilde{\mathsf{G}}_2\mathsf{G}_1\right\|_\infty & \text{if } \det(\mathsf{G}_2^\mathsf{T}\mathsf{G}_1)(j\omega) \neq 0\ \forall\,\omega \in (-\infty, \infty) \\ & \text{and wno } \det(\mathsf{G}_2^\mathsf{T}\mathsf{G}_1) = 0, \\ 1 & \text{otherwise.} \end{cases} \tag{C.31}$$

The winding number condition can be equivalently stated as $\det(I + G_2^TG_1)(j\omega) \neq 0 \forall \omega \in (-\infty, \infty)$, wno $\det(I + G_2^TG_1) + \eta(G_1) - \eta(G_2) = 0$, where wno$(G_i)$ is the winding number of $G_i(s)$ evaluated around the standard Nyquist D-contour. This has obvious similarities to the multivariable Nyquist criterion (Doyle and Stein, 1981).

The ν-gap metric may be considered dual to the maximum stability margin b_{opt} in $\mathcal{H}_\infty$ controller synthesis (Vinnicombe, 1993a). Also, the ν-gap can be extended beyond 1, and also interpreted as a function of frequency, rather than as a single

number. This frequency response interpretation is clear for a SISO system; the ν-gap is equal to the maximum chordal distance between the Nyquist contours of the plants, when the contours are projected onto the Riemann sphere. Naturally, the encirclement condition must be satisfied when applying this interpretation. These facts are intriguing, and offer a lot in terms of system analysis, but in this work only the standard ν-gap is used.

Example C.I Figure C.5 shows two carts connected by a spring and a dash-pot. Nominal model parameters are $m_1 = m_2 = 1\text{kg}$, $k_1 = k_2 = 1\text{N/m}$, $c_1 = 0.02\text{Ns/m}$, $c_2 = 0.01\text{Ns/m}$. We will consider the model uncertainty created by variation in c_2. Table C.1 shows the open loop gap δ_n between five different plants, where the damping ranges from $c_2 = 0.05$ to $c_2 = -0.05$. The entries corresponding to negative damping coefficients do not give any useful information regarding "distance". This is expected as $G_i - G_j$ is unstable when either plant is unstable, so the $\mathcal{H}_\infty$-norm is meaningless. In contrast, Table C.2, which gives δ_ν between the plants, is meaningful when comparing stable and/or unstable plants. The entries in this table are very slightly smaller than δ_g.

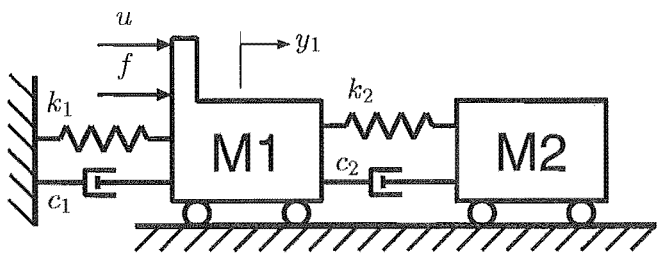

Figure C.5: *Two connected carts.*

Table C.1: $\delta_n(G_i, G_j)$ *for two cart system (Example I).*

		G_j				
	c_2	**0.05**	**0.01**	**0**	**-0.01**	**-0.05**
	0.05	0	26.58	39.46	104.02	1711.38
	0.01	26.58	0	17.51	113.45	1686.44
G_i	**0**	39.46	17.51	0	130.73	1671.22
	-0.01	104.02	113.45	130.73	0	1652.65
	-0.05	1711.38	1686.44	1671.22	1652.65	0

Example C.II If we now consider the uncertainty to be caused by variations in the spring stiffness k_2, so that $k_2 \in \{2, 2.5, 1, 1.5, 1\}$, we find the values for δ_n shown in Table C.3, and those for δ_ν shown in Table C.4. So in this example both metrics give similar results, that is that none of these plants are "close". However, the δ_ν-gap does

Table C.2: *$\delta_\nu(G_i, G_j)$ for two cart system (Example I).*

		G_j				
	c_2	**0.05**	**0.01**	**0**	**-0.01**	**-0.05**
	0.05	0	0.17	0.21	0.25	0.41
	0.01	0.17	0	0.04	0.09	0.25
G_i	**0**	0.21	0.04	0	0.04	0.21
	-0.01	0.25	0.09	0.04	0	0.17
	-0.05	0.41	0.25	0.21	0.17	0

Table C.3: *$\delta_n(G_i, G_j)$ for two cart system (Example II).*

		G_j				
	k_2	**3**	**2.5**	**2**	**1.5**	**1**
	3	0	68.92	72.73	72.64	72.72
	2.5	68.92	0	72.71	72.59	72.73
G_i	**2**	72.73	72.71	0	72.70	72.49
	1.5	72.64	72.59	72.70	0	71.90
	1	72.72	72.73	72.49	71.90	0

produce qualitatively better results, in that it reduces with our intuitive notion of closeness (even though the plants are essentially a long way away from each other).

Example C.III The previous example was very lightly damped; this example considers the same system and uncertainty as the last but with both dash-pots set at ten times their previous values. Tables C.5 and C.6 show the results. So the spring stiffness now has a much smaller effect on the closeness of the plants, as measured by both metrics. The system is therefore more robust, which is exactly as we would expect.

Table C.4: *$\delta_\nu(G_i, G_j)$ for two cart system (Example II).*

		G_j				
	k_2	**3**	**2.5**	**2**	**1.5**	**1**
	3	0	0.976	0.992	0.994	0.997
	2.5	0.976	0	0.972	0.995	0.998
G_i	**2**	0.992	0.972	0	0.964	0.996
	1.5	0.994	0.995	0.964	0	0.943
	1	0.997	0.998	0.996	0.943	0

Table C.5: $\delta_n(G_i, G_j)$ *for two cart system (Example III).*

		G_j				
	k_2	**3**	**2.5**	**2**	**1.5**	**1**
	3	0	1.05	2.60	4.81	6.81
	2.5	1.05	0	1.62	4.08	6.65
G_i	**2**	2.60	1.62	0	2.74	6.25
	1.5	4.81	4.08	2.74	0	4.98
	1	6.81	6.65	6.25	4.98	0

Table C.6: $\delta_\nu(G_i, G_j)$ *for two cart system (Example III).*

		G_j				
	k_2	**3**	**2.5**	**2**	**1.5**	**1**
	3	0	0.492	0.646	0.714	0.792
	2.5	0.492	0	0.538	0.703	0.786
G_i	**2**	0.646	0.538	0	0.592	0.771
	1.5	0.714	0.703	0.592	0	0.652
	1	0.792	0.786	0.771	0.652	0

REFERENCES

D. W. Alspaugh. Torsional vibration of a moving band. *Journal of the Franklin Institute*, 283(4):328–338, 1967.

R.B. Bhat. Natural frequencies of rectangular plates using characteristic orthogonal polynomials in Rayleigh-Ritz method. *Journal of Sound and Vibration*, 102:493–499, 1985.

J. Chen. Natural frequencies and stability of an axially-traveling string in contact with a stationary load system. *Journal of Vibrations and Acoustics, Transactions of the ASME*, 119:152–157, April 1997.

S. Chonan. Steady state response of an axially moving strip subjected to a stationary lateral load. *Journal of Sound and Vibration*, 107:155–165, 1986.

C. J. Damaren and L. Le-Ngoc. Robust active vibration control of a bandsaw blade. *Journal of Vibration and Acoustics*, 122:69–75, January 2000.

M. S. de Queiroz, D. M Dawson, C. D. Rahn, and F. Zhang. Adaptive vibration control of an axially moving string. *Journal of Vibration and Acoustics*, 121(1):41–49, January 1999.

J. Doyle and B. Francis. Linear control theory with an $\mathcal{H}_\infty$ optimality criterion. *SIAM Journal of Control and Optimisation*, 25(4):815–844, 1987.

J. Doyle, K. Glover, P. Khargonegar, and B. Francis. State-space solutions to standard $\mathcal{H}_2$ and $\mathcal{H}_\infty$ control problems. *IEEE Transactions on Automatic Control*, 34(8):831–847, 1989.

J. Doyle and G. Stein. Multivariable feedback design: Concepts for a classical/modern synthesis. *IEEE Transactions On Automatic Control*, 26(1):4–16, 1981.

R.-F. Fung and C.-C. Tseng. Boundary control of an axially moving string via Lyapunov method. *ASME Journal of Dynamic Systems, Measurement, and Control*, 121(1):105–110, 1999.

R.-F. Fung, J.-W. Wu, and S.-L. Wu. Exponential stabilization of an axially moving string by linear boundary feedback. *Automatica*, 35:177–181, 1999a.

R.-F. Fung, J.-W. Wu, and S.-L. Wu. Stabilization of an axially moving string by nonlinear boundary feedback. *ASME Journal of Dynamic Systems, Measurement, and Control*, 121(1):117–121, 1999b.

T. Georgiou. On the computation of the gap metric. *Systems and Control Letters*, 11: 253–257, 1988.

T. Georgiou and M. Smith. Optimal robustness in the gap metric. *IEEE Transactions on Automatic Control*, 36(6):673–686, June 1990.

K. Glover and D. McFarlane. Robust stabilisation of normalised coprime factor plant descriptions with $\mathcal{H}_\infty$-bounded uncertainty. *IEEE Transactions on automatic control*, 34(8):821–830, 1989.

K. Glover and D. McFarlane. A loop shaping design procedure using $\mathcal{H}_\infty$ synthesis. *IEEE Transactions on automatic control*, 37(6):759–769, 1992.

K. Glover and D. C. McFarlane. *Robust Controller Design Using Normalized Coprime Factor Plant Descriptions.* Number 138 in Lecture Notes in Control and Information Sciences. Springer-Verlag, 1990.

J. N. Goodier and S. Timoshenko. *Theory of Elasticity.* McGraw-Hill Book Company, Inc., 1951.

F. B. Hildebrand. *Methods of Applied Mathematics.* Prentice-Hall, Inc., 1965.

H. Kwakernaak and R. Sivan. *Linear Optimal Control Systems.* John Wiley and Sons, Inc., 1972.

S. Lee and C. D. Mote. Vibration control of an axially moving string by boundary control. *Journal of Dynamic Systems, Measurement, and Control*, 118:66–74, 1996.

S. Lee and C. D. Mote. Wave characteristics and vibration control of translating beams by optimal boundary control. *Journal of Vibration and Acoustics*, 121(1): 18–25, 1999.

B. F. Lehmann and S. G. Hutton. The mechanics of bandsaw cutting. Part I: Modelling the interaction between a bandsaw and the workpiece. *Holz als Roh-und Werkstoff*, 54:423–428, 1996.

B. F. Lehmann and S. G. Hutton. The mechanics of bandsaw cutting. Part II: A simulation of the cutting behaviour of bandsaws. *Holz als Roh-und Werkstoff*, 55:35–43, 1997.

A. W. Leissa. *Vibration of Plates.* NASA, 1969.

A. W. Leissa. The free vibration of rectangular plates. *Journal of Sound and Vibration*, 31:257–294, 1973.

L. Lengoc. *Vibration of bandsaws.* PhD thesis, Department of Mechanical Engineering, University of Canterbury, 1990.

L. Lengoc and H. McCallion. Wide bandsaw blade under cutting conditions, Part I: Vibration of a plate moving in its plane while subjected to tangential edge loading. *Journal of Sound and Vibration*, 186(1):125–142, 1995a.

L. Lengoc and H. McCallion. Wide bandsaw blade under cutting conditions, Part II: Stability of a plate moving in its plane while subjected to parametric excitation. *Journal of Sound and Vibration*, 186(1):143–162, 1995b.

L. Lengoc and H. McCallion. Wide bandsaw blade under cutting conditions, Part III: Vibration of a plate moving in its plane while subjected to non-conservative cutting forces. *Journal of Sound and Vibration*, 186(1):163–179, 1995c.

L. Lengoc and H. McCallion. Transverse vibration of a moving string: A comparison between the closed-form solution and the normal-mode solution. *Journal of Systems Engineering*, 6:72–78, 1996a.

L. Lengoc and H. McCallion. Transverse vibration of a moving string: A physical overview. *Journal of Systems Engineering*, 6:61–71, 1996b.

L. Lengoc and H. M. McCallion. Dynamic stiffness of an axially moving string. *Journal of Sound and Vibration*, 220(4):749–756, 1999.

L. Ljung. *System Identification: Theory for the User*, chapter 6, pages 170–172. Prentice Hall, Inc., 2nd edition, 1999.

S. P. Loehnertz, I. V. Cooz, and J. Guerrero. Sawing hardwoods in five tropical countries. Technical report, Forest Products Laboratory, United States Department of Agriculture, 1994.

W. L. Miranker. The wave equation in a medium in motion. *IBM Journal of Research and Development*, 4(1):36–42, 1960.

C. D. Mote. A Study of bandsaw vibrations. *Journal of the Franklin Institute*, 279(6): 430–444, June 1965.

C. D. Mote. On the non-linear oscillation of an axially moving string. *Journal of Applied Mechanics*, 33:463–464, 1966.

C. D. Mote. Dynamic stability of axially moving materials. *Shock and Vibration Digest*, 4(4):2–11, 1972.

C. D. Mote and K. W. Wang. Vibration coupling analysis of band/wheel mechanical systems. *Journal of Sound and Vibration*, 109(2):237–258, 1986.

C. D. Mote and J. A. Wickert. On the energetics of axially moving continua. *Journal of the Acoustical Society of America*, 85(3):1365–1367, March 1989.

C. D. Mote and W. Z. Wu. Vibration coupling in continuous belt and band systems. *Journal of Sound and Vibration*, 102(1):1–9, 1985.

C. D. Mote and B. Yang. Active vibration control of the axially moving string in the s domain. *Journal of Applied Mechanics*, 58:189–196, 1991a.

C. D. Mote and B. Yang. Controllability and observability of distributed gyroscopic systems. *ASME Journal of Dynamic Systems, Measurement, and Control*, 113:11–17, March 1991b.

C. D. Mote and B. Yang. Frequency-domain control of distributed gyroscopic systems. *ASME Journal of Dynamic Systems, Measurement, and Control*, 113:18–24, March 1991c.

R. Okai, S. Kimura, and H. Yokochi. Dynamic characteristics of the bandsaw I. *Mokuzai Gakkaishi*, 42(4):333–342, 1996.

K. Ono. Lateral motion of an axially moving string on a cylindrical guide surface. *Journal of Applied Mechanics*, 46(4):905–912, 1979.

R. Skutch. Uber die bewegung eines geespannten fadens, weicher gezwungen ist, durch zwei feste punkte, mit einer constanten geschwindigkeit zu gehen, und zwischen denselben in transversal-schwingungen von gerlinger amplitude versrtzt wird. *Annalen der Physik und Chemie*, 61:190–195, 1897.

S. Timoshenko and S. Woinowsky-Krieger. *Theory of Plates and Shells.* McCraw-Hill Book Company, Inc., 2nd edition, 1959.

A.G. Ulsoy and C.D. Mote. Vibration of wide band saw blades. *Journal of Engineering for Industry*, 104:71–78, 1982.

M. Vidyasagar. The graph metric for unstable plants and robustness estimates for feedback stability. *IEEE Transactions on Automatic Control*, 29(5):403–417, 1984.

G. Vinnicombe. Frequency domain uncertainty and the graph topology. *IEEE Transactions on Automatic Control*, 38(9):1371–1383, September 1993a.

G. Vinnicombe. *Measuring the Robustness of Feedback Systems.* PhD thesis, Cambridge University, 1993b.

Y. K. Wang and C. D. Mote. Active and passive vibration control of an axially moving beam by smart hybrid bearings. *Journal of Sound and Vibration*, 195(4):575–584, 1996.

R. Weinstock. *Calculus of Variations*. International series in Pure and Applied Mathematics. McGraw-Hill Book Company Inc., 1952.

J. A. Wickert and C. D. Mote. Current research on the vibration and stability of axially-moving continua. *Shock and Vibration Digest*, 20:3–13, 1988.

J. A. Wickert and C. D. Mote. Classical vibration analysis of axially moving continua. *ASME Journal of Applied Mechanics*, 57:738–744, September 1990.

R. Wijesinge. *The Bandmill Book*. Tech Pubs, Western Technigraphs Ltd., 1998.

B. Yang. Vibration control of gyroscopic systems via direct velocity feedback. *Journal of Sound and Vibration*, 175(4):525–534, 1994.

S. Ying and C. A. Tan. Active vibration control of the axially moving strip using space feedfoward and feedback controllers. *Journal of Vibration and Acoustics*, 118:306–312, July 1996.

G. Zames. On the input-output stability of nonlinear time-varying feedback systems, parts I and II. *IEEE Transactions On Automatic Control*, 11:228,465, 1966.

G. Zames. Feedback and optimal sensitivity: Model reference transformations, multipicative seminorms, and approximate inverses. *IEEE Transactions on Automatic Control*, 26(2):301–320, April 1981.

G. Zames and A. El-Sakkary. Unstable systems and feedback: The gap metric. In *Proceedings of the Allerton Conference*, pages 380–385, 1980.

F. Zhan and S. G. Hutton. The causes of washboarding in bandsaws. In *Proceedings of SawTech '89*, Oakland, California, October 1989.

K. Zhou. *Essentials of Robust Control*. Prentice-Hall, Inc., 1998.

K. Zhou, J. C. Doyle, and K. Glover. *Robust and Optimal Control*. Prentice-Hall, Inc., 1996.